The Origin of Large-Scale Magnetic Fields in Galaxies

by

Luke Chamandy

A Thesis For the Degree of

Doctor of Philosophy

(in Physics)

submitted to the

Jawaharlal Nehru University

Supervisor: **Prof. Kandaswamy Subramanian**

Inter-University Centre for Astronomy and Astrophysics

Post Bag – 04, Ganeshkhind, Pune – 411007, INDIA

October 2014

Certificate

This is to certify that the thesis entitled "**The origin of large-scale magnetic fields in galaxies**" submitted by Mr. Luke Chamandy for the award of the degree of Doctor of Philosophy of Jawaharlal Nehru University, New Delhi is his original work. This has not been published or submitted to any other University for any other Degree or Diploma.

Prof. Ajit Kembhavi
(Director of IUCAA)

Prof. Kandaswamy Subramanian
(Thesis Supervisor)

Declaration

I hereby declare that the work reported in this thesis is entirely original. This thesis is composed independently by me at the Inter University Centre for Astronomy and Astrophysics, Pune under the supervision of Prof. Kandaswamy Subramanian. I further declare that the subject matter presented in the thesis has not previously formed the basis for the award of any degree, diploma, membership, associateship, fellowship, or any other similar title of any University or Institution.

Prof. Kandaswamy Subramanian
(Thesis Supervisor)

Luke Chamandy
(Ph.D. Candidate)

Contents

List of Tables

List of Figures

Acknowledgment

First off, I thank my supervisor, Kandu, for mentoring me over the past four years or so. His combination of mathematical prowess and physical insight are rare and I feel lucky to be able to work with him. Not to mention his jolly nature, which can do a lot to counteract any feelings of pessimism. Most importantly, I was given freedom to try things but at the same time he would come through with a key insight when it was most needed. I also appreciate the kindness he and his wife Gayathri showed me and my family throughout the PhD.

Next, I thank Anvar Shukurov, whose expertise spans observation and theory. My discussions with Anvar are informative and stimulating as well as enjoyable, and he is a true master of scientific writing. I also thank Alice Quillen, who provided crucial expertise on galactic dynamics, and who, along with Eric Blackman, kindly hosted me during a brief visit to the University of Rochester. Axel Brandenburg got me started with the numerical work and passed on all his IDL routines, which was a great help. Paul Charbonneau sponsored me to work with him for two months in my hometown of Montreal, Canada. Thanks to him, I am now branching out to work on solar and stellar dynamos, and have a broader understanding of astrophysical dynamos in general. Pat Diamond kindly sponsored me to attend and give a talk at a workshop on plasma physics in South Korea, and Russ Taylor hosted me for a week at the University of Cape Town as this thesis was just ending. Binod Sreenivasan kindly sponsored me to attend and speak at a meeting on dynamos he was organising at the Indian Institute of Science, Bangalore. I also thank Ethan Vishniac for useful discussions about his recent work on helicity fluxes.

I am very grateful to other IUCAA and NCRA faculty, Dipankar Bhattacharya, Raghunathan Srianand, Dipanjan Mitra, Thanu Padmanabhan, among several others, for useful discussions on the thesis work as well as course and project work. I would also like to thank the IUCAA director, Ajit Kembhavi, for making it easy for me to attend various meetings.

I am happy to thank the other students and postdocs from whom I benefited through many interactions. Nishant Singh enthusiastically delved into drafts of my papers and offered great mathematical insight, as well as many useful and enjoyable conversations. I also had many interesting and spirited discussions with my frequent travel companion and fellow 'magnet' Pallavi Bhat, who helped me to learn about small-scale dynamos. Charles Jose was always very willing to provide me with templates for various proposals and even for this thesis, which saved me uncalculable time. Fred Gent generously spent a large portion of his first visit to IUCAA helping me to set up the Pencil Code and teaching me how to run his galactic dynamo simulation, which ought to come in very handy in the near future. Working at IUCAA was all the more rewarding and enjoyable because of the opportunity to interact with people like Kaustubh Vaghmare, Dipanjan Mukherjee, Sharanya Sur, Pranjal Trivedi, Hadi Rahmani, Aritra Basu, Varun Bhalerao, Suprit Singh, Prasanta Bera, Aditya Rotti, and many others.

IUCAA is a well-run institute and I am grateful to the administrative, computing centre and library staff for their help on countless occasions. In particular, Deepika Susainathan was always very helpful with travel arrangements, and both she and Senith Samuel assisted me in obtaining visas. I am also grateful to the caring staff of the IUCAA Creche, which my daughter Tina attended for some time.

This thesis could not have been completed if it were not for the help we received from friends. Many went out of their way to lend us a hand, including Seema Nikalje, Nisha and Himanshu Toshniwal, Geeta Pandhe, Vinod and Sunita Kumar, and especially Bhagyashree and Dhiraj Khot.

My parents Tina and Frank made this thesis possible. I am grateful for their continual support in several senses of the word and their never fading belief in me. I also can't forget the rest of my family, brothers, sister and their significant others, uncles, aunts, nephews and niece and my grandmother, who have all encouraged me with their interest and enthusiasm in what I am doing.

I thank my daughter Tina for being so good-natured and understanding when I had to work on weekends, Tina and Tory for being great sources of fun and inspiration, and Snoofy for being a great dog. Finally, I thank my wife Disha (Rosie) for first of all agreeing to my crazy idea of interrupting a good teaching career to return to studies, and secondly for supporting me throughout with her love, encouragement and patience.

List of Publications

i **Chamandy L.**, Subramanian, K., Shukurov, A., 2014, "Magnetic spiral arms and galactic outflows", MNRAS Letters, under review (arXiv:1408:3937)

ii **Chamandy L.**, Shukurov, A., Subramanian, K., Stoker, K., "Non-linear galactic dynamo theory: A toolbox", MNRAS, 443, 1867 (arXiv:1403:2562).

iii **Chamandy L.**, Subramanian K., Quillen A., 2014, "Magnetic arms generated by multiple interfering galactic spiral patterns", MNRAS, 437, 562 (arXiv:1308.0432).

iv **Chamandy L.**, Subramanian K., Shukurov A., 2013, "Galactic spiral pattern and dynamo action II: Asymptotic solutions", MNRAS, 433, 3274 (arXiv:1301.4761).

v **Chamandy L.**, Subramanian K., Shukurov A., 2013, "Galactic spiral patterns and dynamo action I: A new twist on magnetic arms", MNRAS, 428, 3569 (arXiv:1207.6239).

Abstract

Magnetic fields are an important component of spiral galaxies, and hence it is necessary to understand their origin, structure and evolution. In this thesis, we present models that describe the growth, saturation and physical properties of large-scale galactic magnetic fields. This is done by taking into account the non-linear back-reaction of the magnetic field on the turbulence, and hence on the dynamo action. The primary focus of the thesis is to explain the origin and observed characteristics of the non-axisymmetric components of large-scale magnetic fields in galaxies. Along the way, we develop and analyse various tools of non-linear galactic dynamo theory, and incorporate a number of physical effects into the theory for the first time.

We begin by comparing different models and approximations for non-linear mean-field dynamos in disc galaxies to assess their applicability and accuracy, and thus to suggest a set of simple solutions suitable to model the large-scale galactic magnetic fields in various contexts. The dynamo saturation mechanisms considered are the magnetic helicity balance involving helicity fluxes (the dynamical α-quenching) and an algebraic α-quenching. The non-linear solutions are then compared with the marginal kinematic and asymptotic solutions. We also discuss the accuracy of the no-z approximation. Although these tools are very different in degree of approximation and hence complexity, they all lead to remarkably similar solutions for the mean magnetic field. In particular, we show that the algebraic α-quenching non-linearity can be obtained from a more physical dynamical α-quenching model in the limit of nearly azimuthal magnetic field. This suggests, for instance, that earlier results on galactic disc dynamos based on the simple algebraic non-linearity are likely to be reliable, and that estimates based on simple, even linear models are often a good starting point. We suggest improved no-z and algebraic α-quenching models, and also incorporate galactic outflows into a simple analytical dynamo model to show that the outflow can produce leading magnetic spirals near the disc surface. The simple dynamo models developed are applied to estimate the magnetic pitch angle and the arm-interarm contrast in the saturated magnetic field strength for realistic parameter values.

More refined and detailed global dynamo models are then developed to investigate various properties of galactic large-scale magnetic fields. The effect of the dynamical α-quenching on the magnetic field evolution in an axisymmetric disc galaxy is explored. We confirm the work of earlier models based on the algebraic α-quenching formalism, in that sufficiently strong random seed fields can lead to global reversals of the large-scale field along the radius whose long-term survival depends on specific features of a given galaxy. Within this general framework, coherent large-scale magnetic spiral arms superimposed on the dominant axially symmetric magnetic structure are then considered. We first show that such non-axisymmetric components tend to decay in the non-linear regime in a disc that lacks non-axisymmetric forcing of the dynamo. We find, however, that the enhancement of the kinetic α effect (α_k) in spiral-shaped regions (which may overlap the gaseous spiral arms or be located in the interarm regions) can lead to strong non-axisymmetry, in the form of spiral-shaped regions of enhanced large-scale magnetic field. A non-axisymmetric forcing of the mean-field dynamo by a spiral pattern (either stationary or transient) is invoked. For a stationary dynamo forcing by a rigidly rotating α_k-spiral, we find co-rotating non-axisymmetric magnetic modes enslaved to the axisymmetric modes and strongly peaked around the co-rotation radius. At all galactocentric distances except for the co-rotation radius, we find magnetic arms displaced in azimuth from the α_k-arms, so that the ridges of magnetic field strength are more tightly wound than the α_k-arms. For a forcing by transient gaseous material arms wound up by the galactic differential rotation, the magnetic spiral is able to adjust to the winding so that it resembles the gaseous spiral at all times.

Famously, magnetic arms have in some cases been observed between the gaseous arms of some spiral galaxies; the origin of these phase-shifted magnetic arms remains unclear. With this motivation in mind, we generalise the theory of mean-field galactic dynamos by allowing for temporal non-locality in the mean electromotive force (emf). This arises in random flows due to a finite response time of the mean emf to changes in the mean magnetic field and small-scale turbulence, and leads to the telegraph equation for the mean field. There are profound effects associated with the temporal non-locality, i.e. finite 'dynamo relaxation time'. For the case of a rigidly rotating spiral, a finite relaxation time causes each magnetic arm to mostly lag the corresponding gaseous arm with respect to the rotation. For a transient α_k spiral that winds up, the finite dynamo relaxation time leads to a large, negative (in the sense of the rotation) phase shift between the magnetic and α_k arms, similar to the phase shift between magnetic and gaseous arms observed in NGC 6946 and other galaxies.

The exploration of mean-field galactic dynamos affected by a galactic spiral pattern is then continued with an asymptotic solution. As with the numerical solutions, the mean-field dynamo model used generalizes the standard theory to include the delayed response of the mean electromotive force to variations of the mean magnetic field and turbulence parameters (the temporal non-locality, or τ effect). The axisymmetric and enslaved non-axisymmetric modes of the mean magnetic field are studied semi-analytically to clarify and strengthen the numerical results. Good qualitative agreement is obtained between the asymptotic solution and numerical solutions for a global, rigidly rotating α_{k}-spiral (density wave).

Steady rigidly rotating spirals and transient spirals which co-rotate with the gas at every radius are attractively simple, albeit not completely realistic, models for the morphology and evolution of the gaseous spiral which forces the dynamo. Thus we investigate the effects of more realistic spiral models. Interfering two- and three-arm spiral patterns have previously been inferred to exist in many galaxies and also in numerical simulations, and invoked to explain important dynamical properties, such as lack of symmetry, kinks in spiral arms, and star formation in armlets. We therefore generalize our non-axisymmetric galactic mean-field dynamo model to allow for such multiple co-existing spiral patterns in the kinetic α_{k} effect, leading to the existence of magnetic spiral arms in the large-scale magnetic field with several new properties. The large-scale magnetic field produced by an evolving superposition of two- and three-arm (or two- and four-arm) patterns evolves with time along with the superposition. Magnetic arms can be stronger and more extended in radius and in azimuth when produced by two interfering patterns rather than by one pattern acting alone. Transient morphological features arise in the magnetic arms, including bifurcations, disconnected armlets, and temporal and spatial variation in arm strength and pitch angles. Pitch angles of the large-scale magnetic field and magnetic arm structures (ridges) are smaller than those typically inferred from observations of spiral galaxies for some model parameters, but can become comparable to typically inferred values for certain (still realistic) parameters. The magnetic field is sometimes strongest in between the α_{k}-arms, unlike in standard models with a single pattern, where it is strongest within the α_{k}-arms. Moreover, for models with a two- and three-arm pattern, some amount of $m = 1$ azimuthal symmetry is found to be present in the magnetic field, which is generally not the case for forcing by single two- or three-arm patterns. Many of these results are reminiscent of observed features in the regular magnetic fields of nearby spiral galaxies, like NGC 6946, which has previously been inferred to have significant two- and three-arm spiral patterns, and IC 342, which has been reported to contain an inner two-arm and outer four-arm pattern.

As with the nature of the spiral model forcing the dynamo, the mechanism of the non-axisymmetric forcing itself can be modelled in various, more or less realistic, ways. Spiral modulation of the α_k effect is certainly plausible, though not directly observable. We therefore explore a mechanism of non-axisymmeteric forcing that is physically better motivated, namely the concentration of outflows in the gaseous arms (and their suppression in the interarm regions). We find that magnetic spiral arms can be naturally generated in the interarm regions of some galaxies since the galactic fountain flow or wind, driven by star formation, hinders the large-scale dynamo action and thus the large-scale magnetic field in the gaseous arms. Moreover, in addition to the interfering spiral pattern model, we explore the effects of an evolving linear density wave model. For both spiral models, we find strong interarm magnetic arms for an outflow that is sufficiently large (though not so large as to render the dynamo sub-critical). Magnetic arms are rendered stronger when the τ effect is included in the model. Moreover, magnetic arms in the evolving density wave model are radially extended with arm pitch angles similar to those of the $\overline{U}_z$ (gaseous) arms, i.e. the type of interlacing magnetic arms seen in NGC 6946.

In summary, the thesis explores the implications of various physical effects, from dynamical non-linearities to temporal non-locality to spiral arm evolution to galactic outflows, on large-scale galactic dynamos.

The organization of this thesis is as follows.

- **Chapter 1** provides a brief review of observations of galactic magnetic fields, as well as a brief introduction to galactic dynamo theory, followed by a summary of the motivation for this work.

- **Chapter 2** compares various tools for non-linear galactic dynamos, and briefly discusses two applications of these tools.

- In **Chapter 3**, the τ effect is applied to a non-axisymmetric galactic mean-field dynamo model, and the resulting global solutions for the large-scale magnetic field are presented. The effect of the possible transience of galactic spiral patterns on the large-scale magnetic field is also explored.

- In **Chapter 4** an asymptotic solution for a similar non-axisymmetric galactic dynamo model to that discussed in Chapter 3 is presented, and compared with its numerical counterpart.

- In **Chapter 5** the effects on the dynamo caused by non-axisymmetric forcing by a galactic spiral consisting of multiple components, each with its own pattern speed and multiplicity, are investigated.

- In **Chapter 6** non-axisymmetric dynamo models are presented in which the vertical wind speed is modulated along a spiral.
- **Chapter 7** presents a discussion of our results and conclusions for the thesis.

Chapter 1

Introduction

Magnetic fields are ubiquitous in the universe. Planets, main sequence, pre- and post main sequence stars, compact objects, galaxies, and galaxy clusters are all known to generally possess magnetic fields. This thesis focuses on the magnetic fields in disc galaxies that are found to be coherent on the scales of the galaxies themselves (i.e. the large-scale magnetic fields in galaxies). How did these fields arise, how are they maintained, and what determines their structure? We first give a brief account of how galactic magnetic fields are measured and what has been observed so far. We then introduce galactic dynamo theory, and briefly discuss the different approaches. Subsequently, a short review of mean-field dynamo theory is presented, which includes a description of the effect of magnetic helicity conservation on the dynamo. Finally, we summarize the motivation for the thesis, and describe its structure.

1.1 Observations of magnetic fields in galaxies

Spiral galaxies typically have total magnetic fields in their discs of strength $B \sim 10\,\mu\mathrm{G}$, which translates to an energy density comparable to that of the turbulent motions. These magnetic fields can be divided into a random, or small-scale component, which is coherent on scales up to the outer scale of the turbulence in the interstellar medium ~ 10–$100\,\mathrm{pc}$, and a regular (or mean or large-scale) component, which is coherent on scales approaching the system size, $\sim 10\,\mathrm{kpc}$ for disc galaxies. The primary method of measuring magnetic fields in galaxies, especially external galaxies, is through synchrotron radiation. The total strength of the components of the magnetic field in the plane of the sky can be inferred from the total synchrotron intensity, provided that the cosmic ray electron density can be reliably estimated. Polarized synchrotron emission, on the other hand, can only be produced by magnetic fields with a preferred orientation (i.e. parallel or anti-parallel to some particular direction). Such anisotropic magnetic fields may be large-scale, with a preferred direction (hence have large-scale coherence). However, they may also be small-scale, with a preferred orientation but not direction (hence have only small-scale coherence) (e.g. Haverkorn, 2014). Finally, the amount of Faraday rotation of the polarized synchrotron emission along a given line of sight is determined by the magnetic field along the line of sight as well as the thermal electron density. Only large-scale magnetic fields can produce large-scale patterns in Faraday rotation, although small-scale fields can produce Faraday rotation measure dispersion.

Many disc galaxies have been found to harbour large-scale magnetic fields. Among these, there exists a handful of nearby galaxies for which detailed analyses of magnetic fields have been carried out. The small-scale magnetic field is typically a few times larger than the large-scale magnetic field (Fletcher, 2010). The large-scale magnetic field strength generally declines with distance from the galactic centre (Haverkorn, 2014). The magnetic pitch angle is defined as $p_B = \arctan(\overline{B}_r/\overline{B}_\phi)$ where $\overline{B}_r$ and $\overline{B}_\phi$ are the radial and azimuthal components of the large-scale field in a galactocentric cylindrical polar coordinate system (r, ϕ, z) with the z-axis perpendicular to the disc. Pitch angles are typically between $-10°$ and $-25°$ (Fletcher, 2010; Haverkorn, 2014, and see Beck 2007 for NGC 6946), but are found to be as large as $\sim -45°$ in the galaxy M33, which also happens to have a very open optical spiral pattern ($p = \cot^{-1}(\partial\phi_{\max}/\partial \ln r) \sim -65°$, where $\phi_{\max}$ is where the spiral perturbation peaks in azimuth). For most galaxies the large-scale magnetic field is found to be fairly well-aligned with the optical spiral arms (Fletcher, 2010). Furthermore, the pitch angle is often found to vary with radius (Fletcher, 2010; Haverkorn, 2014).

Another property of large-scale galactic magnetic fields is the parity. Odd (dipole-like) parity implies $\overline{B}_r = \overline{B}_\phi = \partial\overline{B}_z/\partial z = 0$ at the midplane $z = 0$, while even (quadrupole-like) parity implies $\partial\overline{B}_r/\partial z = \partial\overline{B}_\phi/\partial z = \overline{B}_z = 0$ at $z = 0$. Mean-field galactic dynamo models generally predict the quadrupole mode to dominate within the disc (Ruzmaikin et al., 1988), although the situation may be more complicated when the galactic halo (thick disc) is included (Moss et al., 2010). Observationally, our Galaxy seems likely to possess a Disk-Even-Halo-Odd symmetry, consisting of a disk with even parity and a halo with odd parity (Haverkorn, 2014; Beck & Wielebinski, 2013). In external galaxies, the even parity seems to dominate in the discs. The parity of their haloes is more difficult to determine, but there is evidence for even parity in the halo of the galaxy NGC 253 (Beck & Wielebinski, 2013).

When the magnetic field reverses direction across a geometrical surface (on which the field vanishes), this is known as a magnetic field reversal. At least one reversal of the large-scale magnetic field occurs in our Galaxy (Haverkorn, 2014), but such reversals have not yet been found in other galaxies (Beck & Wielebinski, 2013).

Significant non-axisymmetry is present in the regular fields of several galaxies. In some galaxies, the polarized emission forms spiral structures akin to the familiar 'material' spiral arms (i.e. the stellar or gaseous arms). Although this does not necessarily imply that the large-scale field has such a structure since, as noted above, anisotropic small-scale field also emits polarized synchrotron radiation, Faraday rotation analysis does support the existence of such spiral arm structures, called magnetic spiral arms, in the large-scale field. To study non-axisymmetry in the regular magnetic field of disc galaxies, it is natural to study the Fourier decomposition,

$$\overline{B}_i(r,\phi,t) = \sum_{m=0}^{\infty} \widetilde{B}_i^{(m)}(r,t)\cos\left[m\phi + \phi_0^{(m)}(r,t)\right], \tag{1.1}$$

where $\widetilde{B}_i^{(m)}$ is the amplitude of component m and $\phi_0^{(m)}$ is a parameter that determines its phase. In almost all galaxies, the axisymmetric ($m = 0$) component seems to be the strongest component among the components modelled (usually up to $m = 2$) (Fletcher, 2010). This supports mean-field dynamo theory, which predicts that the $m = 0$ mode should have the fastest growth rate (Ruzmaikin et al., 1988) in the kinematic regime, when the regular magnetic field undergoes exponential growth. In chapter 3, we show that the $m = 0$ mode is expected to dominate in the non-linear saturation regime as well.

In some cases, most clearly NGC 6946 and IC342, magnetic spiral arms are phase-shifted from their optical counterparts. This is contrary to what would be expected if the regular magnetic fields in galaxies were the result of flux-freezing of an entrained primordial magnetic field during galaxy formation (Kulsrud & Zweibel, 2008). If that were the case we would expect the regular magnetic field to be concentrated within the material arms since they have a higher density compared to the interarm regions. A map of $\lambda 6\,\mathrm{cm}$ polarized intensity from NGC 6946, along with polarization vectors rotated by $90°$ to reflect the orientation of the magnetic field, is shown in Figure 1.1. Polarization contours are overlaid on a map of Hα emission. Spiral structures in polarized emission are clearly located in between the Hα arms. Importantly, a large-scale pattern is evident in the map of Faraday rotation measure, shown by the colour in Figure 1.2 (also shown are contours of total radio intensity at $\lambda 6\,\mathrm{cm}$). We can infer then that the polarized emission is dominated by the contribution from the large-scale magnetic field, as opposed to the anisotropic small-scale magnetic field.

The leading theory to explain the observational properties of galactic magnetic fields is mean-field galactic dynamo theory. We review this theory below.

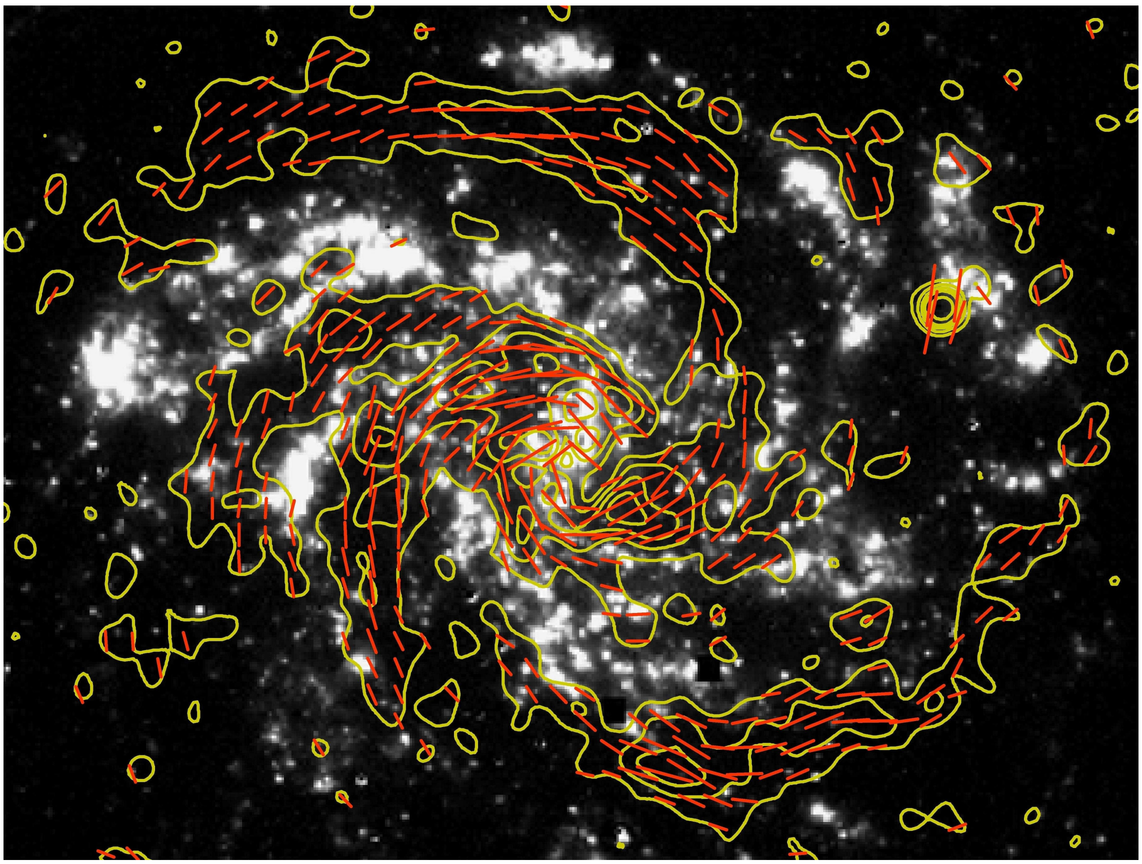

Figure 1.1: Polarized radio emission at 6 cm wavelength from the galaxy NGC 6946 (contours). Magnetic field orientation is shown by the arrowless vectors. The contours and vectors are overlaid on an Hα image. (The image is taken from Beck 2012.)

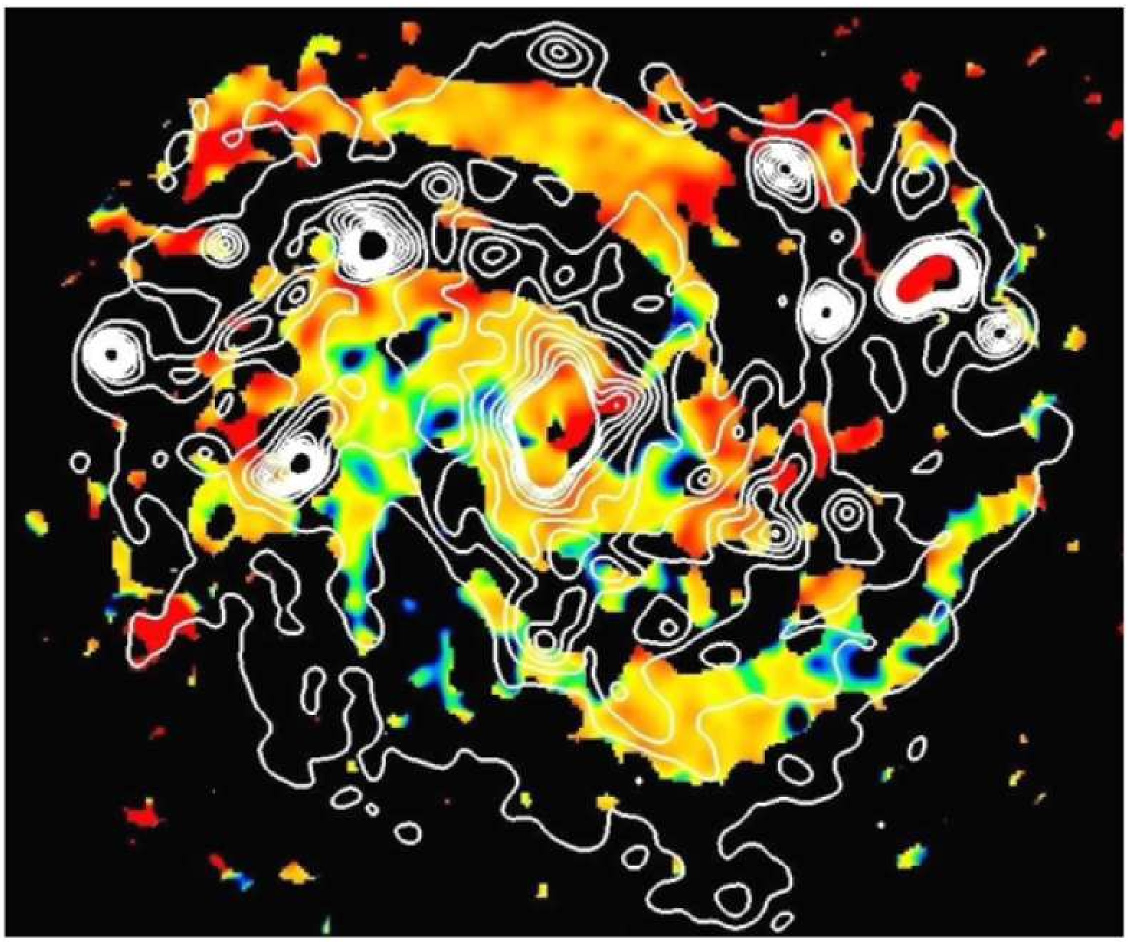

Figure 1.2: Total radio intensity at 6 cm wavelength from the galaxy NGC 6946 (contours). The colour shows the Faraday rotation measure. The scale extends from -75 rad/m^2 to +175 rad/m^2. The average rotation measure of approximately 50 rad/m^2 is produced by the Milky Way foreground. (The image is taken from Beck 2012.)

1.2 Basic galactic dynamo theory

1.2.1 Outline of the dynamo mechanism

It is generally agreed upon that magnetic fields in disc galaxies are generated and maintained by the action of a dynamo on a small seed magnetic field. In particular, the mean or large-scale magnetic field is thought to owe its existence to a turbulent dynamo, whereby the kinetic helicity in the turbulence and differential rotation in the disc combine to transform kinetic energy into magnetic energy of the large-scale field. Mean toroidal field must be generated from mean poloidal field and then mean poloidal field of the same sign must be regenerated from mean toroidal field to close the dynamo feedback cycle. The first process is known as the Ω effect, by which the mean poloidal field is acted on by the radial shear to generate the mean toroidal field. The conversion of toroidal to poloidal field is accomplished by what is known as the α effect (Parker 1955; the reason for the name will become apparent below).

As the ambient pressure in the disc decreases away from the galactic midplane, rising fluid elements expand, and the conservation of angular momentum (or in dynamical terms, the Coriolis force) causes them to increase their angular velocity in the direction opposite to that of the galactic rotation. The reverse is true for falling fluid elements. In any case, the mean kinetic helicity, $\overline{\boldsymbol{u}\cdot\boldsymbol{\nabla}\times\boldsymbol{u}}$, where $\boldsymbol{u}$ is the random velocity field and bar represents ensemble or spatial averaging, is negative (positive) in the northern (southern) hemisphere. In galaxies, magnetic fields are to a good approximation frozen in the fluid as discussed in Section 1.2.5, so in the presence of a strong toroidal field these helical fluid motions naturally lead to the generation of Ω-shaped flux loops which are twisted about a vertical axis. When averaged over, they produce a mean toroidal current density in each hemisphere, which implies the generation of a mean poloidal field component with the sign required to close the dynamo feedback cycle.

This positive feedback cycle causes the field to grow exponentially, until it is 'quenched'. This is the essence of the $\alpha\Omega$ turbulent dynamo mechanism in disc galaxies (Moffatt, 1978; Ruzmaikin et al., 1988). The quenching mechanism can only be explained by relatively sophisticated models that go beyond the linear (kinematic) regime, and incorporate the dynamical feedback of the Lorentz force on the turbulence (Brandenburg & Subramanian, 2005a).

1.2.2 Why a dynamo?

Other ideas have been proposed to explain galactic large-scale magnetic fields. The 'primordial fields' theory posits that large-scale fields, present at the time of galaxy formation, were frozen in and amplified by compression and differential rotation as the galaxy formed and evolved. First, the origin of such a field itself needs to be explained. Further, the primordial fields theory is unable to explain why the magnitude of the pitch angle of the regular magnetic field is not much smaller than that observed, assuming that the primordial field has been amplified to its present strength by the galactic differential rotation, which also winds it up (Shukurov, 2005). Moreover, although Ohmic diffusion may be negligible on galactic scales, turbulent diffusion would presumably severely limit the growth of such fields or cause them to decay (but see Blackman & Subramanian, 2013; Bhat et al., 2014, for an idea for how this fate could still be averted). Mean-field galactic dynamo theory does not suffer these shortcomings. On the contrary, it has had success in explaining general properties of regular magnetic fields in galaxies, such as growth times (from a plausible seed field), parity and radial fall-off. It has also had some amount of success in explaining observed magnetic pitch angles, the presence (or absence) of global reversals and the generation of non-axisymmetric modes (Shukurov, 2005). Moreover, the theory has been used rather successfully to explain large-scale fields in specific galaxies using observationally well-constrained parameters (Ruzmaikin et al., 1988).

1.2.3 The turbulent interstellar medium

Turbulence in the galactic disc is generated mainly by supernova explosions. The root-mean-square speed for the turbulence may be estimated in the following way (Shukurov, 2004). A supernova remnant will expand supersonically with respect to the ambient medium until such time as the pressure inside it is comparable to the ambient pressure. At this point it disintegrates and merges with its surroundings, driving motions in the gas which eventually lead to turbulence. The size of a supernova remnant when it has reached pressure balance with the ambient medium determines the scale of the largest turbulent eddies, and we normally approximate this as $l \sim 100\,\mathrm{pc}$. It is known that a fraction $f \approx 0.07$ of the supernova energy $E_{\mathrm{SN}} \sim 10^{51}\,\mathrm{erg}$ is converted into the kinetic energy of the interstellar medium. Estimating the supernova frequency and total gas mass as those of our own Galaxy, we have, respectively, $\nu_{\mathrm{SN}} \sim (30\,\mathrm{yr})^{-1}$ and $M_{\mathrm{gas}} = 4\times10^9 M\odot$. We can thus calculate the rate of energy input from supernovae per unit mass of the interstellar medium to be

$$\dot{e}_{\mathrm{SN}} = \frac{f\nu_{\mathrm{SN}}E_{\mathrm{SN}}}{M_{\mathrm{gas}}} \sim 10^{-2}\,\mathrm{erg\,g^{-1}\,s^{-1}}. \tag{1.2}$$

This energy supply can drive turbulent motions at a speed u such that $\dot{e}_{\mathrm{SN}} = 2u^3/l$, where the factor of two has been inserted to allow for half of the energy to end up as magnetic energy. Solving for u, we obtain $u \sim 10\,\mathrm{km\,s^{-1}}$, which is our standard estimate for the root-mean-square velocity in the interstellar medium. Note that this value is similar to the sound speed in the warm diffuse medium where the magnetic field is believed to primarily reside , which has a temperature $\sim 10^4\,\mathrm{K}$. Turbulent motions with velocities much greater than $10\,\mathrm{km\,s^{-1}}$ would be damped by the formation of shocks.

1.2.4 The induction equation

In the magnetohydrodynamic approximation, which is a good approximation for the interstellar medium of galaxies, the evolution of the magnetic field is governed by the induction equation, a derivation of which we now present. Rearranging Ohm's law,

$$\boldsymbol{J} = \sigma\left(\boldsymbol{E} + \frac{\boldsymbol{U}\times\boldsymbol{B}}{c}\right), \tag{1.3}$$

where $\boldsymbol{J}$ is the current density, σ is the conductivity, $\boldsymbol{E}$ is the electric field, $\boldsymbol{U}$ is the velocity field, $\boldsymbol{B}$ is the magnetic field and c is the speed of light in vacuum, we have

$$\boldsymbol{E} = \frac{\boldsymbol{J}}{\sigma} - \frac{\boldsymbol{U}\times\boldsymbol{B}}{c}, \tag{1.4}$$

which, when substituted into Faraday's law,

$$\frac{\partial\boldsymbol{B}}{\partial t} = -c\boldsymbol{\nabla}\times\boldsymbol{E}, \tag{1.5}$$

gives

$$\frac{\partial\boldsymbol{B}}{\partial t} = -\boldsymbol{\nabla}\times\left(\frac{c}{\sigma}\boldsymbol{J} - \boldsymbol{U}\times\boldsymbol{B}\right). \tag{1.6}$$

Substituting the Maxwell-Ampere law,

$$\frac{\partial\boldsymbol{E}}{\partial t} = c\boldsymbol{\nabla}\times\boldsymbol{B} - 4\pi\boldsymbol{J}, \tag{1.7}$$

into the time derivative of (1.5), and replacing the conductivity by the magnetic diffusivity,

$$\eta = \frac{c^2}{4\pi\sigma}, \tag{1.8}$$

leads to

$$\frac{\eta}{c^2}\frac{\partial^2\boldsymbol{B}}{\partial t^2} = -\boldsymbol{\nabla}\times\left(\eta\boldsymbol{\nabla}\times\boldsymbol{B} - \frac{c}{\sigma}\boldsymbol{J}\right). \tag{1.9}$$

Adding (1.6) and (1.9), we arrive at the induction equation,

$$\frac{\partial \boldsymbol{B}}{\partial t} + \frac{\eta}{c^2}\frac{\partial^2 \boldsymbol{B}}{\partial t^2} = \boldsymbol{\nabla} \times (\boldsymbol{U} \times \boldsymbol{B} - \eta \nabla \times \boldsymbol{B}). \tag{1.10}$$

If we divide the second term on the left hand side by the first term on the left hand side, we have t_{F}/t, where $t_{\mathrm{F}} = \eta/c^2 \sim 10^{-14}(T/10^4\,\mathrm{K})^{-3/2}\,\mathrm{s}$ is the Faraday time. For typical timescales over which $\boldsymbol{B}$ changes, $t_{\mathrm{F}}/t \ll 1$. For this reason, the second term on the left hand side of (1.10) can be neglected. Since this term comes from the displacement current term on the left hand side of the Maxwell-Ampere law (1.7), that term may also be neglected. The Maxwell-Ampere law then reduces to Ampere's law,

$$\boldsymbol{\nabla} \times \boldsymbol{B} = \frac{4\pi}{c}\boldsymbol{J}, \tag{1.11}$$

i.e. the current density is essentially equal to the curl of the magnetic field, and we obtain the standard induction equation for the magnetic field,

$$\frac{\partial \boldsymbol{B}}{\partial t} = \boldsymbol{\nabla} \times (\boldsymbol{U} \times \boldsymbol{B} - \eta \nabla \times \boldsymbol{B}). \tag{1.12}$$

Note that the induction equation possesses the trivial solution $\boldsymbol{B} = 0$. This implies that any dynamo mechanism based on this equation requires a finite seed magnetic field on which to operate, and cannot generate a magnetic field if none existed previously. Fortunately, mechanisms are known that can generate seed magnetic fields (Brandenburg & Subramanian, 2005a). For example, the Biermann battery effect relies on a more general version of Ohm's law, involving terms that can be ignored for our purposes. It can lead to the generation of magnetic fields in cosmic ionization fronts or in structure formation shocks with strength $\sim 10^{-20}\,\mathrm{G}$ and coherence lengths comparable to galactic scales (Subramanian et al., 1994; Ryu et al., 2012).

Normally regarded as a separate type of dynamo, since it grows the field on scales smaller than that of the turbulence, the small-scale, or fluctuation, dynamo can exponentially grow the small-scale magnetic field on e-folding timescales comparable to the coherence time of the turbulence (Brandenburg & Subramanian, 2005a). As we shall see below, these timescales are significantly smaller than the corresponding timescales for the large-scale dynamo. Thus, the small-scale dynamo can potentially act on small seed fields to produce much stronger seed fields, to be acted upon by the large-scale dynamos studied in this work.

1.2.5 Ohmic diffusion and flux-freezing

Consider the ratio of the induction and diffusion terms in equation (1.12). This ratio will be $\sim LU/\eta$, where L is the typical length scale over which the magnetic field varies, and U is the magnitude of the velocity. This dimensionless ratio is known as the magnetic Reynolds number,

$$\mathcal{R}_\mathrm{m} = \frac{LU}{\eta} \sim 10^{19} \left(\frac{T}{10^4\,\mathrm{K}}\right)^{3/2} \left(\frac{L}{100\,\mathrm{pc}}\right) \left(\frac{U}{10\,\mathrm{km\,s^{-1}}}\right), \tag{1.13}$$

where we have adopted length and velocity scales corresponding to typical turbulent scales. Evidently, for galaxies, Ohmic diffusion can normally be ignored, since $\mathcal{R}_\mathrm{m} \gg 1$.

The perfectly conducting fluid limit $\eta \to 0$ (or, equivalently, $\sigma \to \infty$, $\mathcal{R}_\mathrm{m} \to \infty$) is known as ideal magnetohydrodynamics, and we generally work in this limit below. One important consequence of $\mathcal{R}_\mathrm{m} \gg 1$ in galaxies is that the magnetic field is effectively frozen in the fluid. That is, the total magnetic flux $\int_S \boldsymbol{B}\cdot\hat{\boldsymbol{n}}dS$ through a surface moving with the fluid is conserved. This result, known as Alfven's theorem, can be proven mathematically when turbulence is ignored (e.g. Brandenburg & Subramanian, 2005a). It can also be shown to hold in a statistical sense when the effects of turbulence are included: so-called 'stochastic flux-freezing' (Eyink, 2011). We now turn to a somewhat more rigorous discussion of the dynamo mechanism that grows the large-scale magnetic field, based in part on the theoretical underpinnings of the present section.

1.3 The mean-field dynamo

We now follow the mean-field approach (Krause & Raedler, 1980) where the velocity and magnetic fields are each written as the sum of an average component and a random component,

$$\boldsymbol{B} = \overline{\boldsymbol{B}} + \boldsymbol{b} \quad \text{and} \quad \boldsymbol{U} = \overline{\boldsymbol{U}} + \boldsymbol{u}. \tag{1.14}$$

Here an overbar formally represents ensemble averaging but for practical purposes can be thought of as spatial averaging over scales larger than the turbulent scale but smaller than the system size (Germano, 1992; Eyink, 2012; Gent et al., 2013). Substituting equation (1.14) into the induction equation (1.12) leads to the mean-field induction equation (Moffatt, 1978; Krause & Raedler, 1980),

$$\frac{\partial\overline{\boldsymbol{B}}}{\partial t} = \boldsymbol{\nabla}\times\left(\overline{\boldsymbol{U}}\times\overline{\boldsymbol{B}} + \boldsymbol{\mathcal{E}} - \eta\nabla\times\overline{\boldsymbol{B}}\right). \tag{1.15}$$

where

$$\boldsymbol{\mathcal{E}} = \overline{\boldsymbol{u} \times \boldsymbol{b}} \tag{1.16}$$

is the mean electromotive force.

Expressing $\boldsymbol{\mathcal{E}}$ in terms of the mean field is a standard closure problem. A relatively simple and widely used closure is the quasilinear approximation, also known as the first-order smoothing approximation (FOSA Moffatt, 1978; Krause & Raedler, 1980; Brandenburg & Subramanian, 2005a). In the quasilinear theory or FOSA, one neglects nonlinear terms in the evolution equation for $\boldsymbol{u}$ and $\boldsymbol{b}$, which, however, are retained if an evolution equation for $\boldsymbol{\mathcal{E}}$ is used instead (see below). For isotropic, helical turbulence, it leads to an expansion whose lowest-order terms are given by

$$\boldsymbol{\mathcal{E}} = \alpha \overline{\boldsymbol{B}} - \eta_{\mathrm{t}} \boldsymbol{\nabla} \times \overline{\boldsymbol{B}}, \tag{1.17}$$

where, in the kinematic limit, $\alpha = \alpha_{\mathrm{k}}$ with

$$\alpha_{\mathrm{k}} = -\tfrac{1}{3}\tau_{\mathrm{c}} \overline{\boldsymbol{u} \cdot \boldsymbol{\nabla} \times \boldsymbol{u}}, \quad \eta_{\mathrm{t}} = \tfrac{1}{3}\tau_{\mathrm{c}} \overline{\boldsymbol{u}^2}, \tag{1.18}$$

and τ_{c} is the correlation time of the random flow. The turbulent transport coefficients α and η_{t} are proportional, respectively, to the mean kinetic helicity and mean energy density of the turbulence. Below, we refer to the application of FOSA as the 'standard treatment'.

1.3.1 The τ approximation and temporal non-locality

An alternative treatment, suggested by Rogachevskii & Kleeorin (2000) and Blackman & Field (2002) was to replace the triple correlations which arise in the evolution equation for $\boldsymbol{\mathcal{E}}$ by a damping term proportional to $\boldsymbol{\mathcal{E}}$ itself (see also Vainshtein & Kitchatinov, 1983; Kleeorin et al., 1996; Brandenburg & Subramanian, 2005a). One starts off by considering the time derivative of $\boldsymbol{\mathcal{E}}$,

$$\frac{\partial \boldsymbol{\mathcal{E}}}{\partial t} = \overline{\frac{\partial \boldsymbol{u}}{\partial t} \boldsymbol{b}} + \overline{\boldsymbol{u} \frac{\partial \boldsymbol{b}}{\partial t}}.$$

Then the induction and Navier-Stokes equations can, after subtracting off their mean parts, be used for computing $\partial \boldsymbol{b}/\partial t$ and $\partial \boldsymbol{u}/\partial t$, respectively. Under this approximation, called the minimal-τ approximation (MTA) by Brandenburg & Subramanian (2005a), one obtains, instead of (1.17), the evolution equation

$$\frac{\partial \boldsymbol{\mathcal{E}}}{\partial t} = \frac{1}{\tau_{\mathrm{c}}}(\alpha \overline{\boldsymbol{B}} - \eta_{\mathrm{t}} \boldsymbol{\nabla} \times \overline{\boldsymbol{B}}) - \frac{\boldsymbol{\mathcal{E}}}{\tau}, \tag{1.19}$$

where again in the kinematic limit, α and $\eta_{\rm t}$ are given by equation (1.18) and τ is a relaxation time. For simplicity, this equation has been derived assuming that τ is scale-independent. When one takes into account the Lorentz force, the α-coefficient acquires an additional term proportional to the mean electric current helicity density of the small-scale field (Pouquet et al., 1976; Kleeorin & Ruzmaikin, 1982; Gruzinov & Diamond, 1994; Blackman & Field, 2000; Rädler et al., 2003; Brandenburg & Subramanian, 2005a), and then

$$\alpha = \alpha_{\rm k} + \alpha_{\rm m} = -\tfrac{1}{3}\tau_{\rm c}\left[\overline{\boldsymbol{u}\cdot\boldsymbol{\nabla}\times\boldsymbol{u}} - \frac{1}{4\pi\rho}\overline{\boldsymbol{b}\cdot\boldsymbol{\nabla}\times\boldsymbol{b}}\right], \tag{1.20}$$

where ρ is the density.

The τ-approximation is motivated by the observation that if, hypothetically, the mean fields were suddenly switched off then one would expect the mean emf to decay gradually, over a finite damping time τ. This approximation has been tested in direct numerical simulations of forced turbulence (Brandenburg & Subramanian, 2005a,b, 2007). These simulations of MTA find that τ is positive and the associated Strouhal number is of order unity, $\tau u k_0 \simeq 1$, where k_0 is the wavenumber corresponding to the correlation scale of the random flow, and u is its rms velocity. In principle, the damping or relaxation time τ can be different from the correlation time $\tau_{\rm c}$. For example, if $\tau_{\rm c}$ is determined by the frequency with which expanding supernova shocks encounter a given point in space then it could be shorter than $\tau \simeq (uk_0)^{-1}$ (Shukurov, 2004). Thus, we keep the ratio $c_\tau = \tau/\tau_{\rm c}$ as a dimensionless free parameter in the equations in this chapter; in subsequent chapters we set it to unity. We then have

$$\left(\frac{\partial}{\partial t} + \frac{1}{\tau}\right)\boldsymbol{\mathcal{E}} = \frac{c_\tau}{\tau}\left(\alpha\overline{\boldsymbol{B}} - \eta_{\rm t}\boldsymbol{\nabla}\times\overline{\boldsymbol{B}}\right). \tag{1.21}$$

If the explicit time derivative is neglected (valid if $\boldsymbol{\mathcal{E}}$ varies on timescales long compared to the relaxation time τ), and τ is approximated as $\tau_{\rm c}$, then (1.21) reduces to the expression (1.17) obtained from the standard treatment. An alternative way of arriving at equation (1.21) (with $c_\tau = 1$) is by keeping a time derivative of $\overline{\boldsymbol{B}}$ in the expression (1.17) for $\boldsymbol{\mathcal{E}}$ in order to introduce non-locality in time (Rheinhardt & Brandenburg, 2012).

We now apply the mean-field approach to the induction equation with the MTA closure. Operating on equation (1.15) with $\partial/\partial t + 1/\tau$, using equation (1.21), assuming

$\overline{\boldsymbol{U}}$ to be independent of time, and taking η and $\eta_{\rm t}$ to be spatially uniform, we arrive at

$$\begin{aligned}\left(\frac{\partial}{\partial t}+\frac{1}{\tau}\right)\frac{\partial\overline{\boldsymbol{B}}}{\partial t}=&\boldsymbol{\nabla}\times\left(\overline{\boldsymbol{U}}\times\frac{\partial\overline{\boldsymbol{B}}}{\partial t}\right)+\eta\nabla^2\frac{\partial\overline{\boldsymbol{B}}}{\partial t}\\&+\frac{1}{\tau}\left[\boldsymbol{\nabla}\times\left(\overline{\boldsymbol{U}}\times\overline{\boldsymbol{B}}+c_\tau\alpha\overline{\boldsymbol{B}}\right)+\left(\eta+c_\tau\eta_{\rm t}\right)\nabla^2\overline{\boldsymbol{B}}\right].\end{aligned}$$

After multiplying through by τ, this leaves us with an equation containing new terms proportional to τ (that do not emerge under the standard treatment),

$$\begin{aligned}\tau\frac{\partial^2\overline{\boldsymbol{B}}}{\partial t^2}+\frac{\partial\overline{\boldsymbol{B}}}{\partial t}=&\,\tau\boldsymbol{\nabla}\times\left(\overline{\boldsymbol{U}}\times\frac{\partial\overline{\boldsymbol{B}}}{\partial t}\right)+\tau\eta\nabla^2\frac{\partial\overline{\boldsymbol{B}}}{\partial t}\\&+\boldsymbol{\nabla}\times\left(\overline{\boldsymbol{U}}\times\overline{\boldsymbol{B}}+c_\tau\alpha\overline{\boldsymbol{B}}\right)+(\eta+c_\tau\eta_{\rm t})\nabla^2\overline{\boldsymbol{B}}.\end{aligned}\tag{1.22}$$

The same approach applied with the standard treatment gives the familiar result,

$$\frac{\partial\overline{\boldsymbol{B}}}{\partial t}=\boldsymbol{\nabla}\times(\overline{\boldsymbol{U}}\times\overline{\boldsymbol{B}}+\alpha\overline{\boldsymbol{B}})+(\eta+\eta_{\rm t})\nabla^2\overline{\boldsymbol{B}},\tag{1.23}$$

which is the $\tau\to 0$ limit of equation (1.22) with $c_\tau=1$. For the sake of simplicity, α and $\eta_{\rm t}$ are here assumed to be pseudoscalar and scalar (as appropriate in isotropic turbulence). Equation (1.22) contains a second-order, as well as first-order time derivatives, and belongs to the class of equations known as the telegraph equation (e.g., Courant & Hilbert, 1989). The second time derivative can lead to wave-like properties, with $1/\tau$ as a damping coefficient. Unlike the mean induction equation (1.23), the telegraph equation (1.22) is not invariant under transformation to a rotating frame (see Chapter 4). Equation (1.22) arises when the response time τ of the mean electromotive force (emf) $\boldsymbol{\mathcal{E}}=\overline{\boldsymbol{u}\times\boldsymbol{b}}$ to changes in the mean field or small-scale turbulence is not negligible (e.g. Rheinhardt & Brandenburg, 2012). The τ effect can have various interesting implications (see, e.g., Brandenburg et al. (2004) and Hubbard & Brandenburg 2009, the latter of which also contains a brief review of applications from the literature). The mean field equation (1.22) or (1.23) can have exponentially growing solutions, which describe the dynamo amplification of seed magnetic fields due to helical turbulence and shear.

1.3.2 The conservation of magnetic helicity

The standard treatment discussed above does not take into account the feedback of the Lorentz force onto the dynamo, which becomes important once the growing mean magnetic field nears energy equipartition with the turbulence. We saw, however, that when the Navier-Stokes equation is included in the problem, as in the minimal τ approximation, an extra term in the α effect arises that is proportional to the mean small-scale current helicity in the turbulence. As discussed above, the flux loops that are formed by the helical turbulence become twisted about a vertical axis (this large-scale twist is sometimes called writhe). The key point is that, assuming that the (toroidal) flux tubes are not twisted to begin with, this implies that accompanying the writhe, there is a (small-scale) twist of the flux tube about *its own* axis (known simply as twist). The writhe and twist have opposite signs in this case (one is left-handed while the other is right-handed). The small-scale twist is what opposes the build-up of large-scale writhe and quenches the α effect. A useful analogy is the twist that develops in a garden hose and makes it difficult to wind up in loops; letting go of the hose allows the small-scale twist to 'relax' to larger scales, and the hose starts to unwind.

Mathematically, twist and writhe are measures of the magnetic helicity, which is closely related to the current helicity. Magnetic helicity is a more useful quantity than current helicity, however, because it is very well conserved in highly conducting fluids (and perfectly conserved in ideal magnetohydrodynamics where $\eta = 0$), as we shall see below. Magnetic helicity is defined as

$$H = \int_V \boldsymbol{A} \cdot \boldsymbol{B} dV, \tag{1.24}$$

where A is the vector potential and $\boldsymbol{B} = \boldsymbol{\nabla} \times \boldsymbol{A}$. Consider the case where the volume V is either closed, such that magnetic field lines do not pierce the boundary ($\boldsymbol{B} \cdot \hat{\boldsymbol{n}} = 0$, where $\hat{\boldsymbol{n}}$ is the outward unit vector normal to the boundary), periodic, or unbounded such that the field decreases sufficiently fast at spatial infinity. Then the magnetic helicity is gauge-invariant. To show this, make the transformation $\boldsymbol{A'} = \boldsymbol{A} + \boldsymbol{\nabla}\Lambda$. Then, $H' = \int_V \boldsymbol{A'} \cdot \boldsymbol{B'} dV = \int_V (\boldsymbol{A} \cdot \boldsymbol{B} + \boldsymbol{\nabla}\lambda \cdot \boldsymbol{B}) dV$. Since $\boldsymbol{\nabla} \cdot \boldsymbol{B} = 0$, the second term ends up as a surface integral $\oint_{\partial V} (\Lambda \boldsymbol{B}) \cdot \hat{\boldsymbol{n}} dS$, which vanishes, and thus $H' = H$.

To derive the evolution equation for H, take the time derivative of equation (1.24), and use Faraday's law (1.5) along with its uncurled version

$$\frac{\partial \boldsymbol{A}}{\partial t} = -c(\boldsymbol{E} + \boldsymbol{\nabla}\Phi),$$

where Φ is the scalar potential. Then we obtain

$$\frac{dH}{dt} = -2c \int_V \boldsymbol{E} \cdot \boldsymbol{B} dV + c \int_{\partial V} [\boldsymbol{\nabla} \cdot (\boldsymbol{A} \times \boldsymbol{E}) - \Phi \boldsymbol{B}] \cdot \hat{\boldsymbol{n}} dS,$$

where we have again made use of $\boldsymbol{\nabla} \cdot \boldsymbol{B} = 0$. For the types of domain which make H gauge-invariant, the surface terms vanish. Thus, substituting the rearranged version of

Ohm's law (1.4) for $\boldsymbol{E}$ results in

$$\frac{dH}{dt} = -2\int\limits_V \eta \boldsymbol{B}\cdot(\boldsymbol{\nabla}\times\boldsymbol{B})dV, \tag{1.25}$$

where we have made use of equation (1.8). We see then that magnetic helicity is conserved in the non-resistive case. Crucially, H is also almost conserved for very small η ($R_\mathrm{m} \gg 1$), because in many situations the current helicity density $\boldsymbol{B}\cdot(\boldsymbol{\nabla}\times\boldsymbol{B})$ cannot increase with decreasing η faster than $\eta^{-1/2}$ (Brandenburg & Subramanian, 2005a). Further, note that in the last step of the above calculation, the fluid velocity drops out completely because $(\boldsymbol{U}\times\boldsymbol{B})\cdot\boldsymbol{B} = 0$. Therefore, any effect on the fluid velocity, for example due to turbulence or ambipolar drift, is unable to alter the conclusion that magnetic helicity is conserved. It is because of this fact that, assuming zero net helicity, the buildup of helicity on large-scales by the mean-field dynamo is accompanied by the growth of an equal amount of oppositely signed small-scale helicity.

1.3.3 The mean small-scale magnetic helicity density and its evolution

Now that we have derived the evolution equation for the magnetic helicity H, it is useful to derive evolution equations for the large-scale magnetic helicity $\overline{H} = \int_V \overline{\boldsymbol{A}}\cdot\overline{\boldsymbol{B}}dV$ and mean small-scale magnetic helicity $h = \int_V \overline{\boldsymbol{a}\cdot\boldsymbol{b}}dV$, using the two-scale approach. The derivation of the evolution equation for $\overline{H}$ follows closely that of H, only now the mean of equation (1.4) gives an extra term proportional to $\boldsymbol{\mathcal{E}}$, whose dot product with $\overline{\boldsymbol{B}}$ does not generally vanish. One then arrives at the evolution equation

$$\frac{d\overline{H}}{dt} = 2\int\limits_V \left[\boldsymbol{\mathcal{E}}\cdot\overline{\boldsymbol{B}} - \eta\overline{\boldsymbol{B}}\cdot(\boldsymbol{\nabla}\times\overline{\boldsymbol{B}})\right]dV. \tag{1.26}$$

Now, since $H = \overline{H} + h$, we may subtract equation (1.26) from equation (1.25) to obtain the evolution equation for h,

$$\frac{dh}{dt} = 2\int\limits_V \left[-\boldsymbol{\mathcal{E}}\cdot\overline{\boldsymbol{B}} - \eta\overline{\boldsymbol{b}\cdot(\boldsymbol{\nabla}\times\boldsymbol{b})}\right]dV. \tag{1.27}$$

It is clear that the $\boldsymbol{\mathcal{E}}\cdot\overline{\boldsymbol{B}}$ term transfers helicity between small- and large-scale fields while conserving the total helicity. The quantity h is closely related to the mean small-scale current helicity. We have already discussed how the mean small-scale current helicity *density* contributes a term α_m to the α effect. To derive the evolution equation for α_m, we first need to obtain the evolution equation for the *density* of h, denoted by χ. This requires a reformulation of the textbook definition of magnetic helicity so that it, as well as its density, are explicitly gauge-invariant, even for fields that are not closed over the integration volume.

It becomes possible to define the magnetic helicity in terms of the magnetic field (without appealing to the vector potential) with the realization that helicity can be interpreted as a measure of the magnetic flux linkage in the system (Brandenburg & Subramanian, 2005a; Subramanian & Brandenburg, 2006). This turns out to be completely equivalent to the interpretation in terms of twisting of flux tubes outlined above (Blackman, 2014). With this realization, it becomes more natural to define the magnetic helicity through Gauss' linkage formula (Berger & Field, 1984; Moffatt, 1969; Subramanian & Brandenburg, 2006). This gives

$$H = \frac{1}{4\pi} \int \boldsymbol{B}(\boldsymbol{x}) \cdot \left[\boldsymbol{B}(\boldsymbol{y}) \times \frac{\boldsymbol{x} - \boldsymbol{y}}{|\boldsymbol{x} - \boldsymbol{y}|^3} \right] d^3x d^3y, \tag{1.28}$$

which can be shown to be equivalent to the textbook definition when the Coulomb gauge $\boldsymbol{\nabla} \cdot \boldsymbol{A} = 0$ is chosen. This then leads to the natural definition for the mean small-scale magnetic helicity density (Subramanian & Brandenburg, 2006),

$$\chi(\boldsymbol{R}) = \frac{1}{4\pi} \int\limits_{L^3} \epsilon_{ijk} M_{ij}(\boldsymbol{r}, \boldsymbol{R}) \frac{r_k}{r^3} d^3r. \tag{1.29}$$

Here, ϵ_{ijk} is the Levi-Civita symbol, $\boldsymbol{r} \equiv \boldsymbol{x} - \boldsymbol{y}$, $\boldsymbol{R} \equiv (\boldsymbol{x} + \boldsymbol{y})/2$, and the two-point correlation function $M_{ij}(\boldsymbol{r}, \boldsymbol{R}) \equiv \overline{b_i(\boldsymbol{x}, t), b_j(\boldsymbol{y}, t)}$. In addition, we have assumed that there exists a scale L which is much smaller than the system scale R_s, but much larger than the correlation scale of the random small-scale field $\boldsymbol{b}$, such that $l \ll L \ll R_\mathrm{s}$ with $M_{ij}(\boldsymbol{r}, \boldsymbol{R}) \to 0$ as $\boldsymbol{r} \to L$. Then one can formally let $L \to \infty$ in equation (1.29). It is worth noting that $\chi \simeq \overline{\boldsymbol{a} \cdot \boldsymbol{b}}$ in the Coulomb gauge for weakly inhomogeneous turbulence. One then calculates the quantity $\partial\chi/\partial t$ (the calculation is simpler in Fourier space, using the formalism of Roberts & Soward, 1975), to obtain

$$\frac{\partial \chi}{\partial t} = -2\boldsymbol{\mathcal{E}} \cdot \overline{\boldsymbol{B}} - 2\eta \overline{\boldsymbol{b} \cdot \boldsymbol{\nabla} \times \boldsymbol{b}} - \boldsymbol{\nabla} \cdot \boldsymbol{\mathcal{F}}, \tag{1.30}$$

where $\boldsymbol{\mathcal{F}}$ is the flux density of mean small-scale magnetic helicity density χ. This is not unlike equation (1.27), but now it is a local conservation law including a flux density term, whose contributions can be obtained as part of the calculation. These flux contributions include generalizations of the Vishniac-Cho flux (Vishniac & Cho, 2001) and advective flux (see Subramanian & Brandenburg, 2006, for details). However, contributions resulting from the third and fourth order correlations of small-scale quantities have yet to be studied in detail; it is expected that the analysis of such terms will lead to a turbulent diffusive flux (which has been detected in simulations; see below), in addition to other, less obvious, but potentially important, contributions. Note also that without a helicity flux, a steady state solution $\partial\chi/\partial t = 0$ would imply $\boldsymbol{\mathcal{E}}\cdot\overline{\boldsymbol{B}} = 0$ in the $\eta \to 0$ limit, and the 'catastrophic quenching' of the mean-field dynamo. This is because for any reasonable spectrum of mean small-scale current helicity density $\overline{\boldsymbol{b}\cdot\boldsymbol{\nabla}\times\boldsymbol{b}} \propto \eta^{-\nu}$, with $\nu < 1$. Thus, helicity fluxes are crucial for averting catastrophic quenching of the dynamo. This is supported by results of direct numerical simulations. For example, Brandenburg (2005) shows that only with open boundaries can a large-scale field of equipartition strength develop.

1.3.4 The dynamical α-quenching non-linearity

The evolution of $\alpha_{\rm m}$ is governed by magnetic helicity balance. To relate $\alpha_{\rm m} \propto \overline{\tau\boldsymbol{b}\cdot\boldsymbol{\nabla}\times\boldsymbol{b}}$ with $\chi \simeq \overline{\boldsymbol{a}\cdot\boldsymbol{b}}$, consider that their spectral densities will have the ratio $\tau_k k^2$. If the spectral density of $\alpha_{\rm m}$ decreases with k, then that of χ decreases even faster with k, and both quantities are dominated by the integral scale $l = 2\pi/k_0$. For example, for the Kolmogorov spectrum, the spectral magnetic energy density $M_k = k^{-1}b_k^2 \propto k^{-5/3}$, which implies $b_k \propto k^{-1/3}$. Similarly, the spectral kinetic energy density $E_k = k^{-1}u_k^2 \propto k^{-5/3}$, which gives $u_k \propto k^{-1/3}$ and $\tau_k = k^{-1}u_k^{-1} \propto k^{-2/3}$. Therefore, the contribution to χ per unit logarithmic interval of k-space is $a_k b_k \propto k^{-5/3}$ and that of $\alpha_{\rm m}$ is $\propto k^{-1/3}$, so both are dominated by the energy carrying scale of the turbulence. This is supported by results of direct numerical simulations (Brandenburg & Subramanian, 2005b). It is then reasonable to approximate (Shukurov et al., 2006)

$$\alpha_{\rm m} = \frac{\eta_{\rm t}\chi}{l^2 B_{\rm eq}^2}, \qquad \overline{\boldsymbol{b}\cdot\boldsymbol{\nabla}\times\boldsymbol{b}} = \frac{\chi}{l^2}, \tag{1.31}$$

where $B_{\rm eq} = (4\pi\rho u^2)^{1/2}$ is the equipartition field strength. Using Eqs. (1.31), equation (1.30) can be rewritten as an evolution equation for $\alpha_{\rm m}$,

$$\frac{\partial\alpha_{\rm m}}{\partial t} = -\frac{2\eta_{\rm t}}{l^2}\left(\frac{\boldsymbol{\mathcal{E}}\cdot\overline{\boldsymbol{B}}}{B_{\rm eq}^2} + \frac{\alpha_{\rm m}}{\mathcal{R}_{\rm m}}\right) - \boldsymbol{\nabla}\cdot\boldsymbol{\mathcal{F}}_\alpha, \tag{1.32}$$

where here the magnetic Reynolds number is given by $\mathcal{R}_{\rm m} = \eta_{\rm t}/\eta$. Note that in the absence of fluxes, the magnetic field will be catastrophically quenched due to the buildup of current helicity, and only recover to equipartition levels on the resistive time, which is much longer than a galactic lifetime at galactic scales. This behaviour is seen in direct numerical simulations (Brandenburg, 2001). We generally neglect Ohmic dissipation in equation (1.32), which is justified if the time scales considered are short compared to the resistive time scale or if the Ohmic diffusion is negligible compared to the helicity flux. In this thesis we consider a flux of the form

$$\boldsymbol{\mathcal{F}}_\alpha = \frac{\eta_\mathrm{t}}{l^2 B_\mathrm{eq}^2}\boldsymbol{\mathcal{F}} = \alpha_\mathrm{m}\overline{\boldsymbol{U}} - \kappa\boldsymbol{\nabla}\alpha_\mathrm{m}, \tag{1.33}$$

where the first term is related to the advective flux of magnetic helicity, expected to be present because of galactic winds and fountain flow (Shukurov et al., 2006; Heald, 2012; Bernet et al., 2013), while the second term leads to a Fickian diffusion of α_m (Kleeorin et al., 2002; Brandenburg et al., 2009). The latter term has been argued to exist on physical and phenomenological grounds, and it has been found in direct numerical simulations that $\kappa \approx 0.3\eta_\mathrm{t}$ (Mitra et al., 2010; Hubbard & Brandenburg, 2010, see also Candelaresi et al. 2011). The dynamical quenching equation (1.32) will be used along with the dynamo equation (1.22) or (1.23) to solve the full dynamo problem, including the non-linear saturation. It is worth noting that an alternate quenching formalism has recently been suggested in the literature (Hubbard & Brandenburg, 2011, 2012), but the question of its applicability to the galactic dynamo problem (with, e.g. non-periodic boundary conditions) requires further consideration which is beyond the scope of the thesis.

Figure 1.3 illustrates schematically how the dynamo operates. Panels (a) and (b) show the traditional $\alpha\Omega$ dynamo mechanism, described above, and valid for the kinematic regime. Here, the Lorentz force is not yet strong enough to react back on the flow. Note that magnetic flux, e.g. through the rectangular cross-section shown, can build up through the action of turbulent diffusion or upward advection of the top part of the loop. The modern picture is as shown in Figure 1.3c and d, where magnetic field lines have been replaced by flux tubes or ribbons. It is clear that the production of large-scale writhe now leads to the production of oppositely signed twist. Panel (e) illustrates how for equipartition-strength magnetic fields, this twist helicity leads to a Lorentz force $\boldsymbol{j} \times \overline{B}_\phi$ that opposes the twisting action. By conservation of helicity, this limits the formation of large-scale writhe and hence quenches dynamo action, until the small-scale helicity can Ohmically decay, or unless there is a flux to remove the small-scale helicity from the dynamo-active region.

The idea and equations of the dynamic non-linearity due to the magnetic helicity conservation were suggested in the early 1980s (Kleeorin & Ruzmaikin, 1982). Nevertheless, for 10–20 more years, simple, heuristic prescriptions of the dependence of α on the

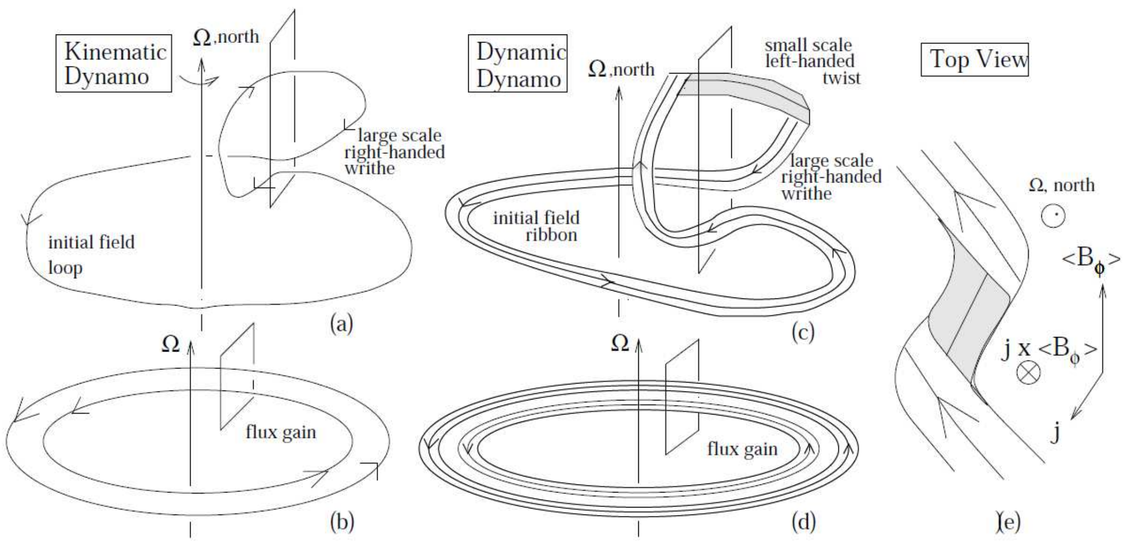

Figure 1.3: (a) The conversion of toroidal to poloidal field in the kinematic regime, where the Lorentz force may be safely ignored. (b) The conversion of poloidal to toroidal field in the kinematic regime. (c) The conversion of toroidal to poloidal field in the non-linear regime, where the Lorentz force, and hence the finite cross-section of the flux tube, must be taken into account. (d) The conversion of poloidal to toroidal field in the non-linear regime. (e) The Lorentz force acts to resist the twisting of the flux tube. (The diagram is taken from Blackman & Brandenburg 2003.)

mean magnetic field had been used widely. This was because the essential role of the magnetic helicity balance in mean-field dynamos was not fully appreciated until recently. Most popular was an algebraic form

$$\alpha = \frac{\alpha_\mathrm{k}}{1 + aB^2/B_\mathrm{eq}^2} \tag{1.34}$$

where $B \equiv |\overline{\boldsymbol{B}}|$ and a is a parameter of order unity, known as an algebraic α-quenching prescription. This algebraic formalism will be tested for consistency with the dynamical quenching theory in Chapter 2.

In the so-called $\alpha\Omega$ approximation, the induction effects of the galactic differential rotation, which produces $\overline{B}_\phi$ from $\overline{B}_r$, are assumed to be stronger than the similar mean induction effects of the random flow. Then the relevant component of the α-tensor responsible for the generation of $\overline{B}_r$ from $\overline{B}_\phi$ is $\alpha_{\phi\phi}$. This approximation is used in some of the models of Chapter 2 and in Chapter 4, but in most of the models, the α-term (α_{rr}) that assists in the generation of $\overline{B}_\phi$ is retained. We now identify the main intent of the thesis and briefly describe its structure.

1.4 Motivation and thesis organization

The main motivation for the thesis is explaining the features observed (or inferred from observations) in the large-scale magnetic fields of disc galaxies, especially with regard to the non-axisymmetry seen in such fields. In order to accomplish this, we develop and apply mean-field dynamo theory in the galactic context. In doing so, we pay considerable attention, not only to the dynamo physics, but also to the model of the underlying disc, its spiral structure and evolution, and the coupling between the disc and dynamo.

Understanding is generally improved when analytical or semi-analytical methods are used in conjunction with numerical methods. With this in mind, we are motivated to develop various approximate methods that can be used to interpret or predict numerical solutions. We come to the satisfying conclusion that solutions using these approximate methods, some of which consist of fairly simple analytical expressions for, e.g., the magnetic field strength and pitch angle in the saturated state, or the evolution of magnetic field modes in a non-axisymmetrically forced disc, generally agree with numerical solutions to a high degree of accuracy. In developing our models and exploring various effects, we come to the general conclusion that three broad physical effects, known in the literature but not (or barely) applied to galactic dynamos, are important in non-axisymmetric galactic dynamo theory:

i the finite response time of the dynamo to changes in the magnetic field and turbulence,

ii the evolution of the galactic spiral structure, and

iii the concentration of outflows in regions of star formation.

By taking these effects into consideration, we show that the observed spiral-shaped structures known as magnetic arms can be better explained.

The thesis is organized as follows. In Chapter 2, we develop various tools for non-linear galactic dynamo theory, and focus on the inter-comparison of such tools. We then develop a global non-axisymmetric galactic dynamo model, and explore numerical solutions for various choices of parameters and input physics in Chapter 3. This is followed up with an asymptotic solution for a suitably simplified, but essentially the same galactic dynamo model in Chapter 4. In Chapter 5, we develop a more realistic model for the spiral structure and evolution and explore its consequences. Chapter 6 investigates the effects on the dynamo of the galactic outflow being concentrated in the spiral arms of the galaxy (and suppressed in the interarm regions). Finally, we summarize and tie together the main results and discuss future directions in Chapter 7.

Chapter 2

Non-linear galactic dynamo theory: A toolbox

2.1 Introduction

The mean-field dynamo theory provides an appealing explanation of the presence and structure of large-scale magnetic fields in disc galaxies (Ruzmaikin et al., 1988; Beck et al., 1996; Brandenburg & Subramanian, 2005a; Shukurov, 2005; Kulsrud & Zweibel, 2008). The dynamo time scale is shorter than the galactic lifetime, and the energy densities of the large-scale galactic magnetic fields and interstellar turbulence are observed to be of the same order of magnitude. It is thus plausible that the galactic large-scale dynamos are normally in a non-linear, statistically steady state. Recent progress in dynamo theory has lead to physically motivated non-linear models where the steady state is achieved through the magnetic helicity balance in the dynamo system (reviewed by Brandenburg & Subramanian, 2005a; Blackman, 2014). To avoid a catastrophic suppression of the mean induction effects of turbulence, the magnetic helicity of small-scale magnetic fields should be removed from the system. In galaxies, this can be achieved through the advection of magnetic fields from the disc to the halo by the galactic fountain or wind (Shukurov et al., 2006; Sur et al., 2007), diffusive flux (Kleeorin et al., 2000, 2002) and helicity flux relying on the anisotropy of the interstellar turbulence (Vishniac & Cho, 2001; Vishniac & Shapovalov, 2014). The first of these mechanisms is the simplest in physical and mathematical terms, and involves galactic parameters that are reasonably well constrained observationally.

Most of the earlier analytical and numerical results in the non-linear mean-field disc dynamo theory rely on a much simpler form of non-linearity in the dynamo equations, the so-called algebraic α-quenching [equation (1.34)] that is based on a simple, explicit form of the dependence of the dynamo parameters, usually the α-coefficient, on the magnetic field. In a thin layer, such as a galactic or accretion disc, approximations such as this one have allowed for a wide range of analytical and straightforward numerical solutions using simple and yet accurate approximations One of the advantages of the resulting theory of galactic magnetic fields is that all its essential parameters can be expressed in terms of observable quantities (the angular velocity of rotation, thickness of the gas layer, turbulent velocity, etc.). As a result, theory of galactic magnetic fields has been better constrained and verified by direct comparison with observations than, arguably, any other astrophysical dynamo theory. Such comparisons require relatively simple, preferably analytical, approximations to the solutions of the dynamo equations. In this chapter we consider numerical solutions of thin-disc dynamo equations with a dynamic non-linearity involving magnetic helicity balance and compare them with a wide range of simpler solutions to develop a set of accessible tools to facilitate applications of the theory. The aim of this chapter is to test to what degree approximations such as algebraic quenching or perturbation theory reproduce the results of the modern dynamical quenching non-linear dynamo theory.

The chapter is organized as follows. In Sections 2.2-2.3, we present the theoretical background and a review of each of the approximations discussed. This is followed by a detailed comparison of the solutions resulting from various physical and mathematical approximations in Section 2.4. In particular, in Section 2.5 we provide an in-depth comparison of the dynamical and algebraic non-linearities. Our overall conclusion is that the earlier, simple models, when applied judiciously, reproduce comfortably well solutions with the dynamical non-linearity. Section 2.6 provides examples of applications of the toolbox, namely the magnetic pitch angle problem and the spiral arm-interarm contrasts in magnetic field. We present a summary and general conclusions in Section 2.7. The details of the asymptototic solutions studied, namely the perturbation and no-z solutions, are given in Appendices A and B, respectively.

Throughout this chapter, we use cylindrical polar coordinates (r, ϕ, z) with the origin at the disc centre and the z-axis aligned with the angular velocity of rotation $\mathbf{\Omega}$.

2.2 Galactic dynamos

We begin with a discussion of the functional forms and parameters of the model. In a thin disc, the kinetic contribution to the α-effect can be written as the product of r-dependent and z-dependent parts,

$$\alpha_{\mathrm{k}} = \alpha_0(r)\,\widetilde{\alpha}(z)\,, \tag{2.1}$$

where α_0 can be estimated as (Krause & Raedler, 1980; Ruzmaikin et al., 1988; Brandenburg & Subramanian, 2005a),

$$\alpha_0(r) = \frac{l^2\Omega(r)}{h(r)}\,, \tag{2.2}$$

with h the disc half-thickness, a function of r in a flared disc, Ω the angular velocity of the gas, also a function of r, and l the correlation scale of the random velocity field. It follows from symmetry considerations that α is an odd function of z and $\alpha > 0$ for $z > 0$ (Ruzmaikin et al., 1988). As in numerous earlier analytical studies of the mean-field disc dynamos, we adopt

$$\widetilde{\alpha} = \sin\left(\frac{\pi z}{h}\right)\,.$$

The mean velocity in a disc galaxy is dominated by the azimuthal component, representing differential rotation, and the vertical (outflow) velocity, a wind or a fountain flow:

$$\overline{\boldsymbol{U}} = (0, r\Omega, \overline{U}_z)\,,$$

where $\overline{U}_z$ is the mass-weighted outflow speed. At small distances from the midplane, one can use

$$\overline{U}_z = U_0\widetilde{U}_z\,, \qquad \widetilde{U}_z = \frac{z}{h}\,. \tag{2.3}$$

We use an axisymmetric disc model that has a thin, stratified, differentially rotating, flared, turbulent disc with the turbulent scale and rms velocity of $l = 0.1\,\mathrm{kpc}$ and $u = 10\,\mathrm{km\,s^{-1}}$, and the mixing-length estimate of the turbulent magnetic diffusivity follows as

$$\eta_\mathrm{t} = \tfrac{1}{3}lu = 10^{26}\,\mathrm{cm^2\,s^{-1}}. \tag{2.4}$$

We also adopt $U_0 = 1\,\mathrm{km\,s^{-1}}$, constant with radius (Sur et al., 2007). For the galactic rotation curve, the Brandt's form

$$\Omega(r) = \frac{\Omega_0}{\left[1 + (r/r_\omega)^2\right]^{1/2}}\,, \tag{2.5}$$

with $r_\omega = 2\,\mathrm{kpc}$, and $U_\phi = 250\,\mathrm{km\,s^{-1}\,kpc^{-1}}$ at $r = 10\,\mathrm{kpc}$ is chosen, resulting in $\Omega_0 \simeq 127\,\mathrm{km\,s^{-1}\,kpc^{-1}}$.

The disc half-thickness is assumed to vary hyperbolically with radius,

$$h(r) = h_\mathrm{D}\left[1 + (r/r_\mathrm{D})^2\right]^{1/2}\,, \tag{2.6}$$

where h_D is the scale height at $r = 0$, and $r_\mathrm{D} = 10\,\mathrm{kpc}$ controls the disc flaring rate.

Table 2.1: Key parameter values for the models studied. From left to right, the radius in the disc r, the disc scale height h, the vertical turbulent diffusion time $t_\mathrm{d} = h^2/\eta_\mathrm{t}$, the equipartition field strength B_eq, the amplitude of the α effect α_0, the radial shear $G = rd\Omega/dr$, the amplitude of the outflow velocity U_0, and the turbulent diffusivity (of α_m) coefficient κ. This is followed by the dimensionless control parameters $R_\alpha \equiv \alpha_0 h/\eta_\mathrm{t}$, $R_\omega \equiv Gh^2/\eta_\mathrm{t}$, $R_U \equiv U_0 h/\eta_\mathrm{t}$, $R_\kappa \equiv \kappa/\eta_\mathrm{t}$ and $D \equiv R_\alpha R_\omega$. For the reader's convenience, both dimensionless and dimensional parameters are provided, e.g. R_U and U_0.

r [kpc]	h [pc]	t_d [Myr]	B_eq $[B_0]$	α_0 $\left[\frac{\mathrm{km}}{\mathrm{s}}\right]$	G $\left[\frac{\mathrm{km}}{\mathrm{s\,kpc}}\right]$	U_0 $\left[\frac{\mathrm{km}}{\mathrm{s}}\right]$	κ $\left[\frac{\mathrm{km\,kpc}}{\mathrm{s}}\right]$	R_α	R_ω	R_U	R_κ	D
4	381	425	0.82	1.50	−45.6	0/1	0/0.1	1.71	−19.8	0/1.14	0/0.3	−33.9
8	453	601	0.67	0.68	−29.1	0/1	0/0.1	0.93	−17.9	0/1.36	0/0.3	−16.6

The value of h at $r = 10\,\mathrm{kpc}$ is chosen to be $0.5\,\mathrm{kpc}$, which gives $h_\mathrm{D} \simeq 0.35\,\mathrm{kpc}$. The equipartition magnetic field strength is taken as

$$B_\mathrm{eq} = B_0 \exp\left[-\frac{r}{R} - \frac{z^2}{2h^2}\right],$$

where $R = 20\,\mathrm{kpc}$. This is equivalent to an exponential scale length of $10\,\mathrm{kpc}$ for the turbulent energy in the ionized gas. For comparison, this is similar to but slightly larger than the scale length $\sim 7\,\mathrm{kpc}$ of the total magnetic energy in the galaxy NGC 6946 (Beck, 2007). The value of B_0 can be chosen as convenient, e.g. $B_0 = 8.2\,\mu\mathrm{G}$ to have $B_\mathrm{eq} \simeq 5\,\mu\mathrm{G}$ at $r = 10\,\mathrm{kpc}$, $z = 0$.

We consider in detail specific models at $r = 4\,\mathrm{kpc}$ and $r = 8\,\mathrm{kpc}$. It is convenient to define the dimensionless control parameters

$$R_\alpha \equiv \frac{\alpha_0 h}{\eta_\mathrm{t}}, \quad R_\omega \equiv \frac{Gh^2}{\eta_\mathrm{t}}, \quad R_U \equiv \frac{U_0 h}{\eta_\mathrm{t}}, \quad R_\kappa \equiv \frac{\kappa}{\eta_\mathrm{t}},$$

where $G = r\,\partial\Omega/\partial r$ is the galactic shear. Using equations (2.2) for α_0 and (2.4) for η_t, the dynamo number is obtained as

$$D \equiv R_\alpha R_\omega = \frac{\alpha_0 G h^3}{\eta_\mathrm{t}^2} \simeq -9\frac{h^2\Omega^2}{u^2}, \tag{2.7}$$

where the last equality applies to a flat rotation curve, $G = -\Omega$. Radially-dependent parameter values are given in Table 2.1.

2.3 Basic equations

We solve equations (1.23) and (1.32) in the thin-disc approximation ($h \ll r_\omega, r_\mathrm{D}, R$, hence $|B_z| \ll |B_r|, |B_\phi|$), where radial derivatives of $\overline{\boldsymbol{B}}$ are neglected, and assume $\eta_\mathrm{t} = \mathrm{const.}$ We also neglect Ohmic terms as the magnetic Reynolds number $R_\mathrm{m} \gg 1$. In cylindrical coordinates, components of equations (1.23) and (1.32) become

$$\frac{\partial \overline{B}_r}{\partial t} = -\frac{\partial}{\partial z}\left(\alpha \overline{B}_\phi\right) + \eta_\mathrm{t}\frac{\partial^2 \overline{B}_r}{\partial z^2} - \frac{\partial}{\partial z}\left(\overline{U}_z \overline{B}_r\right), \tag{2.8}$$

$$\frac{\partial \overline{B}_\phi}{\partial t} = G\overline{B}_r + \frac{\partial}{\partial z}\left(\alpha \overline{B}_r\right) + \eta_\mathrm{t}\frac{\partial^2 \overline{B}_\phi}{\partial z^2} - \frac{\partial}{\partial z}\left(\overline{U}_z \overline{B}_\phi\right), \tag{2.9}$$

$$\frac{\partial \alpha_\mathrm{m}}{\partial t} = -\frac{2\eta_\mathrm{t}}{l^2 B_\mathrm{eq}^2}\left[\alpha\left(\overline{B}_r^2 + \overline{B}_\phi^2\right) - \eta_\mathrm{t}\left(\frac{\partial \overline{B}_r}{\partial z}\overline{B}_\phi - \frac{\partial \overline{B}_\phi}{\partial z}\overline{B}_r\right)\right] - \frac{\partial}{\partial z}\left(\overline{U}_z \alpha_\mathrm{m}\right) + \kappa\frac{\partial^2 \alpha_\mathrm{m}}{\partial z^2}. \tag{2.10}$$

where we have neglected $\overline{B}_z \partial \overline{U}_\phi/\partial z$ in equation (2.9), and assumed $\overline{B}_z^2 \ll \overline{B}_r^2 + \overline{B}_\phi^2$ in equation (2.10). The solenoidality of $\overline{\boldsymbol{B}}$ implies that $\partial \overline{B}_z/\partial z \approx 0$ in a thin disc. Vacuum boundary conditions, $\overline{B}_r = \overline{B}_\phi = 0$ and $\partial^2\alpha_\mathrm{m}/\partial z^2 = 0$ at $z = \pm h$, are used. Under such conditions, the quadrupole mode, such that $\partial \overline{B}_r/\partial z = \partial \overline{B}_\phi/\partial z = \alpha_\mathrm{m} = 0$ at $z = 0$ emerges automatically. The boundary condition for α_m leaves unconstrained the helicity flux through the disc surface.

2.3.1 Solutions of the disc dynamo equations

Now that we have set up the problem, we outline the different methods that can be used to solve it. We present these in order of accuracy, with the most accurate method described first.

Dynamical non-linearity

Equations (2.8)–(2.10) are solved on a grid of 201 gridpoints in $-h \le z \le h$ using the 6th order finite differencing and 3rd order time-stepping schemes given in Brandenburg (2003). The seed field is taken to be $\overline{B}_r = 10^{-3}B_0(1 - z^2/h^2)\exp(-z^2/h^2)$, $\overline{B}_\phi = 0$ at $t = 0$, and $\alpha_\mathrm{m} = 0$ initially. Solutions are not sensitive to the value or form of the seed field, as long as it is sufficiently weak.

Algebraic quenching

In the case of algebraic quenching, α_m no longer enters the equations explicitly and equation (2.10) is not solved. Equations (2.8) and (2.9) are solved in the same manner as above but now with α replaced by expression (1.34), with $B^2 = \overline{B}_r^2 + \overline{B}_\phi^2$ and $a = 1$. Subsequently, equation (1.34) is refined using the no-z approximation to estimate a, and the simulations are repeated using this more accurate version of algebraic quenching.

Marginal kinematic solutions

If the action of the dynamical quenching is to ultimately diminish the value of α without drastically modifying its spatial variation, then it may be reasonable to simpy rescale α in the kinematic problem to a marginal value corresponding to $\partial/\partial t = 0$. Thus, equations (2.8) and (2.9) are solved with $\alpha = \alpha_\mathrm{k}$, as defined in equation (2.1). However, the right hand side of equation (2.2) for α_0 is multiplied by a positive numerical factor < 1, which is varied iteratively until the growth rate of $\overline{\boldsymbol{B}}$ reduces to zero.

Perturbation solutions

It can be useful to have an analytic expression for $\overline{\boldsymbol{B}}$ in the kinematic regime, and such a solution has been derived using perturbation theory for the case $\overline{U}_z = 0$ (Shukurov, 2004; Sur et al., 2007; Shukurov & Sokoloff, 2008). This solution is extended to $\overline{U}_z \neq 0$ in Appendix A. For the exponential growth rate we obtain

$$\gamma = t_\mathrm{d}^{-1}\left[-\frac{\pi^2}{4} + \frac{\sqrt{-\pi D}}{2} - \frac{R_U}{2} + \frac{3\sqrt{-\pi D}R_U}{4\pi(\pi+4)} + \frac{R_U^2}{2\pi^2}\left(1-\frac{\pi^2}{6}\right)\right]. \tag{2.11}$$

As in the marginal kinematic solutions, the corresponding marginal solution is obtained by using the critical values for the dynamo number D and $R_\alpha = D/R_\omega$:

$$\begin{aligned}\overline{B}_r =& C_0 R_{\alpha,\mathrm{c}}\left\{\cos\left(\frac{\pi z}{2}\right) + \frac{3}{4\pi^2}\left(\sqrt{-\pi D_\mathrm{c}} - \frac{R_U}{2}\right)\cos\left(\frac{3\pi z}{2}\right)\right.\\ &\left. + \frac{R_U}{2\pi^2}\sum_{n=2}^{\infty}\frac{(-1)^n(2n+1)}{n^2(n+1)^2}\cos\left[\left(n+\tfrac{1}{2}\right)\pi z\right]\right\},\end{aligned} \tag{2.12}$$

$$\begin{aligned}\overline{B}_\phi =& -\frac{2}{\pi}C_0\sqrt{-\pi D_\mathrm{c}}\left\{\cos\left(\frac{\pi z}{2}\right) - \frac{3R_U}{8\pi^2}\cos\left(\frac{3\pi z}{2}\right)\right.\\ &\left. + \frac{R_U}{2\pi^2}\sum_{n=2}^{\infty}\frac{(-1)^n(2n+1)}{n^2(n+1)^2}\cos\left[\left(n+\tfrac{1}{2}\right)\pi z\right]\right\},\end{aligned} \tag{2.13}$$

where the subscript 'c' denotes critical values, $R_{\alpha,\mathrm{c}} = D_\mathrm{c}/R_\omega$, and C_0 is a normalization constant that controls the steady-state strength of the magnetic field. The critical dynamo number D_c is defined by setting $\gamma = 0$ in equation (2.11). We have

$$D_\mathrm{c} = -\frac{\pi^3}{4}\left\{\frac{1 + 2R_U/\pi^2 - (2R_U^2/\pi^4)(1-\pi^2/6)}{1 + 3R_U/[2\pi(\pi+4)]}\right\}^2 . \tag{2.14}$$

For practical purposes, it is sufficient to retain just a few terms in the infinite sums given in equation (2.12) and equation (2.13).

The no-z approximation

Finally, equations (2.8)–(2.10) can be solved in a steady state, $\partial/\partial t = 0$, in an approximate way as a set of algebraic equations using the no-z approximation (Subramanian & Mestel, 1993; Moss, 1995; Phillips, 2001) to replace z-derivatives by simple divisions by h, e.g. $\partial^2/\partial z^2 \sim -1/h^2$ and $\partial/\partial z \sim \pm 1/h$, with the sign chosen appropriately. This corresponds to using averages over the disc thickness. Using the fact that solutions have the form $B \propto \mathrm{e}^{\gamma t}$ in the kinematic regime, we also solve for the exponential growth rate γ. This leads to (see Appendix B for details):

$$D_\mathrm{c} = -\frac{\pi^5}{32}\left(1 + \frac{1}{\pi^2}R_U\right)^2 , \tag{2.15}$$

$$\gamma = \frac{\pi^2}{4}t_\mathrm{d}^{-1}\left(1 + \frac{1}{\pi^2}R_U\right)\left(\sqrt{\frac{D}{D_\mathrm{c}}} - 1\right) = \sqrt{\frac{2}{\pi}}\,t_\mathrm{d}^{-1}\left(\sqrt{-D} - \sqrt{-D_\mathrm{c}}\right), \tag{2.16}$$

$$\tan p_B = -\left(\frac{2R_{\alpha,\mathrm{c}}}{\pi|R_\omega|}\right)^{1/2} = \frac{1}{4}\,\frac{R_U + \pi^2}{R_\omega}, \tag{2.17}$$

$$B^2 = B_\mathrm{eq}^2\frac{\xi(p_B)}{C}\left(\frac{D}{D_\mathrm{c}} - 1\right)\left(R_U + \pi^2 R_\kappa\right), \tag{2.18}$$

where $t_\mathrm{d} = h^2/\eta_\mathrm{t}$ is the turbulent diffusion time-scale, $p_B \equiv \arctan(\overline{B}_r/\overline{B}_\phi)$ is the magnetic pitch angle, $\xi(p_B) \equiv [1 - 3\cos^2 p_B/(4\sqrt{2})]^{-1}$ and $C \equiv 2(h/l)^2$. Note that γ decreases linearly with R_U in the no-z approximation.

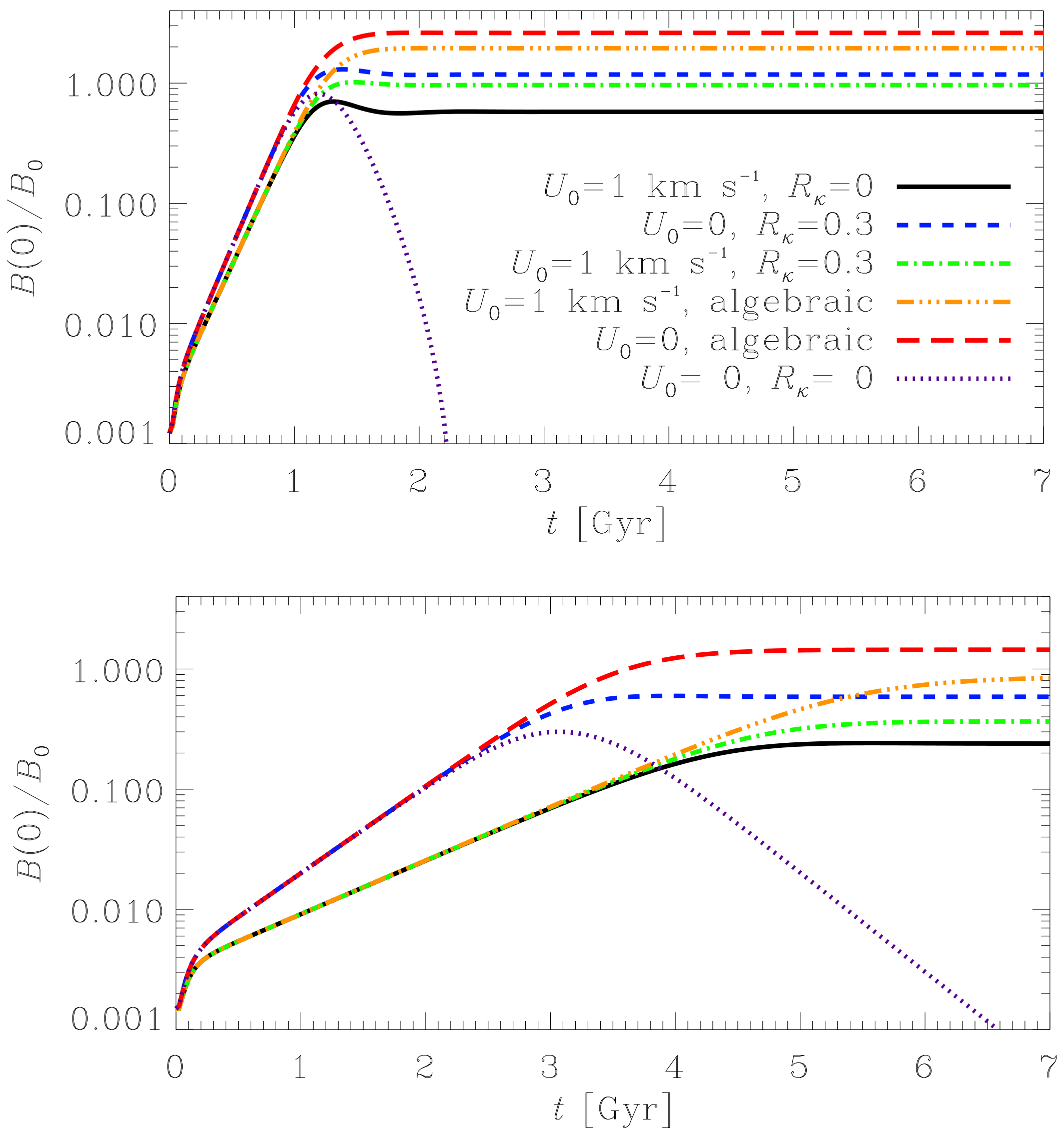

Figure 2.1: Evolution of the magnetic field strength at the midplane, normalized to the local equipartition field strength, for parameters corresponding to $r = 4\,\mathrm{kpc}$ (top) and $r = 8\,\mathrm{kpc}$ (bottom).

2.4 Results

2.4.1 Growth rate, temporal evolution and saturation

The time evolution of the magnetic field strength at the galactic midplane $z = 0$, normalized to the equipartition value B_{eq}, is shown in Fig. 2.1, for parameters corresponding to $r = 4\,\mathrm{kpc}$ (top) and $r = 8\,\mathrm{kpc}$ (bottom). For solutions of the full set of equations (2.8)–(2.10), four different regimes are depicted, with and without the advective and diffusive helicity fluxes, $U_0 = 0$ or $1\,\mathrm{km\,s^{-1}}$ and $R_\kappa = 0$ or 0.3. Two cases with algebraic α quenching are also illustrated, with $U_0 = 0$ and $U_0 = 1\,\mathrm{km\,s^{-1}}$.

There is an initial brief phase of very rapid growth of the field at $z = 0$, but this reflects the arbitrary choice of the seed magnetic field and is not physically relevant. In all cases, the magnetic field then grows exponentially, until $B \sim B_{\mathrm{eq}}$. A steady state follows unless, in the dynamical quenching model, the flux of α_{m} is zero ($R_\kappa = R_U = 0$), in which case the field decays catastrophically (dotted curves). The exponential growth rates γ in the kinematic regime are the same for all solutions with a given value of R_U, as would be expected. The growth rate of the magnetic field at $r = 4\,\mathrm{kpc}$ is larger than that at $r = 8\,\mathrm{kpc}$ since the dynamo number D is larger in magnitude at the smaller radius (Table 2.1). The growth rate at $r = 2\,\mathrm{kpc}$ (not shown here), where the eigenfunction for $\overline{\boldsymbol{B}}$ has a maximum in r (see Chapter 3) , $\gamma = 8.5\,\mathrm{Gyr^{-1}}$ for $U_0 = 0$, is close (albeit slightly greater) to the global growth rate $\Gamma = 7.8\,\mathrm{Gyr^{-1}}$ in the axisymmetric global disc model Model A or Model B) of Chapter 3.

The growth rate in the numerical solutions can be compared with that obtained from the asymptotic solutions. Fig. 2.2 shows γ, in units of the inverse diffusion time t_{d}^{-1}, plotted as a function of R_U, for various values of the dynamo number $-50 < D < -8$. Numerical solutions (solid) are well approximated by the perturbation solution (dashed), and the functional form $\gamma(R_U)$ is remarkably close to that of the numerical solution. The no-z solution gives values of γ that are somewhat less accurate (as might be expected) but still reasonable for growing solutions ($\gamma > 0$) unless D and R_U are both very large.

The steady-state field strength at the midplane, $B(0)$, increases with R_κ in the solutions with dynamical quenching (compare black solid and green dash-dotted curves of Fig. 2.1) since larger R_κ means larger diffusive helicity flux. Conversely, the saturation strength is smaller for larger R_U for the values of R_U considered (compare blue short dashed and green dash-dotted curves). The mean vertical velocity affects the dynamo action in more than one way. On the one hand, the steady-state magnetic field strength increases with R_U as in equation (2.18), but larger R_U means a larger magnitude of the critical dynamo number (2.15), hence a weaker dynamo action. As discussed by Sur et al.

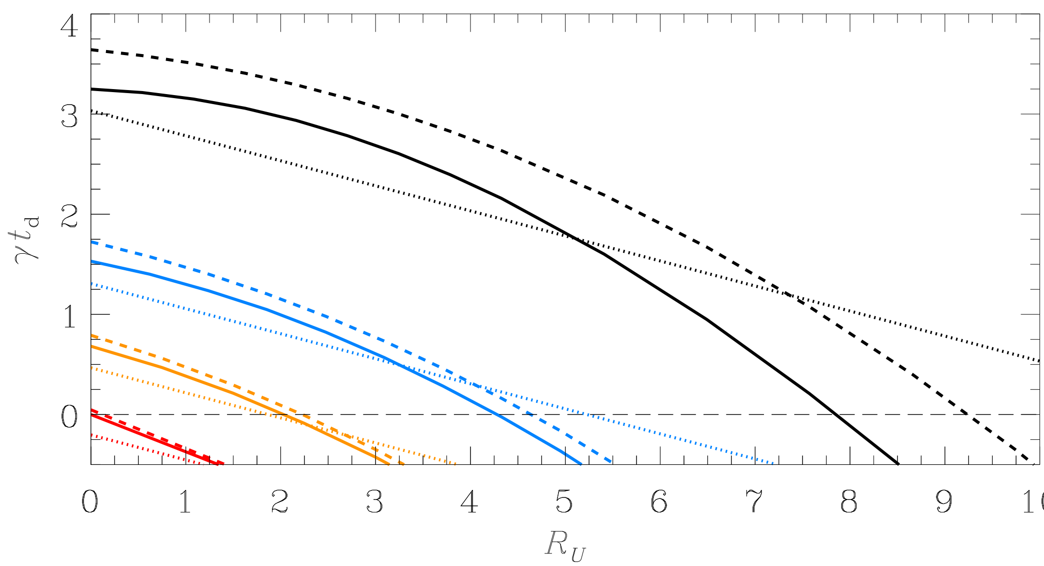

Figure 2.2: The dimensionless growth rate γ (measured in inverse diffusion time $t_{\rm d}^{-1}$) as a function of R_U for the numerical kinematic solutions (solid), the perturbation solution (short-dashed), and the no-z solution (dotted). Each color represents a different dynamo number/disc radius. From top to bottom: $D = -47.5$, $t_{\rm d} = 0.38\,{\rm Gyr}$ (black), $D = -22.4$, $t_{\rm d} = 0.50\,{\rm Gyr}$ (blue), $D = -13.5$, $t_{\rm d} = 0.73\,{\rm Gyr}$ (orange), and $D = -8.1$, $t_{\rm d} = 3.67\,{\rm Gyr}$ (red).

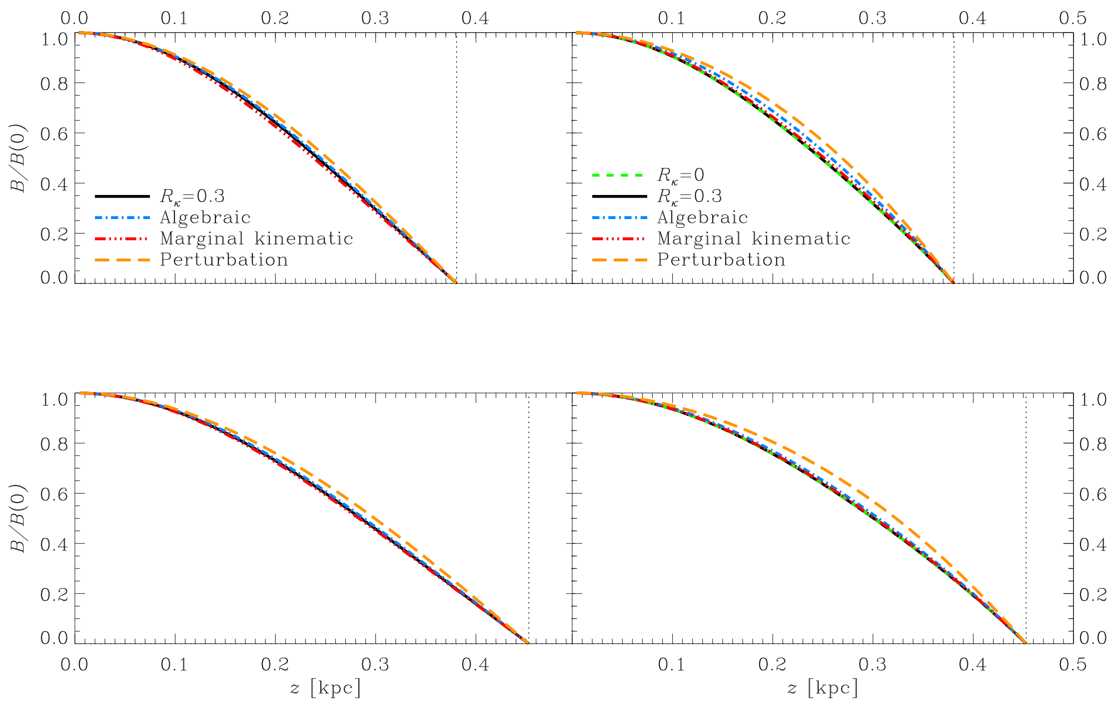

Figure 2.3: Dependence of the magnitude of the large-scale magnetic field B on height z. The upper panel is for $r = 4\,\text{kpc}$ while the lower panel is for $r = 8\,\text{kpc}$. Solutions with $U_0 = 0$ are shown on the left of each panel, while those with $U_0 = 1\,\text{km}\,\text{s}^{-1}$ are shown on the right. The vertical dotted line shows the disk boundary at $z = h$. Solutions are symmetric about $z = 0$.

(2007), there exists a value of R_U optimal for the dynamo action. For $R_\kappa = 0.3$ and $r = 4\,\text{kpc}$, the no-z approximation has the optimal value $R_U = 0.57$, while for $r = 8\,\text{kpc}$ an outflow of any intensity reduces magnetic field strength in the steady state (formally, the optimum value is negative, $R_U = -0.68$). However, in the numerical solution with the dynamical quenching non-linearity (that does not rely on the no-z approximation), $R_U = 0$ gives a higher saturation strength than any $R_U > 0$ at both $r = 4\,\text{kpc}$ and $r = 8\,\text{kpc}$ for $R_\kappa = 0.3$. This is possible because catastrophic quenching is solved by $R_\kappa \neq 0$. Similar, but less transparent dependences on R_U can be noticed in the perturbation solution of Section 2.3.1. Similar dependence on R_U also occurs under the algebraic quenching (compare orange dash-triple-dotted and red long dashed curves), but here the mean vertical velocity can only be damaging for the dynamo action and the steady-state magnetic field decreases with R_U monotonically.

With the dynamical non-linearity, the field undergoes mild non-linear oscillations

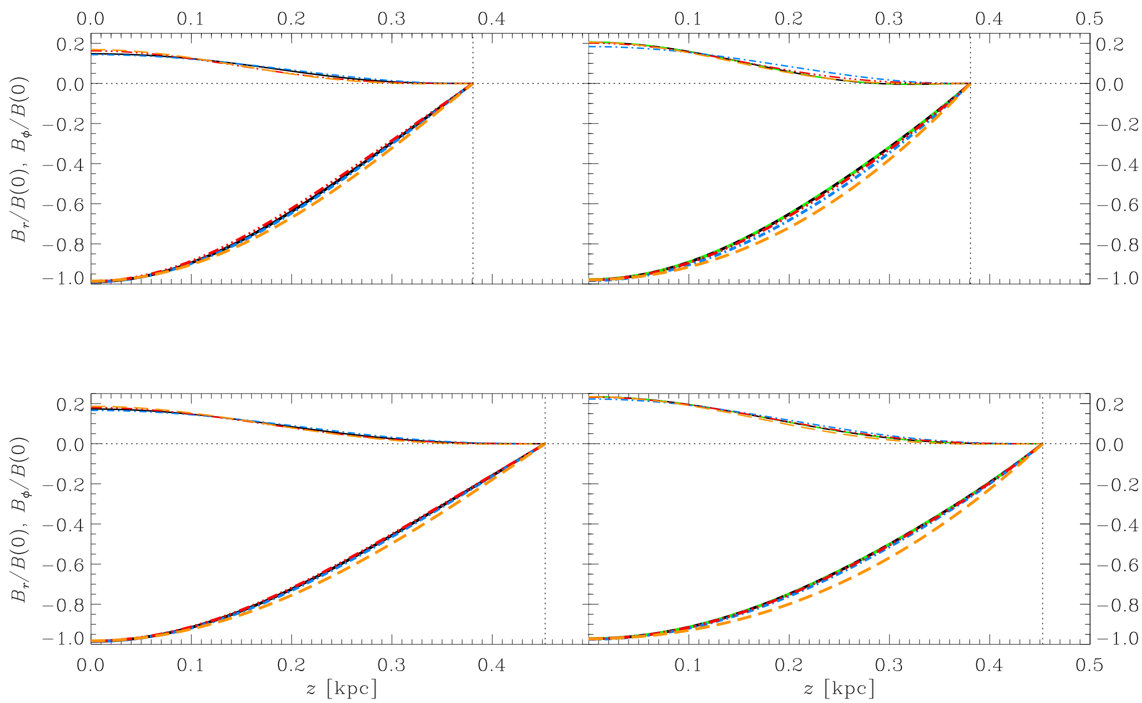

Figure 2.4: Radial (thin) and azimuthal (thick) components of $\overline{\boldsymbol{B}}$ in the saturated state, normalized to the magnetic field strength at the midplane for parameters corresponding to $r = 4\,\mathrm{kpc}$ (top) and $r = 8\,\mathrm{kpc}$ (bottom) and to $U_0 = 0$ (left) and $U_0 = 1\,\mathrm{km\,s^{-1}}$ (right). The sign of each component is arbitrary (see text), but the sign of $\overline{B}_r\overline{B}_\phi$ is not. Solutions are symmetric about $z = 0$. (For the legend, see Fig. 2.3.)

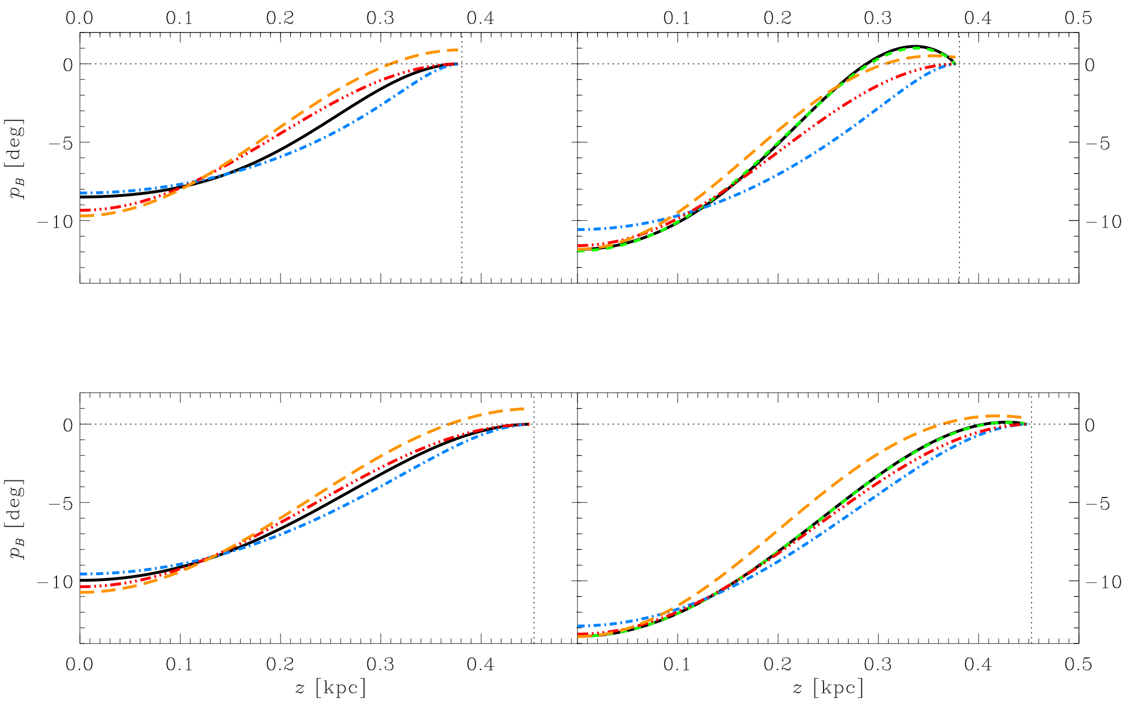

Figure 2.5: Magnetic pitch angle $p_B \equiv \tan^{-1}(\overline{B}_r/\overline{B}_\phi)$ in the saturated (steady) state, as a function of the distance z from the midplane, for parameters corresponding to $r = 4\,\mathrm{kpc}$ (top) and $r = 8\,\mathrm{kpc}$ (bottom) and to $U_0 = 0$ (left) and $U_0 = 1\,\mathrm{km\,s^{-1}}$ (right). p is not plotted for $z = h$, as it is undefined at the disc boundaries, where the boundary conditions enforce $\overline{B}_r = \overline{B}_\phi = 0$. (For the legend, see Fig. 2.3.)

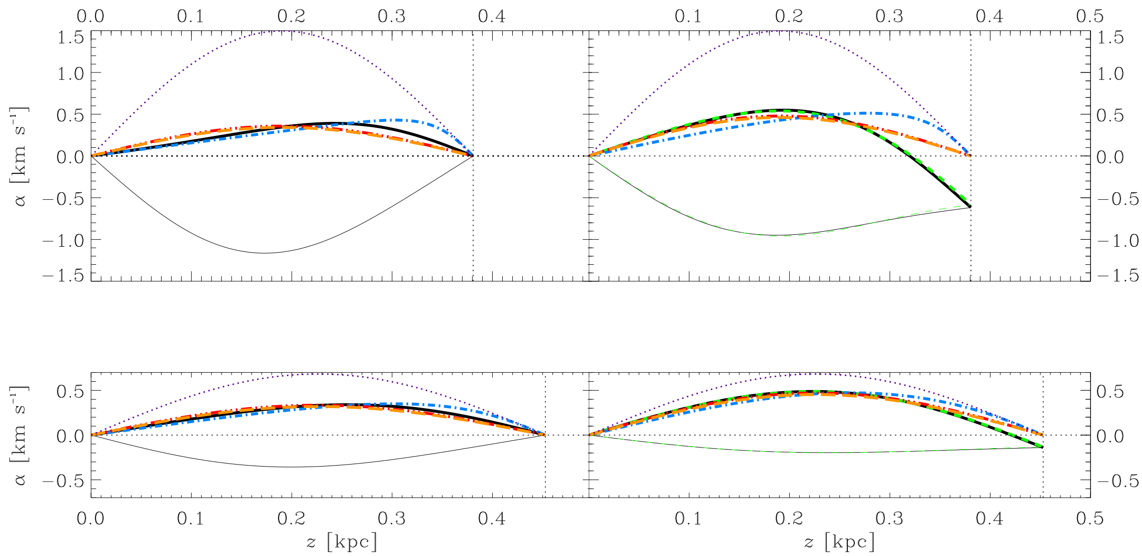

Figure 2.6: α in the saturated state as a function of the distance z from the midplane, for parameters corresponding to $r = 4\,\mathrm{kpc}$ (top) and $r = 8\,\mathrm{kpc}$ (bottom) and to $U_0 = 0$ (left) and $U_0 = 1\,\mathrm{km\,s^{-1}}$ (right). For the asymptotic solution, α has been plotted as $(\pi R_{\alpha,\mathrm{c}}\eta_\mathrm{t}/2h)\sin(\pi z/h)$. α_k is shown as a thin dotted purple line for comparison. For solutions using the dynamical quenching non-linearity, α_m is shown as a thin line of the appropriate linestyle. All functions shown are antisymmetric about $z = 0$. (For the legend, see Fig. 2.3.)

Table 2.2: Comparison of the results of the numerical solution with dynamical α-quenching and the no-z solution. For the numerical solution, vertical averages of p_B and B/B_{eq}, defined in equations (2.19), are given.

			Numerical solution				No-z approximation			
r	R_U	R_κ	D_{c}	γ	$\langle p_B \rangle$	$\langle B \rangle / B_{\mathrm{eq}}$	D_{c}	γ	p_B	B/B_{eq}
[kpc]				[Gyr^{-1}]	[°]			[Gyr^{-1}]	[°]	
4	0.0	0.3	$-\ 8.1$	5.6	-6.6	0.79	$-\ 9.6$	5.1	-7.1	0.74
	1.1	0.0	-10.8	5.2	-7.7	0.40	-11.9	4.5	-7.9	0.39
	1.1	0.3	-10.8	5.2	-7.7	0.66	-11.9	4.5	-7.9	0.74
8	0.0	0.3	$-\ 8.1$	1.7	-7.2	0.39	$-\ 9.6$	1.3	-7.9	0.33
	1.4	0.0	-11.5	1.0	-9.1	0.17	-12.4	0.7	-8.9	0.15
	1.4	0.3	-11.5	1.0	-9.1	0.26	-12.4	0.7	-8.9	0.27

before settling down to a steady state (such oscillations are more evident for parameters corresponding to $r = 4\,\mathrm{kpc}$, but are present for $r = 8\,\mathrm{kpc}$ as well). Much milder oscillations are found for the case of algebraic quenching, for parameters corresponding to $r = 4\,\mathrm{kpc}$, but not at $r = 8\,\mathrm{kpc}$. This oscillatory behaviour is discussed by Sur et al. (2007) who attribute it to repeated over-suppression and recovery of the dynamo action by helicity fluxes.

It can be seen in both the top and bottom panels that for both $U_0 = 0$ and $U_0 = 1\,\mathrm{km\,s^{-1}}$, the saturated field strength obtained using algebraic quenching is higher than that obtained using dynamical quenching, by a factor of about 2–4. Since the algebraic quenching is of an entirely heuristic form, this difference is not of any physical significance. The agreement can thus be restored just by adjusting the factor a in equation (1.34); this is done in Section 2.5.

2.4.2 Magnetic field distribution across the disc

We now explore the dependence of B, $\overline{B}_r$, $\overline{B}_\phi$, p and α on the height z above the galactic midplane, in the saturated (steady) state. In Fig. 2.3, we plot B versus z for the various models, normalized to the value of B at $z = 0$ for each model, with $r = 4\,\mathrm{kpc}$ in the upper panel and $r = 8\,\mathrm{kpc}$ in the lower panel. On the left of each panel, $U_0 = 0$, whereas on the right, $U_0 = 1\,\mathrm{km\,s^{-1}}$. The profiles of $\overline{B}_r$ and $\overline{B}_\phi$, similarly normalized, are plotted in Fig. 2.4, while the magnetic pitch angle p_B is shown in Fig. 2.5 and the α profile in Fig. 2.6.

All of the curves lie strikingly close together. Clearly, the inclusion of a realistic outflow with $R_U \sim 1$ does not drastically affect the functional form of the solution, though some differences between solutions with $R_U = 0$ and $R_U > 0$ are apparent (see below). Furthermore, it is noteworthy that the difference between dynamical and algebraic quenching solutions is very small. The marginal kinematic and perturbation solutions reproduce the functional forms of $\overline{B}_r$ and $\overline{B}_\phi$ quite accurately even though these are linear solutions. The agreement is equally good in the ratio $\overline{B}_r/\overline{B}_\phi$, so all of the models produce similar magnetic pitch angles $p_B \sim -10^\circ$ at $z = 0$ that reduces in magnitude with increasing distance from the midplane.

However, some small differences between the models do exist. As shown in Fig. 2.3, magnetic field strength B decreases with z slower as R_U increases (compare left and right plots in each panel). This is more evident for $r = 8\,\mathrm{kpc}$, where the difference between the solutions with $U_0 = 0$ and $U_0 = 1\,\mathrm{km\,s^{-1}}$ is already apparent at $z \gtrsim 0.15\,\mathrm{kpc}$. This is a natural consequence of the advection of magnetic field to regions with weaker field at larger z: such a redistribution is opposed by magnetic diffusion, and R_U is a measure of the strength of advection relative to diffusion (see also Bardou et al., 2001, who include a halo in their models).

The ratio $\overline{B}_r/\overline{B}_\phi$ of the magnetic field components shown in Fig. 2.4 is larger in magnitude near $z = 0$ when $R_U \neq 0$, and the ratio is larger when R_U is larger. This can be seen more clearly in Fig. 2.5, which shows the magnetic pitch angle p_B as a function of z. The increase of $|p_B|$ with R_U is a direct consequence of equation (2.17).

A notable feature of models with $R_U > 0$ is that the magnetic pitch angle changes sign near the disc surface, so that a trailing (with respect to the overall rotation) magnetic spiral of the inner layers becomes a leading spiral near the disc surface. This is a characteristic feature of any growing dynamo mode in a slab surrounded by vacuum (Ruzmaikin et al., 1979; Ji et al., 2013), but not of a marginal kinematic solution where $p_B < 0$ everywhere in the slab. The outflow extends this feature to the steady state. The reversal of $\overline{B}_r$ responsible for this occurs deeper in the slab as the dynamo number is increased. Thus, a leading, rather than a trailing, magnetic spiral may exist in the disc near the disc-halo boundary (and perhaps in the halo), provided that an outflow is present. However, the robustness of this feature should be checked using other types of boundary condition which may be more suitable for outflows, or by including the galactic halo in the model.

The perturbation solution of Section 2.3.1 also has $p_B > 0$ near the surface for both vanishing and positive R_U. This is an artefact resulting from the loss of accuracy of this solution which is formally applicable only for $|D| \ll 1$ and $R_U \ll 1$. As discussed by Ji et al. (2013), the solution remains accurate even for $D \simeq -50$, but this is, evidently, not the case with R_U. Hence, the perturbation solution should not be used for R_U of order unity if the behaviour of the solution near the surface is important.

The change in the sign of α near the boundaries can be understood as resulting from the advective flux of α_m towards the boundaries. Since the kinetic part of the α-coefficient is small near $z = h$, advection of the (negative) α_m from deeper layers can change the sign of $\alpha = \alpha_\mathrm{k} + \alpha_\mathrm{m}$ near the surface. The effect is more pronounced at smaller radius because α_m has larger magnitude there (see Fig. 2.6 where α_m is shown as a thin line of the appropriate linestyle and color). It would be useful to explore how sensitive is this effect to the boundary conditions.

2.5 The algebraic non-linearity and no-z approximation refined

Both the no-z approximation and the algebraic form of the dynamo non-linearity are simple, convenient and flexible approaches, and we have demonstrated that they approximate quite reasonably the physically motivated dynamo solutions with dynamic non-linearity. Then they deserve to be refined to achieve better quantitative agreement with the results obtained under the dynamic non-linearity.

2.5.1 Improved no-z approximation

Numerical solutions of equations (2.8)–(2.10) are compared with those obtained with the no-z approximation in Table 2.2. Since the latter can be thought of as representing equivalent (averaged over the disc thickness) values of the solution, we present, for the numerical solutions, the averaged magnetic field strength and pitch angle defined as

$$\langle\overline{B}\rangle = \frac{1}{2h}\int_{-h}^{h}\overline{B}\,\mathrm{d}z\,, \quad \tan\langle p_B\rangle = \frac{\displaystyle\int_{-h}^{h}\frac{\overline{B}_r}{\overline{B}_\phi}\,\overline{B}\,\mathrm{d}z}{\displaystyle\int_{-h}^{h}\overline{B}\,\mathrm{d}z}\,. \tag{2.19}$$

We note that these averages may differ from those obtained from observations of polarized intensity or Faraday rotation where the observables are the Stokes parameters that depend on higher powers of magnetic field.

In addition to the terms used in the earlier applications of the no-z approximation, we have additional terms representing magnetic helicity fluxes. Magnetic field components in equations (2.12) and (2.13) depend on z in a more complicated manner if $R_U \neq 0$. This suggests that approximating derivatives in z with division by h would be less accurate and general when $R_U \neq 0$. Adjustments required to approximate the kinematic growth rate of the mean magnetic field with a reasonable accuracy for $-50 < D < 0$ are discussed in

Appendix B.1. We suggest and use the following approximations:

$$\frac{\partial}{\partial z}(\overline{U}_z\overline{B}_r) \simeq \frac{\overline{U}_z\overline{B}_r}{4h}\,, \qquad \frac{\partial}{\partial z}(\overline{U}_z\overline{B}_\phi) \simeq \frac{\overline{U}_z\overline{B}_\phi}{4h}\,,$$
$$\frac{\partial}{\partial z}(\overline{U}_z\alpha_\mathrm{m}) \simeq \frac{\overline{U}_z\alpha_\mathrm{m}}{h}\,, \qquad \frac{\partial^2\alpha_\mathrm{m}}{\partial z^2} \simeq -\pi^2\frac{\alpha_\mathrm{m}}{h^2}\,.$$

2.5.2 Algebraic α-quenching as an approximation to the dynamic non-linearity

The algebraic α-quenching appears to be a reasonable approximation to the dynamic non-linearity arising from magnetic helicity fluxes. We show in this section that this is not a coincidence by deriving an algebraic approximation to the dynamic non-linearity in the steady state, which contains terms responsible for the helicity transport, and discuss conditions for the applicability of this approximation.

To explore the steady state solution, set $\partial\alpha_\mathrm{m}/\partial t = 0$ in equation (1.32). Assuming that the flux term can be approximated as $l^2\boldsymbol{\nabla}\cdot\boldsymbol{\mathcal{F}}_\alpha/(2\eta_\mathrm{t}) = f\alpha_\mathrm{m}$, where f is a positive numerical factor to be determined, and putting $\alpha_\mathrm{m} = \alpha - \alpha_\mathrm{k}$, we obtain

$$\alpha = \alpha_\mathrm{c} = \frac{\alpha_\mathrm{k} + (f + 1/\mathcal{R}_\mathrm{m})^{-1}\,\eta_\mathrm{t}\boldsymbol{\nabla}\times\overline{\boldsymbol{B}}\cdot\overline{\boldsymbol{B}}}{1 + (f+1/\mathcal{R}_\mathrm{m})^{-1}\,B^2}. \tag{2.20}$$

where α_c is the critical value of α and the magnetic Reynolds number is here defined as $R_\mathrm{m} \equiv \eta_\mathrm{t}/\eta$. For $f = 0$ (no flux of α_m), this reduces to equation (14) of Gruzinov & Diamond (1994).

The algebraic form (1.34) follows from equation (2.20) if

$$\eta_\mathrm{t}\boldsymbol{\nabla}\times\overline{\boldsymbol{B}}\cdot\overline{\boldsymbol{B}} = K\alpha_\mathrm{c}B^2, \tag{2.21}$$

with K a factor to be determined. Magnetic helicity balance constrains K to be positive, since α_c has opposite sign to α_m, and large- and small-scale current helicities must have opposite sign to each other.

Equation (2.21) is satisfied reasonably well for typical galactic parameters. Combining equations (B.2) and (2.17) of the no-z solution, recalling that $D_\mathrm{c} = h\alpha_\mathrm{c}R_\omega/\eta_\mathrm{t}$, and assuming $\overline{B}_r^2/\overline{B}_\phi^2 \ll 1$, typical of $\alpha\omega$-dynamos, we obtain

$$K = \frac{3}{4\sqrt{2}} \approx 0.53. \tag{2.22}$$

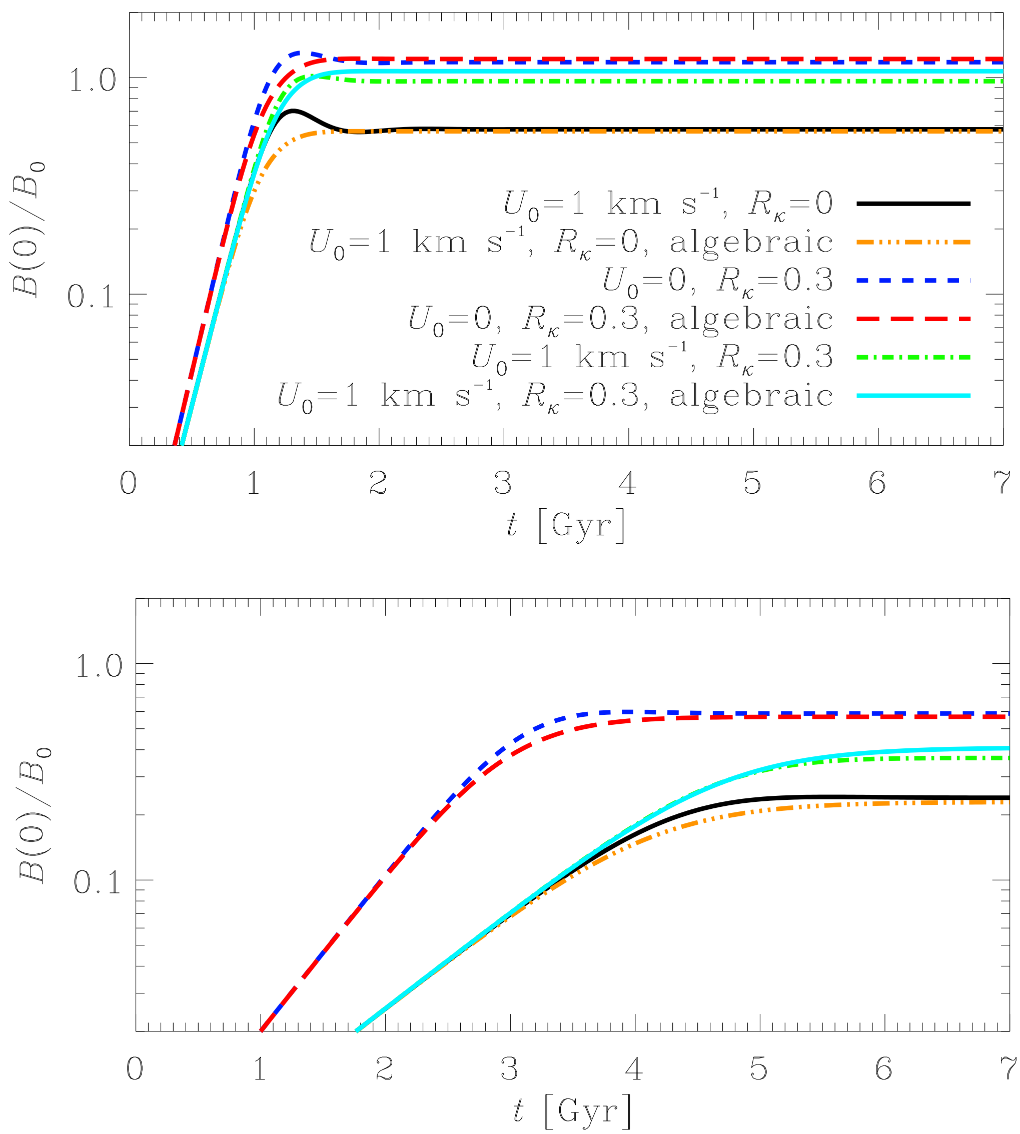

Figure 2.7: Time evolution of the magnetic field strength at $z = 0$ for models using dynamical quenching and models with the same parameters but using generalized algebraic quenching with a given by equation (2.23). Parameters corresponding to $r = 4\,\mathrm{kpc}$ are plotted in the top panel, and to $r = 8\,\mathrm{kpc}$ in the bottom panel.

Furthermore, substituting $\alpha_\mathrm{k}/\alpha_\mathrm{c}$ for D/D_c in equation (2.18), and solving for α_c (assuming $\overline{B}_r^2/\overline{B}_\phi^2 \ll 1$), we obtain the form (1.34) with

$$a = \frac{C}{\xi_0(R_U + \pi^2 R_\kappa)}\,, \tag{2.23}$$

where $\xi_0 = [1 - 3/(4\sqrt{2})]^{-1} \approx 2.1$ and $C \equiv 2(h/l)^2$, and the numerical factors in the no-z approximation estimated in Section 2.5.1 have been used in the helicity flux terms. This result can also be obtained from equations (2.20), (2.21), and (2.22), with $f = (R_U + \pi^2 R_\kappa)/C$. Specific values of a at $r = 4\,\mathrm{kpc}$ and $r = 8\,\mathrm{kpc}$ in the galaxy model adopted range from 3–14 for the combinations of parameter values listed in Table 2.2. Note that this is consistent with the saturation value of B being a factor of about 2–4 too large (compared to that obtained with the dynamical non-linearity) when using algebraic quenching with $a = 1$, as noted in Section 2.4.1. Also note that these values for a are somewhat sensitive to the ratio h/l appearing in equation (2.23). Gressel et al. (2013) find even larger values of a from direct numerical simulations.

Equation (2.23) appears as a natural generalization of the standard α-quenching, as it makes the saturation magnetic field dependent on the magnetic helicity fluxes. Figure 2.7 compares the results obtained numerically with (1.34) and (2.23) with those under dynamical quenching. Clearly, the agreement is much better than for $a = 1$ (see Fig. 2.1). The z-distributions of the resulting magnetic field components are identical to those under the standard algebraic quenching with $a = 1$.

2.6 Examples of application

To illustrate the use of the toolbox, we apply it to estimate the magnetic pitch angle and to explore the nature of the magnetic arms. The analysis below is mainly based on the analytical expressions of the no-z approximation, but results have been checked with numerical solutions.

2.6.1 Magnetic pitch angle

In the kinematic stage, the pitch angle of the mean magnetic field, $p_B = \arctan(\overline{B}_r/\overline{B}_\phi) \simeq -\arctan(R_\alpha/|R_\omega|)^{1/2}$, agrees reasonably well with observations, even if its magnitude remains somewhat smaller than desired (Ruzmaikin et al., 1988). Some galaxies with exceptionally open magnetic spirals with $p_B \simeq -40^\circ$, such as M33 (Tabatabaei et al., 2008; Chyży & Buta, 2008), do not seem to be consistent with this estimate.

Non-linear dynamo effects can only reduce the magnitude of the pitch angle since, effectively, they lead to the reduction of R_α to the smaller $R_{\alpha,\mathrm{c}}$ (see also Elstner, 2005). Indeed, for the fairly typical galactic parameters chosen in the present work, we obtain $p \sim -10^\circ$ in the non-linear solutions, whereas average observed values are closer to -20° (Fletcher 2010; see also the discussion in Chapter 5).

According to equation (2.17), $|p_B|$ increases with R_U, but increasing R_U also causes γ and B^2 to decrease, according to equations (4.26) and (2.18), and there is a maximum value of R_U above which the dynamo action is suppressed. From equation (2.15), the dynamo remains active for $R_U + \pi^2 < 4\sqrt{(2/\pi)\, R_\alpha |R_\omega|}$, which leads to an upper limit on the magnitude of the magnetic pitch angle:

$$\tan p_B > -\sqrt{\frac{2R_\alpha}{\pi |R_\omega|}}\,,$$

so that the outflow can hardly enhance the magnitude of p_B significantly. The right-hand side of the equation is simply the estimate one obtains for the kinematic regime; for the dynamical non-linearity that is assumed, $R_{\alpha,\mathrm{c}} < R_\alpha$, so $|p_B|$ always decreases from its value in the kinematic regime.

It appears that magnetic pitch angle of the dynamo-generated magnetic field is further modified by additional effects, some of which are rather obvious. Most importantly, magnetic field compression in the gaseous spiral arms efficiently aligns magnetic field with the spiral arms. If the ratio of the gas densities in the arm and outside it is ϵ, with $\epsilon > 1$ and $\epsilon = 4$ for a strong adiabatic shock, the angle θ between magnetic field and the arm axis is reduced, under one-dimensional compression, as $\tan\theta_2 = \epsilon^{-1}\tan\theta_1$ from the interarm value θ_1 to that within the arm θ_2. For $\theta_1 = 30^\circ$ and $\epsilon = 4$, magnetic field is diverted by $\theta_1 - \theta_2 \approx 22^\circ$ towards the arm axis. Since such observables as the Faraday rotation measure and polarized synchrotron intensity are dominated by the denser and stronger magnetized interior of the spiral arms, the compressional alignment can significantly affect the magnetic pitch angle observed.

Additional dynamo effects can also make the magnetic spirals more open. For example, the contribution of magnetic buoyancy to the mean-field dynamo action can produce $p_B = -(20^\circ\text{–}30^\circ)$ (Moss et al., 1999). Another, less obvious effect can be due to a radial inflow of interstellar gas (at a speed of order $U_r = 1\,\mathrm{km\,s^{-1}}$ at the Solar radius in the Milky Way, and expected to be stronger in galaxies with more open spiral patterns), driven by the outward angular momentum transfer by the spiral pattern, turbulence and magnetic fields. The inflow can increase the magnitude of p_B by at least 5–10%. (Moss et al., 2000). The effect of the many further additional terms in the mean electromotive force (e.g. Rohde et al., 1999; Rädler et al., 2003; Brandenburg & Subramanian, 2005a) on the pitch angle has never been explored.

2.6.2 Arm-interarm contrast in magnetic field strength

Various solutions of the dynamo equations offer a range of possibilities to explore the effects of spiral arms on the large-scale galactic magnetic fields. Among them are the phenomenon of magnetic arms, the enhancement of polarized intensity (and, presumably, the large-scale magnetic field) in spiral-shaped regions that do not always overlap with the gaseous arms, regions of larger gas density (e.g., Frick et al., 2000). Several explanations have been suggested (Moss 1998; Shukurov 1998; Rohde et al. 1999; Moss et al. 2013; see also Chapters 3 and 4), but there is no convincing explanation.

Equation (2.18) suggests a number of effects that can contribute to a non-monotonic dependence of the large-scale magnetic field strength on gas density. One possibility is that R_U can be larger in the arms owing to a greater frequency of supernova explosions there. This can lead to larger $B^2/B_{\rm eq}^2$ in the interarm regions compared to in the arms, as suggested by Sur et al. (2007). An estimate of this effect can be found in Table 2.2: for $r = 8\,{\rm kpc}$ $\overline{B}$ would be about 1.5 times stronger in the interarm regions in an extreme case where the outflow speed vanishes between the arms remaining modest in the arms at $1\,{\rm km\,s^{-1}}$ ($R_U = 1.36$). This ratio increases to about 4 if $U_0 = 2\,{\rm km\,s^{-1}}$ in the arms. Therefore, this effect may be important and thus deserves a more detailed exploration. This will be done in Chapter 6.

2.7 Conclusions and discussion

We have discussed various simple approximate approaches to estimate the strength of the large-scale galactic magnetic fields, their pitch angle and dynamo thresholds, and compared them with numerical solutions. In particular, we compared the non-linear states established due to magnetic helicity conservation with those obtained with a much simpler, and easier to analyze, heuristic algebraic form of the dynamo non-linearity. These approaches complement one another. For example the perturbation solution provides a reasonably accurate form of the distribution of magnetic field across the disc, whereas the no-z approximation gives useful results for variables averaged across the disc. Remarkably, and reassuringly, where they overlap, all of these methods result in similar solutions. Most importantly, results obtained with the dynamical non-linearity that involves advective and diffusive fluxes of magnetic helicity are very much consistent with those from the algebraic α-quenching. We suggest how the latter can be modified to achieve quite a detailed agreement.

Magnetic lines produced by the mean-field dynamo are believed to be trailing with respect to the galactic rotation because the galactic angular velocity decreases with galactocentric radius. We have found, however, that steady-state magnetic fields obtained for the dynamical non-linearity are trailing near the galactic midplane but leading closer to the disc surface (where $\overline{B}_r$ changes sign) if an outflow is present. This effect is more pronounced when the galactic outflow is stronger or the dynamo number is higher as compared with its critical value. This feature is new and unexpected, as it is not reproduced in models with algebraic quenching. This makes it reasonable to expect that leading magnetic spirals may be observable in the disc-halo interface regions of spiral galaxies (or even higher in the halo). To what extent this feature persists if the boundary conditions are varied or if the galactic halo is included is a question that merits future investigation.

It is also useful for applications that marginal kinematic solutions of the dynamo equations in a thin disc (i.e., those that neither grow nor decay) reproduce with high accuracy non-linear steady-state solutions. The simple analytical perturbation solutions of kinematic dynamo equations, here generalized to include magnetic field advection in a galactic outflow, are particularly useful in this respect. It has been shown here and by Ji et al. (2013) that they remain accurate beyond their formal range of applicability and can be used for the range of dynamo numbers $-50 \lesssim D \lesssim 0$ typical of galactic discs. Here we have also shown that these solutions can be used as a good approximation to the non-linear states.

We have also refined the no-z approximation to allow for vertical advection of the mean magnetic field, as well as advective and diffusive helicity fluxes. We note that advection affects dynamo action through three channels: by reducing the critical dynamo number, by helping the turbulent diffusion to remove flux from the dynamo active region, and by the removal of small-scale magnetic helicity. The heuristic diffusive flux of magnetic helicity has previously been observed in numerical simulations.

The models investigated here are somewhat simplified compared to real galaxies. It is worth extending the models to include spatial variation of η_t, additional terms in the mean electromotive force, and other contributions to the magnetic helicity flux. The possible importance of η_t-quenching, in addition to α-quenching (Gressel et al., 2013), also deserves exploration. More refined modelling will enable better comparison with real galaxies.

In summary, much of the earlier work on galactic dynamos modeled the saturation of the dynamo using algebraic quenching of the α effect. We show here that this algebraic quenching non-linearity (which predates dynamical quenching theory but is still widely used in the dynamo literature) is a good approximation to dynamical quenching for the galactic mean-field dynamo. We also extend the standard algebraic quenching formula to make it more accurate. In addition, we suggest three simple tools, namely marginal kinematic solutions, critical asymptotic solutions from perturbation theory, and no-z solutions, and show that all agree remarkably well with the numerical solutions of the non-linear dynamo. Particularly useful are the analytical expressions (2.12) and (2.13) for the vertical profiles of $\overline{B}_r$ and $\overline{B}_\phi$, as well as equations (2.18) and (2.17) for the saturation field strength B and pitch angle p_B, which, when used along with the analytical expression (2.11) for the kinematic growth rate γ, comprise a surprisingly efficient guide to the parameter space of galactic dynamos.

Thus far, we have focused on local 'thin-slab' dynamo models. Certain features, such as reversals and non-axisymmetric modes, require global disc models for their exploration. Moreover, in this chapter we have made use of FOSA, which implicitly assumes that the mean electromotive force responds instantaneously to changes in the mean magnetic field and small-scale turbulence. This assumption may not be physically appealing; for instance it does not guarantee causality (Brandenburg et al., 2004; Rheinhardt & Brandenburg, 2012). As explained in Chapter 1, closures like the MTA point to the importance of a finite response time. Moreover, it has been argued that memory effects are needed to explain the nature of the dynamo action observed in some direct numerical simulations (Hubbard & Brandenburg, 2009; Rheinhardt et al., 2014). In the next chapter, we make use of global galactic dynamo models to show that important effects not seen under FOSA can occur when temporal non-locality is incorporated into the models.

Chapter 3

Galactic spirals and dynamo action: A new twist on magnetic arms

3.1 Introduction

In many cases, galactic magnetic fields exhibit significant deviations from axial symmetry, in particular where the regular field is enhanced in 'spiral magnetic arms' akin to the gaseous or stellar material arms. (By material arms, we specifically mean the regions where the densities of stars and gas are enhanced, not to be confused with the material arms of galactic dynamics theory, which refer to spiral arm structures that wind up along with the differentially rotating stars or gas.) In most cases, there is clearly a relationship between the material spiral arms and regular magnetic field spiral arms. For instance, there exists a correspondence between the azimuthally averaged pitch angle of the regular field and that of the material spiral (Fletcher, 2010). This would be of little surprise, as the material arms naturally leave their imprint on the magnetic field, if not for the intriguing relation between magnetic and material arms, first discovered in the nearby galaxy NGC 6946 (Beck & Hoernes, 1996). Here the magnetic arms are located almost precisely between the material arms. They appear to be phase-shifted images of the material arms, with a negative phase shift in the sense of the galactic rotation (Frick et al., 2000; Beck, 2007). Importantly, the stronger tangling of the regular field by a (presumably) more intense turbulence within the material arms cannot explain this phenomenon: both the total and regular magnetic fields are stronger within the magnetic arms (Beck, 2007). The nature of magnetic arms remains to be convincingly explained. This issue forms the major focus of the next few chapters.

Turbulent mean-field dynamo theory has been successful in explaining the properties of the axisymmetric mode of regular fields in galaxies Ruzmaikin et al. (1988). Although growing non-axisymmetric modes can arise in this theory, they always have a lower growth rate than the axisymmetric mode if the galactic disc is axially symmetric (Baryshnikova et al., 1987; Krasheninnikova et al., 1989). They can also be substantial only beyond a certain radius in the disc where the rotational velocity shear is sufficiently small. Thus, to explain non-axisymmetric modes as arising in an axisymmetric disc one must typically appeal to strongly non-axisymmetric seed fields and argue that the axisymmetric mode would not have had time to attain dominance.

An alternative, of course, is to appeal to the deviations of the galactic discs from axial symmetry. Mestel & Subramanian (1991) and Subramanian & Mestel (1993) explored analytically and numerically the growth of non-axisymmetric modes under an enhancement of dynamo action along a spiral (presumably, but not necessarily, co-spatial with the material spiral) with a constant global pattern speed. Subsequently, Moss (1996) (see also Moss 1998; Moss et al. 2001) carried out mean-field dynamo simulations to explore the effects of modulating various quantities, such as the α effect, turbulent diffusivity, or the components of the mean velocity, along a spiral arm or bar. Some authors have also addressed directly the question of how the regular field could become enhanced in between the material arms (Shukurov, 2005; Rohde et al., 1999), though none of these explained the phenomenon of a substantial negative phase shift across a wide range of galactocentric distances, including those far away from the corotation radius, as reported by Frick et al. (2000).

In addressing the problem of magnetic arms, new advances in dynamo and spiral structure theories should be incorporated. Much of the recent work on mean-field dynamo theory has been focussed on the nonlinear regime, and the possible catastrophic quenching of the dynamo implied by magnetic helicity conservation. This has led to the development of the dynamical quenching theory (Brandenburg & Subramanian, 2005a). In this theory, catastrophic quenching of the mean-field dynamo action is averted by a magnetic helicity flux, which transports small-scale magnetic helicity away from the region of dynamo action. Dynamical quenching theory has been applied to local galactic dynamo models (Kleeorin et al., 2000; Vishniac & Cho, 2001; Kleeorin et al., 2002; Shukurov et al., 2006; Sur et al., 2007), and to axisymmetric discs (Kleeorin et al., 2002; Smith, 2012; Smith et al., 2012), but not yet to non-axisymmetric mean-field disc dynamos. Past work on the non-axisymmetric disc dynamos focused on the linear (kinematic) regime, or relied on an approximate algebraic quenching formalism.

Another recent development is the emergence of the minimal-τ approximation (MTA) as a more general closure for mean-field electrodynamics that includes the quasilinear or first-order smoothing approximation (FOSA) as a limiting case (Vainshtein & Kitchatinov, 1983; Kleeorin et al., 1996; Rogachevskii & Kleeorin, 2000; Blackman & Field, 2002; Brandenburg & Subramanian, 2005a). MTA is physically more appealing than FOSA because it takes into account the finite response time of the mean electromotive force (emf) to changes in the mean magnetic field and small-scale turbulence. This closure leads to new terms in the mean induction equation, which becomes a telegraph-type equation (Courant & Hilbert, 1989), with second-order time derivative of the mean magnetic field. Separate considerations, motivated in part by the need to incorporate the non-locality in the dynamo coefficients, lead to essentially the same telegraph-type equation (Rheinhardt & Brandenburg, 2012, see also Hughes & Proctor 2010). Such non-locality in time can lead to important astrophysical effects (Hubbard & Brandenburg, 2009, and references therein). In disc galaxies, in particular, we expect memory effects to be important because the product of the gas angular velocity Ω and correlation time of the turbulence τ_c may be of the order unity.

Yet another significant development has been the emergence of strong evidence that spiral patterns are not, at least in some cases, long-lived features rotating at a single constant pattern speed (Shetty et al., 2007; Dobbs et al., 2010; Sellwood, 2011; Quillen et al., 2011; Roškar et al., 2012; Wada et al., 2011; Dobbs, 2011; Kawata et al., 2012; Khoperskov et al., 2012). Theory, observations, and especially simulations of isolated and interacting galaxies point to a wide spectrum of possibilities, from relatively rigidly-rotating and long-lived patterns with fairly constant pattern speeds, to composite spirals comprised of multiple pattern speeds dominating in different radial ranges, to material arms that appear to rotate with the local gas velocity and thus quickly wind up.

The goal of the next few chapters is to draw together these recent developments in dynamo theory and spiral structure and apply the new ideas to examine non-axisymmetric regular magnetic fields in disc galaxies. Here we focus on modes that are enslaved to the axisymmetric mode (and thus have the same growth rate in the kinematic regime); for a two-armed material spiral this would mean the quadrisymmetric mode (or $m = 2$ mode of the Fourier expansion) that corotates with the spiral pattern, as well as other even-m corotating modes, which are weaker. This chapter focuses on numerical models, while Chapter 4 presents a semi-analytical treatment of such modes. Where the present work differs importantly from previous work is that we:

(i) incorporate MTA and explore the effects of a finite dynamo relaxation time;

(ii) include dynamical quenching with an advective helicity flux for non-axisymmetric modes; and

(iii) explore the effects of both steady and transient material arms on the mean magnetic field.

In addition to this work on non-axisymmetric mean-field dynamos, we also briefly report on some new results from mean-field dynamo simulations which use an axisymmetric disc.

The plan of this chapter is as follows. We outline the numerical model in Section 3.2. In Sect. 3.3 we discuss the findings from simulations of axisymmetric discs, while in Sections 3.4 and 3.5 we describe the results of simulations of non-axisymmetric discs. A discussion of results and conclusions of this chapter are presented in Section 3.6.

3.2 Numerical solutions

3.2.1 Method and approximations used

We now examine the evolution of the mean magnetic field numerically. We solve equation (1.22) when τ is finite, while equation (1.23) is solved for the case $\tau \to 0$. The components of equation (1.22) in cylindrical coordinates are given below. The saturation of the dynamo action is controlled by the helicity conservation.

For convenience we define

$$\boldsymbol{F} \equiv \boldsymbol{\nabla} \times \boldsymbol{\mathcal{E}},$$

and assume that η, η_{t}, τ and c_τ are constants. The cylindrical polar components of equation (1.15) can then be written as

$$\begin{aligned}
\frac{\partial \overline{B}_r}{\partial t} =& \frac{1}{r}\frac{\partial}{\partial \phi}(\overline{U}_r\overline{B}_\phi - \overline{U}_\phi\overline{B}_r) - \frac{\partial}{\partial z}(\overline{U}_z\overline{B}_r - \overline{U}_r\overline{B}_z) + F_r \\
&+ \eta\left\{\frac{\partial}{\partial r}\left[\frac{1}{r}\frac{\partial}{\partial r}(r\overline{B}_r)\right] + \frac{1}{r^2}\frac{\partial^2\overline{B}_r}{\partial\phi^2} + \frac{\partial^2\overline{B}_r}{\partial z^2} - \frac{2}{r^2}\frac{\partial\overline{B}_\phi}{\partial\phi}\right\}, \qquad (3.1)\\
\frac{\partial \overline{B}_\phi}{\partial t} =& \frac{\partial}{\partial z}(\overline{U}_\phi\overline{B}_z - \overline{U}_z\overline{B}_\phi) - \frac{\partial}{\partial r}(\overline{U}_r\overline{B}_\phi - \overline{U}_\phi\overline{B}_r) + F_\phi \\
&+ \eta\left\{\frac{\partial}{\partial r}\left[\frac{1}{r}\frac{\partial}{\partial r}(r\overline{B}_\phi)\right] + \frac{1}{r^2}\frac{\partial^2\overline{B}_\phi}{\partial\phi^2} + \frac{\partial^2\overline{B}_\phi}{\partial z^2} + \frac{2}{r^2}\frac{\partial\overline{B}_r}{\partial\phi}\right\}, \qquad (3.2)\\
\frac{\partial \overline{B}_z}{\partial t} =& \frac{1}{r}\frac{\partial}{\partial r}\left[r(\overline{U}_z\overline{B}_r - \overline{U}_r\overline{B}_z)\right] - \frac{1}{r}\frac{\partial}{\partial\phi}(\overline{U}_\phi\overline{B}_z - \overline{U}_z\overline{B}_\phi) \\
&+ F_z + \eta\left[\frac{1}{r}\frac{\partial}{\partial r}\left(r\frac{\partial\overline{B}_z}{\partial r}\right) + \frac{1}{r^2}\frac{\partial^2\overline{B}_z}{\partial\phi^2} + \frac{\partial^2\overline{B}_z}{\partial z^2}\right]. \qquad (3.3)
\end{aligned}$$

Taking the curl of both sides of equation (1.21), we get

$$\tau\frac{\partial F_r}{\partial t} = c_\tau\left[\frac{1}{r}\frac{\partial}{\partial\phi}(\alpha\overline{B}_z) - \frac{\partial}{\partial z}(\alpha\overline{B}_\phi)\right] + c_\tau\eta_{\mathrm{t}}\left\{\frac{\partial}{\partial r}\left[\frac{1}{r}\frac{\partial}{\partial r}(r\overline{B}_r)\right] + \frac{1}{r^2}\frac{\partial^2\overline{B}_r}{\partial\phi^2} + \frac{\partial^2\overline{B}_r}{\partial z^2} - \frac{2}{r^2}\frac{\partial\overline{B}_\phi}{\partial\phi}\right\} - F_r, \tag{3.4}$$

$$\tau\frac{\partial F_\phi}{\partial t} = c_\tau\left[\frac{\partial}{\partial z}(\alpha\overline{B}_r) - \frac{\partial}{\partial r}(\alpha\overline{B}_z)\right] + c_\tau\eta_{\mathrm{t}}\left\{\frac{\partial}{\partial r}\left[\frac{1}{r}\frac{\partial}{\partial r}(r\overline{B}_\phi)\right] + \frac{1}{r^2}\frac{\partial^2\overline{B}_\phi}{\partial\phi^2} + \frac{\partial^2\overline{B}_\phi}{\partial z^2} + \frac{2}{r^2}\frac{\partial\overline{B}_r}{\partial\phi}\right\} - F_\phi, \tag{3.5}$$

$$\tau\frac{\partial F_z}{\partial t} = c_\tau\left[\frac{1}{r}\frac{\partial}{\partial r}(r\alpha\overline{B}_\phi) - \frac{1}{r}\frac{\partial}{\partial\phi}(\alpha\overline{B}_r)\right] + c_\tau\eta_{\mathrm{t}}\left[\frac{1}{r}\frac{\partial}{\partial r}\left(r\frac{\partial\overline{B}_z}{\partial r}\right) + \frac{1}{r^2}\frac{\partial^2\overline{B}_z}{\partial\phi^2} + \frac{\partial^2\overline{B}_z}{\partial z^2}\right] - F_z. \tag{3.6}$$

To evaluate the term containing $\boldsymbol{\mathcal{E}}$ in equation (1.32), we need the evolution equations for its components. From equation (1.21), we find

$$\tau\frac{\partial\mathcal{E}_r}{\partial t} = c_\tau\alpha\overline{B}_r - c_\tau\eta_{\mathrm{t}}\left(\frac{1}{r}\frac{\partial\overline{B}_z}{\partial\phi} - \frac{\partial\overline{B}_\phi}{\partial z}\right) - \mathcal{E}_r, \tag{3.7}$$

$$\tau\frac{\partial\mathcal{E}_\phi}{\partial t} = c_\tau\alpha\overline{B}_\phi - c_\tau\eta_{\mathrm{t}}\left(\frac{\partial\overline{B}_r}{\partial z} - \frac{\partial\overline{B}_z}{\partial r}\right) - \mathcal{E}_\phi, \tag{3.8}$$

$$\tau\frac{\partial\mathcal{E}_z}{\partial t} = c_\tau\alpha\overline{B}_z - c_\tau\eta_{\mathrm{t}}\left[\frac{1}{r}\frac{\partial}{\partial r}(r\overline{B}_\phi) - \frac{1}{r}\frac{\partial\overline{B}_r}{\partial\phi}\right] - \mathcal{E}_z. \tag{3.9}$$

The evolution equations for $\boldsymbol{\mathcal{E}}$ are redundant given those for $\boldsymbol{F}$, since the latter could be obtained by taking the curl of the former. However, we find it convenient to solve separately for $\boldsymbol{\mathcal{E}}$ and $\boldsymbol{F}$. The quantity $\boldsymbol{F}$ has been introduced in addition to $\boldsymbol{\mathcal{E}}$ because this allows us to avoid having to impose boundary conditions on the components of $\boldsymbol{\mathcal{E}}$ and also to avoid applying the no-z approximation to the components of $\boldsymbol{\nabla}\times\boldsymbol{\mathcal{E}}$ (see below). Alternatively, we could have solved for the vector potential $\overline{\boldsymbol{A}}$ and $\boldsymbol{\mathcal{E}}$, so the choice of using $\overline{\boldsymbol{B}}$ and $\boldsymbol{F}$ is a matter of preference.

We make the thin-disc approximation, which implies $r^{-1}\partial/\partial\phi \ll \partial/\partial z$ and $\partial/\partial r \ll \partial/\partial z$. We also assume that the variations of the rotational and radial velocities along the z-axis are negligible. Then we can neglect $\overline{B}_z\partial\overline{U}_r/\partial z$ in the equation for $\overline{B}_r$ and $\overline{B}_z\partial\overline{U}_\phi/\partial z$ in the equation for $\overline{B}_\phi$. The thin-disc approximation and the condition $\boldsymbol{\nabla}\cdot\overline{\boldsymbol{B}} = 0$ together imply that $\overline{B}_z/|\overline{\boldsymbol{B}}| \ll 1$. This approximation also allows us to ignore terms containing the ϕ- and r-derivatives of $\alpha\overline{B}_z$ in equations (3.4) and (3.5), and of $\overline{B}_z$ in equations (3.7) and

(3.8), as well as the term $\mathcal{E}_z\overline{B}_z$ in equation (1.32) for α_m. Thus, the evolution equation for $\mathcal{E}_z$ is no longer needed, and all terms containing $\overline{B}_z$ are eliminated from all the relevant evolution equations. (We note in passing that for solutions with quadrupolar geometry, $\overline{B}_z = 0$ at the midplane, but not elsewhere.) We can estimate the magnitude of $\overline{B}_z$ from $\boldsymbol{\nabla}\cdot\overline{\boldsymbol{B}} = 0$. Within this framework, we do not have to worry about satisfying $\boldsymbol{\nabla}\cdot\overline{\boldsymbol{B}} = 0$ and $\boldsymbol{\nabla}\cdot\boldsymbol{F} = 0$ numerically.

Further, we write $\overline{U}_\phi = r\Omega$, and take Ω to be independent of ϕ. We also adopt $\overline{U}_r = 0$. However, a vertical velocity $\overline{U}_z$, perhaps due to a galactic fountain flow, can be essential for the dynamo action, so it is retained. Note that gas outflowing from the disc can be replenished by the fountain flow from the gaseous halo or accretion from the intergalactic medium (Putman et al., 2012). The vertical flow advects magnetic field as well as magnetic helicity (Shukurov et al., 2006). Crucially, a magnetic helicity flux away from the dynamo region is required to alleviate the catastrophic quenching of the α effect (Brandenburg & Subramanian, 2005a).

The no-z approximation (Subramanian & Mestel, 1993; Moss, 1995; Phillips, 2001) is used as discussed in detail in Appendix C, to approximate the z-derivatives of the mean magnetic field. This reduces the three-dimensional problem to that in two dimensions (r and ϕ), thus greatly reducing the computational time required. The no-z approximation provides remarkably accurate solutions in one-dimensional dynamical quenching models (see Chapter 2 and compare Shukurov et al. 2006 and Sur et al. 2007) and we have also confirmed that it performs equally well in higher-dimensional problems (see Appendix C.5). Under this approximation, $\overline{U}_z$ represents a vertically averaged, mass-weighted vertical velocity.

3.2.2 Dimensionless governing equations

The values of the key parameters for our models are given in Table 3.1. These can be found, for example, in Ruzmaikin et al. (1988); Moss (1996); Beck et al. (1996). We adopt the length scale and rms velocity of the largest turbulent eddies to be $l = 100\,\mathrm{pc}$ and $u = 10\,\mathrm{km\,s^{-1}}$, respectively. These parameters are taken to be constant in space and time. This leads to the following estimate for the turbulent diffusivity: $\eta_\mathrm{t} \simeq lu/3 = 10^{26}\,\mathrm{cm^2\,s^{-1}}$. It is convenient to use dimensionless variables, with distance along the z-axis measured in the unit of the characteristic half-thickness of the disc h_0, horizontal lengths measured in the radial disc scale length R, and time measured in typical vertical turbulent diffusion time $t_0 = h_0^2/\eta_\mathrm{t}$. We take as fiducial values $h_0 = 500\,\mathrm{pc}$ and $R = 20\,\mathrm{kpc}$. For our purposes, it is not necessary to specify the magnetic field unit B_0, so we leave it arbitrary. The quantities h_0 and R enter only in the ratios $\lambda = h_0/R$ and $K = 2(h_0/l)^2$. The rotational shear is denoted $G = rd\Omega/dr$, $B_{\rm eq}$ is a characteristic field that may vary over space and time (normally associated with the equipartition field), and κ is the turbulent diffusivity for $\alpha_{\rm m}$. Then our set of equations can be written in dimensionless form as

$$\frac{\partial \overline{B}_r}{\partial t} = -\Omega\frac{\partial \overline{B}_r}{\partial \phi} - \frac{\overline{U}_z\overline{B}_r}{h} + F_r, \tag{3.10}$$

$$\frac{\partial \overline{B}_\phi}{\partial t} = G\overline{B}_r - \Omega\frac{\partial \overline{B}_\phi}{\partial \phi} - \frac{\overline{U}_z\overline{B}_\phi}{h} + F_\phi, \tag{3.11}$$

$$\frac{\partial F_r}{\partial t} = \tau^{-1}\left[-\frac{2c_\tau}{\pi h}\alpha\overline{B}_\phi - c_\tau\frac{\pi^2}{4h^2}\overline{B}_r + c_\tau\lambda^2\left(\widehat{\mathcal{P}}\overline{B}_r - \frac{2}{r^2}\frac{\partial \overline{B}_\phi}{\partial \phi}\right) - F_r\right], \tag{3.12}$$

$$\frac{\partial F_\phi}{\partial t} = \tau^{-1}\left[-\frac{2c_\tau}{\pi h}\alpha\overline{B}_r - c_\tau\frac{\pi^2}{4h^2}\overline{B}_\phi + c_\tau\lambda^2\left(\widehat{\mathcal{P}}\overline{B}_\phi + \frac{2}{r^2}\frac{\partial \overline{B}_r}{\partial \phi}\right) - F_\phi\right], \tag{3.13}$$

$$\begin{aligned}\frac{\partial \alpha_{\rm m}}{\partial t} = &-K\left(\frac{\boldsymbol{\mathcal{E}}\cdot\overline{\boldsymbol{B}}}{B_{\rm eq}^2} + \frac{\alpha_{\rm m}}{\mathcal{R}_{\rm m}}\right) - \frac{\alpha_{\rm m}\overline{U}_z}{h} - \Omega\frac{\partial \alpha_{\rm m}}{\partial \phi}\\ &+\kappa\left[\frac{\lambda^2}{r}\frac{\partial}{\partial r}\left(r\frac{\partial \alpha_{\rm m}}{\partial r}\right) + \frac{\lambda^2}{r^2}\frac{\partial^2\alpha_{\rm m}}{\partial \phi^2} - \frac{\pi^2}{4h^2}\alpha_{\rm m}\right],\end{aligned} \tag{3.14}$$

$$\frac{\partial \mathcal{E}_r}{\partial t} = \tau^{-1}\left(c_\tau\alpha\overline{B}_r - c_\tau\frac{\pi}{2h}\overline{B}_\phi - \mathcal{E}_r\right), \tag{3.15}$$

$$\frac{\partial \mathcal{E}_\phi}{\partial t} = \tau^{-1}\left[c_\tau\alpha\overline{B}_\phi + c_\tau\frac{\pi}{2h}\left(1 + \frac{3}{4\pi}\sqrt{\frac{-D}{\pi}}\right)\overline{B}_r - \mathcal{E}_\phi\right], \tag{3.16}$$

where

$$\widehat{\mathcal{P}} = -\frac{1}{r^2} + \frac{1}{r}\frac{\partial}{\partial r} + \frac{\partial^2}{\partial r^2} + \frac{1}{r^2}\frac{\partial^2}{\partial \phi^2},$$

$$\boldsymbol{\mathcal{E}}\cdot\overline{\boldsymbol{B}} = \mathcal{E}_r\overline{B}_r + \mathcal{E}_\phi\overline{B}_\phi.$$

We have also neglected terms proportional to the inverse magnetic Reynolds number $\mathcal{R}_{\rm m}^{-1}$ in equations (3.10) and (3.11), as $\mathcal{R}_{\rm m} \gg 1$ in galaxies. We have retained such a term in equation (3.14); however, it can also be neglected if the flux is dominant, which is usually the case.

Table 3.1: List of parameters and key dependent quantities for all models (except Model D).

Description	Symbol	Expression	Value	Dimensionless
Radial location of disc boundary	R		$20\,\mathrm{kpc}$	R
Disc half-thickness at $r = R/2$	h_0		$0.5\,\mathrm{kpc}$	h_0
Characteristic field strength at $r = 0$	B_0		–	B_0
Scale length of the turbulence	l		$0.1\,\mathrm{kpc}$	$h_0/5$
rms velocity of the turbulence	u		$10\,\mathrm{km\,s^{-1}}$	$15h_0t_0^{-1}$
Turbulent diffusivity	η_t	$lu/3$	$10^{26}\,\mathrm{cm^2\,s^{-1}}$	$h_0^2t_0^{-1}$
Vertical diffusion time at $r = R/2$	t_0	h_0^2/η_t	$0.73\,\mathrm{Gyr}$	t_0
Correlation time of the turbulence	τ_c	l/u	$10\,\mathrm{Myr}$	$t_0/75$
Disc flaring radius	r_D		$10\,\mathrm{kpc}$	$R/2$
Disc half-thickness at $r = 0$	h_D		$0.35\,\mathrm{kpc}$	$h_0/\sqrt{2}$
Brandt radius	r_ω		$2\,\mathrm{kpc}$	$R/10$
Angular velocity at $r = 0$	Ω_0		$130\,\mathrm{km\,s^{-1}\,kpc^{-1}}$	$96t_0^{-1}$
Corotation radius	r_cor		$8\,\mathrm{kpc}$	$2R/5$
Pattern speed of spiral	Ω_p	$\Omega(r_\mathrm{cor})$	$31\,\mathrm{km\,s^{-1}\,kpc^{-1}}$	$23t_0^{-1}$

For $\tau \to 0$, these equations reduce to the three standard equations of the slab dynamo:

$$\frac{D\overline{B}_r}{Dt} = -\frac{2c_\tau}{\pi h}\alpha\overline{B}_\phi - c_\tau\frac{\pi^2}{4h^2}\overline{B}_r + c_\tau\lambda^2\left[\widehat{\mathcal{P}}\overline{B}_r - \frac{2}{r^2}\frac{\partial\overline{B}_\phi}{\partial\phi}\right], \tag{3.17}$$

$$\frac{D\overline{B}_\phi}{Dt} = G\overline{B}_r - \frac{2c_\tau}{\pi h}\alpha\overline{B}_r - c_\tau\frac{\pi^2}{4h^2}\overline{B}_\phi + c_\tau\lambda^2\left[\widehat{\mathcal{P}}\overline{B}_\phi + \frac{2}{r^2}\frac{\partial\overline{B}_r}{\partial\phi}\right], \tag{3.18}$$

$$\begin{aligned}\frac{D\alpha_\mathrm{m}}{Dt} =& -K\left[c_\tau\alpha\left(\frac{\overline{B}_r^2+\overline{B}_\phi^2}{B_\mathrm{eq}^2}\right) + \frac{\alpha_\mathrm{m}}{\mathcal{R}_\mathrm{m}} + c_\tau\frac{3\sqrt{-D}}{8\pi^{1/2}h}\frac{\overline{B}_r\overline{B}_\phi}{B_\mathrm{eq}^2}\right]\\ &+\kappa\left[\frac{\lambda^2}{r}\frac{\partial}{\partial r}\left(r\frac{\partial\alpha_\mathrm{m}}{\partial r}\right) + \frac{\lambda^2}{r^2}\frac{\partial^2\alpha_\mathrm{m}}{\partial\phi^2} - \frac{\pi^2}{4h^2}\alpha_\mathrm{m}\right],\end{aligned} \tag{3.19}$$

where

$$\frac{D}{Dt} = \frac{\partial}{\partial t} + \Omega\frac{\partial}{\partial\phi} + \frac{\overline{U}_z}{h}.$$

Note that the numerical factors in the no-z terms are chosen slightly differently from the ones in Chapters 2 and 6 (see the note at the end of Appendix B for details).

Table 3.2: List of numerical models. Resolution is given as $n_r \times n_\phi$. The value of R_U is given at $r = R/2 = 10\,\mathrm{kpc}$. 'R' indicates a Gaussian random seed. 'T' indicates that the imposed spiral is transient, while 'W' indicates that the α-spiral begins as a bar and winds up with the gas.

Model	Resolution	Seed	l (kpc)	u (km s^{-1})	R_U	U_0 (km s^{-1})	$\kappa\eta_\mathrm{t}^{-1}$	ϵ_α	ϵ_U	$-kR$	n
A	100×60	0	0.1	10	0	0	0	0	0	–	–
B	100×60	0	0.1	10	0.45	0.3	0	0	0	–	–
C	100×60	R	0.1	10	0.45	0.3	0	0	0	–	–
D	200×120	1	0.15	5	0.45	0.3	0	0	0	–	–
E	200×120	0	0.1	10	0.45	0.3	0	0.5	0	20	2
F	100×60	0	0.1	10	0.90	0.6	0	0	0.5	20	2
G	100×60	R	0.1	10	0.45	0.3	0	0.5	0	20	2
H	100×60	0	0.1	10	0	0	0	0.5	0	20	2
I	200×120	0	0.1	10	0.45	0.3	0	1	0	20	2
J	200×120	0	0.1	10	0.45	0.3	0	0.5	0	8	2
K	200×120	0	0.1	10	0.45	0.3	0	0.5	0	0	2
L	200×120	0	0.1	10	0.45	0.3	0	0.5	0	20	4
M	200×120	0	0.1	10	0.45	0.3	0	0.5	0	20,T	2
N	200×120	0	0.1	10	0.45	0.3	0	0.5	0	T,W	2
O	200×120	0	0.1	10	0	0	0.3	0.5	0	20	2
P	400×240	0	0.1	10	0.45	0.3	0	0.5	0	20	2

3.2.3 Initial and boundary conditions

The boundary conditions are $\overline{B}_r = \overline{B}_\phi = 0$ at $r = 0$ and $r = R$, where the former condition applies as long as we consider non-axisymmetric modes that are localized far away from the rotation axis. The components of $\boldsymbol{\mathcal{E}}$ are evaluated for the purpose of calculating $\boldsymbol{\mathcal{E}} \cdot \overline{\boldsymbol{B}}$, but not for calculating the components of $\boldsymbol{\nabla} \times \boldsymbol{\mathcal{E}}$, as this can be gotten from equations (3.12) and (3.13). All variables vanish at $t = 0$ except for $\overline{B}_r$ and $\overline{B}_\phi$, whose seed values are chosen either to be Gaussian random fields for $\overline{B}_r$ and zero for $\overline{B}_\phi$, or to have the functional form

$$\overline{B}_\phi = \frac{r}{R}\left(1 - \frac{r}{R}\right)^2 \mathrm{e}^{-r/R}(S_0 + S_1 \cos\phi), \qquad \overline{B}_r = -\overline{B}_\phi,$$

where S_0 and S_1 are dimensionless constants that control the amplitudes (relative to B_0) of the $m = 0$ and $m = 1$ components of the seed field. Choosing $\overline{B}_r$ and $\overline{B}_\phi$ to have opposite sign initially leads to faster convergence of the solution, since the kinematic dynamo solutions studied generally have this property of negative pitch angle p_B. The solenoidality condition $\boldsymbol{\nabla} \cdot \overline{\boldsymbol{B}} = 0$ can be used to obtain the magnitude of $\overline{B}_z$. When we refer to the $m = 0$ seed, this means $S_0 = 1$ and $S_1 = 0$, while the $m = 1$ seed has $S_0 = 0$ and $S_1 = 1$.

The code uses sixth-order finite differences for the spatial derivatives and a third-order Runge–Kutta routine for the time derivatives, using the same algorithms as the publicly available PENCIL CODE[1]. We have tested the code by reproducing various known results including those of Moss (1996).

3.2.4 The galaxy model

For the galactic rotation curve, we use the Brandt curve (2.5). With this profile, $\Omega \to \text{const}$ as $r \to 0$ (solid body rotation) and $\Omega \propto 1/r$ for $r \gg r_\omega$ (flat rotation curve). The rotational shear rate,

$$G(r) = r\frac{d\Omega}{dr} = -\Omega(r)\frac{(r/r_\omega)^2}{1+(r/r_\omega)^2}, \tag{3.20}$$

tends to zero as $r \to 0$ and $G = -\Omega$ for $r \gg r_\omega$, with the maximum magnitude of $2\Omega_0/(3\sqrt{3})$ at $r = \sqrt{2}r_\omega$.

We model the disc half-thickness as a hyperboloid as in equation (2.6) where h_D is the scale height at $r = 0$ and r_D controls the disc flaring rate. With this form, $h \to h_D =$ constant as $r \to 0$ and $h \propto r$ for $r \gg r_D$.

We take the kinetic part of the α-coefficient to decrease with radius according to equation (2.2). For the models of non-axisymmetric disc, we also impose a spiral profile on α_k. For a rigidly rotating spiral, we use

$$\alpha_\mathrm{k}(r,\phi,t) = \alpha_0(r)\left\{1+\epsilon_\alpha\cos[n(\phi-\Omega_\mathrm{p}t)-kr]\right\}, \tag{3.21}$$

where α_0, the azimuthally averaged value of α_k, is given by equation (2.2), ϵ_α sets the degree of deviation from axial symmetry, n is the number of spiral arms, Ω_p is the angular velocity of the spiral pattern (i.e. the pattern speed), and k, negative for a trailing spiral, determines how tightly the arms are wound. The spiral modulation of α could be due to a variety of different effects, including an increase in vorticity produced by spiral shocks (Mestel & Subramanian, 1991), an increased turbulent velocity (Shukurov, 1998), a different coherence scale in arm and interarm regions (Rohde et al., 1999), or even a new form of helicity flux (Vishniac, 2012a). We have therefore refrained from attempting to relate ϵ_α to the other parameters of the model (e.g. l, u). Rather, for simplicity and ease of interpretation, we vary α_k while holding other parameters constant along the spiral. For a spiral winding up with the differential rotation of the gas, we take

$$\alpha_\mathrm{k}(r,\phi,t) = \alpha_0(r)\left[1+\epsilon_\alpha\cos\{n[\phi+\phi_0-\Omega(r)t']\}\right], \tag{3.22}$$

[1] http://pencil-code.googlecode.com (Brandenburg, 2003)

where we have included an arbitrary phase ϕ_0 and defined $t' = t - t_{\rm on}$ where $t_{\rm on}$ is the time of onset of the α-spiral. We have also taken $k = 0$, so that the α-spiral actually starts off as a 'bar' at $t' = 0$. Wherever necessary, we also require that $\alpha_{\rm k} < u$.

The model also allows for a spiral modulation of the vertical advective velocity $\overline{U}_z$ of a similar form:

$$\overline{U}_z = U_0 \left\{1 + \epsilon_U \cos[n(\phi - \Omega_{\rm p} t) - kr]\right\}, \tag{3.23}$$

were U_0 is the azimuthally averaged value of $\overline{U}_z$.

Following other authors (e.g. Ruzmaikin et al., 1988) we define the turbulent magnetic Reynolds numbers to quantify the strengths of the differential rotation, α effect and vertical velocity:

$$R_\omega = Gh^2/\eta_{\rm t}, \quad R_\alpha = \alpha_{\rm k} h/\eta_{\rm t}, \quad R_U = U_0 h/\eta_{\rm t}.$$

The local dynamo number,

$$D = R_\alpha R_\omega = \alpha_{\rm k} G h^3/\eta_{\rm t}^2,$$

is a dimensionless measure of the intensity of the $(\alpha\Omega)$ dynamo action at a given radius. For the mean field to grow due to the local $\alpha\Omega$-dynamo action alone, it is required that $D < D_{\rm c} \approx -10$ (Ruzmaikin et al., 1988, see also Chapter 4). In the limit $r \gg r_\omega$, an axisymmetric disc has $D \simeq -9(\Omega h/u)^2$.

The functional form of the characteristic magnetic field is adopted as

$$B_{\rm eq} = B_0 {\rm e}^{-r/R}; \tag{3.24}$$

if appropriate, this can be identified with the magnetic field strength corresponding to the energy equipartition with the turbulence. Nonlinear dynamo effects are expected to become pronounced as soon as $|\overline{\boldsymbol{B}}| \simeq B_{\rm eq}$.

3.2.5 Models explored and the representation of the results

The various numerical models considered here are summarized in Table 3.2. We adopt $r_\omega = 0.1R = 2\,{\rm kpc}$ and set the circular speed to $\overline{U}_\phi = 375 h_0 t_0^{-1} = 250\,{\rm km\,s^{-1}}$ at $r = R/2 = 10\,{\rm kpc}$, which gives $\Omega_0 = 96 t_0^{-1} = 130\,{\rm km\,s^{-1}\,kpc^{-1}}$. This implies that $\Omega = 18.75 t_0^{-1} = 25\,{\rm km\,s^{-1}\,kpc^{-1}}$, $G \simeq -18 t_0^{-1} = -24\,{\rm km\,s^{-1}\,kpc^{-1}}$, $\overline{\alpha} = 0.75 h_0 t_0^{-1} = 0.5\,{\rm km\,s^{-1}}$ and the azimuthally averaged dynamo number $\overline{D} \simeq -13.5$ at $r = R/2 = 10\,{\rm kpc}$. The resulting radial profiles of h, R_ω, R_α, and D are shown in Fig. 3.1.

The corotation radius for models with steady spiral forcing is chosen as $r_{\rm cor} = 8\,{\rm kpc}$, which is close to the observational estimates for the Milky Way (Gerhard, 2011; Acharova et al., 2011). Moreover, a reasonable estimate for τ is given by $\tau = l/u = (l^2/3h_0^2)t_0 =$

$t_0/75$. It is possible that τ is much smaller than our simple estimate for some galaxies and much larger for others. Therefore, we also consider the $\tau \to 0$ case, as well as $\tau = 2l/u$ for some models.

We decompose each component of the mean magnetic field $\overline{\boldsymbol{B}}$ into a cosine Fourier series, with certain phases $\phi_{0,i}^{(m)}$ (see below),

$$\overline{B}_i(r,\phi,t) = \sum_{m=0}^{\infty} \widetilde{B}_i^{(m)}(r,t)\cos\{m[(\phi - \phi_{0,i}^{(m)}(r,t)]\}, \tag{3.25}$$

where $i = r, \phi$, Thus,

$$\widetilde{B}_i^{(0)} = \frac{1}{2\pi}\int_0^{2\pi} \overline{B}_i(r,\phi,t)\,d\phi, \tag{3.26}$$

and, for $m > 0$,

$$\widetilde{B}_i^{(m)} = \frac{1}{\pi}\int_0^{2\pi} \overline{B}_i(r,\phi,t)\cos\left\{m\left[\phi - \phi_{0,i}^{(m)}(r,t)\right]\right\}\,d\phi. \tag{3.27}$$

The phase $\phi_{0,i}^{(m)}$ is obtained by trying all possible values and choosing the one which maximizes $\widetilde{B}_i^{(m)}$. Using their phases, we also determine the rotation rates of the various Fourier modes by numerically differentiating the phase with respect to time.

The azimuthal average of the magnetic energy can be written as

$$\overline{E}(r,t) = \sum_{m=0}^{\infty} \widetilde{E}^{(m)}(r,t), \tag{3.28}$$

where

$$\widetilde{E}^{(0)}(r,t) = \frac{1}{8\pi}\left\{\left[\widetilde{B}_r^{(0)}(r,t)\right]^2 + \left[\widetilde{B}_\phi^{(0)}(r,t)\right]^2\right\}, \tag{3.29}$$

and, for $m > 0$,

$$\widetilde{E}^{(m)}(r,t) = \frac{1}{16\pi}\left\{\left[\widetilde{B}_r^{(m)}(r,t)\right]^2 + \left[\widetilde{B}_\phi^{(m)}(r,t)\right]^2\right\}, \tag{3.30}$$

where the additional factor 1/2 in the latter equation arises from averaging $\cos^2[m(\phi - \phi_{0,i}^{(m)})]$ over the interval $(0, 2\pi)$. Averaging over the area of the disc, we obtain the average normalized magnetic energy in mode m,

$$\left\langle \frac{\widetilde{E}^{(m)}(t)}{B_{\rm eq}^2} \right\rangle = \frac{2}{R^2}\int_0^R \frac{\widetilde{E}^{(m)}(r,t)}{B_{\rm eq}^2(r)}\,r\,dr. \tag{3.31}$$

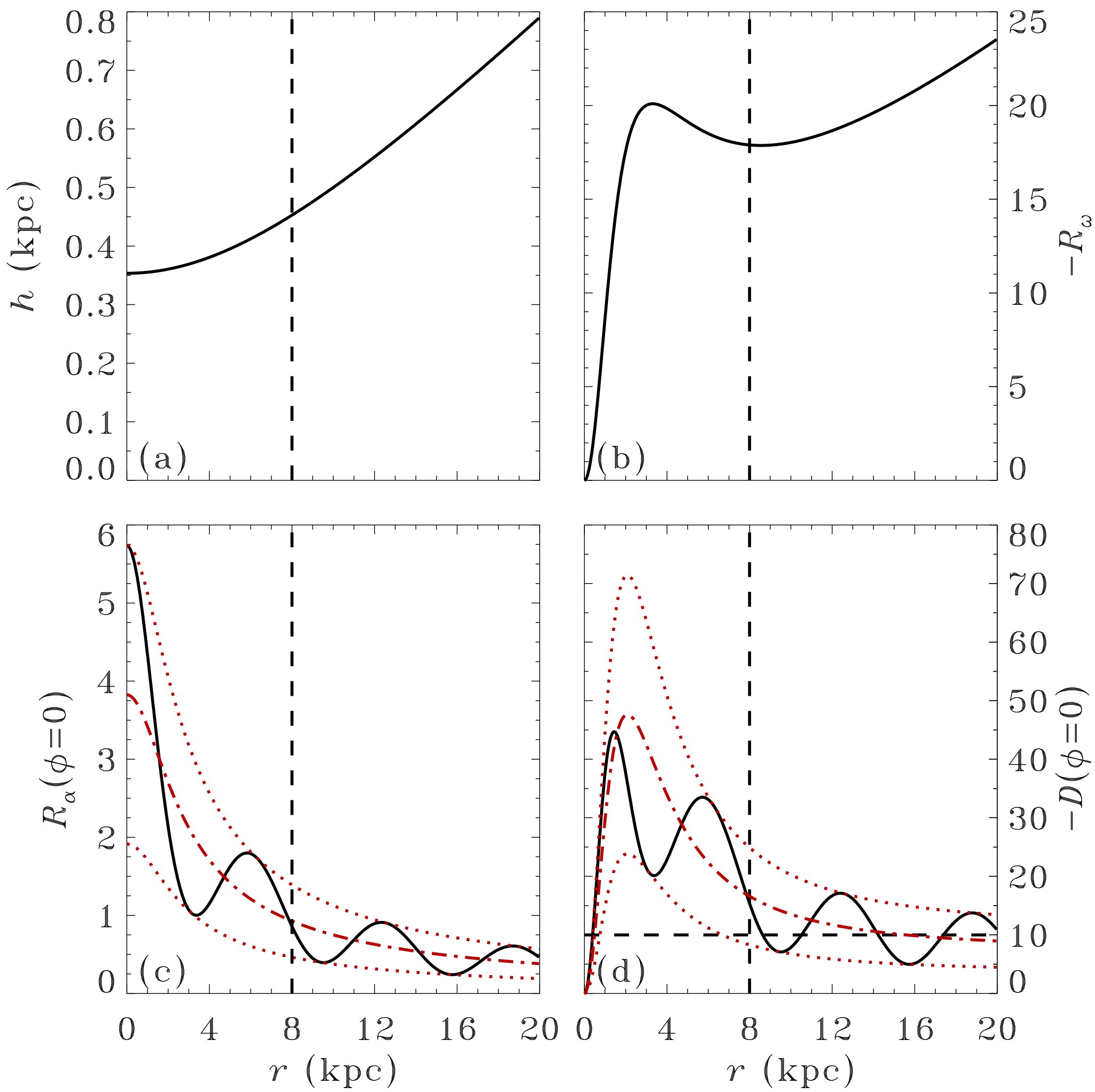

Figure 3.1: Inputs used for the basic non-axisymmetric Model E. **(a)** Disc scale height h, given by equation (2.6). **(b)** The dimensionless quantity $-R_\omega = Gh^2/\eta_\mathrm{t}$ with G given by equation (3.20). **(c)** The dimensionless quantity $R_\alpha = \alpha_\mathrm{k} h/\eta_\mathrm{t}$, with α_k given by equation (3.21), at $\phi = 0$ (solid), azimuthal maximum/minimum (dotted), and azimuthal mean (dash-dotted). **(d)** Negative of the dynamo number $-D = -R_\alpha R_\omega$ at $\phi = 0$ (solid), along with its azimuthal extrema (dotted) and mean (dash-dotted). The azimuthal mean is used in axisymmetric models. Negative of the approximate critical dynamo number $-D_\mathrm{c} \simeq 10$ is shown dashed for reference.

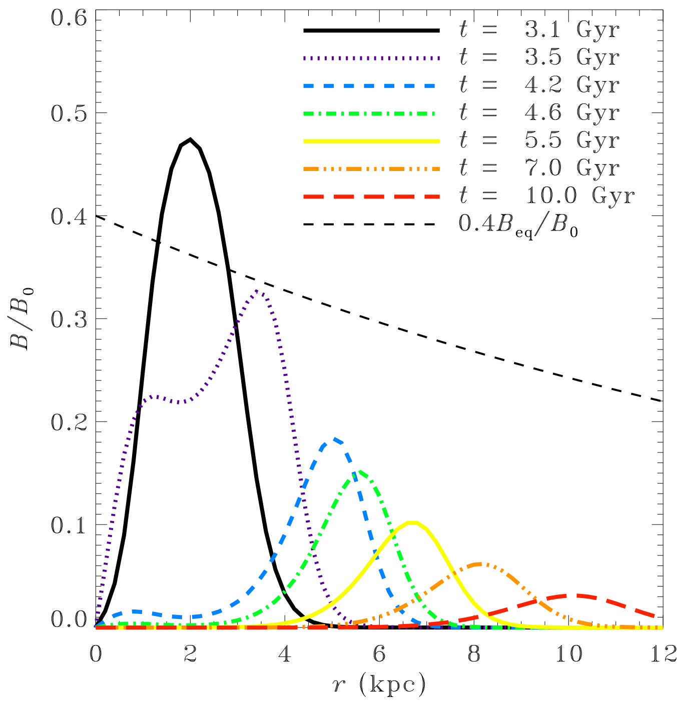

Figure 3.2: Evolution of the field strength $B = (B_r^2 + B_\phi^2)^{1/2}$ in Model A (axisymmetric disc, with $U_0 = 0$, $\kappa = 0$).

3.3 Dynamo in an axisymmetric disc

A number of interesting questions can be addressed by considering dynamo action in an axisymmetric disc. One of them is how a whole young galaxy becomes magnetized with a coherent field given that the radial diffusion time across a galaxy, $t_R \simeq R^2/\eta_{\rm t} \simeq 3\times10^2$ Gyr, is typically larger than the age of the Universe. We examine this in the context of the dynamical quenching model of the galactic dynamo.

3.3.1 Axisymmetric solutions

In local dynamo models the presence of magnetic helicity fluxes have been shown to alleviate the catastrophic quenching of the dynamo (Kleeorin et al., 2002; Shukurov et al., 2006). In the absence of any helicity flux, the mean magnetic field does grow to a fraction of the equipartition value, until $\alpha_{\rm m}$ cancels $\alpha_{\rm k}$, after which magnetic field decays. The result which obtains when the radial dimension is included is more interesting, even in the

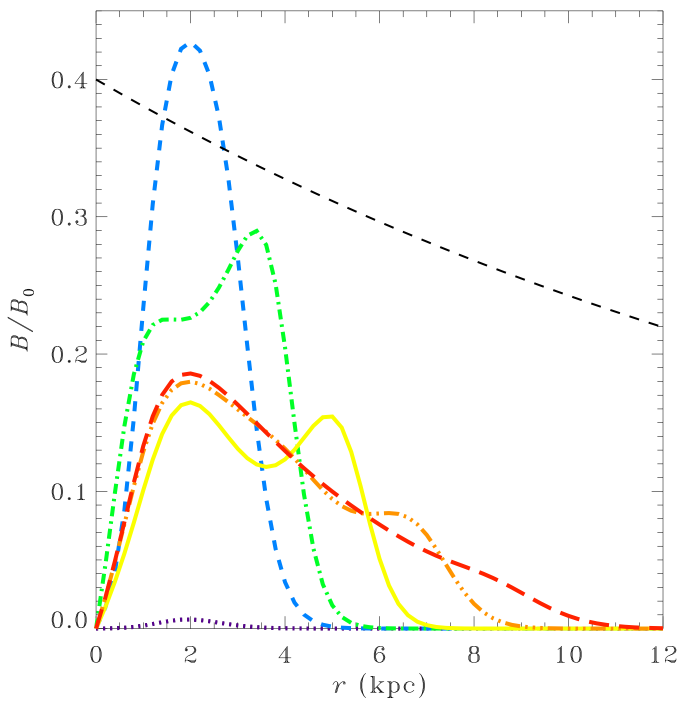

Figure 3.3: Evolution of the field strength in Model B (axisymmetric disc, with $U_0 = 0.3\,\mathrm{km\,s^{-1}}$, $\kappa = 0$). Times plotted are as in Fig. 3.2, with $t = 3.1\,\mathrm{Gyr}$ omitted since $\overline{B}/B_0$ is too small to be visible.

absence of a helicity flux. The evolution of the radial profile of the mean field strength for such a case (Model A) is shown in Fig. 3.2 adopting $\tau \to 0$. No notable differences exist between the $\tau \to 0$ and $\tau = l/u$ cases; for example, the kinematic global growth rate $\Gamma = 5.7t_0^{-1} \simeq 7.8\,\mathrm{Gyr}^{-1}$ is virtually the same.[2] Since the local growth rate of the field depends on the dynamo number, which in turn depends on r, the field maximum travels in radius. More specifically, the maximum is first localised where the dynamo number is the largest (r_M, say), but, at later time, at radii $r_M - \Delta r_1$ and $r_M + \Delta r_2$, etc. This leads to two rings of enhanced mean field, one moving inward and the other moving outward (the outer ring is more prominent in Model A). Because of the catastrophic α-quenching, the mean field eventually becomes negligible. (See Moss et al. (1998) for a discussion of propagating magnetic fronts in disc galaxies.)

On the other hand, if a vertical advective flux or diffusive flux is present, catastrophic quenching is averted. Then magnetic field can persist at about the same strength in a wide radial range, gradually spreading out until it occupies the entire region of the disc where the local dynamo number is supercritical. This is the situation illustrated with Model B, as shown in Fig. 3.3 ($\tau \to 0$ case), for $R_U = 0.45$ at $r = R/2 = 10\,\mathrm{kpc}$ and $\overline{U}_z = 0.3\,\mathrm{km\,s^{-1}}$ at all r. In this model, both $\tau \to 0$ and $\tau = l/u$ cases are again very similar, and the kinematic global growth rate for both cases is $\Gamma = 5.1t_0^{-1} \simeq 7.0\,\mathrm{Gyr}^{-1}$. This is slightly smaller than for Model A, since the vertical flux removes large-scale magnetic field, rendering the dynamo less efficient in the kinematic stage. The results are also similar if we replace the advective flux of α_m with a turbulent diffusive flux. This model clarifies how the whole disc becomes magnetized. It does so by first reaching significant strengths in regions where the dynamo number is largest. Growth then saturates at each radius at a fraction of the local equipartition value, provided the helicity flux is favourable for the dynamo action. The role of the radial diffusion is merely to couple the dynamo action at different radii as to lead to a magnetic structure growing at a single rate. Importantly, the entire disc becomes magnetized over a timescale much shorter than the radial diffusion time.

3.3.2 Reversals of the magnetic field

We find that if the seed magnetic field is weak enough, the steady-state magnetic configuration is independent of its form and strength. However, a relatively strong initial magnetic field can affect the steady-state magnetic configuration if nonlinear dynamo effects become important before the leading dynamo eigenfunction (normally represented

[2]That there is not much difference between the two cases is expected because in an axisymmetric disc, axisymmetric modes are dominant, and effects of a finite relaxation time in the axisymmetric problem are of order $\Gamma\tau \ll 1$; only in the non-axisymmetric case do effects of order $\Omega_\mathrm{p}\tau \lesssim 1$ play a role in our model.

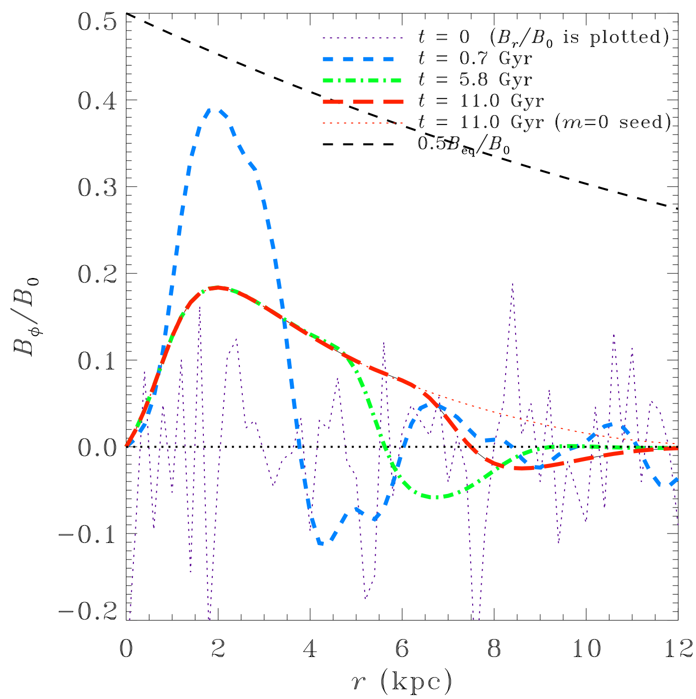

Figure 3.4: Evolution of the magnetic field that starts as a random seed magnetic field (Model C) in the $\tau \to 0$ case. Curves show $\overline{B}_\phi$ at the azimuth $\phi = 0$ at various times, with the exception of the field at $t = 0$, where $\overline{B}_r$ is shown (since $\overline{B}_\phi = 0$). Otherwise, $\overline{B}_r$ is omitted for the sake of clarity, but vanishes at the same set of radii as $\overline{B}_\phi$, indicating reversals of the field at these locations. For the final time, the solution obtained with an $m = 0$ seed is shown as a thin dotted line for reference.

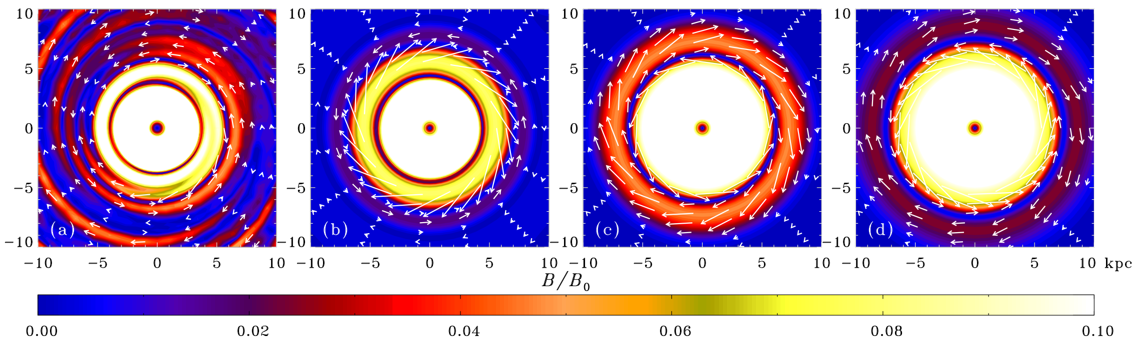

Figure 3.5: The strength of the mean magnetic field (colour coded) at **(a)** $t = 0.7\,\mathrm{Gyr}$, **(b)** $2.8\,\mathrm{Gyr}$, **(c)** $7.3\,\mathrm{Gyr}$, and **(d)** $11.0\,\mathrm{Gyr}$ in Model C (random seed field) for the case $\tau \to 0$. The colour of the central region has been saturated to enhance visibility of the magnetic structure in the outer disc. Field vectors are also shown, with tail length proportional to the magnitude of magnetic field, for $r > 5\,\mathrm{kpc}$ only, to avoid clutter. Reversals which evolve with time are visible (for example, the central dark ring which moves out with time).

by an axisymmetric magnetic field without any reversals along the radius) can become dominant (Shukurov, 2005; Moss et al., 2012). In particular, a random seed magnetic field can lead to long-lived reversals in the (quasi-)steady state magnetic configuration, either global (Poezd et al., 1993) or localised in both radius and azimuth (Bykov et al., 1997). A suitable random seed magnetic field can be readily provided by the fluctuation dynamo action (Poezd et al., 1993). Earlier results in this area have been obtained with a heuristic algebraic nonlinearity in the mean-field dynamo equation (see Chapter 1). Here we revisit this idea, but now with the physically motivated dynamic nonlinearity and finite τ.

In Model C, we have chosen a random seed specified as a two-dimensional Gaussian random field with the root-mean-square value of about one tenth the equipartition value (i.e., a fraction of μG in the Solar neighbourhood).[3] We also tried ten times larger seeds and found almost identical results. The number of radial grid points in this models is $n_r = 100$, corresponding to a resolution $0.2\,\mathrm{kpc}$ in radius, comparable to the correlation scale of the interstellar turbulence. The results are shown in Fig. 3.4. Firstly, large scale fields can develop over kpc scale regions, even in the outer disc, on Gyr timescales. More interestingly, it can be seen that reversals develop and persist for several Gyr in the nonlinear regime. (Because of the random nature of the problem, other random seeds of the same strength or different resolutions can result in field configurations without reversals.) The reversals are also apparent in a time sequence of the magnetic field of Model C shown

[3]The solenoidality of the seed field is ensured by an appropriate choice of $\overline{B}_z$.

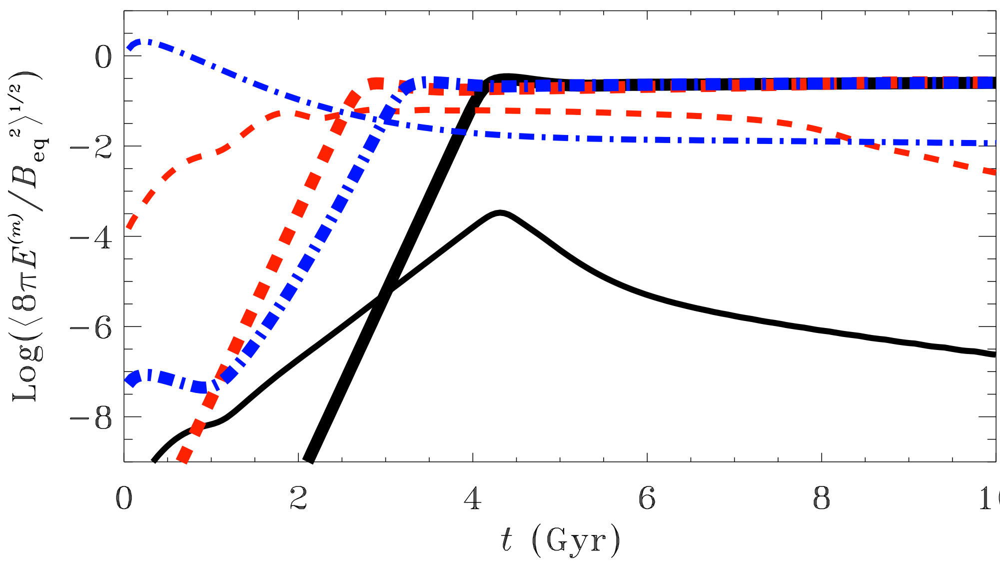

Figure 3.6: Evolution of the normalised magnetic field strength averaged over the disc, in the $m = 0$ (thick) and $m = 1$ (thin) modes, for a purely bisymmetric ($m = 1$) seed magnetic field (Model D) with $\tau \to 0$. Different line styles show three cases with identical parameters, except for the magnitude of the seed field, so that the dynamo action saturates (i) when the $m = 0$ mode dominates (solid), (ii) when $m = 1$ dominates (dashed), and (iii) right from $t = 0$ (dash-dotted).

in Fig. 3.5. At least one reversal in the regular magnetic field has been observed in the Milky Way (Van Eck et al., 2011). It can be seen from both figures that as time goes on, the reversals become global in nature, propagate outward on a timescale of several Gyr, and in the process decrease in number. By $t = 6t_0 = 4.4\,\mathrm{Gyr}$ all reversals inside $r = 16\,\mathrm{kpc}$ are global in nature (i.e. occur at all azimuth for a given radius). In the $\tau = l/u$ case, the noise from the random seed takes much longer to dissipate, and global reversals are only apparent much later on, at large radii where the field is very weak. Poezd et al. (1993) found that the persistence of the reversals at the galactic lifetime scale strongly depends on the rotation curve. Our experiments reported here suggest that memory effects (finite τ) are also important.

3.3.3 Non-axisymmetric magnetic fields in an axisymmetric disc

Staying with axisymmetric discs for the time being, it is useful to ask whether significant non-axisymmetric modes in the large-scale magnetic field can arise and be maintained in such discs. If so, this would obviate any need for introducing non-axisymmetry into the underlying disc. In fact, we find that the non-axisymmetric modes decay in an axisymmetric disc for the parameters used in most of our numerical models (see Table 3.1). However, the $m = 1$ mode (easiest non-axisymmetric mode to excite) can grow for somewhat modified parameters (Model D of Table 3.2), with α_k truncated in the central region to $u/2$.

In Model D, we focus on the case $\tau \to 0$. The results of runs with $\tau \neq 0$ do not show notable differences. The $m = 1$ mode is readily excited with the kinematic growth rate $\Gamma_1 = 1.7 t_0^{-1} = 3.5\,\mathrm{Gyr}^{-1}$. The growth rate for the axisymmetric mode for these parameters is $\Gamma_0 = 4.7 t_0^{-1} = 9.6\,\mathrm{Gyr}^{-1}$. Since $\Gamma_0 > \Gamma_1$ with a significant margin, magnetic field in a mature dynamo hosted by an axisymmetric disc will be axisymmetric unless the seed magnetic field is strongly non-axisymmetric. The latter is, in fact, quite plausible if the seed field arises, for example, from a putative intergalactic field captured as the disc galaxy forms. In order to address this point, we have run Model D, starting from a purely $m = 1$ seed, with the $m = 0$ mode being seeded only by the numerical noise, as in Moss (1996). We adjust the strength of the seed such that nonlinear dynamo effects become significant at various important stages: (i) when the $m = 0$ mode has already come to dominate, (ii) when it is still weaker than the $m = 1$ mode, and (iii) right from $t = 0$.

The results are shown in Fig. 3.6. Thick lines correspond to the normalised magnetic field strength (averaged over the area of the disc) in the $m = 0$ mode while thin lines correspond to that in the $m = 1$ mode. In Case (i), shown by the solid lines, the saturation of the (essentially axisymmetric) field clearly causes the $m = 1$ mode to decay since its growth requires a stronger (unquenched) dynamo action. In Case (ii) (dashed lines), the early saturation of the (stronger) $m = 1$ mode still does not prevent the $m = 0$ mode from growing and evolving as in Case (i). This happens because the magnetic field in between the extrema of the non-axisymmetric magnetic field remains relatively weak when the $m = 1$ mode ceases to grow. Therefore, the growing $m = 0$ mode is supported by the local dynamo action in those regions, to fill the gaps until the field is saturated everywhere to become nearly axisymmetric. However, the $m = 1$ mode, though subdominant, does not immediately decay but remains strong for several Gyr. This is because the outward spreading of the dominant $m = 0$ mode is preceded by the outward spreading of the $m = 1$ mode. Eventually, the axisymmetric mode comes to dominate everywhere and the $m = 1$ decays more quickly (for $t \gtrsim 8\,\mathrm{Gyr}$). In Case (iii) (dash-dotted lines), we find that the

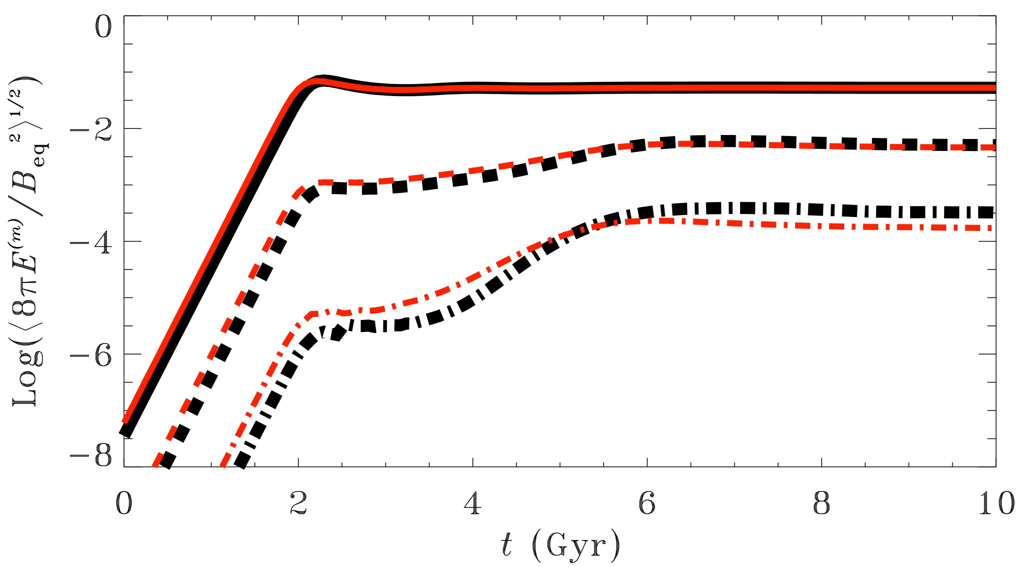

Figure 3.7: Magnetic field strength in the $m = 0$ (solid), $m = 2$ (dashed) and $m = 4$ (dash-dotted) modes of the mean magnetic field, normalized to the equipartition field strength B_{eq} and averaged over the entire disc, for Model E. Results obtained for $\tau = l/u$ are shown in thick black, while those for $\tau \to 0$ are in thin red. All modes have exponential kinematic growth rate $\Gamma^{(m)} = 7.0\,\mathrm{Gyr}^{-1}$. For the convenience of presentation, time has been rescaled so that the simulation in fact starts from $t = -8\,\mathrm{Gyr}$.

$m = 1$ mode first decays and then remains much weaker than the $m = 0$ mode.

As far as the overall survival of non-axisymmetric modes in an *axisymmetric* disc is concerned, we can conclude that (i) a rather special parameter combination is needed for a non-axisymmetric mode to grow; (ii) for a non-axisymmetric mode to persist for several Gyr in the nonlinear stage, it must reach the saturation strength before the $m = 0$ mode can do so; given that non-axisymmetric modes have smaller growth rates, this implies that they must be much stronger initially; (iii) in any case, all non-axisymmetric modes eventually decay in an axisymmetric disc. These conclusions make it all the more reasonable to suggest that deviations from perfect axial symmetry of the underlying disc are required to explain the prevalence of non-axisymmetric regular fields in many galaxies. It is the mechanism of ‘spiral forcing’ of the dynamo to which we now turn.

3.4 Magnetic arms enslaved to a stationary spiral pattern

In this section, we consider the evolution of the mean magnetic field in a non-axisymmetric disc where the α effect is modulated by a stationary spiral pattern. As above, our analysis includes the dynamic nonlinearity, thus extending fully into the saturated states of the dynamo action, and allows for a finite dynamo relaxation time τ.

As a consistency check, we have first made sure that the standard dynamo solutions, obtained by solving equation (1.23) are obtained when solving equation (1.22) with τ approaching zero. Indeed, we found good agreement with them for $\tau = 10^{-3}$. To ensure that the results are not sensitive to the location of the outer boundary, we compared solutions with outer radius of $R = 15\,\text{kpc}$ and $30\,\text{kpc}$, with the standard value $R = 20\,\text{kpc}$ (with the radial resolution modified proportionately). The results are not sensitive to this adjustment.

Our standard model is labelled E, with parameters given in Table 3.2. To explore the parameter space, we have also considered Models F–L.

The evolution of the normalized magnetic field strength in various even-m modes, averaged over the area of the disc, is shown, for Model E, in Fig. 3.7. In the kinematic regime, all modes have about the same growth rate $\Gamma \simeq 5.1t_0^{-1} \simeq 7.0\,\text{Gyr}^{-1}$ for both $\tau \to 0$ and $\tau = l/u$ cases. This growth rate is also in close agreement with the growth rate for the axisymmetric case (Model B). This is not surprising because the average field in the disc is used to calculate the growth rate, and the field is dominated by the axisymmetric field at $r \ll r_{\text{cor}}$. The even-m modes grow together with the $m = 0$ mode because they are driven by (enslaved to) it. The $m = 2$ and $m = 4$ modes corotate with the spiral pattern.

We illustrate in Fig. 3.8 various aspects of the solution in the kinematic stage at $3t_0$ after the simulation has begun (or $t = -5.8\,\text{Gyr}$ in the plots). Some aspects of the solution after the dynamo has saturated are given in Fig. 3.9. In Figs. 3.8a and 3.9a, $\overline{B}_\phi$ (solid), $-\overline{B}_r$ (dashed) and $|\overline{B}_z|$ (dotted) have been plotted for both $\tau \to 0$ (red) and $\tau = l/u$ (black) cases, at $\phi = \phi_{\text{cor}}$, one of the two azimuthal angles where the α-spiral crosses the corotation circle. As expected, the field is strongest inside the corotation radius, where the magnitude of the dynamo number is largest. Importantly, however, there is an excess of magnetic energy near the corotation radius, as compared to what is obtained in an axisymmetric disc, mainly due to the presence of strong additional $m = 0$ and $m = 2$ components near $r = r_{\text{cor}}$. This excess is present at early enough times in the kinematic stage (like we have shown in Fig. 3.8a), disappears at later times, but reappears on saturation.

The presence of the non-axisymmetric component near corotation can be more clearly

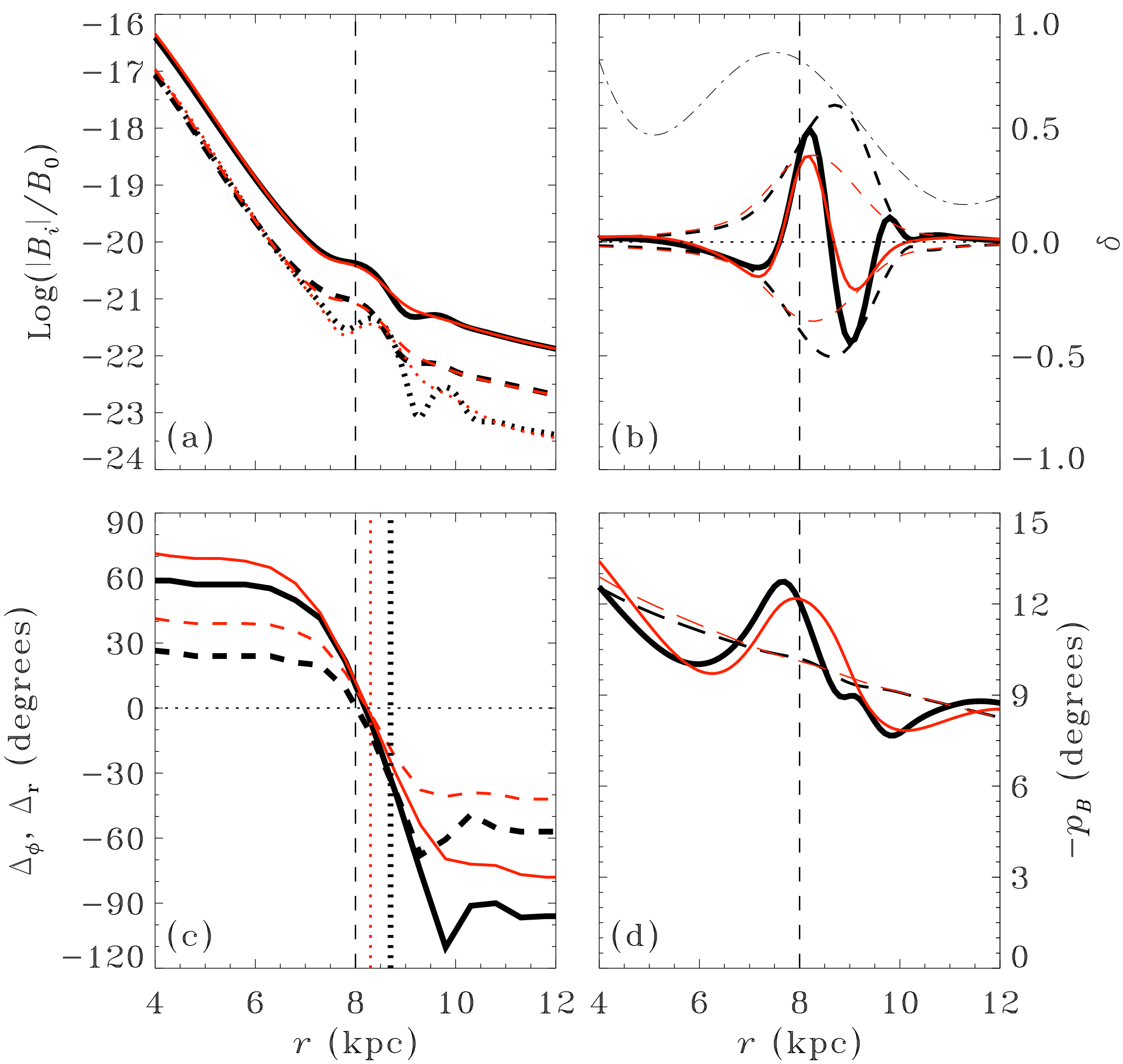

Figure 3.8: Properties of the field in the kinematic regime for Model E at a time $3t_0$ after the simulation is begun. Thick black illustrates the $\tau = l/u$ case while thin red illustrates $\tau \to 0$. In all plots, the corotation radius is shown as a dashed vertical line. **(a)** The normalized azimuthal (solid), radial (dashed), and vertical (dotted) components of the field at the azimuth $\phi = \phi_{\rm cor}$ for which the α-spiral crosses corotation. **(b)** The ratio δ of the non-axisymmetric to axisymmetric ϕ-component of the field at $\phi_{\rm cor}$ (solid), and at azimuthal extrema (dashed). The quantity $\alpha_{\rm k}(r, \phi_{\rm cor})$ is shown as a thin dash-dotted line for reference. **(c)** The phase of the ϕ-component (solid) or r-component (dashed) of the magnetic spiral minus the phase of the α-spiral (smoothed over 5 radial grid points, or 0.5 kpc). The radius $r_{\rm max}$ at which the global maximum of δ occurs is plotted as a vertical dotted line for each τ case. **(d)** Negative of the pitch angle at $\phi = \phi_{\rm cor}$ (solid), with azimuthal mean (dashed).

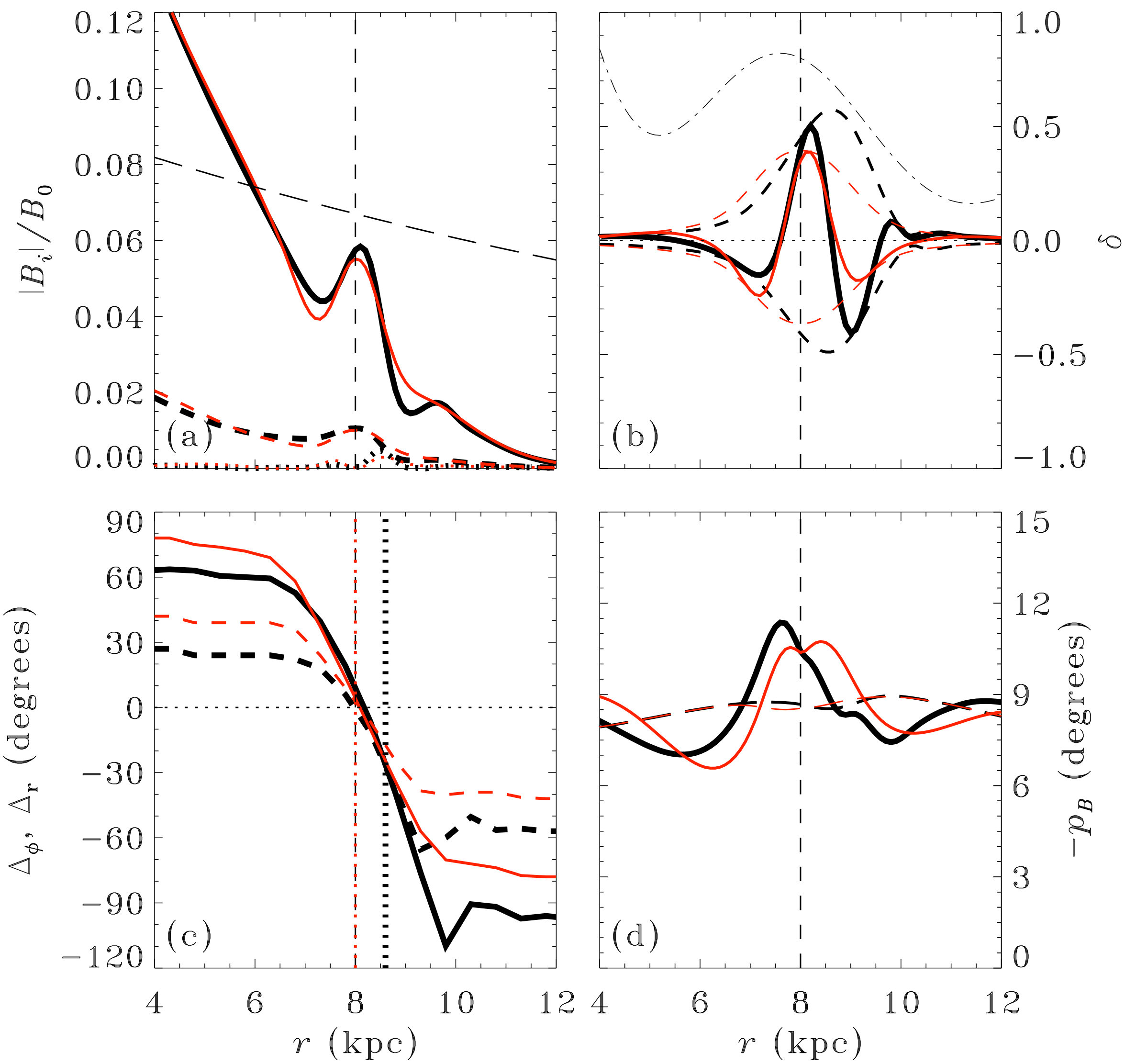

Figure 3.9: Same as Fig. 3.8 (Model E), but now for $t = 10\,\mathrm{Gyr}$ (see Fig. 3.7), when the field has reached equilibrium as a result of dynamical quenching. Note that in (a) The scale is now linear instead of logarithmic. The long dashed curve is equal to $0.1B_{\mathrm{eq}}/B_0$, shown for reference.

seen in Fig. 3.8b. There we plot the ratio of the non-axisymmetric part of B_ϕ to the axisymmetric part,

$$\delta = \frac{B_\phi - B_\phi^{(0)}}{B_\phi^{(0)}}. \tag{3.32}$$

at the azimuth $\phi = \phi_{\rm cor}$. For both vanishing and finite τ, the δ is important within an annulus of width $\approx 4\,{\rm kpc}$, centred near the corotation circle. Note that in both cases, the radial phase varies much more rapidly than that of α (plotted as a thin dash-dotted line in the figure). This indicates that the magnetic arms are much more tightly wound than the material arms. The effect of a finite τ is to strengthen the non-axisymmetry, and also to slightly increase the variation of the radial phase. In addition, the δ extends out to somewhat larger radius in the $\tau = l/u$ case than it does for $\tau \to 0$. This is illustrated by the second maximum with $\delta > 0$ at $r \simeq 10\,{\rm kpc}$ that occurs when $\tau = l/u$, and is caused by the tail of the spiral magnetic field wrapping around an extra half-circle from where it crosses the corotation circle. Also shown in Figs. 3.8b and 3.9b as dashed lines is the envelope of the solid lines as ϕ changes.[4]

The shift between the azimuthal positions where $\overline{B}_\phi$ (or $\overline{B}_r$) is maximum and where α is maximum, denoted Δ_ϕ (or Δ_r), is shown in Figs. 3.8c and 3.9c.[5] Positive values of these quantities imply that the magnetic arms lead the material arms, while negative values imply that they trail them. The position $r_{\rm max}$ of the global maximum of δ (maximum of the dashed envelope in Figs. 3.8b and 3.9b), which is the radius at which the non-axisymmetric component of the field is most important relative to the axisymmetric component, is indicated with a vertical dotted line (red for $\tau \to 0$ and black for $\tau = l/u$): $r_{\rm max} = 8.3\,{\rm kpc}$ (kinematic) and $8.0\,{\rm kpc}$ (saturated) for $\tau \to 0$, and $8.7\,{\rm kpc}$ (kinematic) and $8.6\,{\rm kpc}$ (saturated) for $\tau = l/u$. One can see that $r_{\rm max}$ is nearer $r_{\rm cor}$ for $\tau \to 0$ than for $\tau = l/u$.

In the $\tau \to 0$ case, studied by Mestel & Subramanian (1991) and Subramanian & Mestel (1993), it was found that $\Delta_\phi = \Delta_r = 0$ at $r = r_{\rm cor}$ and $r_{\rm max} = r_{\rm cor}$. In the vanishing τ case in our model, $r_{\rm max}$ is slightly larger than $r_{\rm cor}$ in the kinematic regime, and Δ_ϕ and Δ_r are not precisely zero at $r_{\rm max}$ nor at $r_{\rm cor}$. These differences arise due to interference from the dominant axisymmetric eigenmode, which is concentrated at smaller radius near where the dynamo number peaks, in our model. In any case, for both $\tau \to 0$ and $\tau = l/u$, the magnetic and α-spiral arms intersect in the vicinity of corotation, and the magnetic arms are also strongest in the vicinity of corotation, as in the earlier models.

What is more noteworthy, however, is the phase shift in the magnetic arms, at

[4]The envelope is not perfectly symmetrical about $\delta = 0$ because of interference between the $m = 2$ mode and the much smaller $m = 4$ mode.

[5]Phase shifts quoted have an uncertainty of $\pm 3^\circ$ due to the finite numerical mesh.

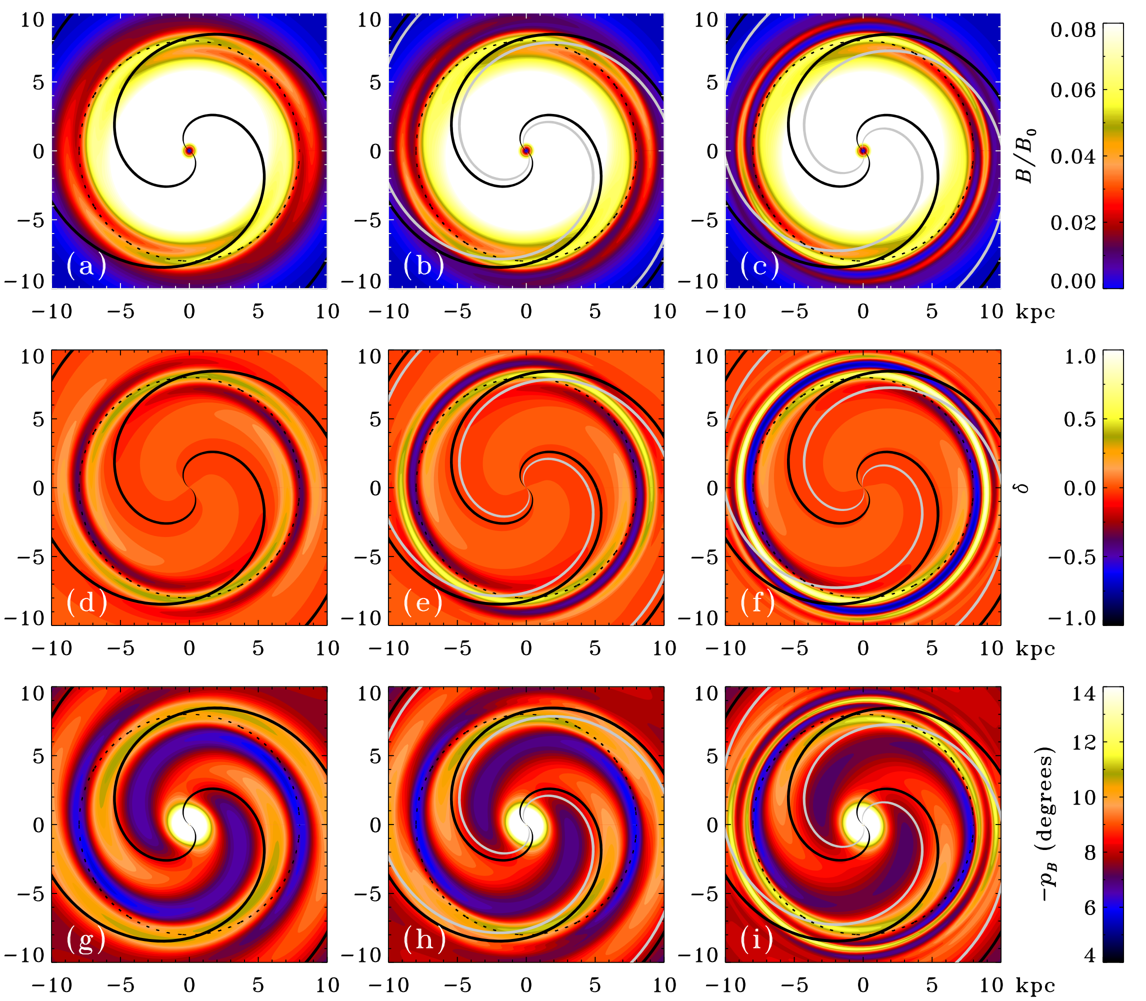

Figure 3.10: The top panels show the magnitude of the magnetic field in the saturated state in the $\tau \to 0$ (left), $\tau = l/u$ (middle) and $\tau = 2l/u$ (right) cases. In all panels, the peak of α_k is shown as a thick black line, the grey shifted line illustrates (for reference) the α_k spiral shifted by the angle $-\Omega_\mathrm{p}\tau$, while the corotation radius is illustrated as a black dotted circle. The colour of the central regions in a–c has been saturated in order to visually bring out the behaviour near corotation, where the non-axisymmetric modes are important. Panels d–f show the ratio δ of the non-axisymmetric to axisymmetric components of $\overline{B}_\phi$. The bottom panels show the magnetic pitch angle. Again, the colour within a region around the center has been saturated.

$r_{\max}$, where they are strongest, resulting from a finite τ. We find, initially, $\Delta_\phi(r_{\max}) = \Delta_r(r_{\max}) = -3^\circ$ for $\tau \to 0$ and -30° for $\tau = l/u$, for an overall phase difference of -27°. On saturation, $\Delta_\phi(r_{\max}) = \Delta_r(r_{\max}) = +3^\circ$ for $\tau \to 0$ and -27° for $\tau = l/u$, for a phase difference of -30°. This is comparable in magnitude to the value $\Omega_{\rm p}\tau = 18^\circ$ that results from an order of magnitude estimate of the phase shift. Non-locality in time produces a delay in the α effect of order τ, so that the α-spiral has rotated through an angle $\approx \Omega_{\rm p}\tau$ before the dynamo has had the chance to respond to it. We recall that a phase shift of $\pm 90^\circ$ would correspond to peaks of the magnetic arms located mid-way between the spiral arms of α.

The magnetic pitch angle

$$p_B = \arctan \frac{\overline{B}_r}{\overline{B}_\phi} \tag{3.33}$$

is plotted (by magnitude) in Figs. 3.8d and 3.9d, with its azimuthal mean shown as a dashed line. The negative value of p_B indicates that magnetic lines have the form of a trailing spiral. The azimuthally averaged value of $|p_B|$ is only slightly perturbed from the corresponding curve obtained in the axisymmetric case (i.e. for Model B, not shown). In the kinematic regime, the azimuthal average decreases with radius such that $\tan p_B \propto 1/h$, as expected (Ruzmaikin et al., 1988; Shukurov, 2005). However, this decreasing trend is no longer present in the nonlinear regime, and the azimuthal average of p_B (dashed curve) is almost constant over a large range of radius.

We have also checked the validity of neglecting the terms $\partial(\alpha\overline{B}_z)/(r\partial\phi)$ and $\partial(\alpha\overline{B}_z)/\partial r$ in equations (3.4) and (3.5), respectively. Although neglecting the former is always justified, we find that the latter is comparable to the term $\partial(\alpha\overline{B}_r)/\partial z \simeq -2\alpha\overline{B}_r/(\pi h)$ in magnitude for some values of ϕ near $r = r_{\rm cor}$, where radial variation of the solution is especially strong. But this term itself, which appears in the equation for $\overline{B}_\phi$, is subdominant to the shear term $G\overline{B}_r$. Therefore we repeated the run with the $\alpha\Omega$ approximation (neglecting the α^2 effect); we find the resulting differences in the solutions to be small and inconsequential.

Figure 3.10 shows a 2D representation of the magnetic field strength (upper panels), the quantity δ (middle panels), and pitch angle (lower panels) obtained in Model E, with the case of $\tau \to 0$ on the left, $\tau = l/u$ in the middle column, and $\tau = 2l/u$ on the right. Magnetic arms are clearly visible near the corotation circle in Fig. 3.10a–f. As they are more tightly wound than the α-arms, they cut across them, as noted above. From Fig. 3.10, we see that the magnetic arms are more pronounced (larger $\overline{B}$ at their centres), are more sharply defined (faster variation of the radial phase), and extend for a longer azimuthal angle outside of the corotation circle for the finite τ case compared to the $\tau \to 0$

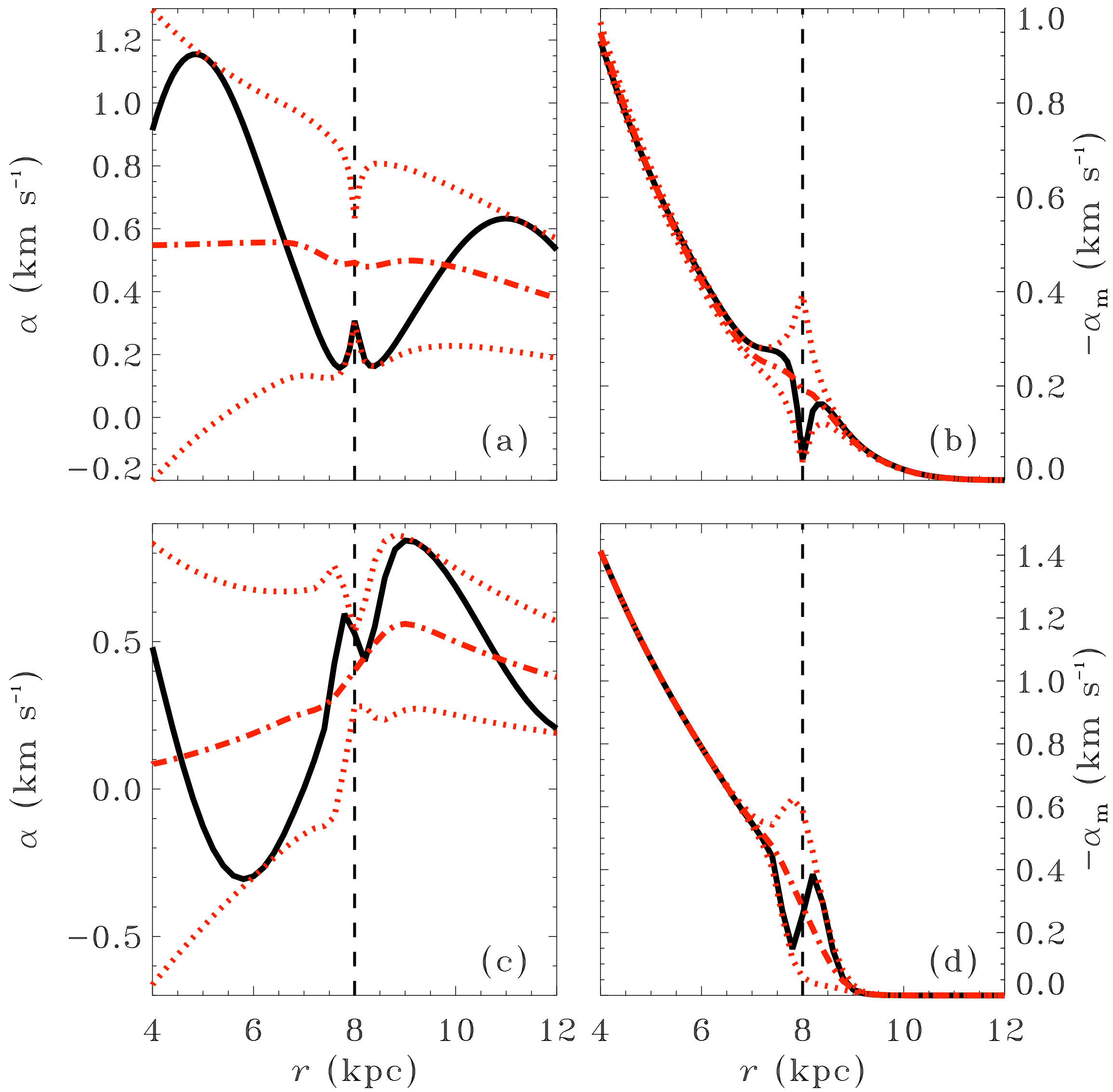

Figure 3.11: **(a)** The profile of α for Model E ($\tau \to 0$ case), in the saturated state, for $\phi = 0$ (solid), azimuthal mean (dash-dotted) and envelope for all azimuth (dotted). **(b)** Same as (a) but now for $-\alpha_{\rm m}$. **(c)** Same as (a) but now for Model H, at the time $t = 4.4\,{\rm Gyr}$, when the outgoing ring is passing the corotation circle. **(d)** Same as (c) but now for $-\alpha_{\rm m}$.

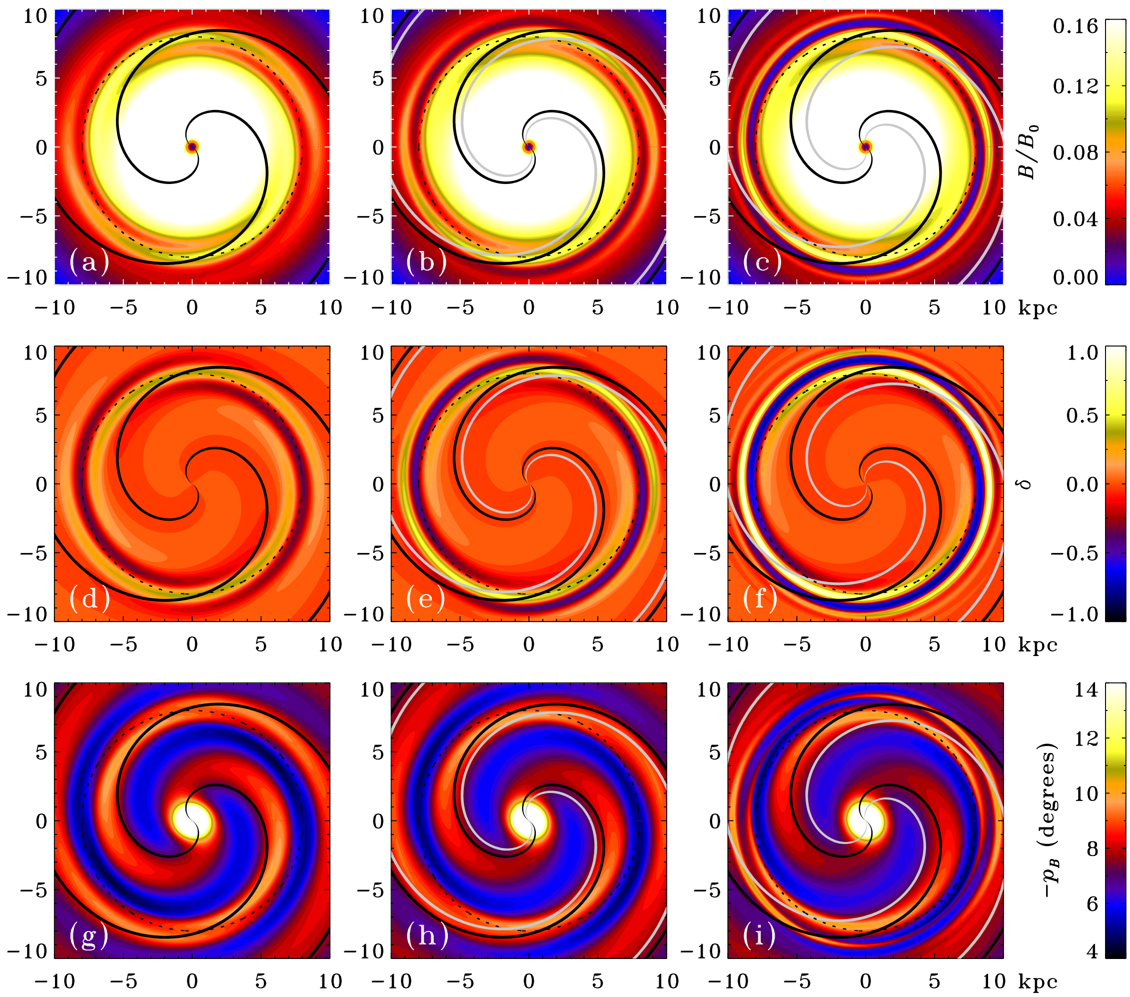

Figure 3.12: Same as Fig. 3.10 but now for the steady state solution of Model O (diffusive flux of $\alpha_{\rm m}$ instead of advective flux). Note the change in plotting range in the top row.

case. Also, the maxima in magnetic field strength are displaced downstream from those of α by an angle of order $\Omega_{\rm p}\tau$. Moreover, in the $\tau = l/u$ case, a more significant part of the magnetic arm clearly lies in between the α-spiral arms. These features can be seen more clearly for $\tau = 2l/u$ in the right hand panels of Fig. 3.10. It is worth noting that we find an enhancement in the amplitude of $\alpha_{\rm m}$ around where the non-axisymmetric mode concentrates, as required to saturate the dynamo. This is visible in Fig. 3.11a and b, which show the profiles of α and $\alpha_{\rm m}$, respectively.

There is a hint of wave-like behaviour in the solutions with finite τ, which is most evident in Fig. 3.10f, where ripple-like features are visible just outside of the corotation circle. But in general, τ is not large enough in our model for such wave-like behaviour to dominate.

The magnitude of the pitch angle is displayed in the lower panels of the figures, and clearly also has a spiral pattern. The pitch angle, as opposed to the field magnitude, does not vary strongly with radius. Because of this, the spiral morphology of the field is more clearly visible in the pitch angle. However, an accuracy of a few degrees would be required to measure the differences.

Another quantity that can be obtained is the pitch angle of the magnetic ridges, i.e. of the magnetic arms themselves as opposed to the magnetic field that constitutes them. This can then be compared with the pitch angle of the α-spiral arms. We find this pitch angle to be quite small as compared to that of the α-spiral. One must keep in mind, however, that the pitch angle of the magnetic ridges is sensitive to the shear near corotation.

In Model P, the run described in this section was performed with the resolution doubled for the cases $\tau = l/u$ and $2l/u$, and the results were found to be consistent with those of the standard resolution runs.

In Model O, the advective flux of $\alpha_{\rm m}$ was replaced with the diffusive flux, and the results in the steady state are illustrated in Fig. 3.12. The magnetic arms are almost identical (middle row), but the overall field strength is about twice as large (top row; as discussed in Sect. 3.3.1), and magnetic field pitch angles are slightly smaller (bottom row). The strength of the saturated field just outside of the corotation radius falls off somewhat more slowly with radius than for Model E, which gives the *appearance* of wider magnetic arms in the top row of Fig. 3.12. The enhancement of $\alpha_{\rm m}$ near corotation, mentioned above, is still present, though the feature is smoothened somewhat by the diffusive flux. We emphasize that the qualitative features of the solutions obtained in both cases (Models E and O) are very similar.

3.4.1 Exploring alternative models and the parameter space

Modulation of the α effect is just one of the mechanisms through which the spiral pattern can affect the dynamo action. Model F has the vertical advection velocity enhanced along a spiral (with the α-spiral turned off), to model stronger galactic outflows from the spiral arm regions, where star formation is enhanced. We use $R_U = 0.90$ at $r = R/2 = 10\,\mathrm{kpc}$ and $\epsilon_U = 0.5$ so that the outflow speed within the arms, corresponding to $R_U = 1.35$, is too large for the optimal field growth near corotation, while the inter-arm value of $R_U = 0.45$ is close to being optimal. This mechanism for producing magnetic arms located between the material spiral arms was first suggested by Sur et al. (2007). We find that this mechanism can indeed lead to a non-axisymmetric field which peaks in the inter-arm regions. For the region of parameter space explored in this chapter, the effect is, however, too weak to be of much consequence. However, it though it turns out to be important for different parameter values, as mentioned briefly in Section 2.6.2. We devote Chapter 6 to a detailed study of this mechanism.

The characteristic strength of magnetic field at which nonlinear dynamo effects become pronounced, B_{eq}, can also be affected by the spiral pattern, e.g., through the variation in the turbulent energy density. We considered a model with B_{eq} enhanced along a spiral in the same way as above for α_{k} and $\overline{U}_z$. Since $B_{\mathrm{eq}} = (4\pi\rho)^{1/2}u$, and we keep u constant, this is tantamount to modulating ρ. Although an enslaved spiral does result, we find the effect to be too weak to be of much consequence, at least for the parameter space explored [c.f. equation (2.18)]. Other possibilities have been explored in the literature, e.g. the modulation of the turbulent magnetic diffusivity η_{t}, but a more extensive study of these effects is left for a future work.

We have also run Models G–L to test the results under reasonable variations of parameters. We have varied the strength of the seed field, the mean vertical velocity $\overline{U}_z$, the strength and the pitch angle of the spiral pattern via ϵ_α and k, respectively, and the number of material spiral arms n. In Model G, we use a seed field that is random Gaussian noise. Model G differs from Model C in that the underlying disc in non-axisymmetric. We find reversals to occur in more or less the same locations as in that model. However, a strong quadrisymmetric magnetic field component is now present, superimposed on an axisymmetric pattern with reversals. The morphology of the magnetic spiral arms is significantly affected by the reversals, as the horizontal magnetic field is necessarily zero wherever a reversal occurs. The effect of vanishing helicity flux is considered in Model H, which differs from Model E only in that it has $\overline{U}_z = 0$. This situation can occur in galaxies after the end of a burst of star formation, when the galactic fountain or wind ceases and the mean-field dynamo action is choked by the magnetic helicity conservation to leave

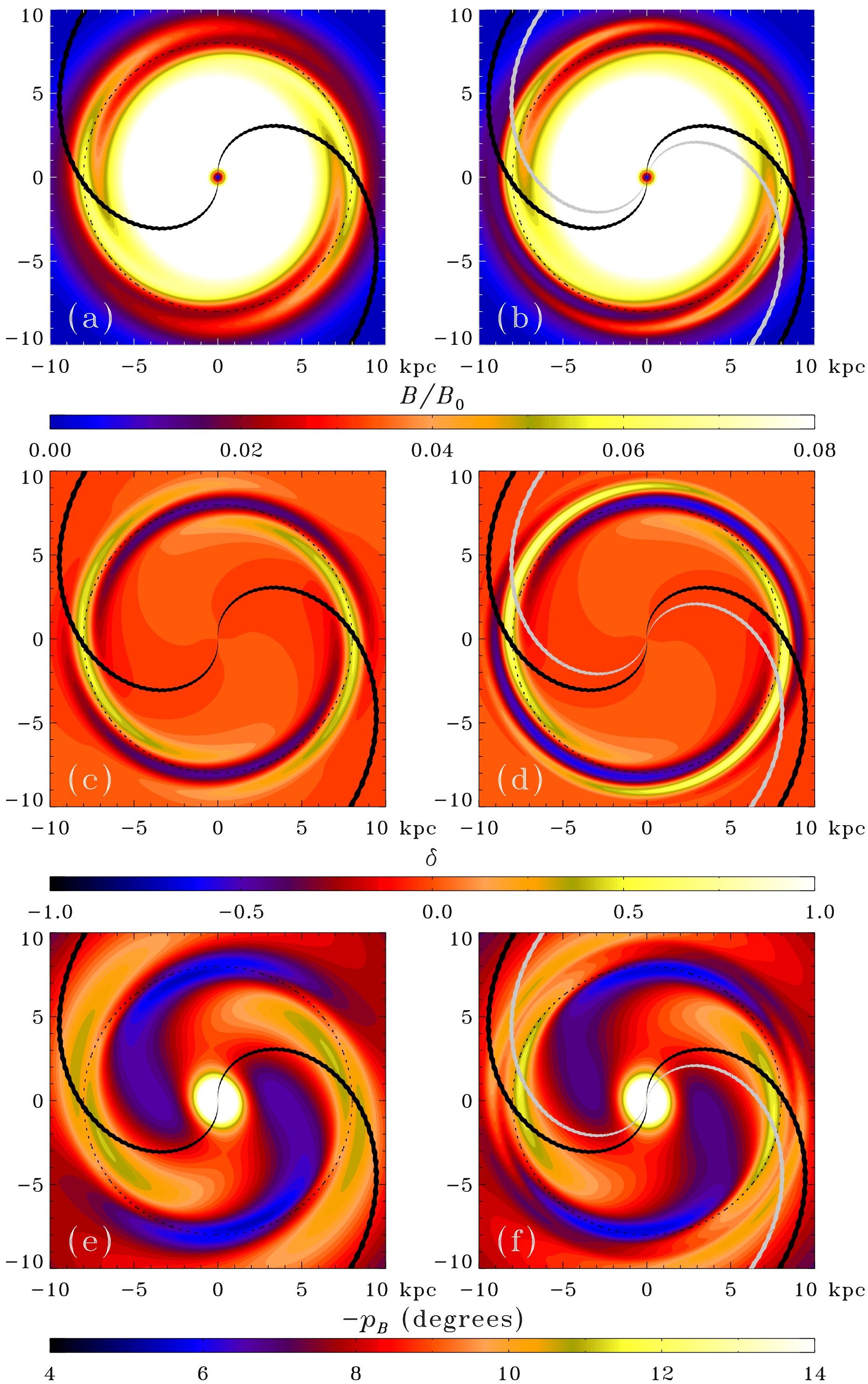

Figure 3.13: Similar to Fig. 3.10, but now for Model J ($k = -8R^{-1}$ instead of $-20R^{-1}$), with $\tau \to 0$ on the left and $\tau = l/u$ on the right.

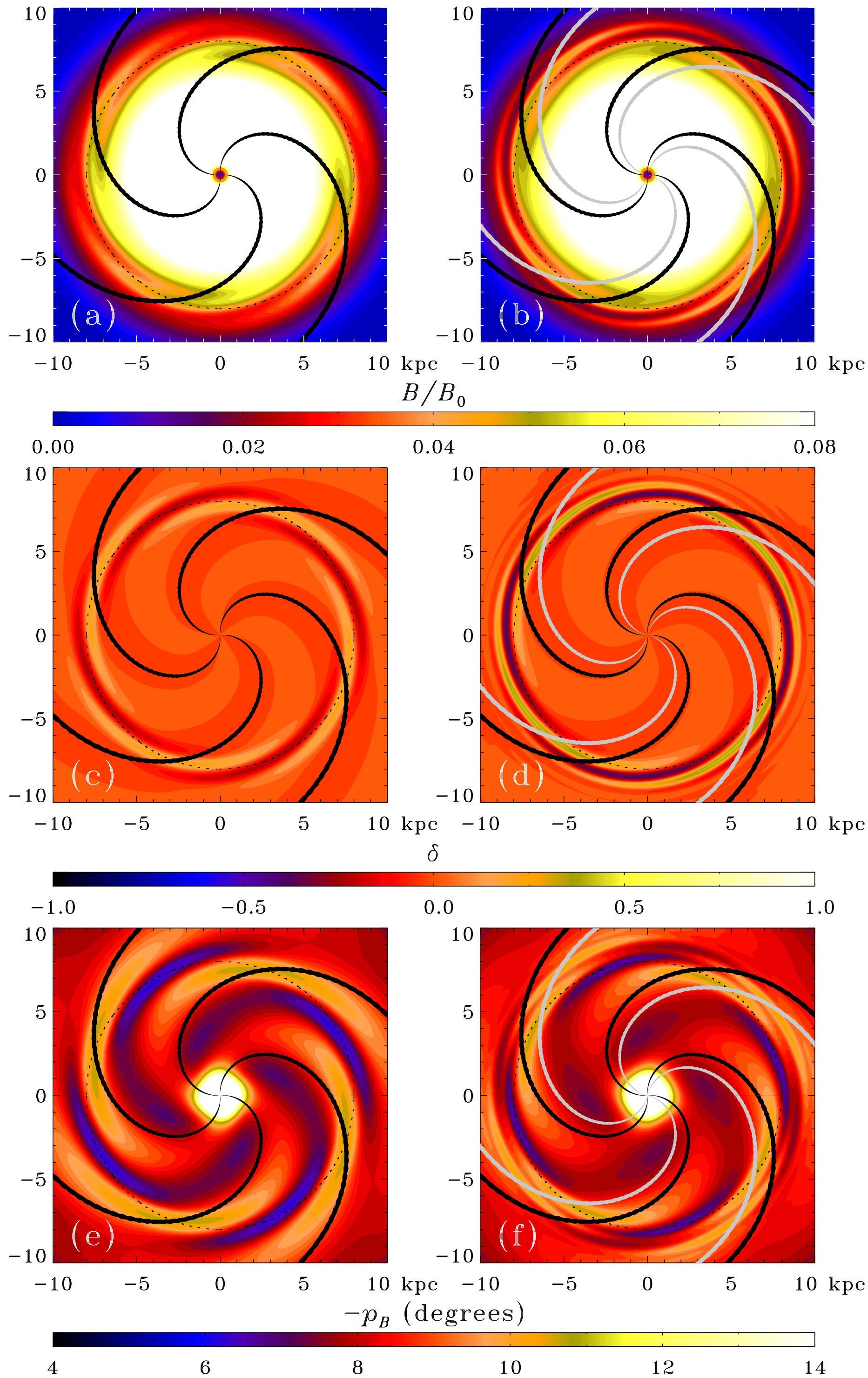

Figure 3.14: Same as Fig. 3.13 but now for Model L ($k = -20R^{-1}$ and $n = 4$ instead of 2).

magnetic field decaying, assuming no other flux is important. As expected, the mean field decays after a period of temporary growth. An expanding annular magnetic structure (see Sect. 3.3.1) is prominent, but develops strong deviations from axial symmetry as the ring approaches and then passes through the corotation circle. As this happens, the amplitude of $\alpha_{\rm m}$ becomes enhanced there, as can be seen in Fig. 3.11c-d, and then remains enhanced subsequently. The magnetic ring fades in intensity and becomes more and more axisymmetric as it moves out.

In Model I, ϵ_α is increased from 0.5, as in Model E, to $\epsilon_\alpha = 1$, so that now $\alpha_{\rm k} = 0$ between the spiral arms. As could be expected, this enhances the deviation of the mean magnetic field from axial symmetry, manifested in more pronounced magnetic arms and a larger azimuthal variation in the magnetic pitch angle. The magnitude of the non-axisymmetric part of the magnetic field mode slightly exceeds the axisymmetric part near $r = r_{\rm max}$ when $\tau = l/u$. This produces small regions of positive pitch angle just outside of the corotation, where the magnetic lines locally have the shape of a leading spiral. Putting $\tau = l/u$ with $\epsilon_\alpha = 1$ also results in a somewhat larger phase shift compared to the $\tau = l/u$, $\epsilon_\alpha = 0.5$ case in Model E. We obtain $\Delta_r(r_{\rm max}) = \Delta_\phi(r_{\rm max}) = -36^\circ$ for $\tau = l/u$, whereas for Model E we had -27°. For $\tau \to 0$, the phase shifts are both equal to $+3^\circ$, the same as in Model E so the overall phase difference is -39°, larger than for Model E. The trailing part of the magnetic spiral is significantly enhanced when τ is finite.

In Models J and K we make the α-spiral less tightly wound by reducing the magnitude of k. It is evident from Fig. 3.13 that changing the value of k from $-20R^{-1}$ [$p_\alpha(r_{\rm cor}) = -14^\circ$, Model E] to $-8R^{-1}$ [$p_\alpha(r_{\rm cor}) = -32^\circ$, Model J] does not have any significant qualitative effect on the magnetic field. Even replacing the material spiral with a bar ($k = 0$, Model K) does not lead to a drastic change in the saturated magnetic field, so that bars also lead to spiral magnetic fields. This happens because of the differential rotation of the gas, which shears out the enhancement of the field due to the bar. An important effect of a more open spiral pattern, visible in Fig. 3.13a–b, is that magnetic spiral arms are now mostly in between the material arms, although still confined to an annular region around corotation. The values of $\Delta_r(r_{\rm max})$ and $\Delta_\phi(r_{\rm max})$ are both -33° for $\tau = l/u$, and $+3^\circ$ for $\tau \to 0$, for an overall phase difference of -36°. The pattern of variation of the magnetic pitch angle is strongly modified from the case of the more tightly wound α-spiral of Model E, though its range is almost the same.

We tried various values of n, both odd and even, and found, unsurprisingly, that the number of magnetic arms is equal to the number of material arms. The results of Model L ($n = 4$) are plotted in Fig. 3.14. The magnetic arms are largely located in between the material arms, especially for $\tau = l/u$. They are also much stronger and more well-defined

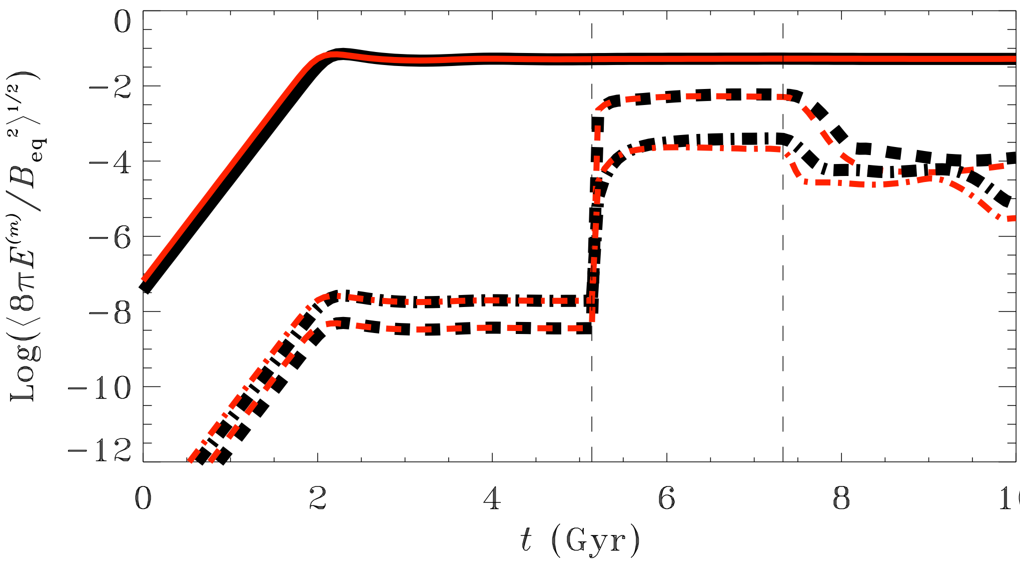

Figure 3.15: Same as Fig. 3.7, but for Model M (transient rigidly rotating spiral). The times at which the α-spiral was turned on and off are indicated by vertical dashed lines.

in the finite τ case.

The possibility of 'mode-switching' in the nonlinear regime has been pointed out by Hubbard et al. (2011). We do not find such solutions in the present framework, but it would be worthwhile to revisit this issue in the context of three-dimensional models which include the galactic halo.

3.5 Magnetic response to transient spiral patterns

3.5.1 A rigidly rotating spiral pattern

As galactic spiral patterns may be transient in nature, we now explore, in Model M, how the magnetic field responds to sudden changes in the spiral forcing. The runs are identical to Model B (axisymmetric disc) up until the α-spiral is turned on, at the time $t_{\mathrm{on}} = 5.1\,\mathrm{Gyr}$, when the dynamo is already in its nonlinear phase. Subsequently, the parameters of the model are identical to those of Model E (standard spiral forcing) up until the time $t_{\mathrm{off}} = 7.3\,\mathrm{Gyr}$, when the spiral modulation of α is turned off.

The evolution of the magnetic field strength in each Fourier mode, averaged over the area of the disc, is shown in Fig. 3.15. The $m = 2$ mode, which initially is present solely

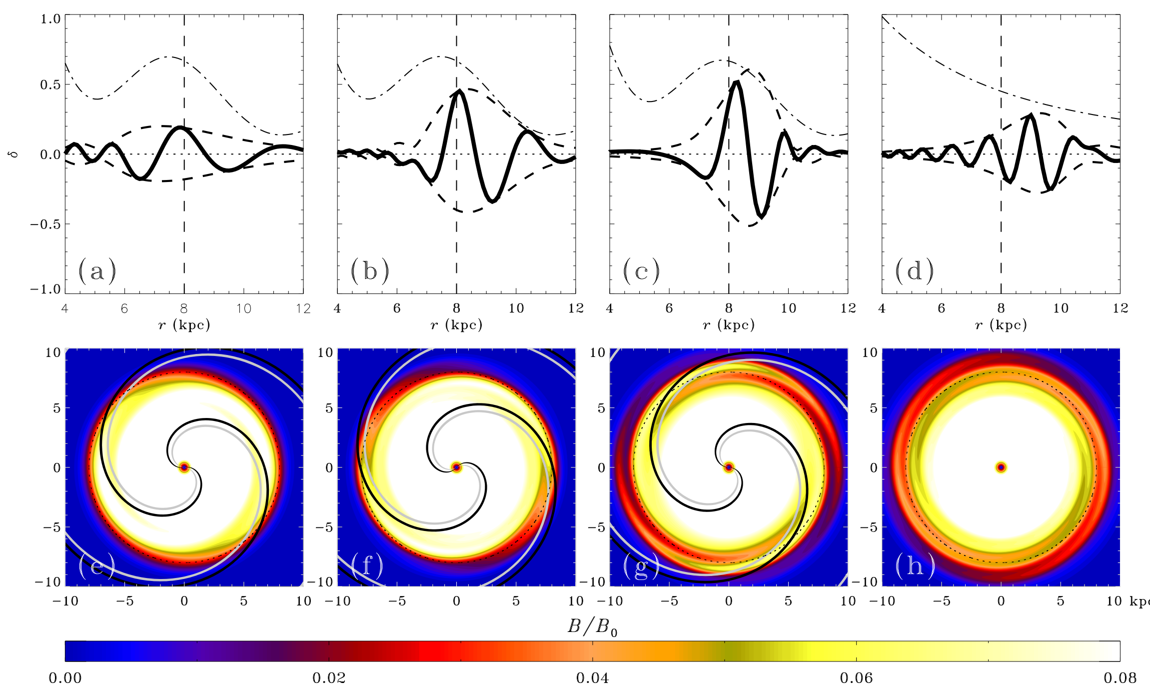

Figure 3.16: Evolution of the magnetic field under the action of a transient, rigidly rotating α-spiral (Model M) for $\tau = l/u$. Each column shows the ratio of non-axisymmetric to axisymmetric part of $\overline{B}_\phi$, as in Fig. 3.8b (top) and magnitude of the field as in Fig. 3.10b (bottom) at the following times after the emergence of the α-spiral: **(a, e)** 0.22 Gyr, **(b, f)** 0.44 Gyr, **(c, g)** 2.2 Gyr, followed by **(d, h)** 0.37 Gyr after the α-spiral is turned off.

because of numerical noise, responds rapidly to the onset of the α-spiral, and then behaves almost exactly as in Model E (compare with Fig. 3.7). In fact, for $\tau = l/u$, magnetic energy in the $m = 2$ part of the mean field slightly exceeds that in Model E before being reduced to the latter. The timescale of the adjustment of the magnetic field, i.e., the time from the onset of the α-spiral, taken for the $m = 2$ part in Model M to grow up to that in Model E, is as short as $\simeq 0.2\,\mathrm{Gyr}$.

Figure 3.16 shows characteristic magnetic configurations for $\tau = l/u$ (the $\tau \to 0$ case is qualitatively similar so only $\tau = l/u$ is shown). After a short period of 0.22 Gyr after the onset of the spiral forcing, the deviation from axial symmetry in the magnetic field is strongest somewhat inside of the corotation circle, (see Fig. 3.16a). This is explained by the dynamo responding more rapidly to sudden changes in the disc at locations where the dynamo number is larger. At $t = t_{\mathrm{on}} + 0.44\,\mathrm{Gyr}$, the non-axisymmetric component of the field has expanded outward in radius, and has become stronger than it was (as compared to the axisymmetric component; panels b and f). This is to be expected since, according to results already discussed, deviations from axisymmetry are most important near the corotation circle. Next, at $t = t_{\mathrm{on}} + 2.2\,\mathrm{Gyr} = t_{\mathrm{off}}$ (Fig. 3.16c and g), the magnetic field has reached nearly the same equilibrium state as in Model E (compare with Figs. 3.9b and 3.10b). After the α-spiral has been switched-off, the magnetic arms remain for a rather long time compared with the time it had taken for them to arise. This can be seen in Figs. 3.16d and h, where we show the field at $t = t_{\mathrm{off}} + 0.37\,\mathrm{Gyr}$. The energy in the $m = 2$ part declines to a quarter of its value at t_{off} within 0.2 Gyr and 0.3 Gyr, respectively, for $\tau \to 0$ and $\tau = l/u$. Therefore, 'ghost' magnetic spiral arms remain after the demise of the material spiral arms, and survive longer when τ is finite. We find an extra delay of about 0.1 Gyr due to the finite τ, larger than the delay $\tau \simeq 0.01\,\mathrm{Gyr}$ that might naively be expected. Similar results were seen in Otmianowska-Mazur et al. (2002) using a quite different model.

3.5.2 A winding-up spiral pattern

The models described so far had a rigidly rotating spiral with a constant pattern speed. As discussed in the introduction, models with a spiral winding up with the differential rotation may be more suitable for some galaxies – in any case rigidly rotating steady spirals and winding-up transient spirals plausibly represent two extreme cases.

We now consider the case of an α-spiral that winds up with the gas. In this model every radius effectively becomes a corotation radius, so based on our results for a rigidly rotating spiral, we would expect the non-axisymmetric part of the magnetic field to be more extended radially, as seen in some observations. In Model N, the field evolves as in Model B

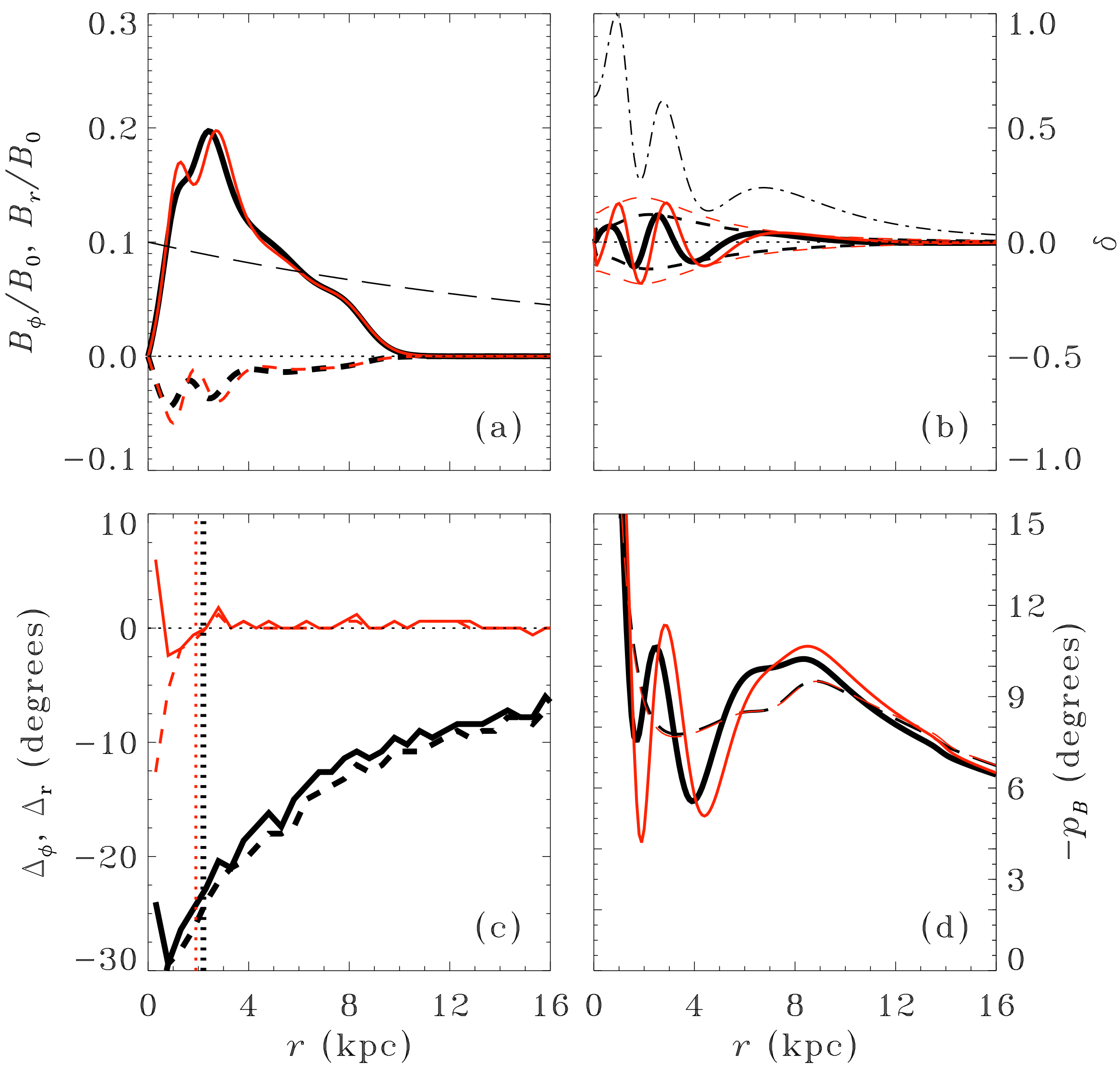

Figure 3.17: Similar to Fig. 3.9, but now for Model N (the α_k-spiral winding up with the gas). The figure shows the field at $0.1t_0 = 73\,\mathrm{Myr}$ after the sudden onset of an α_k bar when the dynamo action has already saturated.

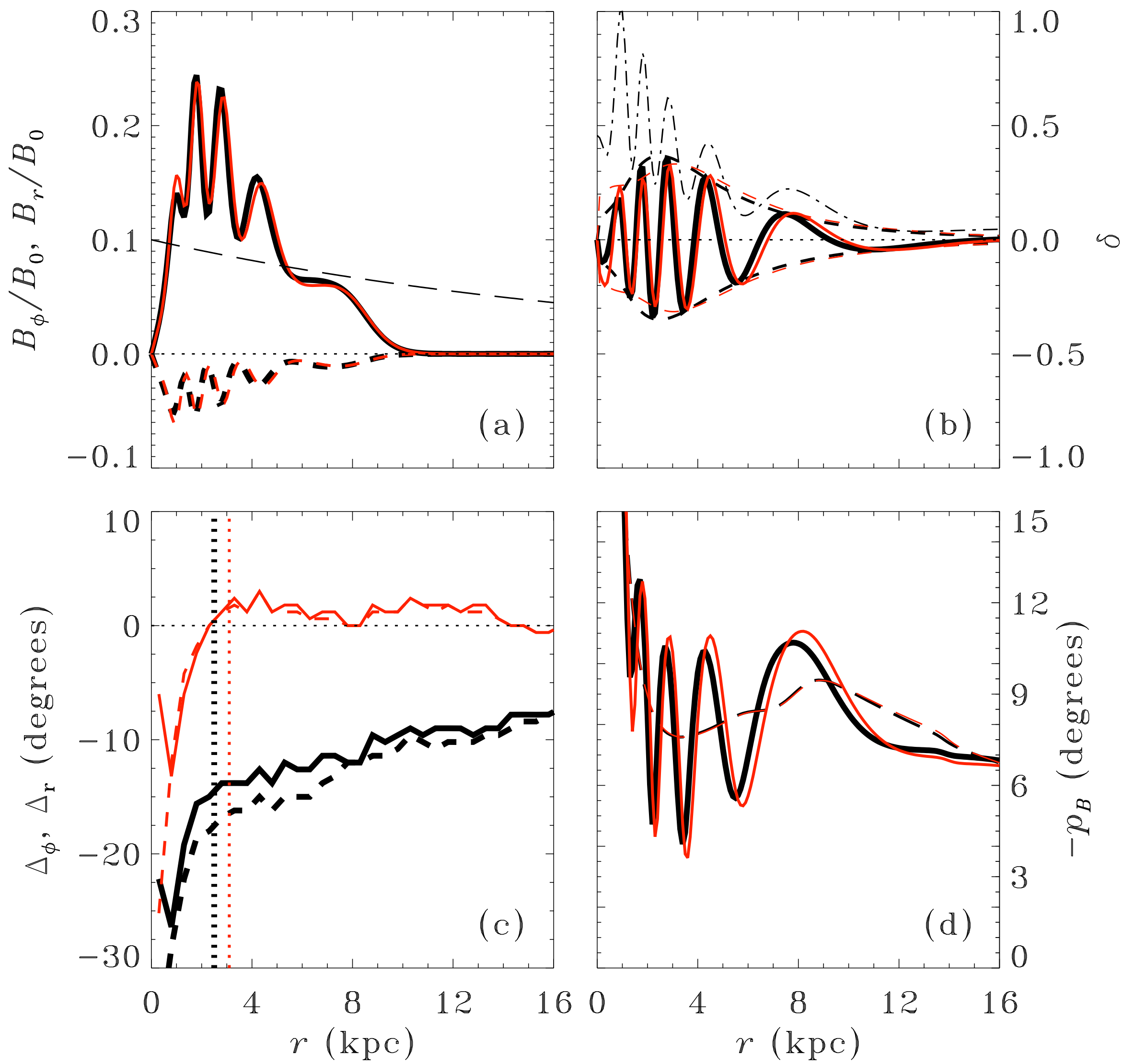

Figure 3.18: Same as Fig. 3.17, but at $0.2t_0 = 146\,\mathrm{Myr}$ after the onset of the α_k bar (which subsequently winds up into a spiral).

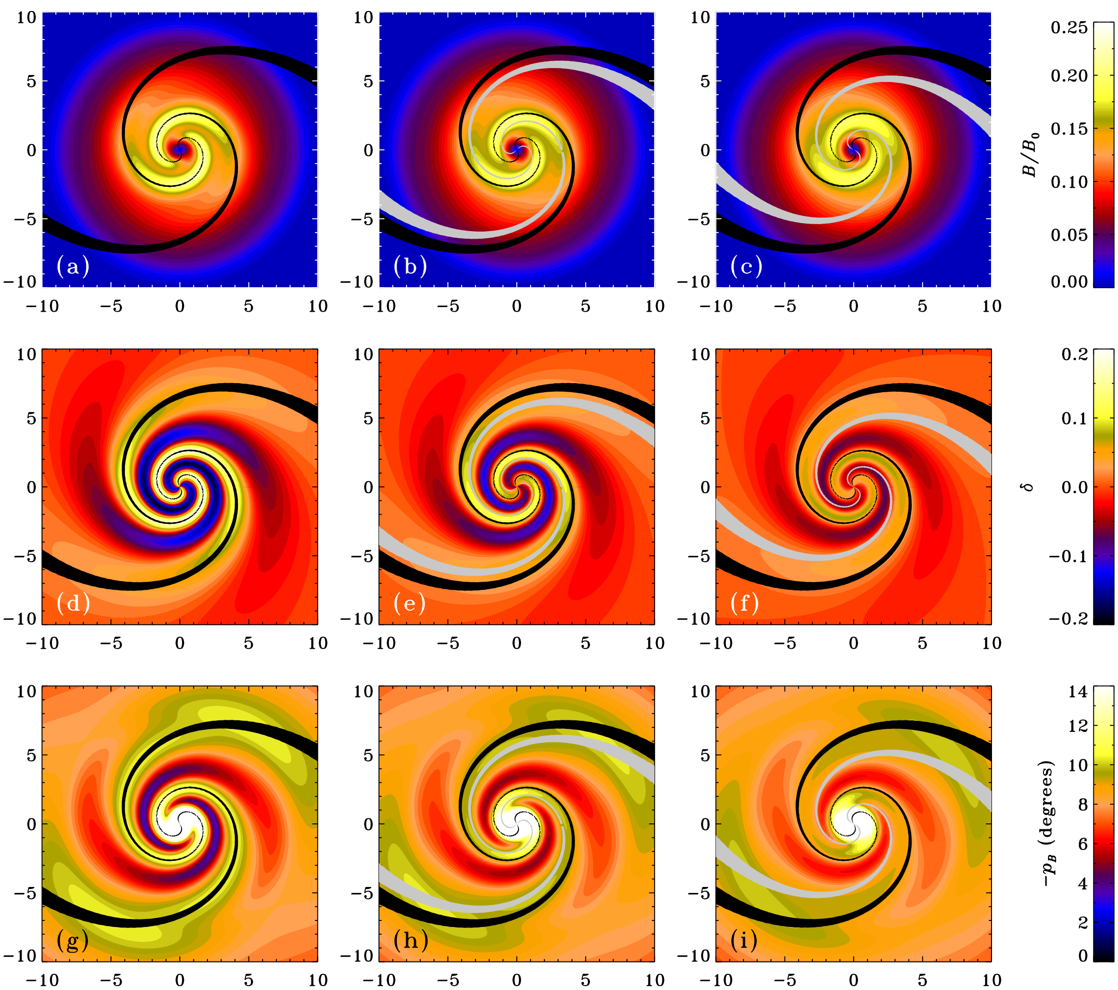

Figure 3.19: Winding-up spiral of Model N. The figure is similar to Fig. 3.10 but now grey spirals represent α_k maxima shifted by $-\Omega\tau$. All panels are snapshots at $0.1t_0 = 73\,\mathrm{Myr}$ after the sudden onset of the α_k 'bar'.

(axisymmetric disc) until the time $t_{\rm on}$. After $t_{\rm on}$ we switch on the $\alpha_{\rm k}$ modulation, but now let the spiral wind up starting from the 'bar' stage ($k = 0$) at $t = t_{\rm on} = 6.6\,{\rm Gyr}$, when the $m = 0$ field is already saturated. We find that strong deviations from axial symmetry in the magnetic field develop during the first $\sim 150\,{\rm Myr}$ after $t_{\rm on}$. In Figs. 3.17 and 3.18 we show the properties of the resulting field at two times, $t = t_{\rm on} + 0.1t_0 = t_{\rm on} + 73\,{\rm Myr}$ and $t_{\rm on} + 0.2t_0 = t_{\rm on} + 146\,{\rm Myr}$, respectively.

As can be seen by comparing panels a and b of Fig. 3.17 ($t = t_{\rm on} + 73\,{\rm Myr}$) and also by comparing panels a and b of Fig. 3.18 ($t = t_{\rm on} + 146\,{\rm Myr}$), the non-axisymmetric and axisymmetric parts of the magnetic field are the strongest at about the same radii, so that the magnetic field is essentially non-axisymmetric. This can also be seen from the 2D plot of Fig. 3.19 ($t = t_{\rm on} + 73\,{\rm Myr}$). In addition, the magnetic spiral arms are extended throughout the disc over a much larger range of radii than with a rigidly rotating spiral pattern (where the non-axisymmetric field concentrates around the corotation circle).

Figures 3.17b and 3.18b show that δ (solid lines) and $\alpha_{\rm k}$ (dash-dotted line) are well-correlated, demonstrating that the dynamo responds rather quickly to the spiral forcing. From Figs. 3.17c and 3.18c, we see that for $\tau \to 0$ the phase difference between the magnetic and material spiral arms is negligible at radii where the magnetic spiral arms are strong. However, for finite $\tau = l/u$, the magnetic arms lag the material ones by a large angle, $\Delta_r \simeq \Delta_\phi \simeq -15^\circ$ to -25° over a range of radius of order 10 kpc. The values vary somewhat with radius and with time. This phase shift is strikingly apparent when comparing panels (a) and (d) of Fig 3.19 for $\tau \to 0$ with, respectively, panels (b) and (e) for $\tau = l/u$. Only in panels (b) and (e) do the yellow-orange regions of high field strength lag the black centres of the α-spiral arms by a significant amount but overlap with the grey spiral phase-shifted by the angle $-\Omega\tau$.

As might be expected, the phase shift is larger for $\tau = 2l/u$ (-20° to -30°), as can be seen from the third column of Fig. 3.19 (but not as large as $2\Omega l/u$). However, as τ is increased, the non-axisymmetric part of the magnetic field tends to weaken, as the spreading of the response of the dynamo in time due to the finite dynamo relaxation time is translated into an effective blurring of the α-spiral in space (the effect is most evident when comparing panels d–f of Fig. 3.19). When the advective flux is replaced by a diffusive flux with $\kappa = 0.3\eta_{\rm t}$, we find almost identical results, save for the fact that the strength of the field is larger by about 75%.

This model, which incorporates a spiral pattern that seems to wind up with the differentially rotating gas, along with a dynamo relaxation time $\tau \gtrsim l/u$, seems to be the most successful, among the models explored in the present chapter, at explaining the large phase shifts between magnetic and material arms, roughly constant over a large radial range, observed in some galaxies, such as NGC 6946.

3.6 Discussion and conclusions

We have presented a set of models of the mean-field galactic dynamo action that include: (i) dynamo forcing by stationary and transient spiral structure, (ii) time delay in the response of the mean electromotive force to changes in the mean magnetic field and small-scale turbulence (finite relaxation time τ), and (iii) dynamo nonlinearity based on magnetic helicity balance.

Whilst some aspects of (i) have been explored earlier in simpler galactic dynamo models, the latter two features present significant generalizations of the galactic dynamo theory which, we believe, make it more realistic and physically appealing. In particular, (ii) affects the mathematical nature of the mean-field dynamo equation, which now has the form of the telegraph equation admitting diffusive wave-like solutions. Solutions presented here do not have any pronounced wave-like properties, but this does not preclude that such solutions of the generalized dynamo equation do exist. Feature (iii) incorporates a physically justifiable form of nonlinearity into galactic dynamo equations (in the form of advective or diffusive helicity fluxes), thus making our solutions significantly more realistic than those explored earlier.

Within this framework, we explore the behaviour of the mean magnetic field in both axisymmetric and non-axisymmetric galactic discs. A novel aspect of the work contained in this chapter is the introduction of a finite relaxation time into the galactic mean-field theory and a detailed exploration of its effects, particularly on the non-axisymmetric dynamo modes. We discuss how the imprints of the galactic spiral pattern on the morphology of the mean magnetic field are affected by the finite relaxation time of the dynamo. Unlike many earlier studies of galactic dynamos, we approach these problems from the evolutionary viewpoint and consider the magnetic response to both steady and transient spiral patterns, and briefly discuss the diverse ways in which galactic spiral arms can affect the dynamo action.

We have confirmed, in the new framework, earlier results on the evolution of axisymmetric magnetic fields in axisymmetric discs, including the spreading of magnetic fronts along radius and the occurrence of reversals. As expected, the magnetic field is able to spread radially to encompass the whole disc within the galactic lifetime, as long as the magnetic helicity flux is sufficient. What is new is that in the absence of any helicity flux, contracting and expanding rings of magnetic field, emanating from the region where the magnitude of the dynamo number is largest, can propagate for several Gyr in the nonlinear regime. This is due to the variation along radius of the time taken for the magnetic field to reach saturation.

The lifetimes of reversals in the galactic disc have been known to be sensitive to the details of the galactic rotation curve, the geometric shape of the gas layer, details of the turbulent energy distribution in the galaxy, etc. We have added another important parameter to this list, the dynamo relaxation time. We also find that such reversals can have non-trivial effects on the morphology of non-axisymmetric magnetic structures in a non-axisymmetric disc. It would be interesting to carry out a more detailed study of magnetic fronts and the possibility of long-lived reversals in the context of the above framework.

We have also shown that it is difficult to maintain non-axisymmetric magnetic structures in an axisymmetric disc, which leaves one little choice but to try to explain such structures as arising from a non-axisymmetric disc. Most of our effort was then directed to the response of the mean magnetic field to the galactic spiral pattern. The focus in this part of our work is the nature of the so-called magnetic arms, spiral-shaped regions of enhanced regular magnetic field (traced by polarised radio emission and Faraday rotation) that are located in between the gaseous and stellar spiral arms in some galaxies (e.g., NGC 6946 and IC 342) but can overlap with or cross the material arms in other galaxies (e.g., M51). We model the effect of the spiral pattern on the dynamo by assuming that the α effect or the galactic/fountain outflow or the equipartition field are enhanced within the spiral arms. A non-axisymmetric α effect, in particular, does lead to strong magnetic arms.

When the dynamo relaxation time $\tau \to 0$, the magnetic and material arms almost coincide at corotation, as expected from earlier work (Mestel & Subramanian, 1991; Subramanian & Mestel, 1993; Moss, 1996). However, a finite relaxation time causes a significant azimuthal lag between the magnetic and material arms at the radius where the magnetic arms are strongest (near corotation). In this respect, our model can explain a wider range of observations than earlier models. However, we concur with the earlier authors in that the non-axisymmetric parts of the mean magnetic field driven by the spiral pattern are mainly localised around the corotation radius, extending about 4 kpc in radius. The radial extent is, of course, model-dependent and can be larger in regions with weaker rotational velocity shear.

The corotation radius is also approximately where each magnetic arm crosses the corresponding material arm, going from leading (with respect to the direction of the galactic rotation) the material arm inside the corotation circle to trailing it outside the corotation. The primary effect of the finite relaxation time, in the case of a steady, rigidly rotating spiral pattern, is to suppress the leading part of the magnetic spiral arms and to enhance, and extend azimuthally, the trailing part. Thus, this effect produces a prominent ‘tail’ of large-scale magnetic field in between the material arms. This is even more true when the number of arms is increased from two, to say, four.

The magnetic arms of the spiral galaxy NGC 6946 are ‘interlaced with’ (in between) the material arms (Beck & Hoernes, 1996; Beck, 2007), and have been called ‘phase-shifted images’ of the preceding (in the sense of the rotation) material arms (Frick et al., 2000). Although the implied phase shifts are more constant with radius than in our model, we have obtained a shift of approximately the same magnitude (30°–40°) and in the right direction. More generally, the shift is of order $\Omega_\mathrm{p}\tau$, where Ω_p is the pattern angular velocity of the material spiral. Larger values of τ thus lead to larger phase shifts. This is caused by the delay in the α effect of order τ, so that by the time the dynamo has had the chance to respond to the enhancement in α along the material arm, the arm has already rotated by an angle $\approx \Omega_\mathrm{p}\tau$.

Spiral density waves may be transient and we consider how quickly the regular magnetic field can respond to changes in the galactic spiral structure. We find that the response time is small. On the other hand, we find that magnetic spiral arms survive for several hundred Myr following the destruction of the material spiral arms in the dynamo nonlinear regime. Moreover, a finite dynamo relaxation time is found to significantly prolong the life of such lingering magnetic arms. This opens the intriguing possibility of ‘ghost’ magnetic arms, which were produced by material arms that have since disappeared.

Despite the wide range of models considered, our success in reproducing magnetic arms interlaced with the material arms as perfectly as it is believed to happen in NGC 6946 is admittedly limited in models assuming forcing of the dynamo by a steady, rigidly rotating spiral. In addition, this type of spiral forcing leads to magnetic arms concentrated over a smaller range in radius than is observed in many galaxies. Another possibility, rendered more likely by several recent studies (e.g. Dobbs et al., 2010; Sellwood, 2011; Quillen et al., 2011), is that the spiral patterns of many galaxies, rather than being rigidly rotating, as is usually assumed in galactic dynamo models, in fact wind up (at least to some extent). This may happen if, for instance, there are interfering two and three-armed spirals rotating at different angular frequencies (Chapter 5). The two-arm grand design spiral pattern of the galaxy M51 (NGC 5194), thought to be caused by tidal forcing by its neighbour, NGC 5195, is also found to wind up in detailed N-body simulations that are able to accurately reproduce its spiral morphology (Dobbs et al., 2010).

With these recent advances in spiral structure theory in mind, we also investigated the opposite extreme to rigidly rotating patterns: material arms that are wound up by the galactic differential rotation. The nonlinear dynamo responds very quickly to such forcing, and for vanishing dynamo relaxation time the mean magnetic field more or less traces the spiral arms over a large range in radius (as seen in many observations) and winds up with them. On the other hand, for finite dynamo relaxation time there is a large azimuthal lag of each magnetic spiral arm compared to the corresponding material arm over a large range in radius. Magnetic arms trail the material arms by 15°–25° (for $\tau = l/u$), varying somewhat with time and radius over the disc. This shift is of order $\Omega\tau$, where Ω is the angular velocity of the gas, and we have shown that larger, but still plausible, values of τ, lead to even larger phase shifts. Increasing the number of spiral arms also causes the (equal number of) magnetic arms to be located closer to the centres of the inter-arm regions, so that they may be described as interlaced with the material arms. Therefore, allowing for the possibility of the spiral winding up can drastically improve agreement with observations of the regular magnetic fields in some galaxies, but with the trade-off that the magnetic arms (that in this model, either trace or interlace the material arms) are almost as short-lived as the spiral patterns that presumably generate them.

In summary, we have incorporated into galactic dynamo theory several well-studied physical effects not previously considered, namely (i) non-locality in time and (ii) forcing by both spiral arms which steadily rotate and those which wind up due to differential rotation. This allows several observed features of magnetic arms to be more naturally reproduced. Particularly interesting are the models we have presented in which magnetic arms extend over a large range of radii and either trace material arms over several kpc, or else are phase-shifted images of material arms, trailing them in the sense of the galactic rotation.

The numerical solutions of non-axisymmetric galactic dynamo models presented in this chapter have brought into light certain new features of large-scale galactic magnetic fields. However, in order to understand such numerical solutions and the underlying dynamo mechanism as completely as possible, asymptotic solutions, though generally more approximate, are indispensible. This echoes the spirit of Chapter 2, where simple (local in r and ϕ) numerical and asymptotic solutions were presented and compared. Therefore, in the next chapter we turn to a study of asymptotic solutions of global, non-axisymmetric galactic dynamos.

Chapter 4

Galactic spirals and dynamo action: Asymptotic solutions

4.1 Introduction

We saw in the last chapter that magnetic arms, seen in disc galaxies, cannot be accounted for if the underlying disc is assumed to be axisymmetric, and they appear to be related (though in a non-trivial way) to the material (gaseous) spiral arms (Frick et al., 2000). Hence the need to develop a theory which relates the non-axisymmetry of the regular magnetic field to that of the underlying disc. This was the general aim of Chapter 3, where we approached the problem from a numerical standpoint and considered not only the linear growth of the field (kinematic regime) but also the non-linear saturation phase. Here we take an analytical approach and therefore restrict the investigation mostly to the kinematic regime, although a nonlinear extension is also suggested. We are motivated, in part, by insights that were provided by analytical treatments in the past (Ruzmaikin et al. 1988, for the axisymmetric case and Mestel & Subramanian 1991, for the non-axisymmetric case). The latter work was focused on how the $|m| = 1$ (bisymmetric) azimuthal modes can be generated in a galactic disc with a two-arm spiral pattern. Numerical models (e.g. Moss 1998; Rohde et al. 1999; Chapter 3 above) showed, however, that $m = 0$ (axisymmetric) and $|m| = 2$ (quadrisymmetric) modes tend to be more prevalent in such discs (or $m = 0$ and $|m| = n$ for discs with n spiral arms). An analytical model that can explain such modes is therefore needed.

Our aim in this chapter is to develop a systematic interpretation of the key numerical results of Chapter 3 by solving suitably simplified but essentially the same mean-field dynamo equations with an approximate semi-analytical method. Here we consider both axially symmetric and enslaved non-axisymmetric modes of a kinematic dynamo. The enslaved modes are those that have the same growth rate as the leading axisymmetric mode; they occur because of deviations of the galactic disc from axial symmetry, e.g., due to a spiral pattern in the interstellar gas. For a two-armed spiral, the enslaved modes include the $|m| = 2$ components that corotate with the spiral pattern, as well as other, weaker, even-m corotating modes. We leave the $|m| = 1$ modes and other odd-m corotating modes for a future work. Our model differs from earlier analytical study of Mestel & Subramanian (1991) in that here we:

(i) provide an asymptotic treatment of the $m = 0$ and even-m modes forced by a rigidly rotating two-arm spiral;

(ii) incorporate the minimal-τ approximation (MTA) and explore the effects of a finite dynamo relaxation time.

The plan of the chapter is as follows. In Section 4.2, we present an asymptotic solution for the axisymmetric and enslaved non-axisymmetric magnetic modes which inhabit a disc containing a global, steady, rigidly rotating spiral density wave. We then compare our results with numerical solutions in Section 4.3, including the saturated states. Conclusions and discussion for both Chapter 3 and this chapter can be found in Sections 4.4 and 4.5.

4.2 Asymptotic solutions for galactic dynamos

Many disc galaxies have a spiral structure which causes deviations from axial symmetry in both turbulent and regular gas flows, leading to non-axisymmetric magnetic fields. Here we follow Mestel & Subramanian (1991) by assuming that the α effect is modulated by the spiral pattern. The nature of such a modulation is largely unexplored (Shukurov, 1998; Shukurov & Sokoloff, 1998), but it is reasonable to assume that α is enhanced along a spiral perhaps overlapping with the gas spiral. The spiral patterns observed in the light of young stars are believed to represent a global density wave rotating at a fixed angular frequency, or possibly a superposition of such waves, with differing azimuthal symmetries and angular frequencies (e.g. Comparetta & Quillen, 2012; Roškar et al., 2012). At least in some galaxies, they can be transient features (e.g. Dobbs et al., 2010; Sellwood, 2011; Quillen et al., 2011; Wada et al., 2011; Grand et al., 2012) whose effect on the mean-field dynamo is discussed in the previous chapter, and also in Chapter 5 and its accompanying appendix (Appendix 5.4). In this chapter, we consider an enduring spiral with n arms and a constant pattern speed $\Omega_{\rm p}$.

4.2.1 Basic equations

Since we are interested in non-axisymmetric magnetic fields that corotate with the spiral pattern, it is preferable to work in the corotating frame where the dynamo forcing is independent of time. Following Mestel & Subramanian (1991), we carry out a coordinate transformation from the inertial cylindrical frame $\Sigma = (r, \phi, z, t)$ (with disc rotation axis as the z-axis) to the frame $\widetilde{\Sigma} = (\widetilde{r}, \widetilde{\phi}, \widetilde{z}, \widetilde{t})$ rotating with the pattern angular velocity Ω_p (assumed constant in both time and position):

$$\begin{gathered}\widetilde{\phi} = \phi - \Omega_\mathrm{p} t, \quad \widetilde{r} = r, \quad \widetilde{z} = z, \quad \widetilde{t} = t, \\ \widetilde{\overline{B}}_r = \overline{B}_r, \quad \widetilde{\overline{B}}_\phi = \overline{B}_\phi, \quad \widetilde{\overline{B}}_z = \overline{B}_z. \end{gathered} \tag{4.1}$$

so that

$$\left(\frac{\partial}{\partial \phi}\right)_t = \left(\frac{\partial}{\partial \widetilde{\phi}}\right)_{\widetilde{t}}, \quad \left(\frac{\partial}{\partial t}\right)_\phi = \left(\frac{\partial}{\partial \widetilde{t}}\right)_{\widetilde{\phi}} - \Omega_\mathrm{p}\left(\frac{\partial}{\partial \widetilde{\phi}}\right)_{\widetilde{t}}. \tag{4.2}$$

The coordinate transformation shifts the mean velocity, $\widetilde{\overline{U}}_\phi = \overline{U}_\phi - r\Omega_\mathrm{p}$, but the random velocity is left unchanged, $\widetilde{\boldsymbol{u}} = \boldsymbol{u}$, as are both the mean and random magnetic fields. Therefore, $\widetilde{\alpha} = \alpha$ and $\widetilde{\eta}_\mathrm{t} = \eta_\mathrm{t}$.

We use the thin-disc approximation, $\partial/\partial z \gg \partial/\partial r$ and, eventually, consider tightly wound magnetic spirals, $\partial/\partial r \gg r^{-1}\partial/\partial\phi$. Thus, we consider magnetic fields whose radial scale is asymptotically intermediate between the scale height of the galactic disc (of order 0.5 kpc) and its radial scale length (of order 10 kpc). We also adopt the $\alpha\Omega$-dynamo approximation where the rate of production of the azimuthal magnetic field by the α effect is negligible in comparison with the effect of the differential rotation. The mean velocity field is taken to be axisymmetric, purely azimuthal, and constant in time,

$$\overline{\boldsymbol{U}} = r\Omega(r)\widehat{\boldsymbol{\phi}}, \tag{4.3}$$

where $\widehat{\boldsymbol{\phi}}$ is the unit azimuthal vector. In the rotating frame, the gas angular velocity is $\widetilde{\Omega}(r) = \Omega(r) - \Omega_\mathrm{p}$. The magnitude of the rotational velocity shear is quantified with $G(r) = r\mathrm{d}\Omega/\mathrm{d}r = r\mathrm{d}\widetilde{\Omega}/\mathrm{d}r$. Applying equations (4.1) and (4.2) to the r- and ϕ-components of equation (1.22), and dropping tildes for ease of notation (except for on $\widetilde{\Omega}$), leads to the following equations in the corotating frame:

$$\widehat{\mathcal{L}}\,\overline{B}_r = -c_\tau \frac{\partial}{\partial z}(\alpha \overline{B}_\phi) + c_\tau \eta_{\rm t} \left(\widetilde{\nabla}^2 \overline{B}_r + \frac{1}{r^2}\frac{\partial^2 \overline{B}_r}{\partial \phi^2} - \frac{2}{r^2}\frac{\partial \overline{B}_\phi}{\partial \phi} \right), \qquad (4.4)$$

$$\widehat{\mathcal{L}}\,\overline{B}_\phi = \left(1 + \tau\frac{\partial}{\partial t} - \Omega_{\rm p}\tau\frac{\partial}{\partial \phi}\right)(G\overline{B}_r) + c_\tau \eta_{\rm t} \left(\widetilde{\nabla}^2 \overline{B}_\phi + \frac{1}{r^2}\frac{\partial^2 \overline{B}_\phi}{\partial \phi^2} + \frac{2}{r^2}\frac{\partial \overline{B}_r}{\partial \phi} \right), \qquad (4.5)$$

where

$$\widehat{\mathcal{L}} = \left(1 + \tau\frac{\partial}{\partial t} - \Omega_{\rm p}\tau\frac{\partial}{\partial \phi}\right)\left(\frac{\partial}{\partial t} + \widetilde{\Omega}\frac{\partial}{\partial \phi}\right)$$

and

$$\widetilde{\nabla}^2 X = \frac{\partial^2 X}{\partial z^2} + \frac{\partial}{\partial r}\left[\frac{1}{r}\frac{\partial}{\partial r}(rX)\right].$$

These equations agree with equations (2.2) and (2.3) of Mestel & Subramanian (1991) in the limit $\tau \to 0$ with $c_\tau = 1$. Since, in the thin-disc approximation, both equations do not include $\overline{B}_z$, the equation for $\overline{B}_z$ can be replaced by the solenoidality condition,

$$\frac{1}{r}\frac{\partial}{\partial r}(r\overline{B}_r) + \frac{1}{r}\frac{\partial \overline{B}_\phi}{\partial \phi} + \frac{\partial \overline{B}_z}{\partial z} = 0. \qquad (4.6)$$

We emphasize that the governing equations acquire additional terms when transformed to the rotating frame whenever τ is finite. On the contrary, the standard mean-field dynamo equation (1.23) does not change form under the transformation to a rotating frame. This can be understood physically in the following way. In the standard theory, $\boldsymbol{\mathcal{E}}$ at time t_0 and position $\mathbf{x}$ depends on $\overline{\boldsymbol{B}}$ and the turbulence parameters at the same time and position. This is not true in the MTA, where $\boldsymbol{\mathcal{E}}(t_0, \mathbf{x})$ depends on the history of $\overline{\boldsymbol{B}}(t, \mathbf{x})$, $\widetilde{\alpha}$ and $\widetilde{\eta}_{\rm t}$ over, roughly, $t_0 - \tau < t \le t_0$. [Here $\widetilde{\alpha}$ and $\widetilde{\eta}_{\rm t}$ refer to the more general version of equation (1.21), wherein we have made the standard assumption $\widetilde{\alpha} \approx \alpha/\tau_{\rm c}$, $\widetilde{\eta}_{\rm t} \approx \eta_{\rm t}/\tau_{\rm c}$ (Brandenburg & Subramanian, 2005a).] Thus, $\boldsymbol{\mathcal{E}}(t_0, \mathbf{x})$ is affected by how fast variations in the field and (α, $\eta_{\rm t}$) are sweeping past the position $\mathbf{x}$.

4.2.2 Approximate solution

When the coefficients of equations (4.4) and (4.5) depend on the azimuthal angle ϕ as $\exp(im\phi)$ with certain m, their solutions can be represented in the form

$$\begin{pmatrix} \overline{B}_r \\ \overline{B}_\phi \end{pmatrix} = \sum_{m=-\infty}^{\infty} \begin{pmatrix} a_m(r,z) \\ b_m(r,z) \end{pmatrix} \exp\left(im\phi + \Gamma t\right), \qquad (4.7)$$

so that equations (4.4) and (4.5) reduce to

$$\sum_{m=-\infty}^{\infty} \mathrm{e}^{im\phi}\left[\mathcal{L}a_m + c_\tau \frac{\partial}{\partial z}(\alpha b_m) - c_\tau \eta_\mathrm{t}\left(\widetilde{\nabla}^2 a_m - m^2\frac{a_m}{r^2} - 2im\frac{b_m}{r^2}\right)\right] = 0, \tag{4.8}$$

$$\mathcal{L}b_m - (1+\Gamma\tau - im\Omega_\mathrm{p}\tau)Ga_m - c_\tau\eta_\mathrm{t}\left(\widetilde{\nabla}^2 b_m - m^2\frac{b_m}{r^2} + 2im\frac{a_m}{r^2}\right) = 0, \tag{4.9}$$

where

$$\mathcal{L} = (1+\Gamma\tau - im\Omega_\mathrm{p}\tau)(\Gamma + im\widetilde{\Omega}).$$

We note that α is, in general, a function of r, ϕ and z, whereas Ω and G are assumed to be functions of r alone. When obtaining equation (4.9) from equation (4.5), the summation can be dropped because the only ϕ-dependence that occurs in this equation is in the common factor $\exp(im\phi)$, whereas α depends on ϕ in equation (4.8).

To make further progress, we model α as an n-armed, rigidly rotating global spiral (thus, in the rotating frame it is time-independent),

$$\alpha = \alpha_0[1 + \epsilon_\alpha \cos(n\phi - \kappa r)] \equiv \alpha_0 + \alpha_n \mathrm{e}^{in\phi} + \alpha_{-n}\mathrm{e}^{-in\phi}, \tag{4.10}$$

where

$$\alpha_n = \tfrac{1}{2}\alpha_0\epsilon_\alpha \mathrm{e}^{-i\kappa r}, \quad \alpha_{-n} = \tfrac{1}{2}\alpha_0\epsilon_\alpha \mathrm{e}^{i\kappa r} = \alpha_n^*, \tag{4.11}$$

where α_0 may depend on r and z, and asterisk denotes complex conjugate. With this convention, $\kappa < 0$ describes a trailing Archimedean spiral. We choose an Archimedean rather than a logarithmic spiral in order to simplify the calculations; this choice does not affect our conclusions. The requirement that each coefficient of equation (4.8) vanishes gives

$$\mathcal{L}a_m - c_\tau\eta_\mathrm{t}\left(\widetilde{\nabla}^2 a_m - m^2\frac{a_m}{r^2} - 2im\frac{b_m}{r^2}\right) = -c_\tau\frac{\partial}{\partial z}(\alpha_0 b_m + \alpha_n b_{m-n} + \alpha_{-n}b_{m+n}). \tag{4.12}$$

This implies that components with $m = ..., -2n, -n, 0, n, 2n, ...$ are coupled to each other, and likewise components with $m = ..., -2n+1, -n+1, 1, n+1, 2n+1, ...$, etc. However, these sets of components are decoupled from one another. Components that are coupled to the generally dominant $m = 0$ components grow along with it, and are thus called 'enslaved' components. One naturally expects the lowest-order enslaved components of order n to dominate the higher-order enslaved components, as the former are forced directly. This was in fact borne out in the numerical work of Chapter 3. Therefore, the $m = \pm n$ components will be the dominant non-axisymmetric components for a galaxy with an enslaved n-armed spiral pattern.

Taking $n = 2$ (a two-armed α-spiral), Mestel & Subramanian (1991) truncated the series of coupled equations by neglecting $|m| \geq 3$. Thus, only the $m = \pm 1$ are coupled and likewise $m = 0$ is coupled to $m = \pm 2$. Here we truncate the series in the same way; the numerical solutions of Chapter 3 confirm that this is an excellent approximation for much of the parameter space. The case of $m = \pm 1$ has already been considered in Mestel & Subramanian (1991). Thus, we focus on the $m = 0, \pm 2$ case here, for which the governing equations are

$$(1+\Gamma\tau)\Gamma a_0 - c_\tau \eta_{\rm t} \widetilde{\nabla}^2 a_0 = -c_\tau \frac{\partial}{\partial z}(\alpha_0 b_0 + \alpha_2 b_{-2} + \alpha_{-2} b_2), \tag{4.13}$$

$$(1+\Gamma\tau)\Gamma b_0 - c_\tau \eta_{\rm t} \widetilde{\nabla}^2 b_0 = (1+\Gamma\tau) G a_0, \tag{4.14}$$

while, for $m = \pm 2$ and $n = 2$,

$$L a_{\pm 2} - c_\tau \eta_{\rm t} \left(\widetilde{\nabla}^2 a_{\pm 2} - 4\frac{a_{\pm 2}}{r^2} \mp 4i \frac{b_{\pm 2}}{r^2} \right) = -c_\tau \frac{\partial}{\partial z}(\alpha_0 b_{\pm 2} + \alpha_{\pm 2} b_0), \tag{4.15}$$

$$L b_{\pm 2} - c_\tau \eta_{\rm t} \left(\widetilde{\nabla}^2 b_{\pm 2} - 4\frac{b_{\pm 2}}{r^2} \pm 4i \frac{a_{\pm 2}}{r^2} \right) = (1+\Gamma\tau \mp 2i\Omega_{\rm p}\tau) G a_{\pm 2}, \tag{4.16}$$

where

$$L = (1+\Gamma\tau \mp 2i\Omega_{\rm p}\tau)(\Gamma \pm 2i\widetilde{\Omega}).$$

Physical effects caused by a finite τ

Already at this stage it is possible to explain the key effects that a finite τ has on non-axisymmetric dynamo modes. In Chapter 3 we saw that for models with $\tau = l/u$ and a rigidly rotating $\alpha_{\rm k}$ spiral, azimuthal maxima in the large-scale magnetic field were phase-shifted by an angle $\sim -(25-40)^\circ$, with the negative sign meaning a shift opposite in direction to the galactic rotation. This is comparable in magnitude to, but somewhat larger than $\Omega_{\rm p}\tau = 18^\circ$. Such phase shifts can be understood by interpreting the above analytical expressions. First, consider equations (4.8) and (4.9), after having divided through by $1+\Gamma\tau - im\Omega_{\rm p}\tau$, and simplifying:

$$\sum_{m=-\infty}^{\infty} \mathrm{e}^{im\phi} \Bigg\{ (\Gamma + im\widetilde{\Omega}) a_m + \frac{\mathrm{e}^{-i\delta_m}}{C_{|m|}} \left[\frac{\partial}{\partial z}(\alpha_{\rm k} b_m) - \eta_{\rm t} \left(\widetilde{\nabla}^2 a_m - m^2 \frac{a_m}{r^2} - 2im\frac{b_m}{r^2} \right) \right] \Bigg\} = 0, \tag{4.17}$$

$$(\Gamma + im\widetilde{\Omega})b_m - Ga_m - \frac{\mathrm{e}^{-i\delta_m}}{C_{|m|}}\eta_\mathrm{t}\left(\widetilde{\nabla}^2 b_m - m^2\frac{b_m}{r^2} + 2im\frac{a_m}{r^2}\right) = 0, \tag{4.18}$$

where

$$C_{|m|} \equiv \left[(1+\Gamma\tau)^2 + (m\Omega_\mathrm{p}\tau)^2\right]^{1/2}, \qquad \cos\delta_m = \frac{1+\Gamma\tau}{C_{|m|}}, \qquad \sin\delta_m = -\frac{m\Omega_\mathrm{p}\tau}{C_{|m|}}.$$

Note that α_k gets multiplied by the phase factor $\mathrm{e}^{-i\delta_m}$ in equation (4.17). Now, looking at equation (4.12), we see that the α_n term is significant for $m > 0$, while the α_{-n} term is significant for $m < 0$, where n is the number of arms in the α_k spiral. Thus, the τ effect effectively causes $\alpha_n \to \mathrm{e}^{-i\delta_{|m|}}\alpha_n$ and $\alpha_{-n} \to \mathrm{e}^{i\delta_{|m|}}\alpha_{-n}$, since $\delta_{-m} = -\delta_m$. This effectively produces a transformation $\phi \to \phi - \delta_{|m|}/n$ in equation (4.10). The azimuthal maxima of α_k are thus shifted by the angle $\delta_{|m|}/n$. We then expect the magnetic field to be a maximum where α_k is effectively a maximum, which implies that a similar phase shift occurs for the magnetic arms. The dominant (directly forced) components have $|m| = n$. In galaxies, $\Gamma\tau \ll 1$ and typical values are $n = 2$ and $\Omega_\mathrm{p}\tau = 0.3$, which implies a phase shift $\sim \arctan(-n\Omega_\mathrm{p}\tau)/n \sim -15°$. Note that the magnitude of the phase shift decreases slightly as n increases, in qualitative agreement with the numerical solutions (compare results for models E and L of Chapter 3). Note also that the phase of η_t gets similarly affected, so if η_t is chosen to be modulated along a spiral rather than α_k, one would expect similar phase shifts. The fact that phase shifts are somewhat larger in magnitude than $\Omega_\mathrm{p}\tau$ in the numerical solutions is attributable to higher order enslaved non-axisymmetric components with $|m| > n$, as also discussed in Section 4.3.1 below. This can be seen by estimating the phase shifts for these modes, $|m| = 2n = 4$, $|m| = 3n = 6$, $|m| = 4n = 8$, etc. For the first three such modes the phase shifts are $\sim \arctan(-2n\Omega_\mathrm{p}\tau)/n \sim -25°$, $\sim \arctan(-3n\Omega_\mathrm{p}\tau)/n \sim -30°$ and $\sim \arctan(-4n\Omega_\mathrm{p}\tau)/n \sim -34°$. Thus, the net shift of the magnetic arm, which is comprised of all enslaved non-axisymmetric components, is significantly larger than those of the $|m| = n$ components alone. This is not the whole story, however, because these higher order components are rather weak compared to the $|m| = n$ components for the $\tau \to 0$ solutions, and so the $|m| = n$ components would be expected to dominate. In fact, the enslaved components with $|m| > n$ are enhanced by the τ effect, with the enhancement being larger for larger $|m|$, as we now explain.

Aside from producing significant phase shifts, the temporal non-locality also affects the strengths of magnetic arms, perhaps best measured by the amplitudes of the enslaved non-axisymmetric components as compared to that of the dominant axisymmetric component. In most of the spiral models explored in the previous chapter and in subsequent chapters, the τ effect causes the amplitudes of non-axisymmetric components to increase–why should this be so? It is evident from equations (4.17) and (4.18) that the magnitudes of α_k and η_t are effectively reduced by the factor $C_{|m|}$, while that of G is unaffected. Physically, the α_k and η_t effects in the magnetic arms, where the mean field is largest, are acting on a mean field that is effectively being averaged over the azimuth $\phi \to \phi - \Omega_\mathrm{p}\tau$, and is thus weaker than the local mean field. Since, according to equation (2.7) the dynamo number $D \propto \alpha_\mathrm{k} G/\eta_\mathrm{t}^2$, this results in an enhancement of the dynamo number by the factor $\sim C_{|m|}$ in the magnetic arms. For $|m| = n = 2$, $C_2 \sim 1.2$. However, as discussed above, magnetic arms are also comprised of higher order enslaved components $m = 2n,\ 3n,\ 4n,\ \ldots$, with corresponding values $C_4 = 1.6$, $C_6 = 2.1$ and $C_8 = 2.6$, and with phase shift increasing in magnitude with $|m|$. This goes some way toward explaining why the phase shift can be significantly larger in magnitude than $\Omega_\mathrm{p}\tau$. It also helps to explain why magnetic arms are 'stretched out' azimuthally, as compared to those in the $\tau \to 0$ case.

For more elaborate spiral models, the situation becomes more complex. If the spiral winds up, then there is the added complication that the τ effect can cause the non-axisymmetric forcing to become smeared out in azimuth (see the discussion in Chapter 3), which *negatively* impacts the strength of magnetic arms, and these two effects compete in more realistic models such as the linear density wave model of Chapter 6.

Non-axisymmetric modes under the no-z and WKBJ approximations

We note that for the modes involving even components $m = 0, \pm 2$ there are six coupled partial differential equations (4.13)–(4.16). Mestel & Subramanian (1991) solved the corresponding simpler problem for the modes involving odd ($m = \pm 1$) components, which involves four coupled PDEs, using WKBJ methods, but they did not do the same for the modes involving even components. Thus we would like to get analytical insights into these perhaps more important modes. Therefore we proceed as follows: Our plan is to first solve for $a_{\pm 2}$ and $b_{\pm 2}$. We do this in Appendix D by using the no-z approximation for the z-derivatives (Subramanian & Mestel, 1993; Moss, 1995; Phillips, 2001), and a WKBJ-type approximation to handle radial diffusion. This yields algebraic equations which can be solved to obtain explicit expressions for $a_{\pm 2}$ and $b_{\pm 2}$. We then substitute them into the $m = 0$ equations, (4.13) and (4.14), and apply the no-z approximation to obtain Schrödinger-type differential equations in r with the effective potential $V(r)$. Bound states in this potential correspond to exponentially growing solutions, and these are obtained using the WKBJ approximation. This is done iteratively using numerical methods, so that the method is semi-analytical rather than analytical. Thus we avoid solving the six coupled differential equations (4.13)–(4.16). We shall see that this procedure, in which four of the six differential equations are approximated as algebraic equations, works well for the case where the vertical turbulent diffusion is much stronger than the radial turbulent diffusion, i.e., for solutions of a large radial scale (wavelength) in a thin disc.

As shown in Appendix D, solutions of equations (4.15) and (4.16) can be represented as

$$a_{\pm 2} = -\frac{|D_0|b_0\epsilon_\alpha}{2}\sqrt{\frac{\widetilde{A}^2+\widetilde{B}^2}{A^2+B^2}}\exp\left[\mp i(\kappa r+\beta+\widetilde{\beta})\right], \tag{4.19}$$

$$b_{\pm 2} = \frac{|D_0|b_0\epsilon_\alpha}{2}\frac{1}{\sqrt{A^2+B^2}}\exp\left[\mp i(\kappa r+\beta)\right], \tag{4.20}$$

where A, B, $\widetilde{A}$ and $\widetilde{B}$, as well as β and $\widetilde{\beta}$, are functions of position defined in Appendix D. Here the dynamo number is defined as

$$D_0 = \frac{\alpha_0 G h^3}{\eta_{\mathrm{t}}^2} = \frac{\alpha_0 G t_{\mathrm{d}}^2}{h} < 0, \tag{4.21}$$

where $t_{\mathrm{d}} = h^2/\eta_{\mathrm{t}}$ is the vertical turbulent diffusion time scale.

Once $a_{\pm 2}$ and $b_{\pm 2}$ are obtained, we can solve equations (4.13) and (4.14) for a_0 and b_0. Following Ruzmaikin et al. (1988) and Mestel & Subramanian (1991) by invoking the thinness of the disc, we factorise the solution into the local ($\widetilde{a}$ and $\widetilde{b}$) and global (q) parts,

$$a_0(r) = \widetilde{a}q(r), \qquad b_0(r) = \widetilde{b}q(r). \tag{4.22}$$

Generally, the local solution depends on z, i.e., $\widetilde{a}(z)$ and $\widetilde{b}(z)$. However, the z-dependence has been removed using the no-z approximation, and the local solution is a vectorial constant.

We substitute equation (4.22) into the no-z versions of equations (4.13) and (4.14), and, in equation (4.13), we also substitute equation (D.5) for $b_{\pm 2}$. In addition, we make use of the relation

$$\alpha_2\alpha_{-2} = \alpha_0^2\epsilon_\alpha^2/4,$$

obtained from equation (4.11). Equations (4.13) and (4.14) then reduce to

$$(1+\Gamma\tau)\Gamma - c_\tau\frac{\eta_{\mathrm{t}}}{q}\left[\frac{(rq)'}{r}\right]' = -\frac{2c_\tau}{\pi h}\alpha_0\frac{\widetilde{b}}{\widetilde{a}}\left[1+\frac{|D_0|\epsilon_\alpha^2}{4}(X_2+X_{-2})\right] - c_\tau\eta_{\mathrm{t}}\frac{\pi^2}{4h^2},$$

$$(1+\Gamma\tau)\Gamma - c_\tau\frac{\eta_{\mathrm{t}}}{q}\left[\frac{(rq)'}{r}\right]' = (1+\Gamma\tau)G\frac{\widetilde{a}}{\widetilde{b}} - c_\tau\eta_{\mathrm{t}}\frac{\pi^2}{4h^2},$$

where $X_{\pm 2}$ are defined in equation (D.6). Note that $\epsilon_\alpha = 0$ corresponds to an axisymmetric forcing of the dynamo. It is convenient to introduce a new quantity $\gamma(r)$ defined as

$$\gamma(r) = (1+\Gamma\tau)\Gamma - c_\tau \frac{\eta_\mathrm{t}}{q}\left[\frac{(rq)'}{r}\right]',$$

which, in the $\tau \to 0$ case, is equal to the growth rate Γ under the local or slab approximation (vanishing radial derivatives). For this reason, γ is sometimes called the 'local growth rate'. In the case of finite τ, γ is also closely related to Γ in the local approximation (since typically $\Gamma\tau \ll 1$, γ can still loosely be thought of as the local growth rate). Now the equations can be separated into a global eigen-equation for $q(r)$,

$$(1+\Gamma\tau)\Gamma q = \gamma q + c_\tau \eta_\mathrm{t}\left[\frac{(rq)'}{r}\right]', \tag{4.23}$$

which only contains derivatives with respect to r (denoted by prime), and two local equations for $\widetilde{a}$ and $\widetilde{b}$,

$$\left(\gamma + \frac{\pi^2 c_\tau}{4t_\mathrm{d}}\right)\widetilde{a} = -\, c_\tau \frac{2\alpha_0}{\pi h}\widetilde{b}\left[1 + \frac{|D_0|\epsilon_\alpha^2}{4}(X_2 + X_{-2})\right], \tag{4.24}$$

$$\left(\gamma + \frac{\pi^2 c_\tau}{4t_\mathrm{d}}\right)\widetilde{b} = (1+\Gamma\tau)G\widetilde{a}, \tag{4.25}$$

which generally only have derivatives with respect to z but become algebraic equations under the no-z approximation.

The local solution

The homogeneous equations (4.24) and (4.25) in $\widetilde{a}$ and $\widetilde{b}$ are easily solved to yield $\widetilde{b}/\widetilde{a}$ and γ. From equation (4.25), we obtain

$$\frac{\widetilde{b}}{\widetilde{a}} = \frac{(1+\Gamma\tau)Gt_\mathrm{d}}{\gamma t_\mathrm{d} + \frac{1}{4}c_\tau\pi^2}.$$

Then the vanishing of the determinant of the coefficients of equations (4.24) and (4.25) yields

$$\gamma = t_\mathrm{d}^{-1}\left\{-\frac{\pi^2 c_\tau}{4} \pm \sqrt{\frac{2c_\tau}{\pi}(1+\Gamma\tau)|D_0|\left[1 + \frac{\epsilon_\alpha^2|D_0|A}{2(A^2+B^2)}\right]}\right\}, \tag{4.26}$$

where the positive sign in front of the square root provides growing solutions, $\gamma > 0$.

With $\epsilon_\alpha = 0$ (axisymmetric forcing) and $\gamma = 0$ (neutral stability of the mean magnetic field), we obtain an estimate for the local critical dynamo number, i.e., the minimum magnitude of the dynamo number for the field to grow rather than decay,

$$|D_{0,\mathrm{c}}| = \frac{\pi^5 c_\tau}{32(1+\Gamma\tau)} \approx \frac{9.6 c_\tau}{1+\Gamma\tau}.$$

It is slightly larger than the $D_{0,\mathrm{c}} = 8$, obtained by the numerical solution of the z-dependent versions of equations (4.24) and (4.25) for $c_\tau = 1$, $\tau = \epsilon_\alpha = 0$ (Ruzmaikin et al., 1988); we note that $\Gamma\tau \ll 1$.

For $\epsilon_\alpha = 0$, the magnetic pitch angle, given by equation (3.33), can be expressed as

$$\tan p_{B,0} = \frac{\widetilde{a}}{\widetilde{b}} = -\sqrt{\frac{2c_\tau}{\pi(1+\Gamma\tau)h}\frac{\alpha_0}{|G|}}. \tag{4.27}$$

A similar result can be obtained from perturbation theory (Sur et al., 2007). With equation (2.2) for α_0 and $G = -\Omega$ (flat rotation curve), this becomes

$$\tan p_{B,0} = -\frac{l}{h}\sqrt{\frac{2c_\tau}{\pi(1+\Gamma\tau)}}.$$

The azimuthal average of the pitch angle in the kinematic regime obtained numerically in Chapter 3, where equation (2.2) was used, agrees very well with this formula. This can be seen by using the relevant parameters from that chapter in the above equation, and then comparing with Fig. 3.8 of that chapter. On the other hand, if, for example, α_0 and h are independent of radius, then equation (4.27) with $|G| = \Omega$ implies that $|p_{B,0}|$ increases with radius, as Ω is a decreasing function of r.

The global solution

Now, substituting equation (4.26) into equation (4.23), we obtain a Schrödinger-type equation for $q(r)$,

$$-\nabla_r^2 q + V(r)q(r) = Eq(r), \tag{4.28}$$

where $\nabla_r^2 = (rq')'/r$ is the radial part of the Laplacian in cylindrical coordinates. Here, the 'potential' is given by

$$V = \frac{1}{r^2} - \frac{\gamma t_\mathrm{d}}{c_\tau h^2} = \frac{1}{r^2} + \frac{\pi^2}{4h^2} - \frac{1}{h^2}\sqrt{\frac{2(1+\Gamma\tau)|D_0|}{\pi c_\tau}}\left[1 + \frac{\epsilon_\alpha^2 |D_0| A}{2(A^2+B^2)}\right], \tag{4.29}$$

and the 'energy' eigenvalue, by

$$E = -\frac{(1+\Gamma\tau)\Gamma t_{\rm d}}{c_\tau h^2}. \tag{4.30}$$

Note that bound states in the 'potential' $V(r)$ with $E < 0$ correspond to growing modes with $\Gamma > 0$. We solve this equation using the WKBJ theory: in terms of a scaled variable x, introduced via $r = h_0 e^x$ (with $h_0 = \text{const}$, $-\infty < x < \infty$ and $dx = dr/r$), equation (4.28) reduces to

$$\frac{d^2q}{dx^2} + p(x)q(x) = 0,$$

where

$$p(x) = h_0^2 e^{2x}[E - V(x)].$$

The boundary conditions are $q = 0$ at $r = 0$ and $r \to \infty$ (or $x \to \pm\infty$). Suppose that $p(x) = 0$ for $x = x_\pm$ (corresponding to $r_\pm$), with $x_- < x_+$ (for our purposes, it is sufficient to consider the case of just two roots). The standard WKBJ theory yields the quantization condition

$$\int_{r_-}^{r_+} \frac{\sqrt{p(r)}}{r} dr = \int_{r_-}^{r_+} [E - V(r)]^{1/2} dr = \frac{\pi}{2}(2k+1), \tag{4.31}$$

with $k = 0, 1, 2, \ldots$, which can be used to obtain the growth rate Γ. Note, however, that Γ enters both the 'potential' and the 'energy', so the WKBJ approach has to be supplemented with an iteration procedure to converge on the correct value of Γ, in addition to the iterations over β and $\widetilde{\beta}$ discussed in Section 4.2.3 and Appendix D.

As we will see below, the ϕ-dependent term in the α effect leads to a deepening of the potential well near the corotation radius, allowing strong non-axisymmetric modes that corotate with the α-spiral to exist there. Outside this region (i.e., far from the corotation radius) axisymmetric modes will dominate, while non-axisymmetric modes will be weaker. The asymptotic solutions developed here apply to the corotating magnetic modes in the kinematic regime, but the numerical simulations of Chapter 3 are, of course, not restrictive.

Substituting equations (4.19) and (4.20) into equation (4.7), and using equations (4.22), we can write the overall solution as

$$\overline{B}_r = \widetilde{a} q\, e^{\Gamma t}\left[1 - \frac{\widetilde{b}}{\widetilde{a}}\sqrt{\frac{\widetilde{A}^2 + \widetilde{B}^2}{A^2 + B^2}}\epsilon_\alpha |D_0| \cos(\psi - \widetilde{\beta})\right], \tag{4.32}$$

$$\overline{B}_\phi = \widetilde{b} q\, e^{\Gamma t}\left[1 + \frac{1}{\sqrt{A^2 + B^2}}\epsilon_\alpha |D_0| \cos\psi\right], \tag{4.33}$$

where

$$\psi = 2\phi - \kappa r - \beta.$$

Magnetic field lines of the mean field are expected to be trailing spirals since $G < 0$, which implies $\widetilde{b}/\widetilde{a} < 0$. Therefore, the overall phase difference between $\overline{B}_r$ and $\overline{B}_\phi$ has magnitude $\widetilde{\beta}$ [without the minus sign introduced in front of $\overline{a}$ in equation (D.1), there would have been an extra phase difference π]. The pitch angle of the magnetic field, defined in equation (3.33), is independent of q.

Each component of the mean magnetic field consists of an axisymmetric part and that having the $m = 2$ symmetry,

$$\overline{B}_i = \overline{B}_i^{(0)} + \overline{B}_i^{(2)} \cos[2(\phi - \phi_i)],$$

where $i = r, \phi$. The magnitude of the r-component of the field is maximum where $2\phi - \kappa r - \beta - \widetilde{\beta} = 0$, while the magnitude of the ϕ-component is maximum for $2\phi - \kappa r - \beta = 0$. On the other hand, the magnitude of α is maximum where $2\phi - \kappa r = 0$. Therefore, the (π-fold degenerate) phase differences between the r and ϕ components of the magnetic field and the α-spiral are given, respectively, by

$$\Delta_r = \frac{\beta + \widetilde{\beta}}{2}, \qquad \Delta_\phi = \frac{\beta}{2}.$$

Non-enslaved non-axisymmetric modes

Non-axisymmetric modes that rotate at an angular speed different from that of the α-spiral and are not enslaved (they rotate at approximately the local angular velocity at the radius where their eigenfunctions are maximum,) can also be maintained but they are sub-dominant everywhere (Mestel & Subramanian, 1991). Such modes have been observed to exist in axisymmetric discs (Ruzmaikin et al. 1988, Moss 1996, Chapter 3). In the previous chapter we showed that the growth of such modes in an axisymmetric disc requires somewhat special parameter values, and that in any case, such modes decay in the nonlinear regime. For a non-axisymmetric disc, such modes could be found by replacing Γ in equation (4.7) (and hence in subsequent equations) with $\Gamma_\mathrm{R} - im\Gamma_\mathrm{I}$, where Γ_R is the growth rate and Γ_I is the angular velocity of the mode in the reference frame that corotates with the α-spiral. However, with this more general approach, the WKBJ treatment above would, strictly speaking, have to be replaced by a *complex* WKBJ treatment. Given the numerical result that non-corotating non-axisymmetric modes are less important than corotating non-axisymmetric modes, we have chosen to leave the study of the former for the future.

4.2.3 Illustrative example

We determine Γ and the properties of the mean magnetic field by varying Γ iteratively until the quantization condition (4.31) is satisfied for $k = 0$ (the fastest growing mode). In addition, there is the complication that β, $\widetilde{\beta}$, and hence θ_a, θ_b, A, B, $\widetilde{A}$, $\widetilde{B}$, etc., are not a priori known (see Section 4.2.2 and Appendix D). We resolve this by iterating these variables as well. That is, we start with $\beta'(r)$, $\widetilde{\beta}'(r)$ and their derivatives equal to zero, and at each iteration, we obtain these functions from equations (D.9) and (D.12) to use them as input for the next iteration. The iterations converge if the terms involving β' and $\widetilde{\beta}'$ are small compared with the turbulent diffusion terms that do not vary with r. In the example below, β' and $\widetilde{\beta}'$ are comparable to κ near the corotation. However, it can be seen from equations (D.10), (D.11), (D.13) and (D.14) that the terms involving the radial derivatives are not very important if the radial diffusion is much weaker than the vertical diffusion, that is if $\theta_a'^2, \theta_b'^2 \ll \pi^2/4h^2$, which may permit the iterations to converge. Therefore, in the example below, we choose the disc half-thickness h to be small enough (somewhat smaller than the standard value) that the iterations do in fact converge.

In order to determine the potential and growth rates of the corotating non-axisymmetric modes, we must first specify the functional forms of the scale height $h(r)$, angular velocity $\Omega(r)$ and $\alpha_0(r)$. For simplicity, we choose $h = 0.1\,\mathrm{kpc} = \mathrm{const}$. We also take $\eta_\mathrm{t} = ul/3$, where u and l are the rms turbulent velocity and scale, and adopt $l = h/4 = 0.025\,\mathrm{kpc}$, and $u = 12ht_\mathrm{d}^{-1} = 5\,\mathrm{km\,s^{-1}}$. These values are different from those usually adopted, $u = 10\,\mathrm{km\,s^{-1}}$ and $l = 0.1\,\mathrm{kpc}$. Our choice is motivated by the desire to improve the convergence of the iterations since our aim here is mainly to illustrate the solution procedure and to discuss the qualitative properties of the eigen-solutions. However, we take care to keep the key parameter, the vertical turbulent diffusion time, at $t_\mathrm{d} = 0.24\,\mathrm{Gyr}$, similar to (about twice smaller than) the standard value.

As in Chapter 3, we use Brandt's rotation curve (2.5) with $r_\omega = 20h = 2\,\mathrm{kpc}$, and Ω_0 set to yield the circular rotation speed $\overline{U}_\phi = 600ht_\mathrm{d}^{-1} = 250\,\mathrm{km\,s^{-1}}$ at $r = 100h = 10\,\mathrm{kpc}$. We choose the corotation radius to be located at $r_\mathrm{cor} = 100h = 10\,\mathrm{kpc}$, which corresponds to a pattern speed $\Omega_\mathrm{p} = 6t_\mathrm{d}^{-1} = 25\,\mathrm{km\,s^{-1}\,kpc^{-1}}$.

Furthermore, we take $\alpha_0 = 2.4ht_\mathrm{d}^{-1} = 1\,\mathrm{km\,s^{-1}}$ at all radii. We also take $\kappa = -0.1h^{-1} = -1\,\mathrm{kpc^{-1}}$ and $\epsilon_\alpha = 1$, the latter chosen to be large to maximize the strength of the non-axisymmetric modes. We also adopt $c_\tau = 1$.

The value of τ is estimated as $\tau \approx 2l/u \approx 2l^2/3\eta_\mathrm{t} \approx 2l^2t_\mathrm{d}/3h^2 = t_\mathrm{d}/24 = 9.8\,\mathrm{Myr}$. We also consider solutions for $\tau \to 0$, both for reference and also because τ could be much smaller than our estimate of $2l/u$ in some galaxies (though it could be much larger in others).

When describing the geometry of the magnetic modes, it is useful to have in mind that magnetic lines have the shape of a spiral with the pitch angle defined in equation (3.33). These spirals have to be distinguished from the spirals along which magnetic field strength is maximum. These can be called magnetic arms or magnetic ridges, and have a different pitch angle (Baryshnikova et al., 1987; Krasheninnikova et al., 1989) (see also Fig. VII.8 of Ruzmaikin et al., 1988).

The converged results for the modes around corotation are shown in Fig. 4.1 for $\tau \to 0$ and $\tau = t_{\rm d}/24 = 9.8\,{\rm Myr}$. (Solutions for intermediate values of τ are intermediate between the two solutions illustrated.) Panel a shows the potential $V(r)$ of equation (4.29), along with the 'energy' $-(1+\Gamma\tau)\Gamma t_{\rm d}/h^2$ of the fastest growing eigenmode. Importantly, due to the non-axisymmetric part of α, the potential has a local minimum near the corotation radius. Therefore, corotating non-axisymmetric modes can be preferentially excited there. The finite value of τ makes the potential deeper and thus enhances the growth of non-axisymmetric modes, with a slightly larger growth rate, $\Gamma = 1.41t_{\rm d}^{-1} = 5.9\,{\rm Gyr}^{-1}$ for $\tau = t_{\rm d}/24$ versus $\Gamma = 1.33t_{\rm d}^{-1} = 5.6\,{\rm Gyr}^{-1}$ for $\tau \to 0$.

Figure 4.1b shows the ratio

$$\delta \equiv \frac{\overline{B}_\phi - \overline{B}_\phi^{(0)}}{\overline{B}_\phi^{(0)}} = \delta^{(2)} = \frac{1}{\sqrt{A^2+B^2}}\epsilon_\alpha |D_0| \cos(2\phi - \kappa r - \beta), \tag{4.34}$$

where the equality between δ and $\delta^{(2)}$ does not hold for numerical solutions, which include higher-order azimuthal components, and where,

$$\delta^{(m)} \equiv \frac{\overline{B}_\phi^{(m)}}{\overline{B}_\phi^{(0)}} \cos\left[m(\phi - \phi_\phi)\right]. \tag{4.35}$$

The quantity $\delta^{(2)}$ is given by the second term in the brackets of equation (2.9). The figures show δ at the azimuth $\phi = \phi_{\rm cor} = \kappa r_{\rm cor}/2$ where one of the α-spiral arms crosses the corotation circle. The (ϕ-independent) amplitude (envelope) of this ratio is shown with dashed curves, and $\alpha(r, \phi_{\rm cor})$ is represented with a dash-dotted curve for reference. For both finite and vanishing τ, the envelope of δ exceeds unity near the corotation, so that the $|m| = 2$ components dominate there. The dominance is stronger when τ differs from zero. Importantly, the radius $r_{\rm max}$ where the envelope of δ is maximum is somewhat larger for the finite τ.

The azimuthal phase differences Δ_ϕ and Δ_r between the maximum in, respectively,

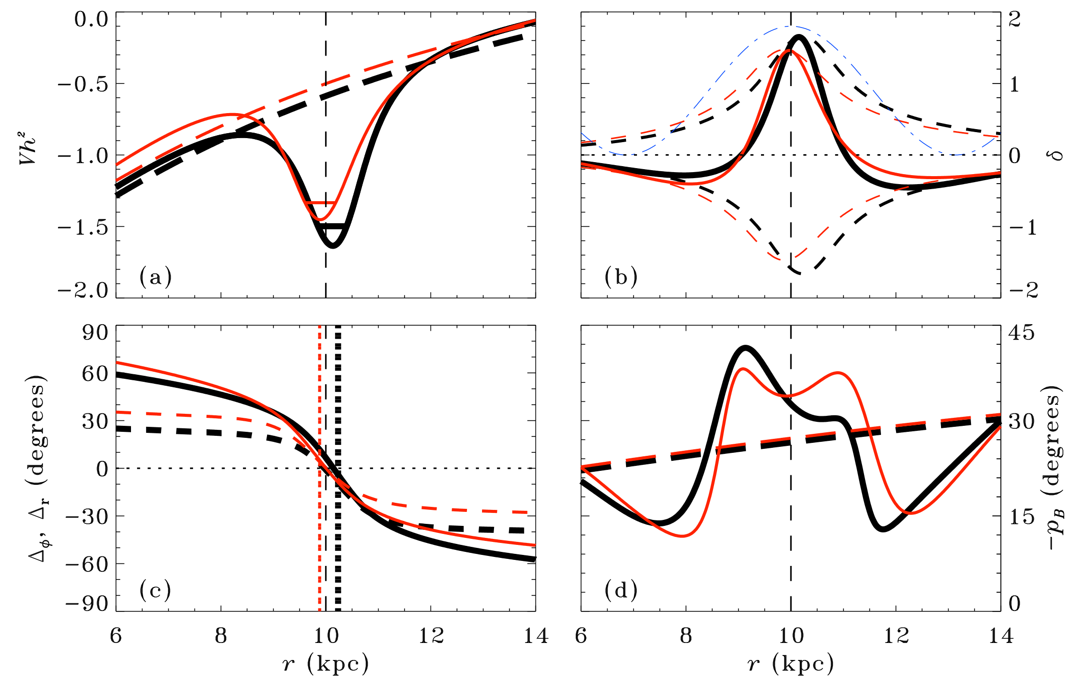

Figure 4.1: **(a)** The potential (4.29) of (4.28) for $\tau = 2l/u$ (thick, black, solid curve) and $\tau \to 0$ (thin, red, solid curve), near the corotation radius (dashed vertical line). The 'energy' eigenvalues (4.30) of (4.28) are represented by horizontal lines inside the wells. The axisymmetric part of the potential is also shown as a dashed line in both cases. **(b)** The solid curves represent the ratio of non-axisymmetric to axisymmetric parts of $\overline{B}_\phi$ at the azimuth $\phi = \phi_{\rm cor} = \kappa r_{\rm cor}/2$, while the dashed curves show the corresponding magnitudes of the ratios $\pm\overline{B}_\phi^{(2)}/\overline{B}_\phi^{(0)}$. The dash-dotted curve shows the variation of $\alpha(r, \phi_{\rm cor})$. **(c)** The phase differences, Δ_ϕ (solid) and Δ_r (dashed), between the components of the magnetic spiral arms and the α-spiral arms. The radius $r_{\rm max}$ where the envelope of $\overline{B}_\phi^{(2)}/\overline{B}_\phi^{(0)}$ is maximum is shown as a dotted vertical line of the appropriate colour and thickness. **(d)** Pitch angle p_B, shown with the opposite sign, at $\phi = \phi_{\rm cor} = \kappa r_{\rm cor}/2$ (solid). Also shown is $-p_B$ for the purely axisymmetric case (dashed).

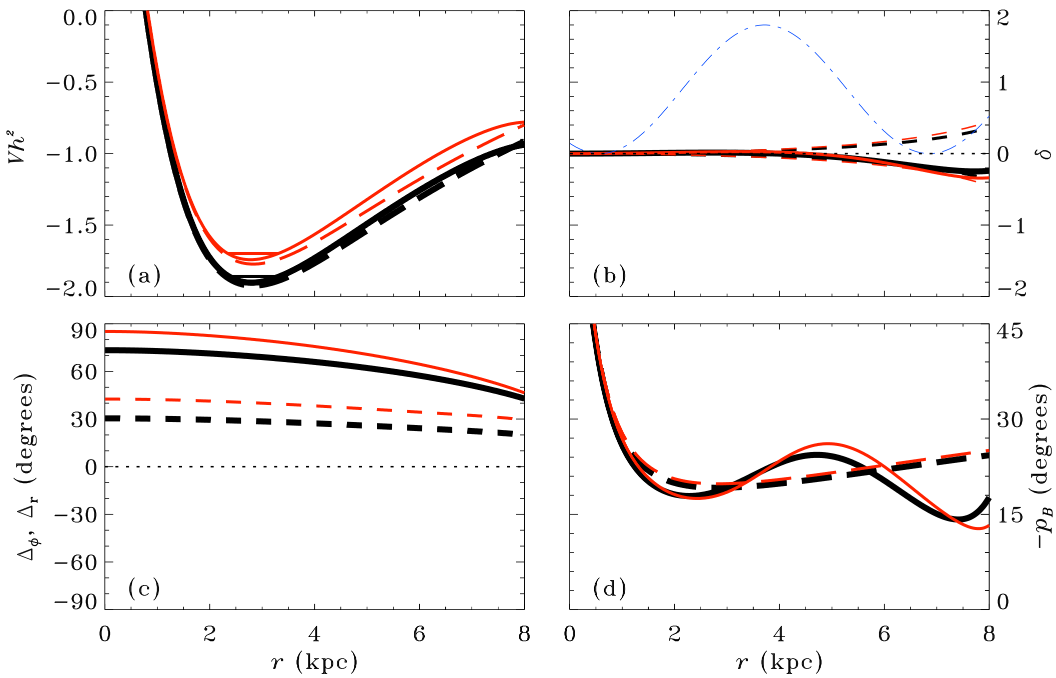

Figure 4.2: Same as Fig. 4.1 but for the fastest growing mode in the inner region of the disc, at $r \simeq 2.8\,\mathrm{kpc}$.

the azimuthal and radial magnetic field components, and the maximum of α, are shown in Fig. 4.1c. For both $\tau \to 0$ and $\tau \neq 0$, the magnetic spiral arms (whose phase shift is given approximately by Δ_ϕ since $\overline{B}_\phi$ dominates over $\overline{B}_r$) cross the α-spiral near the corotation radius, so that each magnetic arm precedes the α-arm in azimuth inside the corotation circle and lags it at larger radii. This implies that the magnetic arms are more tightly wound than the material arms.

The τ effect produces a phase shift in the magnetic arm such that the part of the arm that precedes the corresponding α-arm is weakened, while the part that lags the α-arm is enhanced. This can be seen from Fig. 4.1c. For the $\tau \to 0$ case, $r_{\max}$ (vertical dotted red line) is located slightly inside the circles at which $\Delta_\phi = 0$ and $\Delta_r = 0$. At these circles, the $\overline{B}_\phi$ and $\overline{B}_r$ magnetic arms respectively cross the α-arm. This means that for $\tau \to 0$, the part of the magnetic arm that precedes the α-arm is somewhat stronger than that which lags. (For the more realistic numerical solutions of Chapter 3, the preceding and lagging parts are of equal strength for $\tau \to 0$ as can be seen in Fig. 3.8c of that chapter.) On the other hand, for $\tau = 2l/u$ in our asymptotic solution, we see that $r_{\max}$ is located to the right of the radii for which $\Delta_\phi = 0$ and $\Delta_r = 0$, which tells us that the lagging part of the magnetic arm is stronger than the preceding part. This is consistent with the findings of Chapter 3. Thus, the lagging, outer part of the magnetic arm is enhanced for finite τ, while the preceding, inner part is weakened. For example, the phase shift between the magnetic and α-arms is $\Delta_\phi(r_{\max}) = 5.2^\circ$ for $\tau \to 0$ but -3.7° for $\tau = 2l/u$. However, what we are most interested in is the effect of a finite τ, so from now on we will mostly consider the phase *difference* between the vanishing and finite τ cases. Crucially, we shall show below in Section 4.3.4 that the general behaviour of the phase difference as a function of $\Omega_\mathrm{p}\tau$ is nicely reproduced by the asymptotic solution. Thus, defining the difference between the phase shifts obtained for $\tau = 0$ and finite τ,

$$\Delta(\tau) = \Delta_\phi\left[\tau, r_{\max}(\tau)\right] - \Delta_\phi\left[0, r_{\max}(0)\right], \tag{4.36}$$

we have $\Delta(2l/u) = -9^\circ$ for the asymptotic solution, which is of the same order of magnitude as $-\Omega_\mathrm{p}\tau = -14^\circ$. The phase difference $\Delta(\tau) \simeq -\Omega_\mathrm{p}\tau$, obtained here and in the models of Chapter 3, is a natural consequence of the finite response time τ of $\boldsymbol{\mathcal{E}}$ to variations in α.

In Fig. 4.1d, we plot the pitch angle of the magnetic field p_B at the same azimuth $\phi = \phi_\mathrm{cor} = \kappa r_\mathrm{cor}/2$, shown with the opposite sign for presentational convenience. The pitch angle obtained for the axisymmetric disc (dashed lines) is about $p_B = -(20\text{–}30)^\circ$ in the region shown, and increases with radius in agreement with equation (4.27). Its large magnitude is due to the large, constant value of α_0 used in this model, whereas the increase of $|p_B|$ with r is due to our choice of a constant disc scale height here, as discussed above. The azimuthal variation in α leads to a large variation in the pitch angle, with $-p_B$ being large where α is large and small where α is small (compare with the dash-dotted curve for α in Fig. 4.1b). The magnitude of the variation depends on ϵ_α. This variation is explained by the fact that the $\alpha\Omega$ dynamo mechanism tends to produce $|\overline{B}_r/\overline{B}_\phi| < 1$ due to the velocity shear; hence, $|p_B| \propto |\alpha_0/G|^{1/2}$, equation (4.27). (By contrast, the α^2-dynamo would generate rather open magnetic spirals with $|\overline{B}_r/\overline{B}_\phi| \simeq 1$.)

4.2.4 Modes localised away from the corotation radius

As discussed above in this chapter and in the previous chapter, strong enslaved non-axisymmetric modes are excited near $r = r_\mathrm{cor}$. These modes corotate with the α-spiral pattern and are enslaved to the $m = 0$ component, but have very strong $m = \pm 2$ components (with the relative amplitude $\delta \sim 1$). Apart from the corotating enslaved non-axisymmetric modes localised near the corotation radius, other types of modes exist within the disc.

The fastest growing modes in the disc are located between $r = 0$ and $r = r_\mathrm{cor}$, near to the radius r_D for which the azimuthally averaged dynamo number is maximum in magnitude. In this region of the disc, the axisymmetric component dominates, with enslaved non-axisymmetric components that corotate with the α-spiral also present, but negligible in comparison to $m = 0$.

We illustrate these modes in Fig. 4.2, which is similar to Fig. 4.1, except that it shows the results for the fastest growing mode near $r = r_{\rm D}$. Because the potential (4.29) includes Γ, the potentials in Figs. 4.1 and 4.2 are different, though they are qualitatively similar and both have two minima, one near $r_{\rm D}$ and the other near $r_{\rm cor}$. Figure 4.2a shows that the minimum in the potential is located at a radius of $\simeq 2.8\,{\rm kpc}$, which corresponds almost exactly to the radius $r_{\rm D}$ for which the magnitude of the dynamo number (and hence the shear G since α and h are constant with r) is maximum. The growth rates are $\Gamma = 1.73 t_{\rm d}^{-1} = 7.2\,{\rm Gyr}^{-1}$ for $\tau = t_{\rm d}/24$ and slightly smaller, $\Gamma \simeq 1.70 t_{\rm d}^{-1} = 7.1\,{\rm Gyr}^{-1}$, for $\tau \to 0$. The above growth rates are similar to those seen in the more realistic disc models of Chapter 3. They produce ~ 7 e-folding times, or a factor $\sim 10^3$ in the growth of the field in 1 Gyr. That is, our models can comfortably explain the existence of μG strength large-scale fields even in young disc galaxies of age 1 Gyr if the seed field is of nG strength. It can be seen in Fig. 4.2b that $\delta \ll 1$ around $r \sim r_{\rm D}$, which means that non-axisymmetric components are very weak there. Figure 4.2c is shown for completeness, though the large phase shift near $r_{\rm D}$ that it illustrates is of little consequence, given that the $m \neq 0$ components are so weak there. Finally, Fig. 4.2d illustrates that the azimuthal variation of the pitch angle of the magnetic field caused by the α-spiral is quite strong, even deep inside the corotation radius, in agreement with the results of Chapter 3 (e.g., the bottom row of Figure 10 there). This can be seen by comparing the solid lines for the non-axisymmetric disc ($\epsilon_\alpha = 1$), with the dashed lines for the axisymmetric disc ($\epsilon_\alpha = 0$).

4.3 Comparison with numerical results

4.3.1 Numerical solutions of Chapter 3

The semi-analytical solution obtained agrees well, qualitatively, with the numerical solutions of Chapter 3, which can be seen by comparing Fig. 4.1 with Fig. 3.8 of Chapter 3, which shows the solution of the fiducial non-axisymmetric model of that chapter (Model E) in the kinematic regime. This is especially true in the $\tau \to 0$ case. The numerical solution, however, does reveal a greater difference between the finite and vanishing τ cases than what is seen in the semi-analytical solution. For example, the phase difference for Model E of Chapter 3 during the kinematic stage is $\Delta(l/u) = -27^\circ \pm 4^\circ$ where the range of Δ reflects the finite resolution of the numerical grid. This is comparable to but somewhat larger in magnitude, than $-\Omega_{\rm p}\tau = -18^\circ$ for that model, while in our semi-analytical

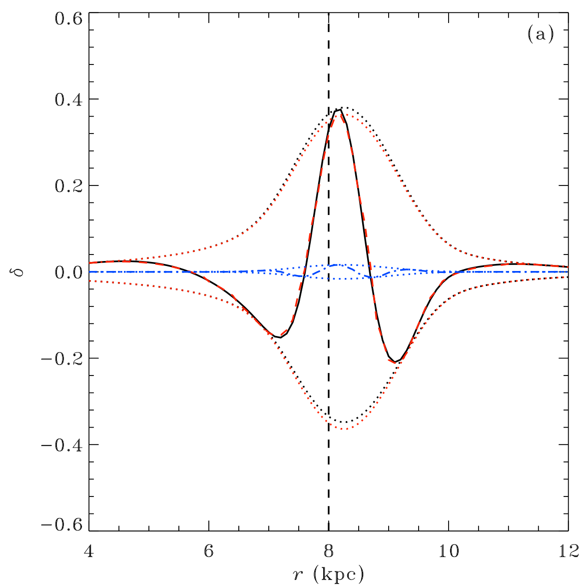

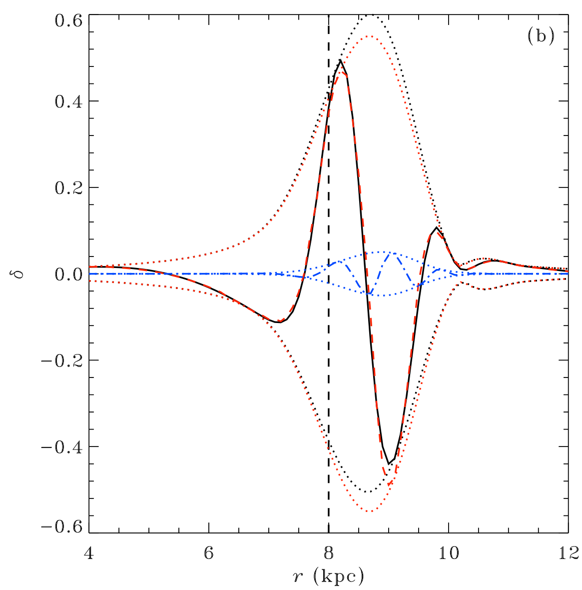

Figure 4.3: The relative strength δ of the non-axisymmetric part of the mean magnetic field in Model E of Chapter 3, defined as in equation (4.34), as a function of the galactocentric radius near the corotation circle at $\phi = \phi_{\rm cor}$ (black solid), and the envelope of this dependence at all values of ϕ (black dotted). The individual contributions of the $|m| = 2$ [red dashed for $\delta^{(2)}(r_{\rm cor})$ and red dotted for its envelope] and $|m| = 4$ [blue dash-dotted for $\delta^{(4)}(r_{\rm cor})$ and blue dotted for its envelope] components are also shown. **(a)** $\tau \to 0$; **(b)** $\tau = l/u$.

solution, presented above, Δ was found to be comparable, but somewhat smaller in magnitude, than $-\Omega_{\mathrm{p}}\tau$ for the disc model used. This apparent discrepancy suggests that there is an additional physical element missing in the asymptotic solution. In fact, the larger phase shift in the numerical solution can be partly attributed to higher-order even corotating components, especially $m = \pm 4$. Figure 4.3a shows the relative strength of the non-axisymmetric magnetic field δ, defined in equation (4.34), at the azimuthal angle $\phi = \phi_{\mathrm{cor}}$, where the α-spiral crosses the corotation circle, for the case $\tau \to 0$ in Model E of Chapter 3. Fig. 4.3b shows $\delta(\phi_{\mathrm{cor}})$ for the case $\tau = l/u$. These panels are similar to Fig. 8b of Chapter 3, with the envelope of δ over all ϕ plotted here as a dotted line. The quantities $\delta^{(2)}$ and $\delta^{(4)}$ [see equation (4.35)], are also plotted. It is clear that the $|m| = 2$ components dominate, as assumed in the asymptotic solution. However, it is also clear that the ratio of the amplitude of $|m| = 4$ to that of $|m| = 2$ is larger when τ is finite. Moreover, for $\tau = l/u$, the $\delta^{(4)}$ envelope peaks at a larger radius than that of $\delta^{(2)}$. This suggests that the $|m| = 4$ components have the effect of shifting r_{max} outward. Since $\Delta(\tau)$ is sensitive to $r_{\mathrm{max}}(\tau)$, this can cause a significant increase in $\Delta(\tau)$. This is consistent with the discussion of Section 4.2.2, which was based on an interpretation of the analytical expressions obtained by introducing a spirally-modulated α_{k} into the dynamo equation.

4.3.2 Direct comparison of asymptotic and numerical solutions

It is also useful to compare an asymptotic solution such as that presented above with a numerical solution for *the same disc model* (with e.g. a much smaller half-thickness h than the models of Chapter 3). An example is shown in Figs. 4.4 and 4.5 for $\tau \to 0$ and $\tau = l/u$, respectively. The model uses the same parameters as the asymptotic solution above, except that $\epsilon = 0.6$ instead of 1, for both the asymptotic and numerical solutions. Plots are shown at $t = 10t_{\mathrm{d}}$, when the relative strength of higher-order *radial* modes has become quite low (though they can still be seen as wiggles at $r > 11\,\mathrm{kpc}$). In Figs. 4.4a (asymptotic) and c (numerical), we compare the quantity δ for the two types of solution, while in 4.4b (asymptotic) and d (numerical), the quantities Δ_r and Δ_ϕ are compared, for the $\tau \to 0$ case. For $\tau \to 0$, the profiles of δ, Δ_ϕ and Δ_r do not undergo much subsequent evolution. If, however, $\tau = l/u$, the envelope of δ grows and becomes somewhat more asymmetric with time after $t = 10t_{\mathrm{d}}$, though the profile of the central (solid) peak at $\phi = \phi_{\mathrm{cor}}$ remains almost unchanged. Moreover, the asymmetry subsides in the saturated state, and the profile of δ resembles the one shown.

For the case of vanishing τ, the two types of solution are in fairly good agreement. However, as can be seen by comparing panels a and c of Fig. 4.4, magnetic arms are

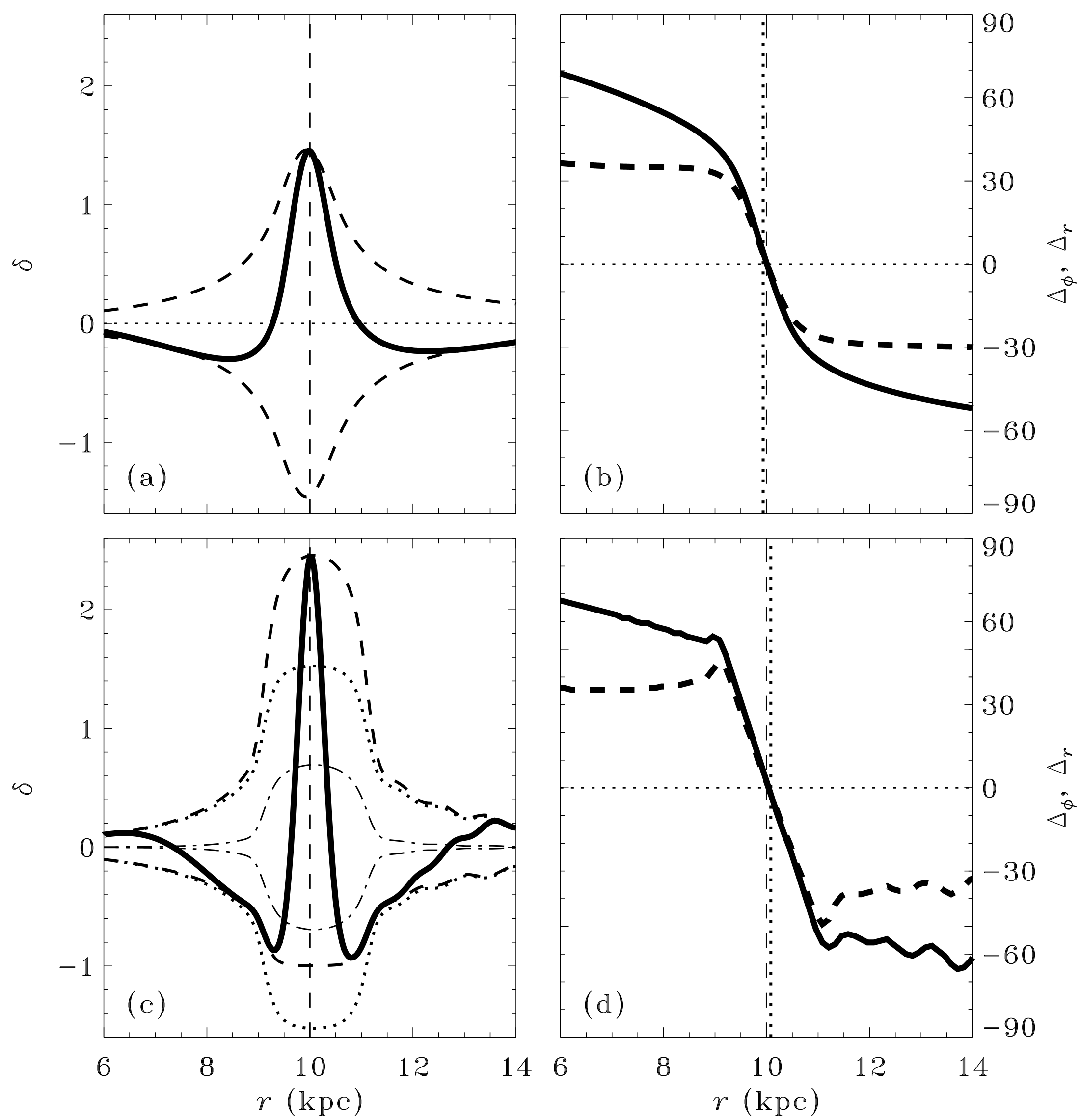

Figure 4.4: Direct comparison of asymptotic (a–b) and numerical (c–d) solutions for the same disc model, for the case $\tau \to 0$. Panels a and c are similar to panel b of Fig. 4.1, whilst panels b and d are similar to panel c of that figure. In a and c the $|m| = 2$ and $|m| = 4$ envelopes are represented by dotted and dash-dotted curves, respectively. In Panel (d), the curves are smoothed over 0.125 kpc.

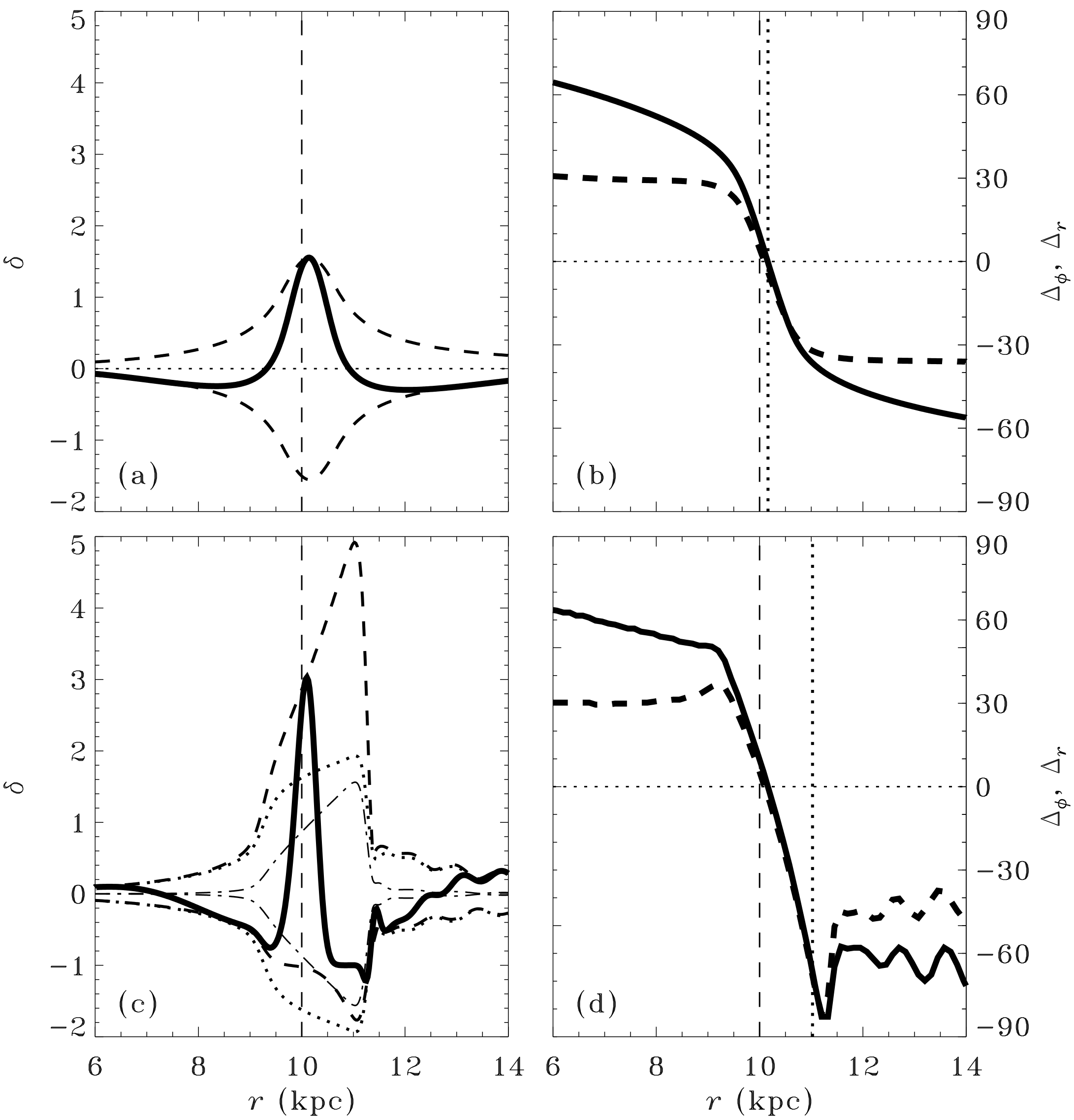

Figure 4.5: As in Fig. 4.4 but now for $\tau = l/u$ (note the change in the plotting range of δ).

more pronounced in the numerical solution than in the asymptotic solution. This can be attributed to higher order enslaved components in the numerical solution, as can be seen by comparing the overall envelope (dashed) with the envelopes of the $|m| = 2$ (dotted) and $|m| = 4$ (dash-dotted) components in panel c,

For the $\tau = l/u$ case, shown in Fig. 4.5, qualitative features of the solution are in reasonable agreement, but the effect of a finite τ is more dramatic in the numerical solution than in the asymptotic solution. For instance, $r_{\max}$ is much larger in the numerical solution due to the asymmetric envelope of δ, resulting in a larger phase shift. This is seen by comparing panels b and d, where it is evident that the dotted vertical line crosses the solid and dashed lines at much larger values of $|\Delta_\phi|$ and $|\Delta_r|$ in the numerical solution. As with the solutions from Chapter 3, enslaved components with $|m| > 2$ are stronger in the finite τ case than in the $\tau \to 0$ case, as can be seen by comparing the dash-dotted envelopes for the $|m| = 4$ components in Figs. 4.5c and 4.4c. The assertion, made above, that higher-order enslaved components are responsible for enhancing the phase shift is therefore strengthened.

The fact that non-axisymmetric components can be more easily generated in a thinner disc, where the difference in the global mode structure is less important because of the stronger dominance of the local dynamo action (due to the shorter magnetic diffusion time across the disc), is well known (Section VII.8 in Ruzmaikin et al., 1988). However, the importance of the finite relaxation time in this respect was not appreciated earlier. We emphasize that this disc model is used for the sake of illustration only, and is not as realistic as the models of Chapter 3, where enslaved components with $|m| > 2$ are anyway much less important.

It is also interesting to compare the growth rates of the asymptotic and numerical solutions. Both types of solution give the same growth rate for the inner mode located near r_D: $\Gamma = 1.73 t_\mathrm{d}^{-1}$ for $\tau = l/u$ and $\Gamma = 1.72 t_\mathrm{d}^{-1}$ for $\tau \to 0$. The magnetic field in the inner disc is maximum at $r = 2.9\,\mathrm{kpc}$ in the numerical solution, for both values of τ considered, in close agreement with the asymptotic solution where the minimum of the potential is situated at $2.8\,\mathrm{kpc}$ in both cases. For the modes near the corotation radius, the semi-analytical model predicts the growth rates of $\Gamma = 0.99 t_\mathrm{d}^{-1}$ for $\tau = l/u$ and $\Gamma = 0.97 t_\mathrm{d}^{-1}$ for $\tau \to 0$, while the numerical solution gives $\Gamma = 1.06 t_\mathrm{d}^{-1}$ and $\Gamma = 1.02 t_\mathrm{d}^{-1}$, respectively. Again, the agreement between the prediction of the asymptotic solution and the numerical solution is quite satisfactory. The growth rates for non-axisymmetric modes near the corotation radius are thus about half as large as those of the inner axisymmetric modes.

Although one could, in principle, include magnetic components with $|m| > 2$ in the asymptotic solution presented above, including $m = \pm 4$ adds four new differential equations as well as new terms to the existing equations (4.15), increasing the complexity of the model. Moreover, from our analytical expressions (4.19) and (4.20) for $a_{\pm 2}$ and $b_{\pm 2}$ we find that the WKBJ-type approximations (D.2) turn out to be strictly valid only out to $\sim 0.5\,\mathrm{kpc}$ on either side of the minimum (near $r = r_{\mathrm{cor}}$) in the potential. At those locations, the magnitude of the rate of change of the amplitude with r is comparable to that of the phase, in violation of equation (D.2). This limitation becomes more severe for $|m| \geq 4$. We take the view that the asymptotic solution presented above anyway does a very good job of reproducing the key qualitative features of the numerical solution, and thus we do not include the $m = \pm 4$ components.

4.3.3 Competition between the inner and outer modes

Due to their larger growth rate, $m \neq 0$ components in the inner disc, although weaker than the $m = 0$ component there, soon come to be stronger than the $m \neq 0$ components near the corotation circle (assuming a relatively uniform seed field). In fact, in the kinematic regime the local extremum of the magnetic field near the corotation radius is gradually overcome by the tail of the dominant $m = 0$ eigenfunction (which has it maximum near r_{D}). However, the non-axisymmetric magnetic structure near the corotation radius becomes prominent again in the saturated state (see also Section 3.5 of Chapter 3).[1]

In Fig. 4.6, the square root of the magnetic energy density in a component with a given azimuthal symmetry m, averaged over the area of the disc, is plotted as a function of time for the numerical solution (only the $\tau \to 0$ case is shown to avoid clutter, though the behaviour is very similar when τ is finite). Solid, short-dashed and dash-dotted lines show $m = 0$, $|m| = 2$ and $|m| = 4$ components, respectively. The long-dashed reference line has slope corresponding to a growth rate of $1.72 t_{\mathrm{d}}^{-1}$, while the dotted reference line corresponds to $0.97 t_{\mathrm{d}}^{-1}$. These reference lines correspond to the growth rates obtained from the asymptotic solution; they illustrate the general agreement between asymptotic and numerical solutions discussed above. Clearly, the modes localised near the corotation radius dominate at early times, until the modes spreading from r_{D} catch up at about $t = 2\,\mathrm{Gyr}$. Under normal circumstances, the inner nearly-axisymmetric mode would dominate its counterpart situated near corotation right from $t = 0$, while the $|m| = 2$ and $|m| = 4$ inner-mode components would quickly come to dominate over their counterparts situated near corotation. We have delayed this inevitable outcome for illustrative purposes using

[1] Due to the different disc parameters used, the $m = 0$ eigenfunction becomes dominant much earlier in the standard Model E of Chapter 3 [about $5t_0$ after the simulation is begun, where t_0 is defined in Chapter 3] than it does in the models presented in this chapter (about $70t_{\mathrm{d}}$ after the simulation is begun).

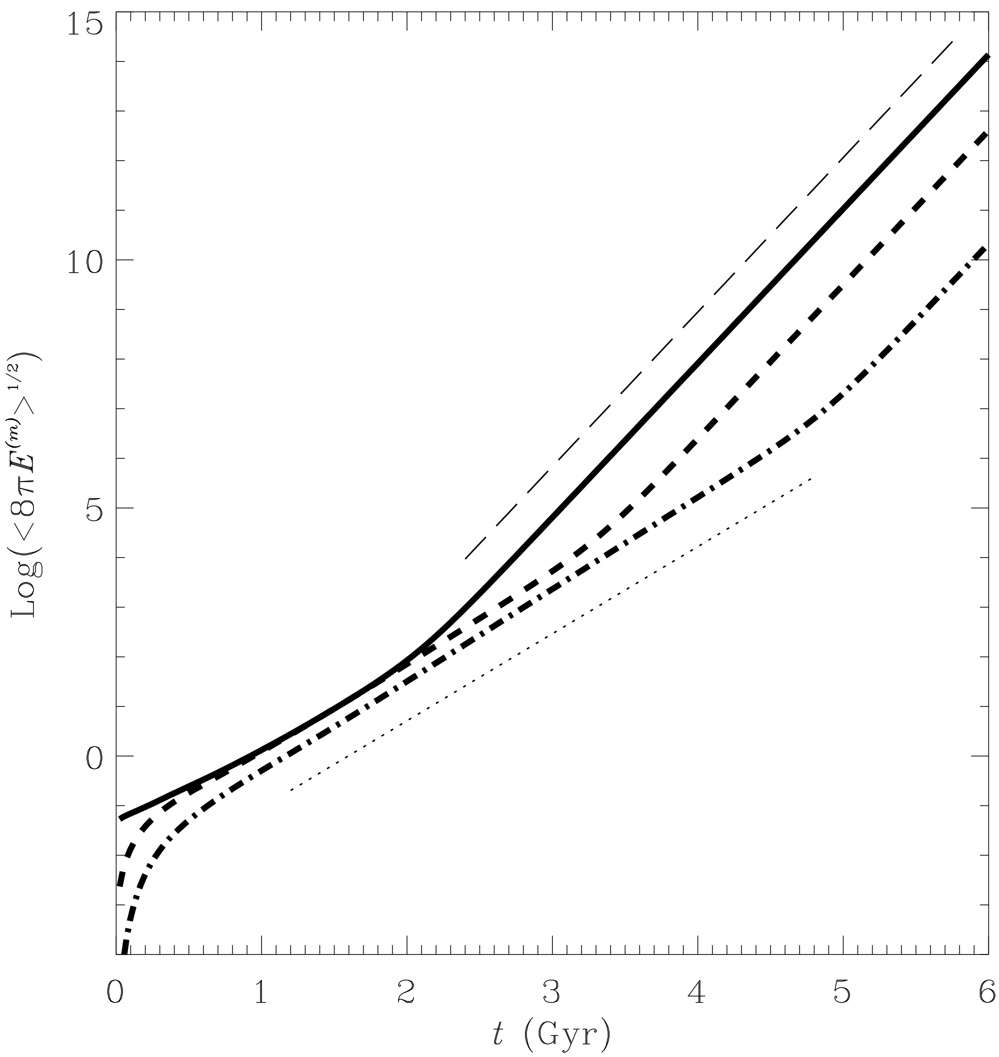

Figure 4.6: Evolution of the magnetic field strength in each Fourier component for the $\tau \to 0$ case: $m = 0$ (solid), $|m| = 2$ (short-dashed) and $|m| = 4$ (dash-dotted). Also plotted are reference lines corresponding to growth rates predicted by the semi-analytical model: $\Gamma = 1.72 t_{\mathrm{d}}^{-1}$ (long-dashed) and $\Gamma = 0.97 t_{\mathrm{d}}^{-1}$ (dotted).

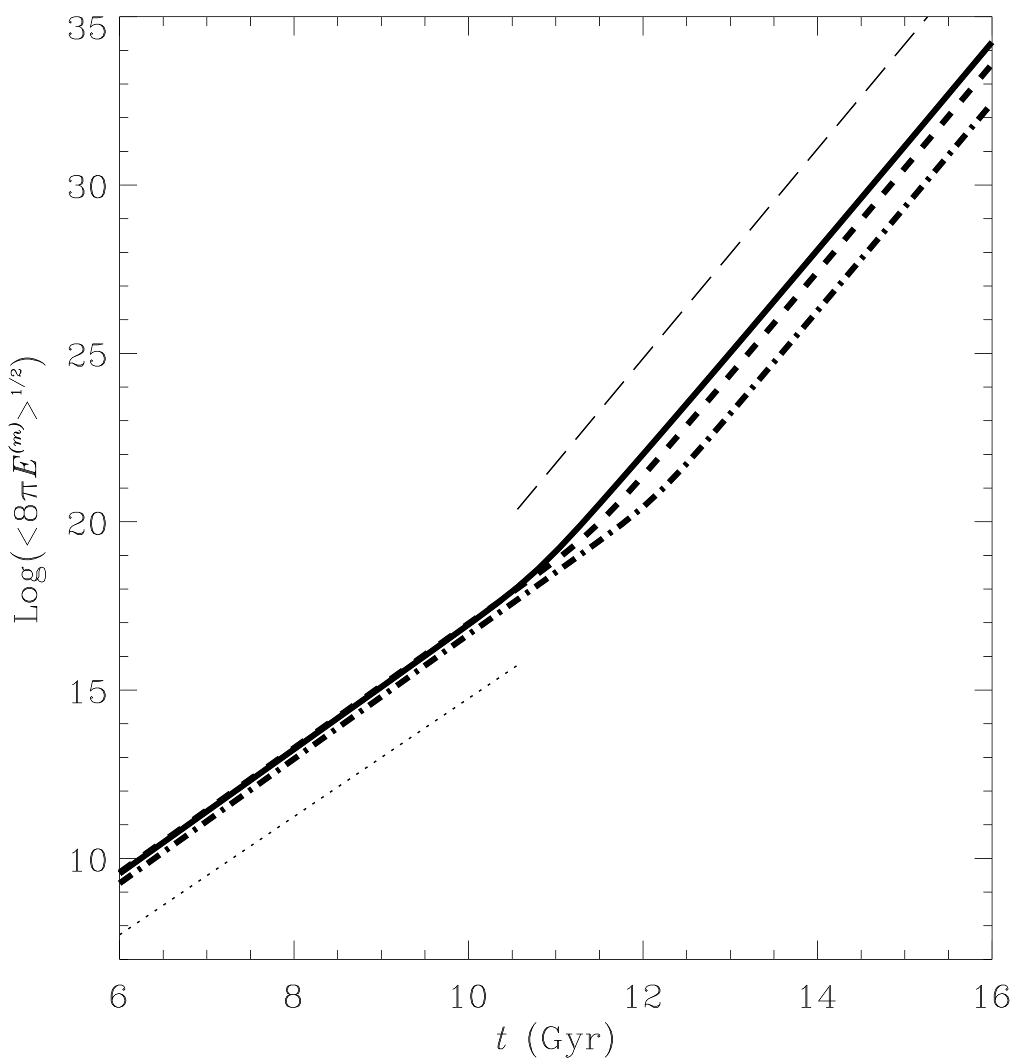

Figure 4.7: As in Fig. 4.6 but now with the average taken over the annulus of 4 kpc in width centred on $r = r_{\rm cor}$.

a seed magnetic field that is about 1000 times stronger within an annulus of width 4 kpc centered on $r = r_{\rm cor}$. Thus, the growth rates of both types of mode can be easily calculated from the same graph. Moreover, it is clear from the figure that, for the modes situated near the corotation, the $|m| = 2$ component has almost the same strength as $m = 0$, while $|m| = 4$ is somewhat weaker (about 0.4 times as strong). For the modes situated near $r = r_{\rm D}$, on the other hand, $m = 2$ is more than 30 times weaker than $m = 0$, and $|m| = 4$ is almost 200 times weaker than $|m| = 2$.

In Fig. 4.7, we show a similar plot (obtained without any enhancement of the seed magnetic field near the corotation), but here the averaging is taken over the 4 kpc-wide annulus around the corotation radius. Clearly, the fastest growing mode localized near $r = r_{\rm cor}$ dominates until $t \approx 12$ Gyr, when the tail of the dominant eigenfunction (which peaks near $r = r_{\rm D}$) overtakes it. However, as in the solutions of Chapter 3, an enhancement in the axisymmetric and non-axisymmetric components of the field near $r = r_{\rm cor}$ re-establishes itself in the saturated state.

In summary, good agreement is obtained between asymptotic and numerical solutions, especially in the growth rates and various qualitative features. The semi-analytical model presented thus generally succeeds in capturing the key properties of the system. However, certain details of the solution, especially for finite τ, such as the extent of the phase shift between the magnetic and material arms, are underestimated by the asymptotic analysis.

4.3.4 The phase difference caused by a finite dynamo relaxation time

It is also interesting to explore how the phase difference Δ varies with the dimensionless quantity $\Omega_{\rm p}\tau$. Here we retain the disc model (of the asymptotic example or of Model E from Chapter 3 but vary τ. Figure 4.8 shows the phase difference Δ as a function of $\Omega_{\rm p}\tau$ for the asymptotic solution of Section 4.2.3, shown by crosses in the plot, confirming that $\Delta \approx -C\Omega_{\rm p}\tau$ with C a constant of order unity. It can be seen that the relation is not strictly linear and tends to flatten as $\Omega_{\rm p}\tau$ increases, but is approximately linear for $\Omega_{\rm p}\tau < 0.5$, which is the region of parameter space that normally applies to disc galaxies. Figure 4.8 also presents results from the numerical solution of Model E from Chapter 3, discussed in Section 4.3.1 above, where the galaxy model is more realistic than in the analytical solution obtained in Section 4.2.3. For Model E, the scaling relation $\Delta \propto \Omega_{\rm p}\tau$ (for small $\Omega_{\rm p}\tau$) quickly establishes itself in the kinematic regime, as soon as the leading eigenfunction becomes dominant. Remarkably, it applies to both kinematic dynamo solutions and to the steady state, with more or less the same proportionality constant. The magnitude of the proportionality constant $C \approx 1.7$ (represented by the solid line in the figure) is still of order unity, but is significantly larger than $C \approx 0.65$ (dashed line) found in the asymptotic

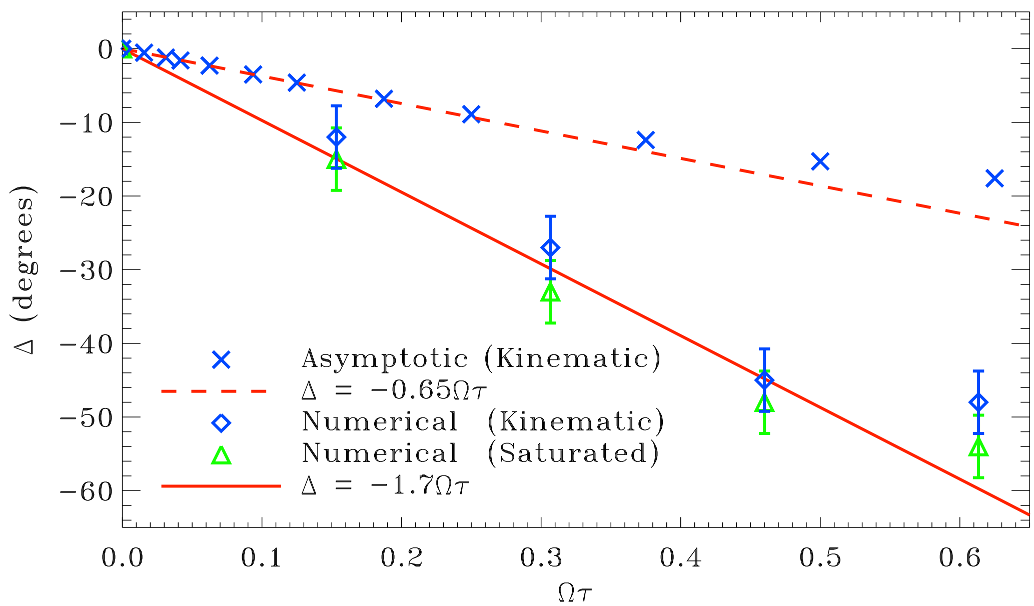

Figure 4.8: The phase difference Δ between the solutions with $\tau \neq 0$ and $\tau = 0$ as a function of $\Omega_{\mathrm{p}}\tau$. Results for the parameter values used in the illustrative example are shown with blue crosses; those from Model E of Chapter 3 are shown during the kinematic regime (at $t = 3t_{\mathrm{d},0}$ after the simulation has begun) and in the steady state.

solution. Although this difference may be partly attributable to the different disc models used, the larger value of C in the numerical model is also partly due to higher-order even modes, as discussed in Sections 4.2.2 and 4.3.1 above.

4.3.5 Extrapolation to the nonlinear regime

The asymptotic solution obtained here is strictly valid only in the kinematic (linear) regime. However, we find that the general properties of the nonlinear numerical solution are very similar to the asymptotic one, and we discuss here the generalisation of the asymptotic solution to nonlinear, saturated states.

In the dynamic nonlinearity model (Pouquet et al., 1976; Kleeorin & Ruzmaikin, 1982; Gruzinov & Diamond, 1994; Blackman & Field, 2000; Rädler et al., 2003; Brandenburg & Subramanian, 2005a), the modification of the α-effect by the Lorentz force is represented as an additive magnetic contribution α_{m}, so that the total α-coefficient becomes

$$\alpha = \alpha_{\mathrm{k}} + \alpha_{\mathrm{m}}, \tag{4.37}$$

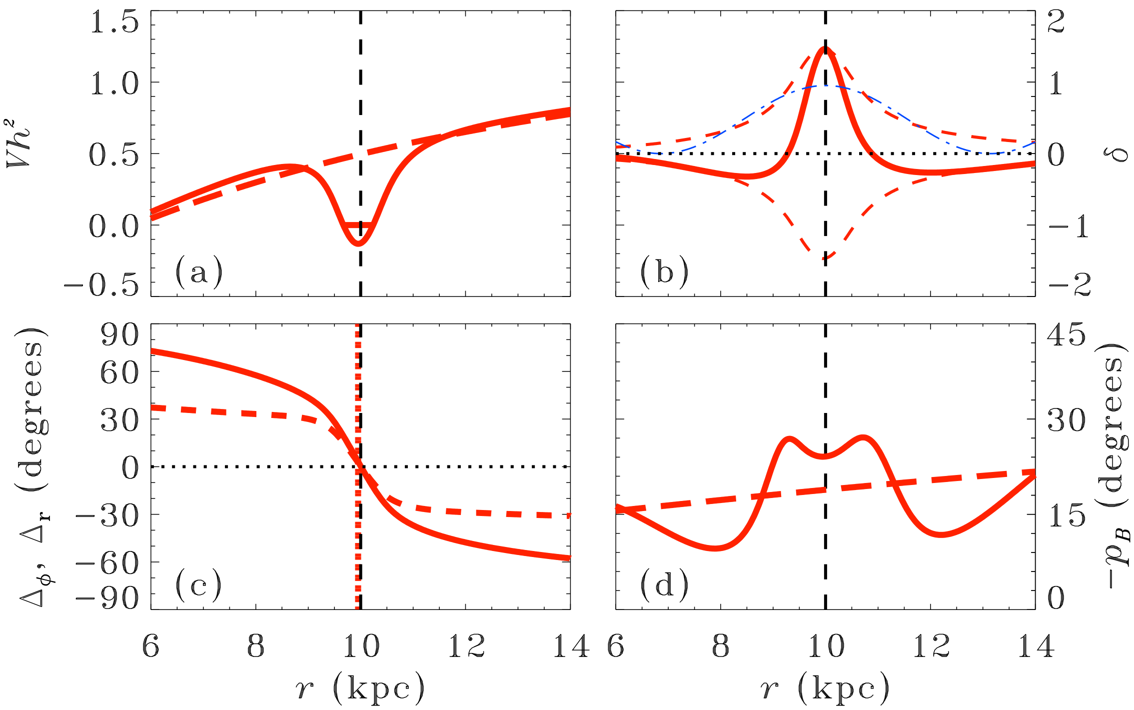

Figure 4.9: As in Fig. 4.1 (with $\tau \to 0$) but for $\alpha_0 = 0.441\,\mathrm{km\,s^{-1}}$, which ensures that $\Gamma = 0$.

where α_k is proportional to the kinetic helicity $\overline{\boldsymbol{u} \cdot \nabla \times \boldsymbol{u}}$ of the random flow and is independent of magnetic field, whereas α_m is proportional to the small-scale current helicity $\overline{\boldsymbol{b} \cdot \nabla \times \boldsymbol{b}}$. At an early stage, magnetic force is negligible and $\alpha \approx \alpha_\mathrm{k}$, but α_m (whose sign is opposite to that of α_k) builds up as the mean magnetic field grows. This reduces (quenches) the net α-effect and leads to a steady state.

As an approximation to the steady-state nonlinear solution, we consider the marginal asymptotic solution, i.e., the one with $\Gamma = 0$ (see also Chapter 2). To obtain it, we iterate the values of α_0, defined in (4.10), until the quantization condition (4.31) is satisfied. (We recall that the procedure to find other solutions is to iterate Γ.) The value of α_0 after the iterations is smaller than the starting one; the difference is attributed to α_m.

Results for $\tau \to 0$ are shown in Fig. 4.9, in a form similar to Fig. 4.1. Equation (4.31) (with $k = 0$) is satisfied for $\alpha_0 = 0.44\,\mathrm{km\,s^{-1}}$, with the starting value $\alpha_0 = 1\,\mathrm{km\,s^{-1}}$. The solution is not very different from the kinematic solution of Fig. 4.1, with somewhat shallower potential well and smaller magnitude of the pitch angle near $r = r_\mathrm{cor}$. The marginal solution for the dominant inner mode near $r = r_\mathrm{D}$ obtained in this way has $\alpha_0 = 0.35\,\mathrm{km\,s^{-1}}$.

We also solved the mean-field equations with the nonlinearity (4.37) and the same disc

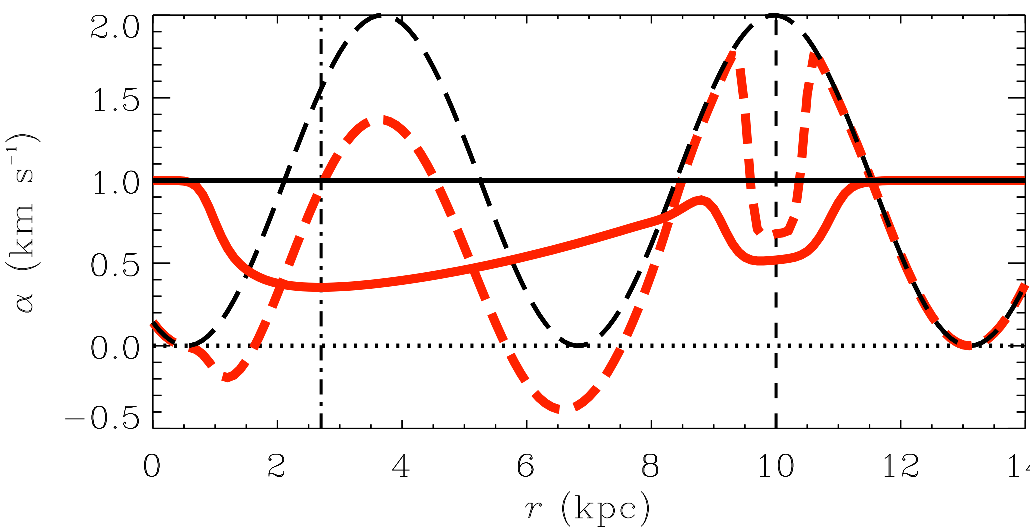

Figure 4.10: The steady-state numerical solution based on dynamical quenching, (4.37), for the same disc parameters as in the asymptotic model. Dashed lines show $\alpha_{\rm k}$ (thin black) and the total α (thick red) as functions of r at $\phi = \phi_{\rm cor}$, whereas solid lines are for the respective azimuthal averages. The vertical lines indicate the corotation radius $r_{\rm cor} = 10\,{\rm kpc}$ and the radius (about 2.6 kpc) where magnetic field strength is maximum.

parameters as those used in the marginal asymptotic solution (for details see Chapter 3). We include a diffusive magnetic helicity flux with a diffusivity $0.3\eta_{\rm t}$ (Mitra et al., 2010; Candelaresi et al., 2011). The resulting steady-state form of $\alpha(r)$ is shown in Fig. 4.10. At the radius where magnetic field has maximum strength, the azimuthally averaged value of α obtained numerically is $\alpha = 0.35\,{\rm km\,s^{-1}}$, in surprisingly good agreement with that from the asymptotic solution. At $r = r_{\rm cor}$, the azimuthal average is $\alpha = 0.52\,{\rm km\,s^{-1}}$ as compared to $0.44\,{\rm km\,s^{-1}}$ from the asymptotic solution. Thus, the steady-state nonlinear state of the galactic mean-field dynamo, obtained with the dynamical nonlinearity, is reasonably well approximated by the marginal kinematic solution.

In summary, asymptotic solutions obtained here clarify numerical results of Chapter 3 and help us to isolate their generic features. Figure 4.1 can be compared with Fig. 3.8 of Chapter 3, which shows similar kinematic results, confirming the presence of a strong $|m| = 2$ magnetic component near $r = r_{\rm cor}$. Around this radius we see clearly from the asymptotic analysis that the effective potential $V(r)$ has a new minimum, allowing new bound states (or growing modes) of $q(r)$ near corotation. Both asymptotic and numerical solutions reveal stationary modes with even azimuthal components in the frame corotating with the spiral pattern of the α-coefficient. Both have magnetic spiral arms more tightly wound than the α-arms, with the two types of arm crossing near the corotation circle. Moreover, both numerical and asymptotic results, the latter, e.g., in equation (4.26), also agree in that the response of the mean magnetic field to the α-spiral pattern is stronger when τ is finite. Furthermore, they agree in that magnetic arms undergo a (against the direction of the galactic rotation) phase shift of order $-\Omega_{\rm p}\tau$ such that the part of the magnetic arm which trails the α-arm is enhanced when τ is finite. Enslaved components with $|m| > 2$, though weak, can substantially enhance the phase shift because they are located further out in radius than the $|m| = 2$ component, where magnetic arms lag α-arms.

4.4 Conclusions

We have extended non-axisymmetric mean-field dynamo theory in two ways. Firstly, we have obtained semi-analytic solutions for the axisymmetric and the dominant enslaved non-axisymmetric components ($m = 0$ and $m = \pm 2$ for a two-armed α-spiral). Previously, the only analytical treatment that existed was for the sub-dominant non-enslaved modes (with $m = \pm 1$). Secondly, we have included and explored the effects of the finite relaxation time τ of the mean electromotive force, related to the finite correlation time of the random flow.

We assume that galactic spiral arms lead to the α-effect enhanced along spirals which may coincide with the material arms or may be located in between them. The asymptotic solutions employ the WKBJ approximation applicable to tightly wound magnetic spirals; to obtain explicit expressions for the growth rate of the mean magnetic field and its radial and azimuthal distributions we use the no-z approximation to solve the local dynamo equations.

We find overall good qualitative agreement with the numerical results of Chapter 3 for a global, rigidly rotating spiral pattern (which is the type of spiral forcing most amenable to analytical treatment) to grow around the corotation radius. In particular, the asymptotic solution obtained here agrees with the numerical solution of Chapter 3 in the following key features.

(i) Strong magnetic modes with the azimuthal wave numbers $m = \pm n$ are supported by the dynamo action, which corotate with the α-spiral (here n is the number of α-spiral arms). Non-axisymmetric modes are confined to a radial range of a few kiloparsecs around the corotation radius and enslaved non-axisymmetric components are comparable in strength with the $m = 0$ component.

(ii) Magnetic arms (understood as ridges of the mean magnetic field strength that have a spiral shape) cross the α-spiral near the corotation radius and are more tightly wound than the α-arms.

(iii) In the model considered here, the only effect of the galactic spiral pattern is the enhancement of the dynamo α-coefficient by the spiral pattern. As a result, the magnetic lines of the mean field are less tightly wound (larger magnitude of the pitch angle p_B) within the α-spirals than between them.

(iv) The amplitude of the non-axisymmetric modes increases with the magnitude of the relaxation time τ.

(v) Another effect of the finite magnitude of τ is that the part of the magnetic arm that lags behind the α-arm with respect to the galactic rotation (i.e., outside the corotation radius) becomes stronger than the part that precedes the α-arm (inside the corotation radius). This leads to the overall appearance of magnetic arms that are phase-shifted from the α-arms (material arms) in the direction opposite to the galactic rotation.

(vi) For $\Omega_\mathrm{p}\tau \lesssim 0.5$, the phase shift produced by a finite value of τ (relative to that for $\tau \to 0$), is directly proportional to $-\Omega_\mathrm{p}\tau$, with a proportionality constant of order unity.

4.5 Discussion

Results obtained in Chapter 3 and in the present chapter for a rigidly rotating α-spiral demonstrate the ability of the mean-field dynamo mechanism to produce magnetic arms that do not overlap with the material arms in the regions where the former are best pronounced, which is outside the corotation circle in our model. Due to a finite magnitude of the relaxation time of the mean electromotive force, τ, the lagging part of the magnetic arm is better pronounced than that ahead of the material arm, which can make it difficult to detect their intersection in the observations. As a result of advection of the mean magnetic field by the differentially rotating gas, magnetic arms are, in these models, more tightly wound than the α-spiral which drives them, and are localized to within a few kiloparsecs of the corotation circle. The phase shift between the magnetic and α-arms in our model vanishes at or near the corotation radius and then increases, first rapidly and then at a lower rate, up to a value as large as 60° at a distance of a few kpc from the corotation circle.

The morphology of magnetic arms in spiral galaxies and their position relative to the material arms is rather diverse. One extreme is the galaxy NGC 6946 where magnetic arms appear to have the same pitch angle as the optical arms, and the two patterns do not intersect. The azimuthal phase shifts between the individual optical arms and their magnetic counterparts identified by Frick et al. (2000) are $-26^\circ \pm 12^\circ$, $-36^\circ \pm 11^\circ$ and $-45^\circ \pm 17^\circ$ at $r \approx 4\,\mathrm{kpc}$ and, for an outer arm, $-68^\circ \pm 17^\circ$ at $r \approx 8\,\mathrm{kpc}$, where negative phase shift corresponds to a position behind a gaseous arm (all distances have been reduced to a distance of 5.5 Mpc to NGC 6946 – Kennicutt et al., 2003). According to the Hα observations and analysis of Fathi et al. (2007), the corotation radius of the outer spiral pattern in this galaxy is at about 8.3 kpc, whereas the interlaced magnetic and optical spiral arms occur at $1 \lesssim r \lesssim 9\,\mathrm{kpc}$. The dynamo action at $r \gtrsim 9\,\mathrm{kpc}$ may be too weak to make the magnetic arms observable there, but there are no indications of the magnetic and optical arms crossing at or near the corotation radius. Nevertheless, the right magnitude of the azimuthal phase shifts obtained in our models (15–40°) is arguably encouraging.

Another possibility is that the spiral structure in NGC 6946 is more complex than that of a single, rigidly rotating pattern. For instance, the arms may be winding up to some extent, and thus transient (e.g. Dobbs et al., 2010; Sellwood, 2011; Quillen et al., 2011; Wada et al., 2011; Grand et al., 2012). The model of Comparetta & Quillen (2012) invokes multiple rigidly rotating patterns, which interfere to produce spiral features that wind up. Magnetic arms which are present over several kiloparsecs in radius, and which have a large negative phase shift from the α-arms that varies only weakly with radius, like in NGC 6946, are indeed found in our 'winding-up' spiral model of Chapter 3.

On the other hand, the mutual arrangement of magnetic and material arms is more complicated in M51 (Patrikeev et al., 2006; Fletcher et al., 2011) where the two patterns overlap in some regions but are systematically offset by about 0.5–0.6 kpc elsewhere (adopting 7.6 Mpc for the distance to M51 – Ciardullo et al., 2002). This linear displacement corresponds to the angular phase difference of 5–10° at $r = 3$–6 kpc where such an offset is best pronounced. The two arms visible in polarized emission at $\lambda 6.2$ cm intersect the material arms observed in other tracers at $r = 5$–6 kpc. Elmegreen et al. (1989) suggest that M51 has two spiral arm systems, with the corotation radii at $r = 4.8$ kpc and $r = 12$ kpc. García-Burillo et al. (1993) determine the corotation radius to be 5.8 kpc from CO observations and modelling of M51. Then the region at $r = 3$–6 kpc is (mostly) inside the corotation radius and the magnetic arms in the inner galaxy are displaced downstream of the material arms, as expected in our model. The two magnetic arms are positioned differently with respect to the material arms at larger galactocentric distances. Outside the corotation circle, magnetic Arm 1 (on the east of the galactic centre) is systematically lagging the material arm, in accordance with our model, but the magnetic Arm 2 overlaps the material arm.

Our model appears to be better applicable to this galaxy, but the diverse mutual arrangement of the magnetic and material arms in M51 strongly suggests that more than one physical effect is involved in its genesis. Dobbs et al. (2010) suggest that the spiral arm morphology in M51 evolves rapidly due to the interaction with its satellite galaxy. Magnetic arms driven by evolving material arms are explored in Section 3.5.1 of Chapter 3. It also appears that M51 may be a good candidate for the 'ghost' magnetic arms, where the magnetic arms trace the spiral arms as they were in the past up to a few hundred Myr earlier. The simulations of Dobbs et al. (2010) show that the material spiral arms are being wound up by the galactic differential rotation, so the model with transient material spirals of Chapter 3 may be more relevant to M51 than the model with a rigidly rotating, stationary spiral pattern explored here.

Still another morphology of magnetic and gaseous arms is observed in the nearby barred galaxy M83. Beck et al. (2003) applied the same approach involving wavelet transforms as Frick et al. (2000) to determine the positions of the spiral arms as seen in optical light, dust, Hα, CO, as well as the total and polarized intensities at $\lambda\lambda 6$ and 13 cm. The morphology of M83 is dominated by a well-pronounced two-armed spiral pattern in each tracer, with some substructure within the arms. The magnetic and material arms in this galaxy are clearly separated but intersect at the galactocentric radius 6.4 kpc (given the distance to M83 is 4.5 Mpc – Thim et al., 2003). The corotation radius of M83, determined by Hirota et al. (2009) as 2.4 arcmin, or 6.2 kpc, is practically equal to the intersection radius given the uncertainties involved. This galaxy is a good candidate for the formation of magnetic arms by the mechanism suggested here.

An important assumption of all or most of the available models of magnetic arms is that the α-effect is stronger within, or at least correlated with, the material spiral arms. We note that the effects of the spiral arms on the scale height of the interstellar gas, its turbulent scale and velocity, local velocity shear, and other parameters that control the intensity of the dynamo action are far from being certain, either observationally or theoretically (see Shukurov, 1998; Shukurov et al., 2004, and references therein). Shukurov & Sokoloff (1998) argue that the magnitude of the α effect within the material arms can be four times smaller than between the arms, whereas the turbulent diffusivity is plausible to be only weakly modulated by the spiral pattern. As a result, the local dynamo number within the material arms can be four times smaller than between them, and the dynamo action can, in fact, be more vigorous between the material arms. Direct numerical simulations by Elstner & Gressel (2012) find that both the α effect and turbulent diffusivity increase with star formation rate σ, which itself will be larger within the arms, but this leads to an overall dynamo number that scales inversely with σ. However, even if the dynamo number is larger in the interarm regions, this does not necessarily imply that the steady-state mean magnetic field there should be stronger than within the arms, since the gas density is lower in between the arms than within them. Significant effort in observations, theory of interstellar magnetohydrodynamics and dynamo theory are still required to establish a clear understanding of the various mechanisms that produce the diverse morphology of magnetic arms in spiral galaxies. Our work here and in the previous chapter provides the beginnings of such a study.

In Chapter 3 we found that one of the ingredients that strongly affects the structure and evolution of the non-axisymmetric large-scale magnetic fields generated is the time evolution and morphology of the spiral arms that force the dynamo. The steady rigidly rotating spiral explored in this chapter and the previous one, and the transient corotating spiral that corotates with the gas at every radius explored in the previous chapter, are useful but extreme models. In the next two chapters we adapt these spiral models to make them more realistic. In particular, some of the galaxies that contain magnetic arms have previously been inferred to contain multiple global density waves, rather than a single one. These density waves mutually interfere as they rotate at their respective angular velocities, and it is not a priori obvious what effect this would have on the dynamo. Therefore, a natural extension of our work is to explore how the mean magnetic field evolves when multiple spiral patterns (rather than a single pattern) simultaneously force the dynamo.

It is this topic to which we turn next, using numerical solutions.

Chapter 5

Magnetic arms generated by multiple interfering galactic spiral patterns

5.1 Introduction

We saw in Chapter 3 that the morphology of magnetic arms can be sensitive to the morphological *evolution* of the spiral that forces them. This was especially apparent when we considered two extreme (but oft discussed in the literature) cases: that of a steady rigidly rotating spiral and that of a transient spiral that corotates with the underlying differentially rotating gas, and hence winds up with it. The steady model leads to steady, relatively strong [quantified by δ; see equation (3.32)] magnetic arms, concentrated within just 1–2 kpc of the corotation circle. The magnetic arm structures are azimuthally (but not radially) extended, and hence of small pitch angle ($< 10^\circ$). The τ effect leads to large phase shifts of up to $\sim -40^\circ$ for this spiral model. The transient spiral model leads to somewhat short-lived ($\sim$ 100–200 Myr), relatively weak magnetic arms. However, these magnetic arms are geometrically well-aligned with the underlying spiral arms of the disc, and can extend several kpc in radius, which compares better with most observations. For finite τ, phase shifts as significant as $\sim -25^\circ$ can occur.

It is then natural to ask what effects other, perhaps more realistic, models for the morphological evolution of galactic spirals have on the properties of the magnetic arms generated. This endeavour is promising for two reasons: (i) more realistic models are generally intermediate between the steady and transient models just mentioned, and so would be expected to produce intermediate (and thus potentially interesting) results, and

(ii) the problem could potentially be inverted to probe the evolution of galactic spiral structure, offering the chance of helping to solve a long-standing fundamental problem in astrophysics. Therefore, in this chapter and the next, we introduce two new models of spiral structure and evolution into our galactic dynamo simulation: a model with multiple interfering rigidly rotating patterns (in this chapter and the next), and a linear density wave model (in the next chapter).

To evaluate the level of success of a given spiral model in explaining observations, it is useful to identify generic (or close to generic) observed properties of magnetic arms (if such properties exist). Certain properties of magnetic arms do indeed seem to be rather generic: (i) large radial and azimuthal extents, comparable to those of the gaseous spiral arms (e.g. Krause et al., 1989; Frick et al., 2000; Chyży, 2008; Fletcher et al., 2011), (ii) pitch angles of the magnetic arms (ridges) comparable to those of the spiral arms (e.g. Frick et al., 2000), (iii) pitch angles of the field within the magnetic arms again comparable to those of the gaseous arms (e.g. Fletcher, 2010; Beck & Wielebinski, 2013, and references therein), and (iv) cases where magnetic arms are concentrated in interarm regions or, in any case, not confined to the gaseous arms (Krause et al., 1989; Ehle et al., 1996; Beck & Hoernes, 1996; Beck, 2007; Beck et al., 2005; Chyży, 2008; Fletcher et al., 2011).

None of the above properties have been easy to explain using mean-field dynamo models. As we saw in Chapters 3 and 4, properties (i) and (ii) do not arise naturally when the dynamo is forced by a steady rigidly rotating spiral because magnetic arms tend to be localized to within only $\sim$1-2 kpc of the corotation radius of the spiral pattern invoked to force the dynamo, and to be rather tightly wound, crossing the gaseous arms. However, these two assumptions, typical of most models, viz. that the spiral pattern is both steady and rigidly rotating, are likely unrealistic (Sellwood, 2011; Grand et al., 2012; Quillen et al., 2011; D'Onghia et al., 2013). Indeed, spiral arms that do not rotate rigidly but rather follow the galactic rotation curve and hence rapidly wind up as 'corotating' arms (Wada et al., 2011; Grand et al., 2012) can resolve both of these issues, although the resulting magnetic arms are both relatively weak and short-lived as compared to those produced by a steady rigidly rotating spiral pattern.

Property (iii) is difficult to reproduce in dynamo models for two separate reasons: firstly, standard galactic dynamo parameter values yield pitch angles $\sim -(8^\circ - 20^\circ)$ for the magnetic field $\overline{\boldsymbol{B}}$, which is reasonably consistent with the range of pitch angles of the large-scale magnetic field inferred from observations (Fletcher, 2010). However, there is at least one notable exception: the pitch angle in M33 is inferred from observations to be $\sim -40^\circ$ (Tabatabaei et al., 2008). Secondly, it is not clear how the magnetic field could get aligned to the spiral arms (with pitch angles often in the range $\sim 30 - 40^\circ$), although large-scale streaming motions and shocks may play a role.

Interesting ideas have been put forward to explain property (iv), including the one presented in chapters 3 and 4. Another explanation for interarm concentration of the large-scale magnetic field is presented in Chapter 6.

It should be noted, however, that the above properties are not strictly universal. For example, at least one magnetic arm (ridge) of IC 342 seems to cross an optical arm (Krause et al., 1989). Typical pitch angles of the regular magnetic field in M33, though large in magnitude compared to other galaxies, are significantly smaller in magnitude than those of the optical arms (Fletcher, 2010). In both NGC 6946 and M51 pitch angles of the polarized component of the magnetic field match quite well with those of the magnetic arm structure (ridge) in one of the main arms, but the correspondence is much poorer in the other arm (Beck, 2007; Patrikeev et al., 2006).

To complicate matters, polarized intensity is produced by a combination of regular field and anisotropic random field (e.g. due to compression in spiral shocks and shearing motions), and these two contributions must be disentangled using Faraday rotation measures, which depends on modelling (e.g. Fletcher et al., 2011). Given that compression in shocks would tend to align the magnetic field with the spiral arms (Patrikeev et al., 2006), polarization angles would be expected to be larger than pitch angles of the regular magnetic field within spiral arms, especially for galaxies with strong density waves. All in all, the above four properties can serve to guide the present investigation, but should not be taken as absolute.

As seen in Chapter 3, the structure and dynamics of the gaseous spiral can strongly affect the strength, morphology, and time evolution of the resulting magnetic arms. Therefore, it is important to explore what effect different types of spiral structure and dynamics have on the mean-field dynamo. There is a rapidly growing body of literature that argues for alternate theories of spiral structure and dynamics. Aside from the steady rigidly rotating spiral pattern and corotating (winding up with the gas) arms models mentioned above, galactic spirals can also be modeled as resulting from multiple interfering transient patterns (density waves). This latter possibility is explored in the present chapter. Other models, such as density waves that wind up and propagate (Binney & Tremaine, 2008), are explored in Chapter 6.

Both observational and numerical studies of spiral morphology have provided justification for the existence of more than one spiral pattern in some disc galaxies. On the observational side, Elmegreen et al. (1992), Shetty et al. (2007) and Meidt et al. (2009) have found that galaxies can contain more than one spiral symmetry, with different pattern speeds and multiplicities. On the numerical side Sellwood (2011), Quillen et al. (2011) and

Roškar et al. (2012) have detected multiple spiral patterns (that may overlap in time) in their N-body simulations. Generally, these patterns do not survive for galactic lifetimes, but can survive (in a quasi-steady state) for several rotation periods. Non-linear coupling between density waves at different locations in the disc (Masset & Tagger, 1997) may even lead to (composite) spiral patterns that last for $\gtrsim 10$ rotation periods (D'Onghia et al., 2013). A criticism of many spiral structure studies, e.g. those pertaining to the galactic dynamo, is that evolving spiral patterns have not been considered. We begin to address this issue here with a study of time dependent phenomena due to the presence of multiple patterns.

The chapter is organized as follows. In Section 5.2, the non-axisymmetric galactic dynamo model is presented. In Section 5.3, numerical solutions are described, and where necessary, explained in the light of existing theory. Key results are summarized and discussed in Section 5.5. The relevance of the possible transience of individual spiral patterns, already partially explored in Chapter 3, is taken up in Appendix 5.4.

5.2 The model

The galactic disc dynamo model and numerical code of Chapter 3 are mostly retained. This model is based on the $\alpha^2\Omega$ dynamo model (Ruzmaikin et al., 1988), with the Ω effect produced by the differential rotation, and the α effect presumed to result from helicity in the small-scale turbulence in a rotating and stratified medium (Brandenburg & Subramanian, 2005a). The dynamo equations are solved on a polar grid, linear in r. The numerical code makes use of the thin disc approximation (Ruzmaikin et al., 1988) to avoid having to calculate z-components of the magnetic field and mean electromotive force. It also uses the 'no-z' approximation, which approximates z-derivatives as simple divisions by the disc thickness (Subramanian & Mestel, 1993; Moss, 1995; Phillips, 2001), to reduce the problem to two dimensions. The resolution is $n_r = 300$, $n_\phi = 150$, the outer radius is $R = 20\,\mathrm{kpc}$, and vacuum boundary conditions are imposed at $r = 0, R$.

5.2.1 The galactic disc

The kinetic contribution to α is given by

$$\alpha_\mathrm{k} = \alpha_0\widetilde{\alpha}, \tag{5.1}$$

where α_0 is given by equation (2.2) and $\widetilde{\alpha}$ has an azimuthal mean of unity. As in previous chapters, non-axisymmetry in the disc is imposed by modulating $\widetilde{\alpha}$, and hence α, along a spiral, assumed to be correlated in some way with the gaseous spiral of the galaxy.

For the galactic rotation curve, the Brandt profile (2.5) is used with the same parameters as in Chapters 2 and 3. The disc half-thickness varies hyperbolically with radius according to equation (2.6), with the same parameter values as in previous chapters. The extent to which the ionized component of galactic discs is flared has not been firmly established, and is an assumption of the model. However, there is recent evidence that supports flaring (see the discussion in Chapter 6). Some models that use an unflared disc with constant h have also been explored, and the differences in the results are very minor. The equipartition magnetic field strength is given by (3.24) with the same parameter values as in Chapter 3.

5.2.2 The α_k-spirals

Non-axisymmetric forcing of the dynamo is modelled as an enhancement of the α effect within multiple spiral patterns, which are situated at different radii and hence rotate with different pattern speeds according to the galactic rotation curve. The individual spiral patterns are taken to be steady, rigidly rotating, and logarithmic in shape. The prescription used is close to that of Comparetta & Quillen (2012); the analogous quantity in that paper is the surface density. In polar coordinates (r, ϕ),

$$\widetilde{\alpha}(r, \phi, t) = 1 + \epsilon_1 A_1(r) f_1(r, \phi, t) + \epsilon_2 A_2(r) f_2(r, \phi, t) \tag{5.2}$$

for all models except one; see below. Using $i = 1, 2$ to represent the two spiral patterns, the overall amplitude of each pattern is set by the parameter ϵ_i, modulated by the envelope (Comparetta & Quillen, 2012)

$$A_i = \exp\left\{-\frac{[\log_{10}(r/r_{0,i})]^2}{2w_i^2}\right\}, \tag{5.3}$$

where w_i is a parameter that determines how sharply peaked in radius is the amplitude, and $r_{0,i}$ is the radius at which the amplitude peaks. The values $w_i = 1$ and $r_{0,i} = r_{\mathrm{c},i}$ (Table 5.1) are used, corresponding to a fairly flat envelope function gently peaked at the corotation radius of the respective pattern. Values $w_1 = 0.14$, $w_2 = 0.17$, $r_{0,1} = 5\,\mathrm{kpc}$, $r_{0,2} = 6\,\mathrm{kpc}$ were also tried for the standard model A23, making the patterns more localized in radius and peaked slightly inward of corotation, and thus closer to the model of Comparetta & Quillen (2012) and the patterns seen in Quillen et al. (2011). However, this was found to affect the results only very slightly, showing that the model is insensitive to modest adjustments to the envelope function. Values $w_i = 1$ and $r_{0,i} = r_{\mathrm{c},i}$ are therefore retained to keep the number of independent parameters to a minimum. Non-axisymmetry is implemented using

$$f_i = \cos(\chi_i) + 0.25\cos(2\chi_i), \tag{5.4}$$

where the second term makes the function more peaked at $\phi = 0$ than a simple cosine (Comparetta & Quillen, 2012), and the angular part

$$\chi_i = -n_i(\phi - \Omega_{\mathrm{p},i}t) + \kappa_i \ln(r/R) \tag{5.5}$$

leads to a logarithmic spiral. The quantity n_i designates the number of arms in the pattern, κ_i (< 0 for a trailing spiral) determines how tight is the spiral, and $\Omega_{\mathrm{p},i} \equiv \Omega(r_{\mathrm{c},i})$ is the pattern angular speed. Using the standard definition for pitch angle,

$$\text{pitch angle} \equiv \cot^{-1}\left(\frac{\partial\phi_{\max}}{\partial \ln r}\right),$$

where $\phi_{\max}$ is the azimuth at which a given spiral perturbation ($\epsilon_i A_i f_i$ in this case) is maximum, it can easily be shown that the pitch angle of each individual α_{k} spiral pattern is

$$p_{\alpha,i} = \tan^{-1}\left(\frac{n_i}{\kappa_i}\right),$$

which gives $p_{\alpha,1} = -34^\circ$ and $p_{\alpha,2} = -27^\circ$ for the two- and three-arm models, and $p_{\alpha,1} = p_{\alpha,2} = -34^\circ$ for the two- and four-arm models studied.

5.2.3 The parameter space studied

A list of models (runs), as well as the parameter values used for each, is given in Table 5.1. For each set of parameter values in Table 5.1, the dynamo relaxation time τ is taken to be alternately equal to zero or the eddy turnover time $l/u = 9.8\,\mathrm{Myr}$, where $l = 0.1\,\mathrm{kpc}$ is the scale and $u = 10\,\mathrm{km\,s^{-1}}$ the rms velocity of the largest turbulent eddies. Those models suffixed with 'τ' have $\tau = l/u$ while those without this suffix have $\tau = 0$. Models A2, A3 and A23 are the fiducial two-, three-, and the combined two- and three-arm models, respectively. Model B2 (B3) has the same parameters as A3 (A2), except for the number of arms, to explore the effect of the number of arms on the solution. Model L23 (S23) is the same as A23 but with the inner pattern moved inward (outward) to explore the effect of a larger (smaller) radial separation between the two- and three-arm patterns. Model A24 again has the same parameters as Model A23 except that the outer pattern now contains four arms. Model T23 also has the same parameters, except now the transient nature of galactic spiral patterns are explored. In this model, both patterns are imposed from the

Table 5.1: Parameter values for the various models studied: pattern index i, multiplicity n_i, parameter κ_i, α_k-spiral pitch angle $p_{\alpha,i}$, normalized spiral perturbation amplitude ϵ_i, corotation radius $r_{\mathrm{c},i}$, activation and de-activation times for spiral forcing $t_{\mathrm{on},i}$ and $t_{\mathrm{off},i}$, respectively. All models were run with $\tau = 0$ and $\tau = l/u$ (the latter designated with 'τ' after the model name). A2: Standard two-arm model. A3: Standard three-arm model. B2: Alternate two-arm model. B3: Alternate three-arm model. A23: Standard two- and three-arm model. A24: Two- and four-arm model. T23: Transient two- and three-arm model. L23: Large separation two- and three-arm model. S23: Small separation two- and three-arm model. X23: Alternate disc two- and three-arm model. Distances $r_{\mathrm{c},i}$ are in kpc, while times $t_{\mathrm{on},i}$ and $t_{\mathrm{off},i}$ are in Gyr.

Model	i	n_i	κ_i	$p_{\alpha,i}$	ϵ_i	$r_{\mathrm{c},i}$	$t_{\mathrm{on},i}$	$t_{\mathrm{off},i}$
A2/A2τ	1	2	-3	$-34°$	0.5	6	0	–
A3/A3τ	1	3	-6	$-27°$	0.5	7	0	–
B2/B2τ	1	2	-6	$-18°$	0.5	7	0	–
B3/B3τ	1	3	-3	$-45°$	0.5	6	0	–
A23/A23τ	1	2	-3	$-34°$	0.5	6	0	–
	2	3	-6	$-27°$	0.5	7	0	–
A24/A24τ	1	2	-3	$-34°$	0.5	6	0	–
	2	4	-6	$-34°$	0.5	7	0	–
T23/T23τ	1	2	-3	$-34°$	0.5	6	4.5	5
	2	3	-6	$-27°$	0.5	7	4.5	5
L23/L23τ	1	2	-3	$-34°$	0.5	5	0	–
	2	3	-6	$-27°$	0.5	7	0	–
S23/S23τ	1	2	-3	$-34°$	0.5	6.5	0	–
	2	3	-6	$-27°$	0.5	7	0	–
X23/X23τ	1	2	-3	$-34°$	1.0	6	0	–
	2	3	-6	$-27°$	1.0	7	0	–

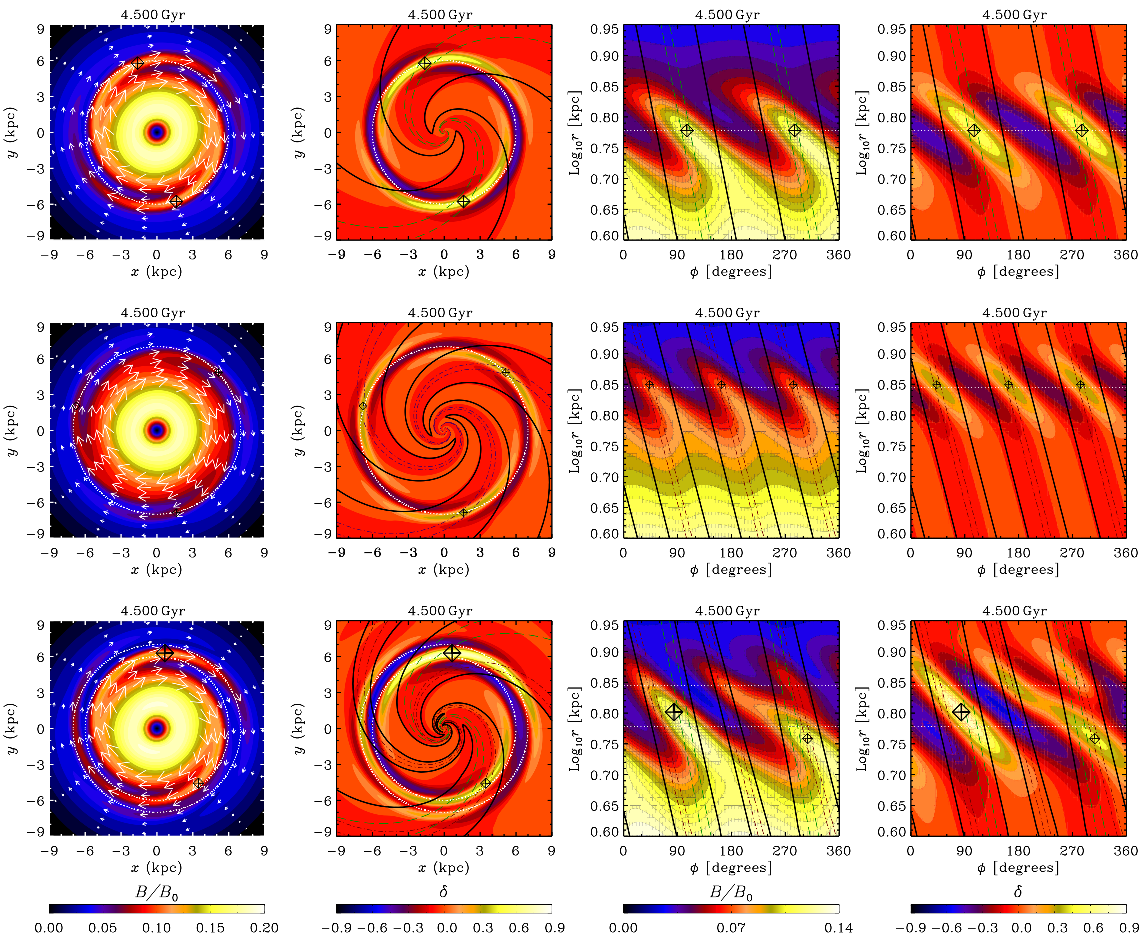

Figure 5.1: Left column: magnitude of the total mean magnetic field, normalized to the equipartition field at $r = 0$ (see Chapter 3) at $t = 4.5\,\mathrm{Gyr}$ for Model A2 with two-arm forcing (top), Model A3 with three-arm forcing (middle) and Model A23 with both two- and three-arm forcing (bottom). Field vectors show the relative magnitude and pitch angle of the field. Corotation circles for the two patterns are shown by white dotted lines. A cross within a diamond designates the locations of the two largest local maxima of δ, defined in Eq. (3.32); the symbol size is proportional to the local value of δ. Second column from left: the quantity δ. Black contours identify the 50% level of α_k, normalized to the azimuthal mean, while dashed and dash-dotted lines are the 95% contours of the two- and three-arm perturbations to α_k, respectively. Third column from left: the mean magnetic field strength in 'unwound' $\log_{10}(r)$ vs. ϕ coordinates (with ϕ starting at the positive x-axis and increasing in the counter-clockwise direction). Right column: δ in $\log_{10}(r)$ vs. ϕ coordinates.

time $t = 4.5\,\mathrm{Gyr}$ (magnetic field already in the saturated state), and turned off at the time $t = 5\,\mathrm{Gyr}$. Although this is admitedly an oversimplication, it is sufficient for its intended purpose, which is to test how rapidly and in what manner the magnetic field can adjust to the turning on and turning off of a transient spiral pattern, in the saturated state. For all other models, the spiral patterns are imposed from $t = 0$, and their governing parameters are kept constant for the duration of the simulation ($\sim 5\,\mathrm{Gyr}$). The magnetic field is then studied at $t > 4.5\,\mathrm{Gyr}$, which corresponds to the saturated state. However, the field is studied for only a few rotation periods of the pattern (i.e. few $\times\, 0.15\,\mathrm{Gyr}$ for the innermost pattern in Model A23), comparable to the typical lifetimes of such patterns seen in some simulations (e.g. Quillen et al., 2011). Model X23 uses disc and dynamo parameters that, while still realistic, are found to be better suited to producing the observed properties of Sect. 5.1: $\overline{U}_\phi(10\,\mathrm{kpc}) = 180\,\mathrm{km\,s^{-1}}$, $\epsilon_1 = \epsilon_2 = 1$, $h_\mathrm{D} \simeq 0.32\,\mathrm{kpc}$ and $\overline{U}_z = 2\,\mathrm{km\,s^{-1}}$ at $r = 0$, decreasing smoothly to $0.2\,\mathrm{km\,s^{-1}}$ at $r = 10\,\mathrm{kpc}$. Moreover, f_i in equation (5.2) is replaced by $(0.75 + f_i)$ so that $l^2\Omega/h$ (Krause's law) now represents the *minimum* of α_k [see equations (2.2) and (5.4)].

5.3 Results

The magnetic arm morphology that arises when two patterns force the dynamo is substantially more complex than that which arises from forcing by a single pattern. This can be seen from Figure 5.1, part of which shows the large-scale magnetic field strength $B \equiv |\overline{\boldsymbol{B}}|$, normalized to the equipartition field strength at $r = 0$, $B_0 \equiv B_\mathrm{eq}(0)$, in the leftmost and third from left columns. All snapshots are taken at the same time, 4.5 Gyr after the start of the simulation, when the magnetic field is in the saturated (almost steady) state. In the left two columns Cartesian coordinates are used, while in the right two columns, $\log_{10}(r)$ vs. ϕ coordinates are used. In the second from left and rightmost columns, the quantity illustrated is δ [equation (3.32)]. (The quantity δ is, in some sense, more useful than $|\overline{\boldsymbol{B}}|$ when discussing magnetic arms because it is not biased to small radii, where the axisymmetric field itself is stronger. For this reason, it represents quite faithfully the degree of non-axisymmetry as a function of r.) The top row shows the result of forcing by the two-arm pattern alone (Model A2), the middle row shows the same for the three-arm pattern alone (Model A3), and the bottom row shows the result obtained when both patterns are included (Model A23). In all plots showing $|\overline{\boldsymbol{B}}|$ or δ, a cross enclosed within a diamond has been plotted at the two largest local maxima of δ, with symbol size proportional to the local δ.

5.3.1 Relative strength of two- and three-arm magnetic field patterns

The effect of the three-arm α_k-pattern, whose corotation radius is $r_{\mathrm{c},2} = 7\,\mathrm{kpc}$, on the magnetic field, is somewhat weaker than that of the two-arm α_k-pattern ($r_{\mathrm{c},1} = 6\,\mathrm{kpc}$). This can be seen by comparing the strength of the large-scale field within the magnetic arms for Models A2 and A3 in, e.g., the third column from the left of Figure 5.1, or by noting that the two-arm ($m = 2$) symmetry of the magnetic field dominates over the three-arm ($m = 3$) symmetry for Model A23. As it turns out, δ also attains larger values for Model A2 than for Model A3. This is mainly due to the number of arms being smaller in the former case, rather than to the location of the corotation radius. In going from Model A2 (A3) to B3 (B2), only the multiplicity n has been altered, resulting in a weaker (stronger) δ profile. This is shown in Figure 5.2, where the δ profile for Model A2 in the top left panel can be compared with that of B3 in the top right, and that of A3 in the bottom left can be compared with that of B2 in the bottom right. Therefore, the amplitude of δ is not greatly affected by the location of the corotation radius, but it is inversely related to the pattern multiplicity n. This result was not previously appreciated in studies of forcing by non-axisymmetric α_k.

5.3.2 Strength and spatial extent of magnetic arms

Magnetic arms generated in Model A23 can be stronger, as well as more radially and azimuthally extended than those generated in Models A2 or A3. However, arms that are weaker and less extended than those of Models A2 or A3 can co-exist with these more extended arms. These attributes can be seen most clearly by comparing profiles of δ for Models A2 (top right) and A3 (middle right) of Figure 5.1, with those of panel A23 (bottom right). Peaks of δ can be significantly larger when more than one spiral is invoked (about 1.4 times as large in Model A23 compared to Model A2). Moreover, the contours corresponding to the regions of high δ, diagonally oriented yellow/orange 'fingers' in the panels, can clearly be more elongated for Model A23 than for the models with only a single pattern. In Models A2 and A3, magnetic arms are centred and have maximum amplitude near the corotation radius, whilst in Model A23, magnetic arms can extend from inside the inner corotation to outside the outer corotation, and be peaked either in between the two corotation circles, or inside the inner corotation circle. The extent of a magnetic arm may be defined as a contiguous region for which $\delta > 0.1$. Then the extents of the magnetic arms in Models A2 are approximately $(\Delta r,\, \Delta\phi) = (2.7\,\mathrm{kpc},\, 210^\circ)$, while those of A3 are approximately $(2.2\,\mathrm{kpc},\, 140^\circ)$. On the other hand, the extents of the magnetic arms in Model A23 at $t = 4.5\,\mathrm{Gyr}$ are approximately $(3.5\,\mathrm{kpc},\, 230^\circ)$, (3.5 kpc,

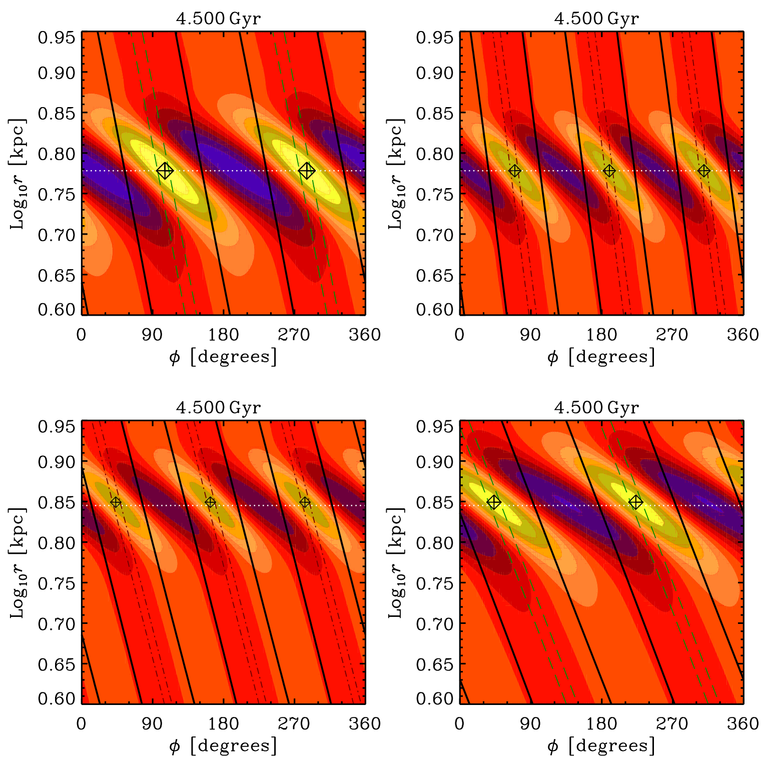

Figure 5.2: Left column: the same as the upper panels of the rightmost column of Figure 5.1, showing δ for Model A2 (top) and A3 (bottom). Right column: the same but now for Model B3 (top) and B2 (bottom).

290°), ($1.3\,\mathrm{kpc}$, 90°) (for arms I, II and III in the order that they intersect the $n = 3$ corotation radius when going from small to large ϕ). The extents for magnetic arms for this model at other times are generally similar to these. It is therefore seen that the two main magnetic arms in Model A23 have significantly larger radial and azimuthal extents than magnetic arms from Models A2 and A3, while the third, less prominent arm (or armlet), has smaller radial and azimuthal extent than the other two arms or the arms of Models A2 and A3. At the same time, the strengths of the arms in Model A23 are quite drastically different, with arm I having a peak strength [$\max(\delta) = 0.83$] of about 1.7 times that of arm II [$\max(\delta) = 0.49$] and 3.2 times that of arm III [$\max(\delta) = 0.26$]. For comparison, $\max(\delta) = 0.60$ for Model A2 and $\max(\delta) = 0.38$ for Model A3. Therefore, arm I has greater strength than arms of both the two- and three-arm models, arm II has comparable, though slightly smaller strength than arms of Model A2, while arm III has even smaller strength than the arms of Model A3. It should be emphasized, however, that the cutoff at $\delta = 0.1$ is arbitrary, and a higher cutoff would imply more magnetic arms. This is because while magnetic arms may be relatively thick and uniform in δ (e.g. arm I), they may also be thin and non-uniform, with an inner maximum in δ, followed by a clear minimum and another maximum as one moves out along the arm (e.g. arm II).

It is clear from Figure 5.1 that the δ-pattern in Model A23 can loosely be thought of as a superposition of those from Models A2 and A3. Where these two patterns overlap, there is effectively constructive and destructive interference. A magnetic arm 'segment' from the two-arm pattern can become 'merged' with one from the three-arm pattern, with the region between the two being 'filled in' due to effective constructive interference, resulting in a more extended magnetic arm. The remarkably high accuracy of the superposition approximation can be understood, qualitatively, as due to the superposition of the effective potentials, when the dynamo model is mapped to an eigenvalue problem as in Chapter 4. This approximation works less well as the radial separation between the two patterns is decreased.

The effect of changing the radial separation between the two spiral patterns has also been explored. In Model L23 ('large separation'), the two sets of magnetic segments (i.e. the two-arm and three-arm sets) are more disjoint, i.e. undergo less effective interference. The magnetic field evolves more rapidly with time, as the beat frequency between the two patterns is greater due to their increased separation. In Model S23 ('small separation'), magnetic arms are less elongated than those in Model A23, and the field configuration evolves less rapidly than in Model A23. It should be noted, however, that for real galaxies, the rotation curve may vary more rapidly with radius than the Brandt curve used here, and therefore, a small separation in corotation radii need not imply a small separation in pattern speed.

5.3.3 Effect of a finite dynamo relaxation time τ

As discussed in Chapters 3 and 4, the effects of a finite relaxation time τ are to strengthen the magnetic arms and cause them to be more tightly wound, as well as to shift their peaks outward in radius, and backward in azimuth (relative to the sense of the galactic rotation). These effects are evident in Figure 5.3, where a copy of the rightmost column of Figure 5.1 ($\tau = 0$) is shown on the left, and the corresponding plots for the $\tau = l/u$ case are shown on the right. The bottom row illustrates δ for $t = 4.5\,\mathrm{Gyr}$ in Model A23 on the left and for Model A23τ on the right. Magnetic arms are significantly stronger in Model A23τ than in Model A23. Magnetic arms produced for $\tau = 0$ are found to be close in shape to logarithmic spirals in the single pattern case, as they appear as straight lines in the plots for Models A2 and A3, while those produced for $\tau = l/u$ in Models A2τ and A3τ show obvious deviations from logarithmic spirals. Qualitatively, the effects, discussed throughout this chapter, that are caused by the presence of two α_k patterns rather than one, occur in both $\tau = 0$ and $\tau = l/u$ cases. In order to separate the effects of multiple interfering spiral patterns from those of a finite τ, the focus is placed on the $\tau = 0$ case in what follows.

5.3.4 Evolution in time and transient morphological features

In the case of forcing by two patterns, the morphology evolves with time along with the interference pattern of the α_k-spirals. For ease of interpretation, all plots are shown in the frame corotating with the gas situated at $r = 6\,\mathrm{kpc}$, which corresponds to the frame of the two-arm pattern for, e.g., Models A2 and A23. In Figure 5.4 the evolution of the magnetic field is illustrated for Model A23, for a total duration of $0.175\,\mathrm{Gyr}$, which is roughly equal to half the period of the total α_k pattern in this reference frame $2\pi/[3(\Omega_\mathrm{p,1} - \Omega_\mathrm{p,2})] = 0.387\,\mathrm{Gyr}$. [To save space, only half of a full period is plotted, but the full information is effectively recovered if, after reaching the end of the time sequence, one loops back from the beginning, while switching one's attention from the left (right) half of each panel, to the right (left) half.]

Firstly, it may be noted that three magnetic arms (yellow/orange regions) are always visible, with one arm generally weaker than the other two, and also less extended, being confined to the outer disc. Secondly, the spatial relations of the arms with one another evolve with time. The third relatively weak arm usually appears to result from a bifurcation of one of the prominent arms, but sometimes it would be better described as a

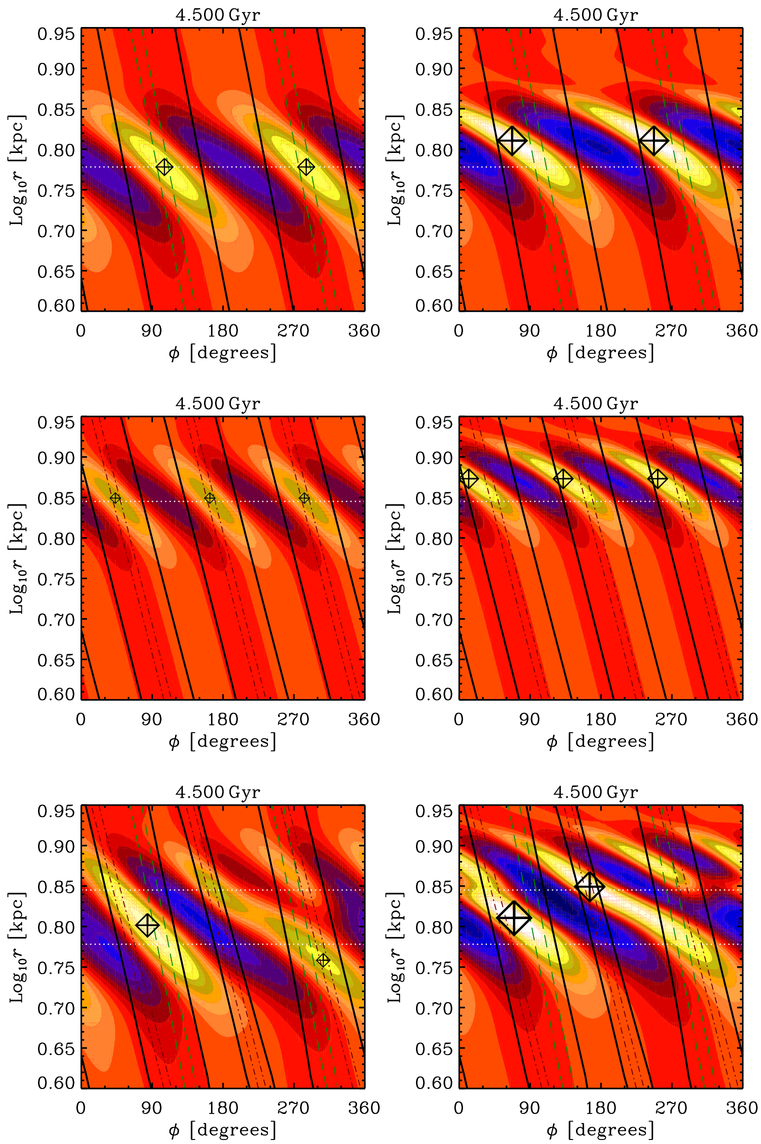

Figure 5.3: Comparison of $\tau = 0$ and $\tau = l/u$ cases. Left column: the same as the rightmost column of Figure 5.1 (Models A2, A3 and A23). Right column: shows the same plots, but for Models A2τ, A3τ and A23τ. For $\tau = l/u$, the colour table has been clipped at $\delta = 0.9$, though δ exceeds this value in some regions.

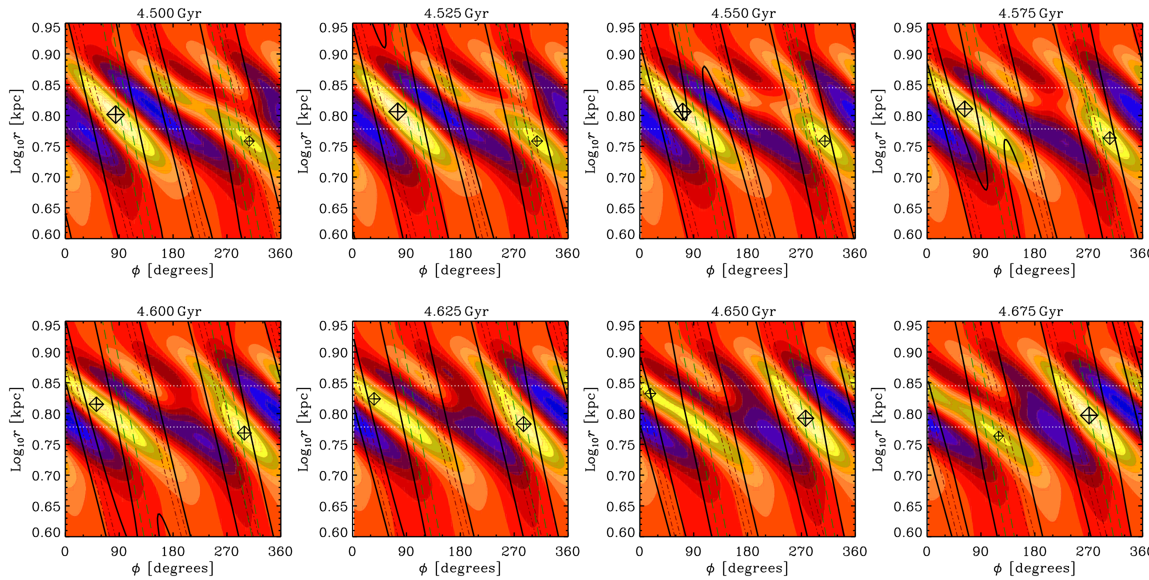

Figure 5.4: Time sequence showing the ratio δ of the non-axisymmetric to axisymmetric part of $\overline{B}_\phi$ for Model A23, with times shown on panels. Colours, contours, corotation radii, and symbols are as in Figure 5.1.

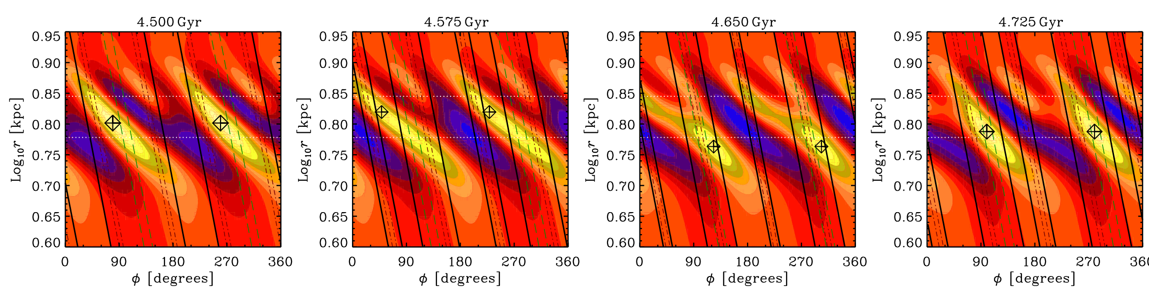

Figure 5.5: Same as figure 5.4, but now for Model A24, and with spacing between successive snapshots increased.

disconnected armlet/filament. As mentioned above, the sequence of plots may be loosely interpreted as effective interference patterns between two inner magnetic arm segments (caused by the two-arm α_k-pattern) and three outer magnetic arm segments (caused by the three-arm α_k-pattern). When a bifurcation is present, two of the three outer magnetic arm segments are joined to the same inner segment, while the third outer segment is joined to the remaining inner segment (‘3a’ and ‘3b’ joined to ‘2a’ and ‘3c’ joined to ‘2b’, say), e.g. at $t = 4.55\,\mathrm{Gyr}$. When a disconnected filament is instead present, two of the three outer segments are each joined to different inner segments, while the third outer segment is isolated from the inner segments (‘3a’ to ‘2a’, ‘3b’ to ‘2b’ and ‘3c’ isolated, say), e.g. at $t = 4.65\,\mathrm{Gyr}$.

Since certain galaxies, such as IC 342, have been reported to contain an inner $n = 2$ and outer $n = 4$ pattern (Crosthwaite et al., 2000), Model A24 is studied, which is identical to Model A23 except that $n_2 = 4$ instead of 3; a time sequence is shown in Figure 5.5. Morphological features of magnetic arms discussed in Sect. 5.3.2, 5.3.4 and 5.4.1 below, such as bifurcations, isolated armlets, and variation in pitch angle and extent, are also seen for this model. Note also that π-fold symmetry is always present in this model.

Although each individual spiral pattern has been modelled as steady and rigidly rotating, it is known that spiral patterns may in fact be transient. A brief discussion of the implications of spiral transience vis-à-vis the dynamo is presented in the next section.

5.4 Effect of making the α-spirals transient

Galactic spiral patterns may typically last for only a few galactic rotation periods, and so it is important to explore how magnetic arms develop and evolve when forced by transient patterns. For this purpose, Model T23 invokes both two- and three-armed patterns from the time $t = 4.5\,\mathrm{Gyr}$, when the axisymmetric field is saturated. These patterns are subsequently turned off at the time $t = 5\,\mathrm{Gyr}$, i.e. 3.3 rotation periods of the innermost pattern later. Figure 5.6 shows a sequence of snapshots of δ, starting from $0.125\,\mathrm{Gyr}$ after the time when spiral forcing is turned on. It can be seen that it takes only about $0.3\,\mathrm{Gyr}$ from the onset of spiral forcing (about 2 rotation periods of the innermost pattern) for the δ pattern to have amplitude and morphology comparable to that of Model A23, for which the spiral forcing was present from $t = 0$. After spiral forcing is stopped, magnetic arms remain at the level $\delta > 0.1$ for a few hundred Myr, but their pitch angles p get gradually smaller because of the galactic differential rotation. For $\tau = l/u$, the magnetic arms last for a few hundred Myr longer still. This is consistent with what was seen for the transient rigidly rotating spiral models of Chapter 3.

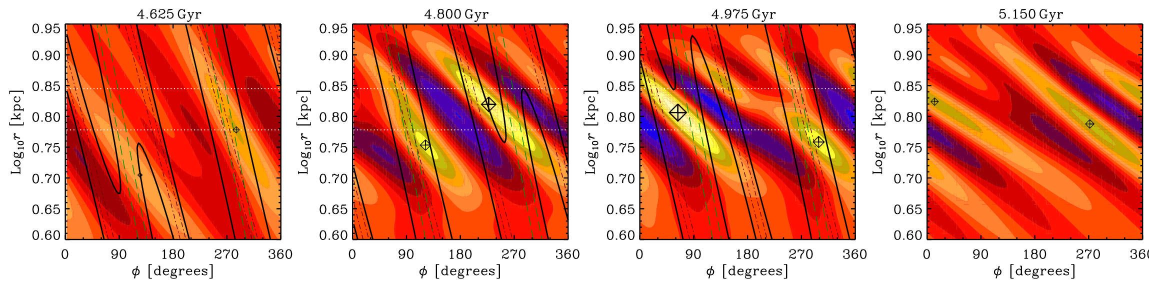

Figure 5.6: Time sequence showing the evolution of δ for Model T23 (transient spiral patterns). The α_k-spirals are turned on at $t = 4.5\,\text{Gyr}$ and turned off at $t = 5\,\text{Gyr}$. Contours and symbols are the same as in previous figures.

Of course, in reality, the interfering spiral patterns would probably turn on and off at different times, i.e. $t_{\text{on},1} \neq t_{\text{on},2}$ and $t_{\text{off},1} \neq t_{\text{off},2}$. However, the above discussion is not meant to cover all the possible scenarios, but only to study to what extent the dynamo can respond to the spiral forcing by multiple patterns during the finite lifetimes of these patterns. In summary, it is clear that even for transient spiral patterns, magnetic arms may have ample time to develop and then evolve along with the superposition of the α_k-spirals. Therefore, the above results for other models generally continue to be valid even when the spiral patterns are transient. However, the growth and decay times of magnetic arms may in fact be comparable to the lifetimes of the spiral patterns that produce them, adding complexity to the problem. This should always be kept in mind, especially when considering models that invoke steady spiral forcing of the dynamo.

5.4.1 Pitch angles

The pitch angle p of the magnetic arms, as well as the pitch angle of the regular field p_B, can be inferred from observations, and are thus important to explore in the models. Model A23 has variable pitch angles of the arms, given by

$$p = \cot^{-1}\left(\frac{\partial \phi_{\text{max}}}{\partial \ln r}\right) \simeq \tan^{-1}\left[\ln(10)\frac{\Delta \log_{10} r}{\Delta \phi_{\text{max}}}\right], \tag{5.6}$$

where ϕ_{max} is the location of the azimuthal maximum of δ. The quantity p is seen to vary from arm to arm and also with time for any individual arm. For example, whenever a bifurcation of an arm is seen, as discussed above, the pitch angle of the outer branch is necessarily larger than that of the inner branch, at least in the vicinity of the bifurcation. Furthermore, the two main magnetic arms may have different pitch angles from one another. For example, this is true at the time $t = 4.625\,\text{Gyr}$, when the magnetic arm from

$300°$ to $360°$ and $0°$ to $210°$ has a smaller pitch angle, (about $6°$) than the magnetic arm from $180°$ to $360°$ and $0°$ to $30°$ (about $9°$). This can be thought of as simply a consequence of the variable azimuthal spacing between adjoining two- and three-arm segments that effectively combine to form a magnetic arm. For smaller azimuthal separation, p is larger and the arm thicker, while for larger azimuthal separation, p is smaller and the arm thinner because as the two- and three-arm segments separate, they effectively stretch out the magnetic arm between them. The pitch angles seen in Model A23 are not very different from the (constant) pitch angle found for magnetic arms in Model A2 ($p \simeq 7°$) or A3 ($p \simeq 8°$). In all cases, p is much smaller than the analogous quantity p_α for the α arms, where $p_\alpha \simeq 34°$ for the two-arm α_k-spiral and $p_\alpha \simeq 27°$ for the three-arm α_k-spiral, as also discussed in Chapter 3 for the single-pattern case. Nevertheless, it is interesting that two interfering patterns can produce magnetic arms with different pitch angles and with pitch angles that evolve with time.

The pitch angle of the magnetic field $p_B < 0$ also shows small differences between the models, most notably in its extrema within the radial region of interest. In Model A23, $|p_B|$ has extrema of approximately ($3°$, $13°$), whereas for Models A2 and A3 the extrema are approximately ($5°$, $12°$) and ($6°$, $11°$), respectively. However, the mean value of the pitch angle of $-8°$ is virtually the same for all three models.

5.4.2 Magnetic field in interarm regions

As a consequence of magnetic arms being more tightly wound than α_k-arms, it can sometimes be difficult to decide, based on visual inspection, whether magnetic arms are stronger within α_k-arms or in between them. This question is important because α_k-arms can be assumed to be correlated (or, possibly, anti-correlated) with the gaseous spiral arms of the galaxy, and, as mentioned in Sect. 5.1, magnetic arms have been reported to be present within the interarm regions of some galaxies like NGC 6946. In spite of the small values of p relative to p_α, it is possible to answer this question by determining where δ peaks; i.e. whether it peaks inside or outside one of the α_k-arms. It is reasonable to adopt the definition that those regions for which $\alpha_\mathrm{k} > 0.5 \max(\alpha_\mathrm{k})$ can be regarded as arms, while those regions for which this condition is not satisfied are interarm. (The arms of the original two- and three-arm patterns are now referred to as 'constituent' arms.) It can then be seen from Figure 5.7 that the peak of δ is usually situated inside an α_k-arm (white regions), for example at $t = 4.9\,\mathrm{Gyr}$. However, at other times, the peak of δ is clearly located in interarm (grey) regions, for example at $t = 4.975\,\mathrm{Gyr}$, when it lies between constituent arms from the two- and three-arm patterns whose approximate separation is $70°$. Inspection of Figure 5.7 shows that magnetic arms are strongest in the interarm

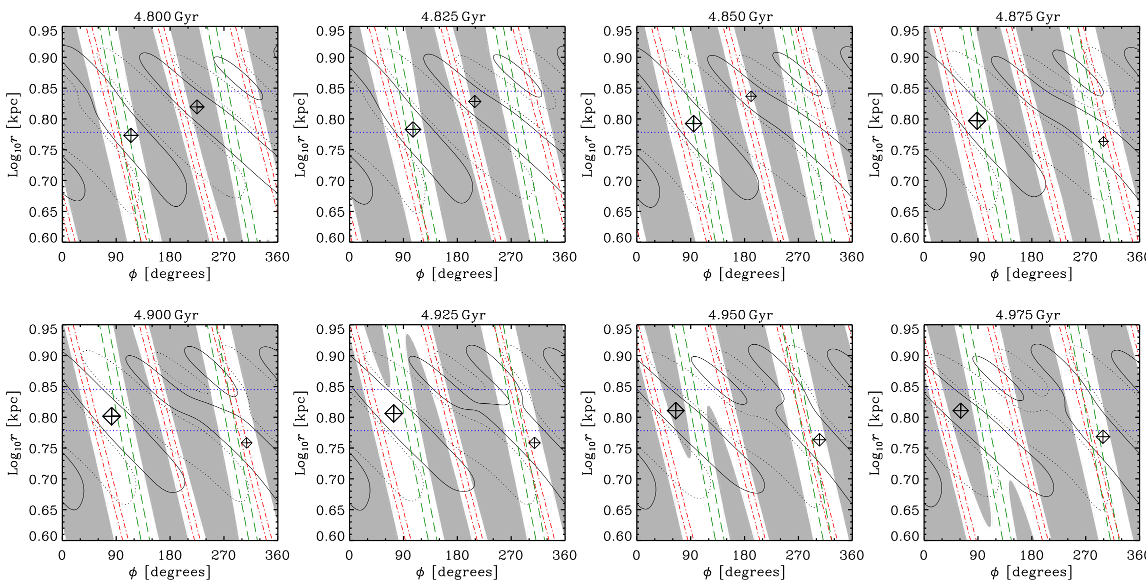

Figure 5.7: Time sequence showing the locations of the largest two local maxima of δ for Model A23, with respect to arm/interarm regions. White regions designate spiral arms $[\alpha_\mathrm{k} > 0.5\max(\alpha_\mathrm{k})]$, while grey designates interarm regions. $\delta = 0.1$ (-0.1) contours are shown with a solid (dotted) line. Other contours and symbols are the same as in previous figures.

regions about 1/4 of the time (i.e. for four out of sixteen diamonds in the figure). Note, however, that for this model, both diamonds (i.e. strongest local maxima) are never in the interarm regions at the same time.

5.4.3 Azimuthal Fourier components

It is also interesting to ask to what degree various azimuthal components are present, as a function of radius. To address this question, Figure 5.8 has been plotted for Models A2, A3, A23, L23, S23 and S23τ at the time $t = 4.5\,\mathrm{Gyr}$. For other times in the nonlinear regime, the plots do not show any important differences from $t = 4.5\,\mathrm{Gyr}$. Modes up to $m = 6$ are illustrated, although it is worth noting that only modes up to $m = 2$ have so far been detected observationally (Fletcher, 2010). In the single pattern model A2 (A3), $m = 2$ ($m = 3$) dominates, and is localized around the corotation radius. In addition, the $m = 4$ ($m = 6$) enslaved component is also present, and is also localized around the $n_1 = 2$ ($n_2 = 3$) corotation, as expected (Mestel & Subramanian 1991, Chapters 3 and 4).[1] In the dual pattern models, it can be seen, unsurprisingly, that the $m = 2$ component is dominant, followed by the $m = 3$ component, and that each is concentrated around the $n_1 = 2$ or $n_2 = 3$ corotation radius, respectively, as in the single pattern models. More interestingly, the $m = 1$ component (solid black), though relatively weak, is clearly present in the models with two patterns, whereas $m = 1$ is negligible when only a single pattern is invoked. This is important because $m = 1$ symmetry has been observed in some galaxies (Fletcher, 2010) and was reported to be the dominant azimuthal symmetry in the galaxy M81 (Krause et al., 1989), though the three-arm gaseous spiral symmetry of this galaxy has been found to be rather weak (Elmegreen et al., 1992), so it may not be well-suited to the model. A small but finite $m = 5$ component is also present in the dual arm models, which is natural given that there are in total five α_k constituent arms forcing the dynamo.

If the pattern separation is increased from that in the standard model A23, this causes a decrease in $m = 1$ and $m = 5$ components, as seen from Figure 5.8 (middle right panel), for Model L23. As the pattern separation is instead reduced from that in A23, as in Model S23, the $m = 3$ symmetry becomes less obvious compared to $m = 2$, and for S23 the field may best be described as having two asymmetric magnetic arms. This can be seen from Figure 5.8 (bottom left panel), which shows the Fourier decomposition for Model S23. The range of radii at which $m = 3$ dominates is much smaller than in Model A23 (middle left), and moreover, the difference between $m = 3$ and $m = 2$ at those radii is also much smaller. The $m = 1$ component is also much more important in

[1] The $m = 6$ component is also present in Model A2, since even modes are enslaved, though it is much weaker than $m = 4$.

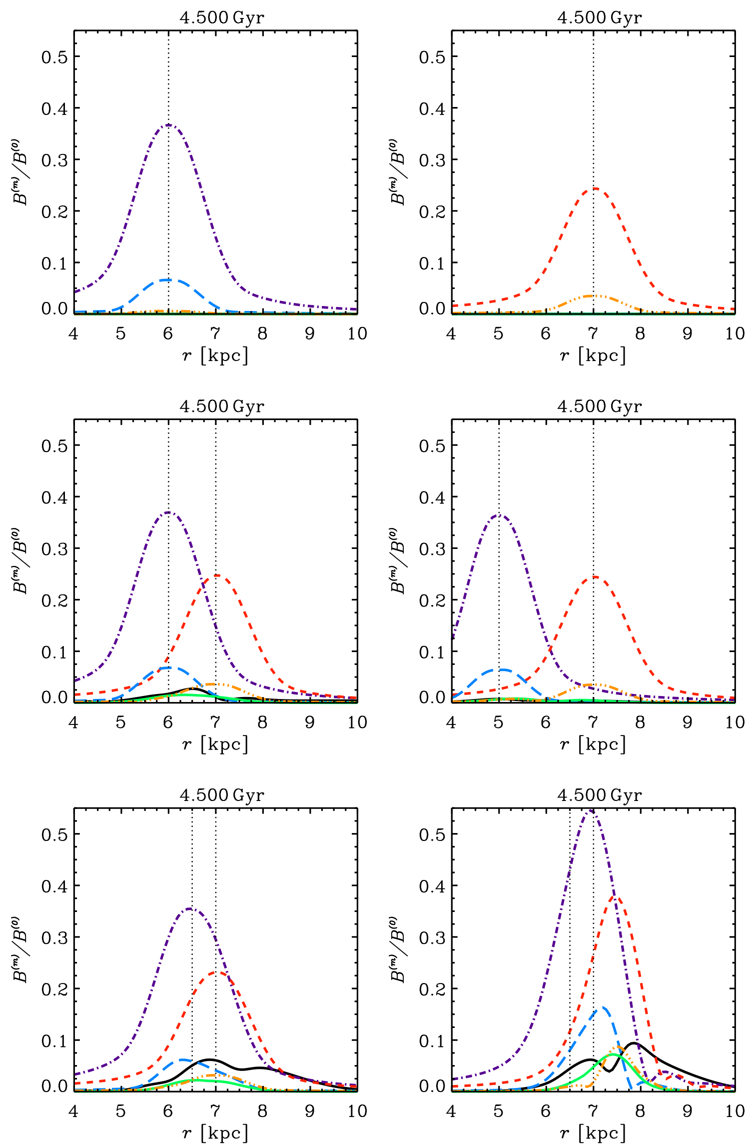

Figure 5.8: The square root of the ratio of the magnetic energy in component m relative to that in the axisymmetric component $[E^{(m)}/E^{(0)}]^{1/2}$, as a function of radius, at $t = 4.5$ Gyr: $m = 1$ (solid black), $m = 2$ (dash-dotted purple), $m = 3$ (short dashed red), $m = 4$ (long dashed blue), $m = 5$ (solid green), $m = 6$ (dash-tripple dotted orange). Modes with $m > 6$ have much smaller energy and are hence not included in the plots. Corotation radii for each α_k-pattern are marked with vertical dotted lines. Top left: Model A2. Top right: Model A3. Middle left: Model A23. Middle right: Model L23. Bottom left: Model S23. Bottom right: Model S23τ.

Model S23 than in Model A23 (resulting in the asymmetric appearance of the two main magnetic arms), as is $m = 5$. This is not surprising, as stronger coupling between the two patterns, and hence larger $m = 1$ $(= |n_1 - n_2|)$ and $m = 5$ $(= n_1 + n_2)$ components, would naively be expected to result from a reduction in pattern separation. Interestingly, $m = 1$ is comparable to $m = 2$ and $m = 3$ for $r \gtrsim 8\,\mathrm{kpc}$. The situation is similar for Model S23τ, which has $\tau = l/u$ rather than $\tau = 0$ (bottom right panel of Figure 5.8). However, in this case τ has enhanced and shifted each maximum away from the corresponding corotation radius, as discussed in Sect. 5.3.3 above.

5.4.4 Optimizing the model

The galactic disc model used thus far is meant to be rather typical, and has not been optimized to obtain any of the rather generic observational properties listed in Sect. 5.1, e.g. better alignment of magnetic and gaseous arms, larger radial extents of magnetic arms, and larger pitch angle p_B as compared to the models presented above. In Model X23, parameter values are chosen to make the model as conducive as possible to obtaining these properties, while still being realistic. In this model, the disc is flared with $h_\mathrm{D} \simeq 0.32\,\mathrm{kpc}$, giving $h = 0.45\,\mathrm{kpc}$ at $r = 10\,\mathrm{kpc}$. This smaller value of h naturally leads to larger $|p_B|$ in the kinematic regime, and this seems to be true also in the non-linear regime. α_k-arms are now taken to *add* to the axisymmetric α_k, rather than just modulate it. In other words, $l^2\Omega/h$ is now the minimum value of α_k. Furthermore, ϵ_1 and ϵ_2 are now taken to be equal to unity, but $\alpha_\mathrm{k} < u$ everywhere for all times, and $\alpha_\mathrm{k} < u/2$ for $r > 4.7\,\mathrm{kpc}$ for all times. Finally, the rotation velocity at $r = 10\,\mathrm{kpc}$ is reduced to $\overline{U}_\phi = 180\,\mathrm{km\,s^{-1}}$, which happens to be similar to the value in NGC 6946 (Fathi et al., 2007; Jałocha et al., 2010). This decreases the differential rotation in the disc. Differential rotation acts to reduce the pitch angle of the magnetic arms, as magnetic field gets advected along with the flow (though α_k also depends on Ω so the effect on pitch angle is non-trivial). By enhancing the strength of α_k-arms and reducing the differential rotation, magnetic arms tend to become more aligned with α_k-arms. More severe deviations from the Brandt profile, as would be appropriate for some galaxies, could make a substantial difference, but such a change is not explored here. The vertical velocity $\overline{U}_z$, which can be thought of as a mass-weighted velocity over all phases of the ISM due to a galactic fountain/wind, could take on values from $\sim 0.2 - 2\,\mathrm{km\,s^{-1}}$ (Shukurov et al., 2006). Taking $\overline{U}_z = 2\,\mathrm{km\,s^{-1}}$ further increases $|p_B|$ by $\sim 5°$ as compared to $0.3\,\mathrm{km\,s^{-1}}$ (see also the discussion in Chapter 2), but at the cost of the dynamo being too weak at large radius $r \sim 10\,\mathrm{kpc}$. The functional form

$$\overline{U}_z = U_0 \mathrm{e}^{-r^2/(2r_U^2)}$$

is thus adopted, with $U_0 = 2\,\mathrm{km\,s^{-1}}$ and $\overline{U}_z$ made to equal $0.2\,\mathrm{km\,s^{-1}}$ at $r = 10\,\mathrm{kpc}$ so that $r_U \simeq 4.66\,\mathrm{kpc}$. Other parameters $r_\omega = 2\,\mathrm{kpc}$, etc., are retained.[2]

The results for Model X23 are illustrated in Fig. 5.9. Top panels show the field strength and pitch angle, while bottom panels shown snapshots of δ. Magnetic arms are much more radially extended than in Model A23. They are also more closely aligned with α_k-arms, especially at some times and places (e.g. for the strongest magnetic arm at $t = 4.5\,\mathrm{Gyr}$). Moreover, $|p_B|$ reaches up to $\sim 23^\circ$ in the magnetic arms, but is smaller in between magnetic arms. Large-scale magnetic field is strongest within α_k arms in this model, though δ can be comparably large in arm and interarm regions. This can be seen at $t = 4.5\,\mathrm{Gyr}$, when the magnetic arm between about $150^\circ - 360^\circ$ clearly stretches across an interarm region. Qualitative features observed in Model A23, such as isolated armlets and bifurcations, can also be identified in Model X23.

Model X23 comes closer to explaining the properties mentioned in Sect. 5.1. However, extreme cases with $|p_B|$ as large as $\sim 40^\circ$ as in the galaxy M33 and near-perfect alignment of magnetic and optical arms as in NGC 6946 are clearly not possible to explain using such models. The τ-effect helps to shift the large-scale magnetic field into the interarm regions. However, as seen in Sect. 5.3.3, alignment of the two types of arms only gets worse, and the radial extent gets smaller, when the τ effect is included. As seen in Chapter 3, allowing each individual spiral pattern to wind up, at least to some extent, would help to further improve the alignment and increase the radial extent. This idea is explored further with a transient spiral density wave model in the next chapter.

5.5 Discussion and conclusions

Galactic mean-field dynamo solutions are obtained numerically for the case of non-axisymmetric forcing of the dynamo by multiple co-existing steady rigidly rotating spiral patterns. Each pattern is modelled as a spiral modulation of the α effect with a fixed number n of equally spaced arms. Specifically, the cases of an inner two-arm and outer three-arm spiral pattern, with corotation radii separated by 0.5, 1 or $2\,\mathrm{kpc}$, are investigated. A model with an inner two-arm and outer four-arm pattern is also studied.

The resulting magnetic field is found to exhibit magnetic arms that can be stronger, as well as more extended in radius and in azimuth, than those produced by any individual pattern acting alone. This helps to explain the occurrence of pronounced magnetic arms

[2] Deviations from Krause's law can also significantly affect the dynamo. For example, putting the azimuthal mean value of α_k constant with radius allows the dynamo to remain supercritical at large r, even if $\overline{U}_z$ is large. However, there is currently little theoretical justification for imposing an axisymmetric α_k radial dependence different from the one used.

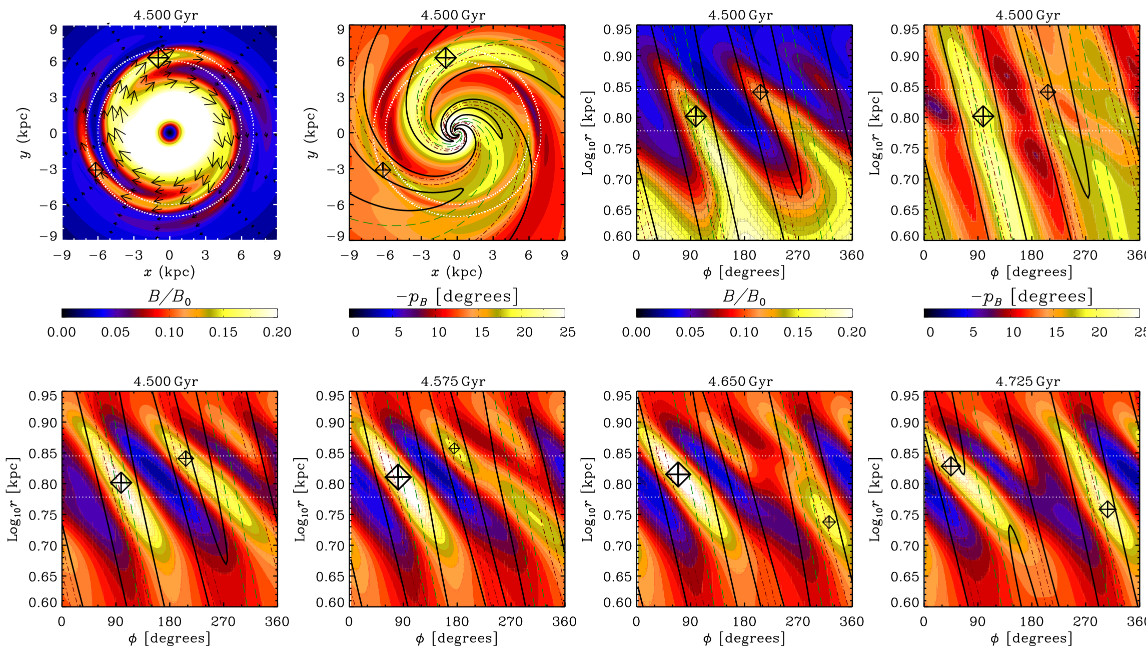

Figure 5.9: Results for Model X23. Top panels show, from left to right, magnetic field strength and negative of the pitch angle of the magnetic field in Cartesian coordinates, and then the same quantities in $\log r$-ϕ coordinates. Bottom panels show δ at various times. Color scheme for δ is the same as that in Fig. 5.1.

with radial extents similar to those of the gaseous arms that have been observed in some galaxies.

The morphology of the magnetic arms in the models evolves with time on the scale of the beat period of the two patterns, as it depends on how the α_{k}-arms from the two-arm and three-arm patterns interfere to generate the magnetic arms. For instance, the pitch angle of magnetic arms can vary significantly in time and from one arm to another, and at times, magnetic arms can become quite well-aligned with the gaseous arms, though never as precisely aligned as sometimes seen in observations. Furthermore, bifurcations of magnetic arms and isolated magnetic segments (filaments/armlets) are produced.

Interestingly, magnetic arms in some models are found to have maximum strength sometimes in between the α_{k}-arms, i.e. in the interarm regions, and at other times within an α_{k}-arm. However, these models do not produce a systematic shift (for the whole galaxy and for all times) of large-scale magnetic field toward the inter-arm regions unless the τ effect is included. (The effect of a finite τ was discussed in detail in Chapters 3 and 4.)

It is also noteworthy that the magnitude of the pitch angle of the large-scale magnetic field can exceed $20°$ for the most favourable (yet still realistic) parameters, but pitch angles $> 25°$ are not possible to explain as of yet.

Unsurprisingly, the $m = 2$ magnetic azimuthal component is found to dominate near the $n = 2$ corotation radius, while the $m = 3$ component dominates near the $n = 3$ corotation radius. However, other components, including $m = 1$, are also present to some degree; this is important because $m = 1$ is negligible for the cases of single two-arm or three-arm patterns, though it has been detected observationally in a number of galaxies (Fletcher, 2010).[3] However, there is no reason why asymmetry in either the spiral arms or the coupling of spiral arms with the dynamo could not be present and produce significant power in $m = 1$, e.g. as touched on in Moss (1998). This possibility should be explored in the future.

Some of the features found in the solutions are also found in the galaxy NGC 6946, which is thought to contain an $n = 2$ and an $n = 3$ pattern (Elmegreen et al., 1992), and is famous for harbouring magnetic arms that are localized in the interarm regions (Beck, 2007). This galaxy is inferred to have five magnetic arms, with some extending radially for $\gtrsim 10\,\mathrm{kpc}$ and others located only in the inner or outer regions (Frick et al., 2000). This is reminiscent of the complex morphology seen in Model A23 or X23, including magnetic 'armlets' that are shorter than the magnetic arms and localized to the outer regions of the galaxy, as well as bifurcations of magnetic arms. Another galaxy whose magnetic

[3]Mestel & Subramanian (1991) show, however, that $m = 1$ has a growth rate comparable to that of $m = 0, 2$ for the different disc model used in that work.

field has been studied in some detail, and that has also been shown to contain strong two- and three-arm spiral structure by Elmegreen et al. (1992) is IC 342. More recently, Crosthwaite et al. (2000) find a two-arm spiral pattern in the inner part of the galaxy, and four-arm spiral structure in the outer part. The magnetic field literature for this galaxy is not as extensive as for NGC 6946, but IC 342 is known to have a significant regular field, largely interarm, extending $\sim 8\,\mathrm{kpc}$ in radius, and apparently filamentary in structure in the outer regions (Krause et al., 1989; Sokoloff et al., 1992; Beck & Wielebinski, 2013). The large radial extent and outer filamentary structure are reminiscent of the magnetic field resulting from models such as A23 and A24.

Taken together, the studies of forcing by a corotating (winding up along with the gas) spiral and by a transient rigidly rotating spiral in Chapter 3, and the present chapter represent initial steps in the direction of systematically exploring the effects of alternate (i.e. non-steady) spiral morphology and dynamics on the galactic mean-field dynamo. Such an exploration is beginning to lead to a better understanding of magnetic arms, but, as mentioned at the beginning of the chapter, there exists an additional motivation: to invert the problem, using magnetic arms to learn about gaseous spirals. The thesis, up until now, already hints that the presence of radially extended magnetic arms that trace the optical arms in some galaxies implies the presence of spiral patterns that wind up (to some degree) with time. However, more evidence needs to be gathered before such a claim is made. In the next chapter, we study how the mean field dynamo responds to forcing by spiral patterns whose pitch angles and envelope functions evolve with time according to linear density wave theory. Given that spiral structure and dynamics involve non-linear effects, it would also be interesting to use data from an N-body simulation as direct input into the dynamo model, as first attempted by Otmianowska-Mazur et al. (2002). Quite separately, it is important to determine how robust basic features of the solutions are when the spiral pattern and dynamo are coupled differently, through the parameter η_t say, instead of through α_k, or by imposing large-scale spiral streaming flows. A brief discussion of how the spiral modulation of different parameters affects the strength of the saturated mean magnetic field, based in part on the simple expression (2.18), was presented in Chapter 2. In the next chapter, we modulate the outflow velocity $\overline{U}_z$, so that it is larger within the gaseous spiral arms, as observed in some galaxies. Because it has been directly observed, this type of spiral forcing is very natural. We shall see below that it can also have important consequences for non-axisymmetric large-scale magnetic fields in galaxies.

Chapter 6

A natural connection of magnetic spiral arms with galactic outflows

6.1 Introduction

In this chapter we explore a simple, natural and direct effect of the gaseous spiral arms on the mean-field dynamo suggested by Sur et al. (2007). They found that the dynamo action is sensitive to the galactic outflow (fountain or wind). Such an outflow leads to two countervailing effects. Whereas advection of the mean magnetic field from the disc suppresses the dynamo action, the advection also allows for the removal of the magnetic helicity needed to avoid catastrophic quenching of the dynamo. Indeed, magnetic helicity flux owing to advection (and turbulent diffusion, and possibly other effects) allows the dynamo to saturate with a magnetic field of an energy density comparable to that of interstellar turbulence. This links the dynamo efficiency directly to the star formation rate which is confidently known to be higher within the gaseous arms. In the Milky Way, OB associations that drive gas outflows concentrate in spiral arms (Higdon & Lingenfelter, 2013). The H I holes caused by hot superbubbles and chimneys, and the vertical flows driven by them tend to be concentrated in the spiral arms of NGC 6946 (Boomsma et al., 2008). There is also evidence for non-axisymmetric distributions of the extra-planar H I in other galaxies, suggesting a non-axisymmetric outflow pattern (Kamphuis et al., 2013).

The purpose of the work in this chapter is to demonstrate, using a nonlinear galactic dynamo model and a variety of spiral models, that magnetic arms can be sustained between the gaseous arms due to a stronger gas outflow along the gaseous spiral arms. The main ingredient of this mechanism, a stronger outflow in gaseous arms, is firmly based on observational and theoretical evidence.

6.2 The effect of an outflow on the mean-field galactic dynamo

Galactic outflows (winds or fountains), facilitate the mean-field dynamo action by removing helical turbulent magnetic fields from the gaseous disc (Shukurov et al., 2006). Since the large-scale magnetic field is also removed by the outflow, it also affects the dynamo negatively, so that there is a range of outflow speeds optimal for the dynamo action. These effects are conveniently captured by a simple approximate solution of the dynamo equations (the no-z approximation) augmented with a dynamic equation for the α effect. As we discussed in Chapter 3, this yields the following expression for the steady-state (saturated) strength of the mean magnetic field $B \equiv |\overline{\boldsymbol{B}}|$,

$$B^2 = K(R_U + \pi^2 R_\kappa)\left(\frac{D}{D_\mathrm{c}} - 1\right), \qquad K = \frac{\xi(p_B)B_\mathrm{eq}^2}{C}\,. \tag{6.1}$$

Here $R_U = \overline{U}_z h/\eta_\mathrm{t}$ is a dimensionless measure of the outflow intensity, with $\overline{U}_z$ the mass-weighted mean vertical velocity, h is the scale height of the dynamo-active layer, η_t is the mean-field magnetic diffusivity dominated by the turbulent contribution, and $R_\kappa = \kappa/\eta_\mathrm{t}$ is the ratio of the turbulent diffusivities of the current helicity (κ) and magnetic field. Further, $B_\mathrm{eq} = (4\pi\rho u^2)^{1/2}$ is the magnetic field strength corresponding to energy equipartition with interstellar turbulence (with ρ the gas density and u, the turbulent velocity), $C = 2(h/l)^2$ with l the turbulent scale, and $\xi(p_B) = [1 - 3\cos^2 p_B/(4\sqrt{2})]^{-1}$ is a function of the magnetic pitch angle p_B ($\tan p_B = \overline{B}_r/\overline{B}_\phi$). Finally, D is the dynamo number, a dimensionless measure of the induction effects of differential rotation and helical turbulence (normally, $D < 0$ since Ω decreases with r), and

$$D_\mathrm{c} = -(\pi/2)^5(1 + R_U/\pi^2)^2 \tag{6.2}$$

is the critical dynamo number, such that the mean magnetic field can be sustained for $D/D_\mathrm{c} \geq 1$ and decays otherwise. Equation (6.1) applies if $D/D_\mathrm{c} \geq 1$; otherwise, B is effectively zero. Numerical values of various coefficients in these equations are model-dependent, but in Chapter 2 we showed that the forms shown reproduce accurately numerical solutions of the dynamo equations obtained without any crude approximations.

The idea of this chapter is that magnetic arms displaced from the gaseous ones can occur when the value of R_U between the gaseous arms is closer to its optimum value for the dynamo action than within the arms. Then the outflow suppresses the dynamo action in the gaseous arms but facilitates it between the arms, producing magnetic arms displaced

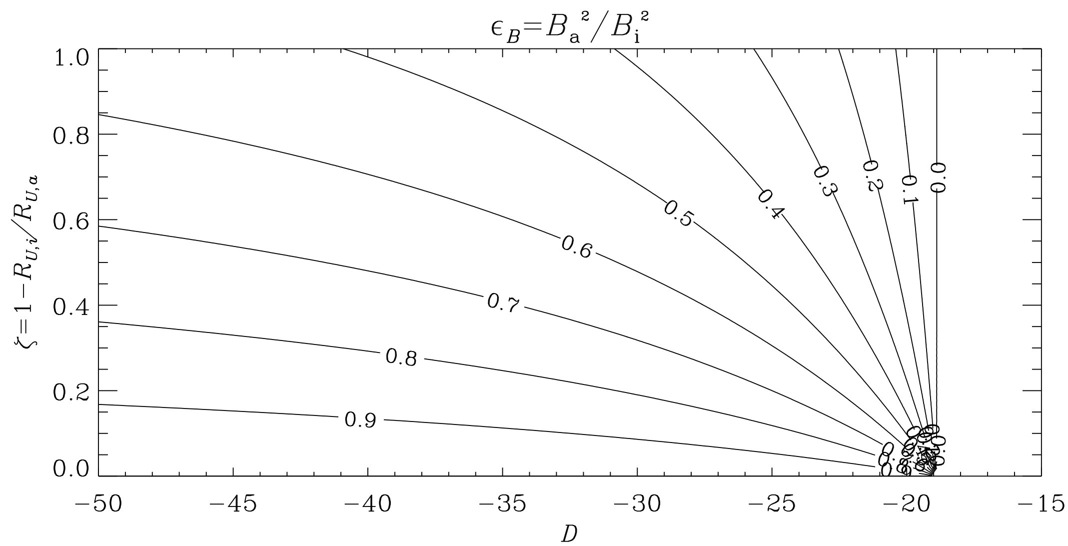

Figure 6.1: Contours of the arm-interarm contrast in magnetic field strength, $\epsilon_B = B_a^2/B_i^2$, in the (D, ζ)-plane for $\epsilon_K = 1$, $R_{U,a} = 4$ and $R_{\kappa,a} = R_{\kappa,i} = 1$. All the contours are at $D < D_c|_{R_U=0} = -(\pi/2)^5 \simeq -9.6$ – see equation (6.2). Note that in our definition D is negative. The contour $\epsilon_B = 1$ traces the D-axis.

from the gaseous ones.

To verify and test this idea, consider whether this can occur for realistic values of galactic parameters. We denote with subscripts 'a' and 'i' quantities within the gaseous arms and between them. For convenience, we define the parameters

$$\epsilon_K \equiv \frac{K_a}{K_i}, \qquad \epsilon_\kappa \equiv \frac{R_{\kappa,a}}{R_{\kappa,i}}, \qquad \zeta \equiv 1 - \frac{R_{U,i}}{R_{U,a}}, \qquad \epsilon_D \equiv \frac{X_a}{X_i} = \frac{D_{c,i}}{D_{c,a}} = \left[\frac{\pi^2 + (1-\zeta)R_{U,a}}{\pi^2 + R_{U,a}}\right]^2,$$

where, in the last equation, we have assumed $D_a = D_i$ and used equation (2.15). We then obtain from equations (6.1) and (6.2) the arm–interarm contrast in the magnetic field strength:

$$\epsilon_B \equiv \frac{B_a^2}{B_i^2} = \frac{K_a}{K_i}\left(\frac{R_{U,a} + \pi^2 R_{\kappa,a}}{R_{U,i} + \pi^2 R_{\kappa,i}}\right)\left(\frac{X_a - 1}{X_i - 1}\right) = \epsilon_K \left[\frac{R_{U,a} + \pi^2 \epsilon_\kappa R_{\kappa,i}}{(1-\zeta)R_{U,a} + \pi^2 R_{\kappa,i}}\right]\left(\frac{\epsilon_D X_i - 1}{X_i - 1}\right).$$

For η_t and h constant with ϕ, from equation (6.1) for K we then have $\epsilon_K = (\xi_a/\xi_i)(\rho_a/\rho_i)$. The first of these ratios $\simeq 1$, which leaves $\rho_a/\rho_i > 1$; we adopt $\epsilon_K = 1$ or 2 for illustrative examples. The parameter ζ is a measure of the arm–interarm contrast in the outflow

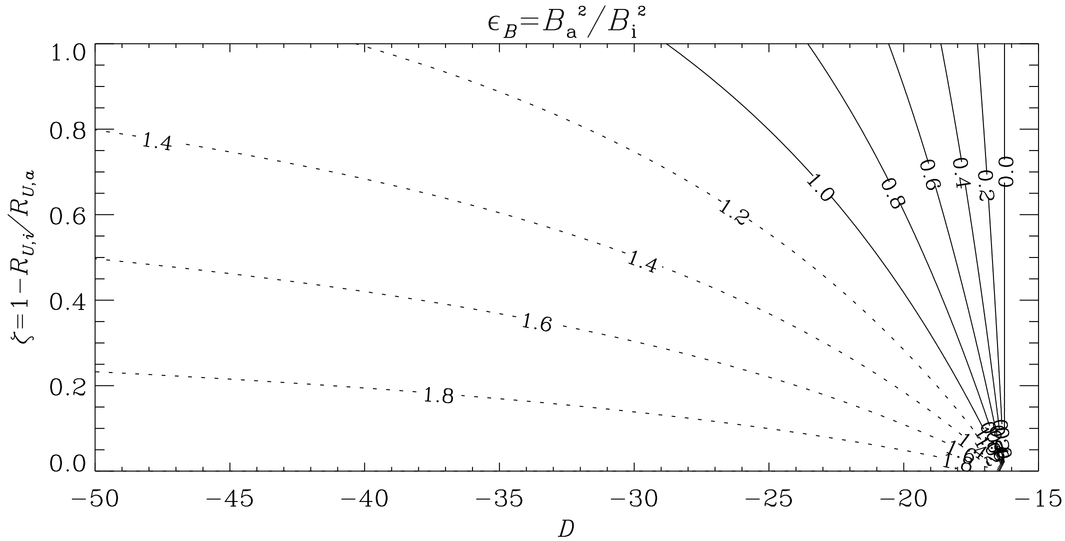

Figure 6.2: Same as Figure 6.1 but now $\epsilon_K = 2$ and $R_{\mathrm{U,a}} = 3$. Contours with $\epsilon_B > 1$ are shown as dotted lines. The contour $\epsilon_B = 2$ traces the D-axis.

speed; it vanishes if there is no such contrast, and equals to unity if there is no outflow in the interarm regions. Figure 6.1 shows the contours of $\epsilon_B \equiv B_{\mathrm{a}}^2/B_{\mathrm{i}}^2$ in the (D, ζ)-plane for $\epsilon_K = 1$, $R_{\mathrm{U,a}} = 4$, $R_{\kappa,\mathrm{i}} = 1$ and $\epsilon_\kappa = 1$. The $\epsilon_B = 1$ contour traces the D axis, while the $\epsilon_B = 0$ contour is located at $D = D_{\mathrm{c,a}} \simeq -18.9$. We see that $\epsilon_B < 1$ for all values of $|D| > |D_{\mathrm{c,i}}|$ and ζ, but decreases with increasing ζ and with decreasing $|D|$. In Figure 6.2 we show the same type of plot, but for more stringent constraints, $\epsilon_K = 2$ and $R_{\mathrm{U,a}} = 3$. With $\epsilon_K = 2$, the contour $\epsilon_B = 2$ now traces the D-axis, so that the condition $\epsilon_B < 1$ is satisfied in the top right corner of the diagram as well as to the right of the contour $\epsilon_B = 0$ up to $|D_{\mathrm{c,i}}|$. The effect of doubling ϵ_K is just to shift the contours so that what was e.g. $\epsilon_B = 0.5$ now becomes $\epsilon_B = 1$. On the other hand, the smaller value of R_U has caused the value of $|D_{\mathrm{c,a}}|$ to decrease, shifting the contours to the right. We see then that a larger value of the magnetic field in the interarm regions as compared to the arms is possible for realistic dynamo parameters. Note that the mechanism is most effective for dynamo numbers close to critical, large ratios of the arm/interarm outflow speeds (ζ), and large (in absolute terms) outflow speeds in the arms ($R_{\mathrm{U,a}}$). Thus, magnetic arms can be displaced from the gaseous ones in galaxies with a relatively weak large-scale dynamo action. Shukurov (1998) made this conclusion from similar arguments. We now put these ideas on a firmer footing by considering a more detailed numerical model.

6.3 The global galactic dynamo model

The dynamo model is similar to that of previous chapters; the main differences are (i) spiral modulation of R_U rather than R_α, and (ii) in addition to a spiral model similar to that of Chapter 5, we also separately try a linear density wave model. To allow for the back-reaction of the Lorentz force on the flow, the α effect is written as the sum of kinetic and magnetic contributions, $\alpha = \alpha_\mathrm{k} + \alpha_\mathrm{m}$, with $\alpha_\mathrm{k} = l^2\Omega/h$, as in previous chapters. We consider two contributions to $\boldsymbol{\mathcal{F}}_\alpha$, advective and diffusive: $\boldsymbol{\mathcal{F}}_\alpha = (\overline{\boldsymbol{U}} - \kappa\boldsymbol{\nabla})\alpha_\mathrm{m}$. It is reasonable to assume that $\kappa = \eta_\mathrm{t}$. Limited numerical experiments suggest $\kappa = 0.3\eta_\mathrm{t}$ (Mitra et al., 2010), and we also consider $\kappa = 0$ to explore the admissible parameter space.

We solve equations (1.15), (1.19) and (1.32) numerically using the no-z approximation proved to be adequate in galactic discs (Chapters 2 and 3 and Appendices B and C), which approximates the derivatives of $\boldsymbol{B}$ in z by suitable ratios of $\boldsymbol{B}$ to h, but retains the derivatives in r and ϕ. The Ohmic terms are negligible and we take $\tau = l/u$ or $\tau \to 0$. The equations are solved on a polar grid of 200×180 mesh points in $r \times \phi$, with $\overline{B}_r = \overline{B}_\phi = \partial\alpha_\mathrm{m}/\partial r = 0$ at $r = 0$ and $r = R$, and a weak magnetic field $\overline{B}_r = -\overline{B}_\phi = 0.05 B_\mathrm{eq} r(1 - r^2)\mathrm{e}^{-r/R}$ and $\alpha_\mathrm{m} = 0$ at $t = 0$; the results are not sensitive to the specific form of the initial conditions.

The canonical values $l = 0.1\,\mathrm{kpc}$, $u = 10\,\mathrm{km\,s^{-1}}$ and $R = 15\,\mathrm{kpc}$ (Beck et al., 1996) are adopted throughout the disc. As in previous chapters, the galactic rotation curve follows a Brandt profile $\Omega = \Omega_0/\sqrt{1 + r^2/r_\omega^2}$; setting $\overline{U}_\phi = 250\,\mathrm{km\,s^{-1}}$ at $r = 10\,\mathrm{kpc}$ with $r_\omega = 2\,\mathrm{kpc}$ requires $\Omega_0 \simeq 127\,\mathrm{km\,s^{-1}\,kpc^{-1}}$. The disk is exponentially flared $h = h_\mathrm{D}\exp[(r - 8\,\mathrm{kpc})/r_\mathrm{D}]$ with $h_\mathrm{D} = 0.5\,\mathrm{kpc}$ and $r_\mathrm{D} = 10\,\mathrm{kpc}$. This is taken from the exponential fit of Kalberla & Dedes (2008) to their model for the Galactic H I disc, but scaled up for the ionized disc so that the standard value of $h = 0.5\,\mathrm{kpc}$ at the solar radius is maintained. (See Westfall et al. 2011; Eigenbrot & Bershady 2013 for evidence for flared ionized discs in galaxies.) The equipartition field varies as $B_\mathrm{eq} = B_0\mathrm{e}^{-r/R}$, with $R = 15\,\mathrm{kpc}$ (Beck, 2007). For simplicity, we take the azimuthally averaged mean vertical velocity U_0 to be constant and usually set it to $3\,\mathrm{km\,s^{-1}}$, which is approximately consistent with the estimate $\overline{U}_z \approx 0.2 - 2\,\mathrm{km\,s^{-1}}$ of Shukurov et al. (2006) for $0 < r < 15\,\mathrm{kpc}$.

6.3.1 Models of the galactic spiral pattern

Two models of the spiral pattern are explored; both have trailing gaseous arms implemented via an enhanced mean vertical velocity $\overline{U}_z = U_0\widetilde{U}$ in the arms.

Model I contains two interfering steady, rigidly rotating spiral patterns as in Chapter 5. Such a model could represent the spiral structure in some galaxies (Elmegreen et al., 1992; Shetty et al., 2007; Meidt et al., 2009). Here $\widetilde{U} = \max[1+\epsilon\cos\chi_1+\epsilon\cos\chi_2,\ 0]$, with $\chi_i = n_i(\phi-\Omega_{\mathrm{p,i}}t) - k_i\ln(r/R)$. A two-arm spiral perturbation $n_1 = 2$ with the corotation radius $r_{\mathrm{cor},1} = 6\,\mathrm{kpc}$ (giving $\Omega_{\mathrm{p},1} \simeq 40\,\mathrm{km\,s^{-1}\,kpc^{-1}}$) as well as a three-arm perturbation $n_2 = 3$ with $r_{\mathrm{cor},2} = 7\,\mathrm{kpc}$ ($\Omega_{\mathrm{p},2} \simeq 35\,\mathrm{km\,s^{-1}\,kpc^{-1}}$) are imposed. Furthermore, we choose $k_1 = -3$, which implies a pitch angle of the two-arm pattern $p = \tan^{-1}(n/k) \simeq -34^\circ$, and $k_2 = -6$ for the three-arm pattern, so that $p \simeq -27^\circ$.

Model D approximates an evolving density wave (Binney & Tremaine, 2008). Once activated, the spiral winds up according to[1] $d(\cot p)/dt = -\Omega_{\mathrm{p}}$. We set $\widetilde{U} = 1+\epsilon\cos\lambda$, with $\lambda = n\{\phi - \Omega[1-\ln(r/r_{\mathrm{cor}})](t-t_{\mathrm{on}})\}$, and $n = 2$. Here $t_{\mathrm{on}} = 10\,\mathrm{Gyr}$, is the time at which the spiral is turned on (the disk is axisymmetric for $t < t_{\mathrm{on}}$ and at $t = t_{\mathrm{on}}$ the mean magnetic field is already in a steady state). The corotation radius is taken to be $r_{\mathrm{cor}} = 8\,\mathrm{kpc}$, resulting in $\Omega_{\mathrm{p}} \simeq 31\,\mathrm{km\,s^{-1}\,kpc^{-1}}$. The spiral starts from a 'bar' configuration and winds up. Winding up spiral arms are indeed found in simulations (e.g. Grand et al., 2012; Baba et al., 2013). The amplitude of the spiral is modulated by the envelope function $\exp\{-[\log_{10}(r/r_0)]^2/(2w^2)\}$ (Chapter 5), with maximum at $r_0 = 6.5\,\mathrm{kpc}$ and $w = 0.2$. Various modifications to this model were explored: (i) the amplitude truncated at $r \gtrsim r_{\mathrm{cor}}$ to account for the 'forbidden' region around the corotation radius, (ii) allowing r_0 to increase at a rate $10-20\,\mathrm{km\,s^{-1}}$ to approximate a wave packet travelling with this group velocity, and (iii) modulating the amplitude in time, so that the density wave turns on from zero amplitude, grows in strength, and then decreases in amplitude before turning off [this is the type of behaviour predicted by the swing amplification theory and seen in some simulations (Baba et al., 2013)]. None of the modifications (i)–(iii) had a large impact on the solutions, so they were omitted for the sake of simplicity.

6.4 Results

We now present solutions at $t \approx 10\,\mathrm{Gyr}$, when the magnetic field is well into the saturated state. Fiducial parameters are $U_0 = 3\,\mathrm{km\,s^{-1}}$, $\epsilon = 1$, $\kappa = \eta_{\mathrm{t}}$, and $\tau \to 0$.

Results for spiral model I are presented in Fig. 6.3. In Fig. 6.3a, the magnetic field strength $B = (\overline{B}_r^2 + \overline{B}_\phi^2)^{1/2}$ is shown. The field strength is close to equipartition in the central region and is smaller at larger radius. The magnetic field configuration varies with the beat period of the two interfering spiral patterns. We arbitrarily selected a snapshot at $t = 10\,\mathrm{Gyr}$, but the following analysis is valid for all times in the saturated regime. The field is axisymmetric near the centre, but magnetic arms (red-purple) are

[1] See equation (6.78) of Binney & Tremaine (2008). The negative sign on the right hand side is included here because we define trailing spirals to have negative pitch angle. Strictly speaking, this expression applies to a Mestel disc with constant Toomre parameter Q in the tight-winding approximation.

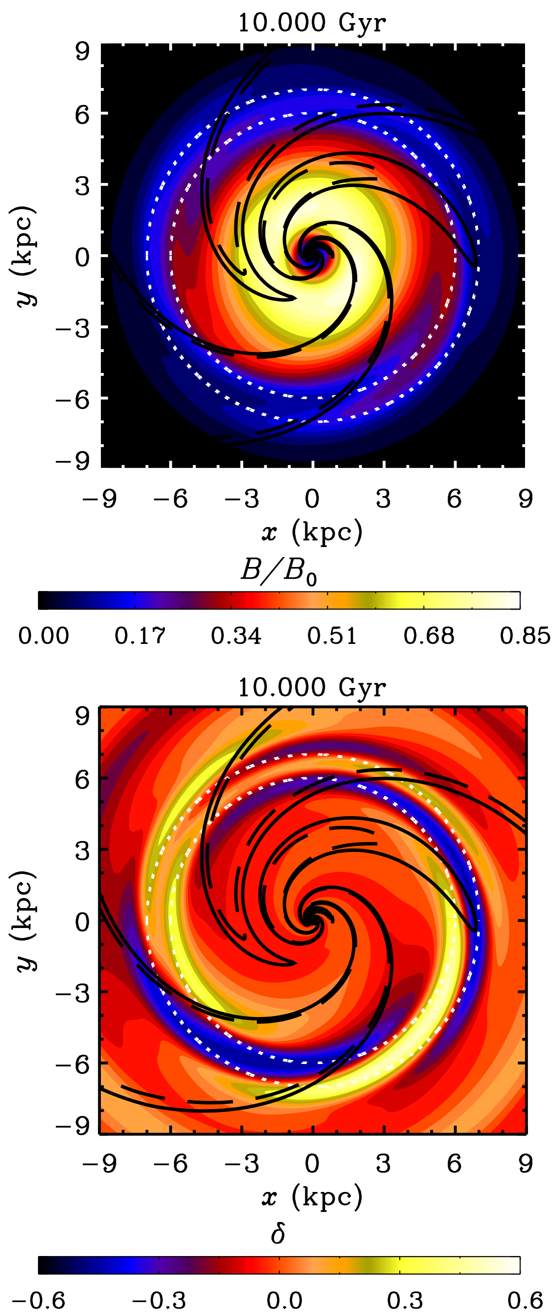

Figure 6.3: Top panel: Magnetic field strength, normalized to the equipartition field strength at $r = 0$, for the interfering spiral pattern model at the time $t = 10\,\mathrm{Gyr}$. Corotation circles for the inner two-arm and outer three-arm patterns are shown by dotted white lines. The gaseous ($\overline{U}_z$) spiral is shown by contours at $0.5\max_\phi(\overline{U}_z)$ (dashed) and $0.4\max_\phi(\overline{U}_z)$ (solid). Bottom panel: Degree of non-axisymmetry $\delta = (\overline{B}_\phi - \overline{B}_\phi^{(0)})/\overline{B}_\phi^{(0)}$.

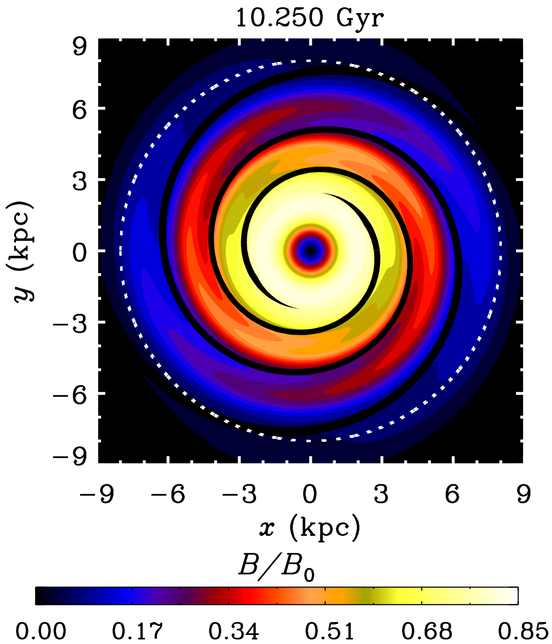

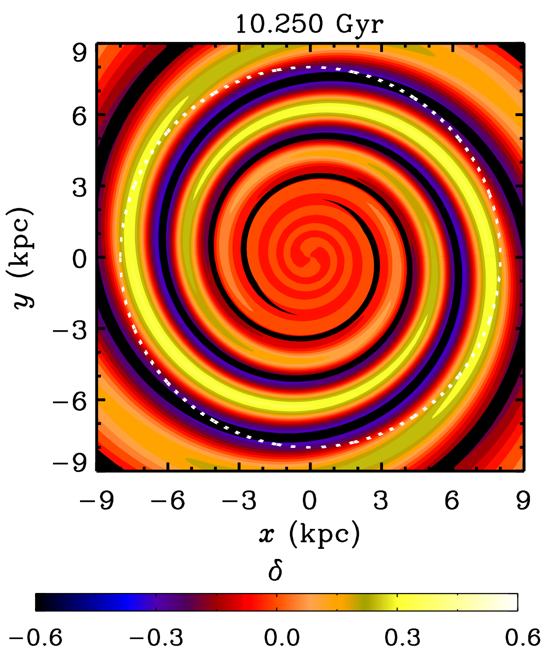

Figure 6.4: Top panel: Magnetic field strength, normalized to the equipartition field strength at $r = 0$, for the transient density wave model. The snapshot shown is at 250 Myr after the spiral peturbation is turned on. The corotation radius is shown by a dotted white circle, while the peak of the gaseous ($\overline{U}_z$) spiral is shown by a filled black contour [at $0.96\max(\overline{U}_z)$]. The spiral peak is not shown in the central region where the amplitude of the spiral perturbation is less than 0.1 of the axisymmetric contribution to $\overline{U}_z$. Bottom panel: Degree of non-axisymmetry $\delta = (\overline{B}_\phi - \overline{B}_\phi^{(0)})/\overline{B}_\phi^{(0)}$.

visible near the cororation radii of the patterns (dotted circles). These arms are located mostly in the interarm regions, i.e. outside of the contours which demarcate regions of enhanced $\overline{U}_z$. This is more evident in Fig. 6.3b, where the degree of non-axisymmetry $\delta(r) = [\overline{B}_\phi(r) - \overline{B}_\phi^{(0)}(r)]/\overline{B}_\phi^{(0)}(r)$ is plotted. Here $\overline{B}_\phi^{(0)}$ is the amplitude of the axisymmetric ($m = 0$) component of $\overline{B}_\phi$ at radius r (we note that $\overline{B}_\phi$ generally dominates over $\overline{B}_r$ for the models considered here). Yellow-white magnetic arm regions are clearly concentrated where the outflow is weakest, viz. in between the gaseous arms. Note that δ reaches values as high as ~ 0.6 in this model.

Results for spiral model D are presented in Fig. 6.4, which is similar to Fig. 6.3 except that now the peaks of $\overline{U}_z$ (i.e. the centres of the gaseous arms) are identified by filled black contours. Results are shown at 250 Myr after the onset of the non-axisymmetric perturbation in $\overline{U}_z$, with Fig. 6.4a showing the field strength and Fig. 6.4b the degree of non-axisymmetry δ. Magnetic arms are clearly visible in both panels. They are fairly strong ($\delta \sim 0.3 - 0.4$), very extended in radius, have pitch angles comparable to those of the gaseous spiral, and are clearly concentrated in the interarm regions. The run with $\tau = l/u \approx 10\,\mathrm{Myr}$ leads to very similar solutions, with very similar field strength and magnetic arm positions, but with larger δ. Fig. 6.5 shows how the peak value of δ varies with time as the spiral winds up for models with $\tau \to 0$ (solid) and $\tau = l/u$ (dashed) (the pitch angle of the gaseous spiral is shown as a dotted line). The degree of non-axisymmetry increases with time as the spiral winds up, reaching a maximum $\delta_{\max} = 0.41$ at $t = t_{\mathrm{on}} + 375\,\mathrm{Myr}$ ($\delta_{\max} = 0.60$ at $t = t_{\mathrm{on}} + 425$) for $\tau \to 0$ ($\tau = l/u$) (data was recorded every 25 Myr). The location of this maximum moves outward with radius, from $r = 6.0\,\mathrm{kpc}$ (5.8 kpc) at $t = t_{\mathrm{on}} + 100\,\mathrm{Myr}$ to $r = 8.2\,\mathrm{kpc}$ (7.8 kpc) at $t = t_{\mathrm{on}} + 500\,\mathrm{Myr}$ for $\tau \to 0$ ($\tau = l/u$). This outward propagation is explained by the increase of the local dynamo growth time with radius as discussed in Chapter 3.

It is worth exploring the parameter space by varying ϵ, κ, and U_0. Predictably, the effect of reducing the amplitude ϵ of the non-axisymmetric forcing is to produce a reduction in the degree of non-axisymmetry of the magnetic field, with $\delta_{\max}$ decreasing by about a factor of two when ϵ is reduced to 0.5 from 1 in model D. Changing κ, on the other hand, has little effect on δ. For example, δ decreases marginally as κ is decreased from $1 \to 0$; the field strength B, however, decreases by more than a factor of two. This is expected as the flux of α_m is limited to the advective flux when $\kappa = 0$, as discussed above. The effect of changing U_0 is more complicated, as discussed in Section 6.2. For runs with $\kappa = 1$, δ decreases substantially when U_0 is reduced, while B increases somewhat (e.g. δ decreases by almost 40% when U_0 is reduced from $3\,\mathrm{km\,s^{-1}}$ to $2\,\mathrm{km\,s^{-1}}$ in the $\tau = l/u$ case, while B increases by about 10%). For the mechanism to be viable, winds must be strong enough to

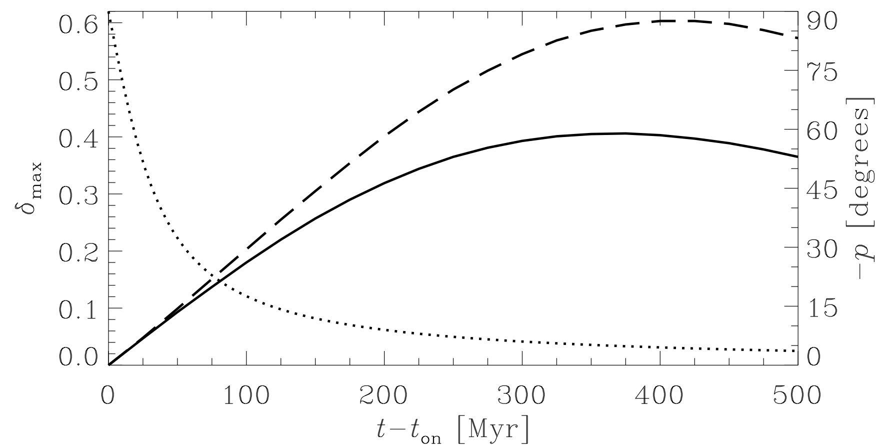

Figure 6.5: The maximum degree of non-axisymmetry δ_{max} for model D, plotted as a function of time since the onset of the spiral perturbation at $t = t_{\mathrm{on}}$, for the case $\tau \to 0$ (solid) and $\tau = l/u \approx 10\,\mathrm{Myr}$ (dashed). The magnitude of the pitch angle of the winding-up gaseous spiral is also shown for comparison (dotted).

suppress the dynamo in the gaseous arms, but not strong enough to suppress it globally.

6.5 Summary and conclusion

We have shown that strong interarm magnetic arms can be generated when the vertical outflow velocity $\overline{U}_z$ is stronger in the gaseous spiral arms as compared to the interarm regions. This result is independent of the spiral model used.[2] Moreover, we have presented results for a linear density wave spiral model (Binney & Tremaine, 2008) which leads to relatively long-lived (hundreds of Myr) radially extended interarm magnetic arms with arm pitch angles similar to those of the $\overline{U}_z$ gaseous spiral forcing the dynamo. These results are very encouraging for explaining observations, especially those of NGC 6946, which has magnetic arms that interlace the optical arms (Beck & Hoernes, 1996; Frick et al., 2000; Beck, 2007). This work tentatively predicts that gas-rich galaxies with high star formation rates, and large outflows concentrated in the spiral arms, are more likely than others to possess interarm magnetic arms (provided the outflow is not so strong as to suppress the large-scale dynamo altogether); indeed, the galaxies in which magnetic arms have been identified are found to be gas-rich (Beck & Wielebinski, 2013).

[2]In addition to the spiral models presented, our conclusion also holds when the other models of Chapter 3 are instead used.

The mechanism to explain the interarm concentration of the large-scale magnetic field put forth in this chapter has certain advantages over the τ effect of Chapters 3 and 4. The concentration of outflows within spiral arms is observed in NGC 6946 and some other galaxies, and is theoretically predicted. On the other hand, it is not clear whether the α_k effect is, in actuality, enhanced within the gaseous arms, though it is certainly plausible. The τ effect can produce large negative phase shifts for a rigidly rotating spiral model, but the effect is somewhat smaller for spirals that wind up. Also, with a circular velocity of only $\sim 180\,\mathrm{km\,s^{-1}}$, the quantity $\Omega_\mathrm{p}\tau$ in NGC 6946 may be sub-optimal for producing phase shifts. On the other hand, the τ effect is made more enticing by the conclusion of Frick et al. (2000) that magnetic arms are 'phase-shifted images' of the optical arms which precede them (in the sense of the rotation). In toto, we feel that the τ effect and the modulation of $\overline{U}_z$ discussed in this chapter can both be important, and their specific roles depend on the particular galaxy being considered.

As for the structure and evolution of the spiral forcing the dynamo, the linear density wave model considered here is the most successful at reproducing the kinds of extended, aligned (with the gaseous arms) magnetic arms seen in some galaxies. Moreover, it is better grounded in theory than models using rigidly rotating patterns or spirals that corotate with the gas at every radius. Possible improvements would be to extend the spiral model to include non-linear dynamical effects, and to invoke multiple co-existing density waves. We re-emphasize the importance of investigating the role of the evolution of the spiral structure on the dynamo, both for its usefulness in modelling the dynamo, and as a probe of the evolution of galactic spiral structure.

Chapter 7

Conclusion

7.1 Highlights of the Research

This thesis is concerned with *The origin of large-scale magnetic fields in galaxies*. Here, we have constructed physically realistic dynamo models to explore the growth and saturation of large-scale magnetic fields in spiral galaxies. We first developed various tools for solving the non-linear galactic dynamo problem in Chapter 2, and demonstrated their accuracy, as compared to fully numerical solutions. This toolbox, which includes no-z analysis, perturbation theory, marginal kinematic solutions, and generalized algebraic quenching, was put to use in the subsequent chapters. An asymptotic solution for a non-axisymmetric dynamo that makes use of WKBJ theory and numerical iteration was added to the toolbox in Chapter 4. In Chapter 3–Chapter 6, we focused considerable effort on understanding magnetic spirals, incorporating several new physical effects into the models:

i the dynamical α-quenching non-linearity, incorporated here for the first time in non-axisymmetric dynamo models;

ii temporal non-locality in the response of the mean electromotive force to variations in the mean magnetic field and small-scale turbulence;

iii realistic spiral morphology and evolution, based on results from N-body simulations from the literature and on linear density wave theory;

iv non-axisymmetric forcing of the dynamo by spiral modulation of the galactic outflow, taken to be concentrated within the spiral arms.

We found that each of these physical effects can have a significant impact on the resulting large-scale magnetic field structure.

The dynamical quenching non-linearity is well motivated by the theory of magnetic helicity balance and by numerical simulations, which demonstrate that a buildup of magnetic helicity density at small scales can impede dynamo action. This non-linearity was compared with the traditional, heuristically motivated algebraic quenching non-linearity. It was found that, for the most part, the saturation and steady solutions for the mean magnetic field that result are very similar. We went on to explain why this is true, and how the algebraic non-linearity can be modified to achieve better agreement with dynamical quenching. This helps to validate the results of many previous works which use the algebraic non-linearity. We found, however, that dynamical quenching causes magnetic spirals to go from trailing near the midplane to leading near the disc edges when an outflow is present, for the models considered; this is not the case with algebraic quenching. On a different note, we showed that, when no magnetic helicity flux is present to remove small-scale current helicity from the dynamo-active region, a double ring structure arises in the mean magnetic field, and propagates with radius on Gyr timescales. Conversely, when a large enough magnetic helicity flux is present, the magnetic field saturates on the local growth timescale at every radius out to where the dynamo ceases to be supercritical.

The temporal non-locality explored in the models (the τ effect) is well-motivated by the minimal τ closure approximation, as well as by numerical simulations. In the case where the underlying galaxy has axial symmetry, the τ effect may not be very important, assuming that the relaxation time τ is of the order of the timescale for the largest turbulent eddies to turn over. As an exception, we do find that global reversals along the radial direction, which can result from near-equipartition noisy seed magnetic fields, can be partly suppressed when the τ effect is incorporated. Where the τ effect is clearly important is in the case of non-axisymmetric galaxies and magnetic fields. Subject to a spiral forcing of the dynamo, the large-scale magnetic field becomes enhanced along a spiral in the saturated state; these spiral-shaped enhancements are known as magnetic spiral arms. The τ effect can produce phase shifts of the magnetic arms in the direction opposite to the galactic rotation. The magnitude of these shifts is up to $\sim 40^\circ$, with precise values mainly dependending on the choice of spiral model and on the value of $\Omega_\mathrm{p}\tau$, where Ω_p is the spiral pattern speed. For the range of $\Omega_\mathrm{p}\tau$ typical in galaxies, the phase shift is proportional to $\Omega_\mathrm{p}\tau$, with proportionality constant $\sim$ 1–2. Such phase shifts have been observed in many galaxies.

Asymptotic solutions for mean magnetic fields in non-axisymmetric discs, incorporating the τ effect, were also obtained using a newly devised semi-analytic method. These solutions were found to be in good qualitative agreement with numerical solutions using the same disc model. The asymptotic solutions lead to a better understanding of certain features of the numerical solutions, e.g. the competition between axisymmetric and non-axisymmetric modes. The phase shifts and increase in strength of magnetic arms resulting from the τ effect can also be understood by studying the analytical expressions of the model. The importance of higher-order enslaved non-axisymmetric modes when τ is finite was elucidated. In addition, it was shown that the non-linear saturated solution obtained numerically using the dynamical quenching non-linearity is well-approximated by the marginal (zero growth rate) asymptotic solution. This echoes our results with the thin-slab (axisymmetric) dynamo models that demonstrate that marginal asymptotic solutions quite faithfully reproduce the key features of numerical solutions.

There had been much work in recent years to understand the nature of spiral structure and evolution in galaxies. N-body simulations, theory, and observations have all suggested that a single steady rigidly rotating spiral perturbation, which has been the spiral model most often used in previous studies of non-axisymmetric galactic dynamos, may not always be a good representation of what happens in real galaxies. With this in mind, we explored the effects, on the dynamo and magnetic arms, of various alternate models of spiral morphology and evolution. First, maintaining the assumption of rigid rotation, we asked what happens to the mean magnetic field if the spiral perturbation is transient, lasting only for a few galactic rotation periods, as found in some N-body simulations. Although dynamo growth timescales are generally smaller than this, they are not smaller by much. Therefore, such spiral transience can lead to a temporal delay between the growth/decay of a spiral perturbation and the growth/decay of the magnetic arms, and potentially result in 'ghost' magnetic arms whose 'parent' gaseous spiral arms no longer exist. This delay in the decay is enhanced by the τ effect.

As already alluded to, many simulations, as well as linear density wave theory, suggest that spiral perturbations wind up. We find that allowing the spiral to wind up leads to magnetic arms that are less tightly wound than those produced by a rigidly rotating spiral, and are in fact closely aligned with the gaseous arms which cause them, extending several kpc in radius, as seen in some galaxies. In particular, the linear density wave spiral model produces strong, extended, open magnetic arms that can survive for several hundred Myr. Some authors have argued that the winding up of spiral patterns observed in simulations and observations is only apparent, and is caused by the interference between two rigidly rotating patterns which are centered at different radii, and which have different pattern speeds. We studied such models extensively, and found that they lead to magnetic arms that are stronger and more extended than in the simplest single-pattern rigidly rotating models. In this multi-pattern picture, magnetic spirals generally acquire a more complex morphology, including bifurcations and magnetic 'armlets', and can contain a significant amount of $m = 1$ azimuthal symmetry. In the future, such studies can be inverted to discriminate between spiral evolution models based on their abilities to reproduce the observed structure of the magnetic field.

Throughout most of the thesis, the non-axisymmetric forcing assumed was the spiral modulation of the α_k effect. We had earlier come to the conclusion that some kind of non-axisymmetry in the disc must be invoked, because non-axisymmetric modes in axisymmetric discs, which are anyway subdominant compared to the fastest growing axisymmetric mode, decay in the non-linear regime. Many parameters could be modulated along the spiral to produce non-axisymmetry in the magnetic field [c.f. equation (2.18)]. Although an enhancement of the α effect within the gaseous arms (or possibly in the interarm regions) is plausible, and can lead to strong non-axisymmetry in the mean magnetic field, a perhaps more obvious and natural coupling is spiral modulation of the outflow speed, as such an outflow is expected (and in some cases observed) to be larger within the gaseous spiral arms as compared to the interarm regions. We performed mean-field simulations that incorporated this effect, and found magnetic arms that are situated in the interarm regions, and are interlaced with gaseous arms, as in the galaxy NGC 6946. This is encouraging because NGC 6946 is one of the galaxies that is observed to have an outflow that is concentrated in the spiral arms. A possible next step would be to directly model that galaxy in more detail. We caution, however, that every galaxy is different and the source of the spiral forcing that presumably leads to non-axisymmetry in the magnetic field may be different in different galaxies.

7.2 Future directions

There are several possibilities for extending the work of the thesis.

The models discussed above have arguably reached a level of sophistication and precision such that detailed modelling of specific galaxies, such as M31 (NGC 224), M51 (NGC 5194) or NGC 6946, has become worthwhile. It would be interesting and important to test the models by applying them to such galaxies, for which the rotation curve, velocity dispersion, spiral structure, etc., can be constrained by existing data from observation and simulation. This would build on earlier mean-field dynamo models for specific galaxies (e.g. Ruzmaikin et al., 1988; Rohde et al., 1999), making use of recent observational data as well as the new theoretical ideas discussed above. Such modelling would benefit from adding more features to the simulations, e.g. a more accurate characterization of the vertical structure of the galaxy. We have explored the vertical structure of the mean magnetic field in one-dimensional (thin-slab) models, and the radial and azimuthal structure using two-dimensional (no-z) models. It is then natural to extend the models to three dimensions to make them more realistic and more accurate. Such models should include the galactic halo (thick disc), as well as a realistic outflow geometry. First steps in this direction would be to run three-dimensional simulations confined to the disc, on the one hand, and two-dimensional axisymmetric simulations (in r and z) that include both the disc and halo. Previous work has been done on the role of galactic haloes in dynamo action (e.g. Moss et al., 2010). We wish to extend this work, for example by including dynamical quenching and the transport of $\alpha_{\rm m}$. A detailed modelling of the vertical structure would also involve exploring the role of the vertical shear $r\partial\Omega/\partial z$, observed to be present in several galaxies. It would also be possible to generate polarization and Faraday rotation maps using the models, which would be done after adding a stochastic component to the field to account for the turbulent (random) field. Such maps would allow direct comparison with observations.

Progress in mean-field dynamo theory is another important avenue for improving our galactic dynamo models. We have considered only a simple form of the mean electromotive force $\boldsymbol{\mathcal{E}}$; in reality other terms may also be important, for example the off-diagonal components of the α and $\eta_{\rm t}$ tensors. It would be useful to build on existing derivations of analytical expressions for such additional terms, and to explore the effects of such terms on the galactic dynamo. As we have argued, the minimal τ approximation leads to important effects for galactic dynamos, not seen under the first order smoothing approximation. It is possible that yet more accurate closure approximations, perhaps along the lines of the direct interaction approximation (McComb, 1990) also lead to important new effects.

Another point of contention in mean-field dynamo theory concerns the magnetic helicity flux; the fluxes considered above liberate the dynamo from catastrophic quenching, but other flux terms not considered may also have profound effects. Determining the nature of the small-scale magnetic helicity flux presents a formidable challenge, and yet has the potential to drastically alter our understanding of galactic dynamos. Recently, helicity fluxes have been studied in direct numerical simulations (Mitra et al., 2010; Hubbard & Brandenburg, 2011; Candelaresi et al., 2011; Shapovalov & Vishniac, 2011; Vishniac & Shapovalov, 2014; Ebrahimi & Bhattacharjee, 2014). In some cases (Vishniac & Shapovalov, 2014; Ebrahimi & Bhattacharjee, 2014), such fluxes have been found to be the main drivers of large-scale dynamo action. However, a theoretical understanding of these fluxes is lacking. Such analyses have so far been performed on output from simulations that are rather idealized, and it is not yet clear to what extent these fluxes depend on the boundary conditions, nature of the random forcing driving the turbulence, and other aspects of the simulation. It would be useful to perform similar analyses on local direct numerical simulations of galaxies (Gent et al., 2013). The analytically derived flux of Vishniac & Cho (2001), whose effects on the galactic dynamo have been explored by Sur et al. (2007) is not, by itself anyway, able to explain the fluxes seen in such simulations. Analytical approaches to the problem are certainly needed, but these come with their own challenges. Getting a handle on the helicity flux requires grappling with third and fourth order correlations of the fluctuating quantities (Subramanian & Brandenburg, 2006). Nevertheless, such a calculation has recently been performed by E. Vishniac, in the context of a stratified, rotating turbulent medium with shear (Vishniac, 2012b), and we have now begun to explore the effects of this New Vishniac flux in our galactic dynamo models.

As noted in the previous paragraph with regard to helicity fluxes, more sophisticated kinds of simulation than the mean-field simulations studied in the thesis could greatly help in understanding the nature of galactic dynamos. Using the output from N-body galaxy simulations as input in our mean-field dynamo simulations, in order to generate realistic spiral structure, velocity fields, etc., would be an interesting extension of the work on magnetic arms. Galactic dynamo simulations in a local shearing box (Gressel, 2010; Gent et al., 2013) could be used to explore various aspects of galactic dynamos in different parameter regimes, and to test assumptions of our models. Another possibility is to somehow couple our models with cosmological structure formation simulations to explore how galactic magnetic fields grow and evolve during the formation and evolution of galaxies.

In summary, many opportunities to extend the work, using analytical approaches, mean-field simulations, and direct numerical simulations, are indeed possible. We plan to take up this work in the future.

Appendix A

Perturbation solutions of the dynamo equations with an outflow

The kinematic $\alpha\Omega$ dynamo in a thin disc is governed by equation (2.8) and equation (2.9) with the α term omitted in equation (2.9). These can be written in dimensionless form as (e.g. Shukurov, 2004):

$$\frac{\partial \overline{B}_r}{\partial t} = -R_\alpha \frac{\partial}{\partial z}(\widetilde{\alpha}\overline{B}_\phi) + \frac{\partial^2 \overline{B}_r}{\partial z^2} - R_U \frac{\partial}{\partial z}(\widetilde{U}_z \overline{B}_r), \tag{A.1}$$

$$\frac{\partial \overline{B}_\phi}{\partial t} = R_\omega \overline{B}_r + \frac{\partial^2 \overline{B}_\phi}{\partial z^2} - R_U \frac{\partial}{\partial z}(\widetilde{U}_z \overline{B}_\phi), \tag{A.2}$$

with the vacuum boundary conditions at the disc surface,

$$\overline{B}_r|_{z=\pm 1} = \overline{B}_\phi|_{z=\pm 1} = 0,$$

and where $\overline{B}_z$ can be recovered from the solenoidality condition. We make the equations time-independent by substituting the solution $\overline{\boldsymbol{B}} = \boldsymbol{\mathcal{B}}(z)\mathrm{e}^{\gamma t}$, and make the transformation

$$\mathcal{B}_r' \equiv R_\alpha^{-1}\mathcal{B}_r, \quad \mathcal{B}_\phi' \equiv \mathcal{B}_\phi/\sqrt{|D|}, \tag{A.3}$$

where $D \equiv R_\omega R_\alpha$, and then drop primes for presentational convenience, so that equations (A.1) and (A.2) become

$$\gamma \mathcal{B}_r = -\sqrt{|D|}\frac{d}{dz}(\widetilde{\alpha}\mathcal{B}_\phi) + \frac{d^2 \mathcal{B}_r}{dz^2} - R_U \frac{d}{dz}(\widetilde{U}_z \mathcal{B}_r),$$

$$\gamma \mathcal{B}_\phi = \sqrt{|D|}\,\mathrm{sign}(D)\mathcal{B}_r + \frac{d^2 \mathcal{B}_\phi}{dz^2} - R_U \frac{d}{dz}(\widetilde{U}_z \mathcal{B}_\phi).$$

We then seek an asymptotic solution to this eigenvalue problem by treating terms involving $\sqrt{|D|}$ and R_U as a perturbation to the eigensolutions of the 'free-decay' modes ($D = R_U = 0$) of the diffusion equation. This generalizes the treatment of Shukurov (2004); Sur et al. (2007); Shukurov & Sokoloff (2008), who solve the case $R_U = 0$. We may write

$$(\widehat{W} + \epsilon\widehat{V})\boldsymbol{\mathcal{B}} = \gamma\boldsymbol{\mathcal{B}}, \tag{A.4}$$

where $\epsilon = \text{const}$ is a mathematical device to keep track of the orders, and is taken to be $\ll 1$ for the perturbation analysis before being 'restored' to its true value of unity at the end of the calculation (e.g. Griffiths, 2005). The unperturbed operator $\widehat{W}$ is given by

$$\widehat{W} = \begin{pmatrix} \dfrac{d^2}{dz^2} & 0 \\ 0 & \dfrac{d^2}{dz^2} \end{pmatrix},$$

while the perturbation operator $\widehat{V}$ is given by

$$\widehat{V} = \begin{pmatrix} -R_U\dfrac{d}{dz}(z\cdots) & -\sqrt{-D}\dfrac{d}{dz}\left[\sin(\pi z)\cdots\right] \\ -\sqrt{-D} & -R_U\dfrac{d}{dz}(z\cdots) \end{pmatrix},$$

where we have adopted the forms (2.2) and (2.3) for $\widetilde{\alpha}$ and $\widetilde{U}_z$, and taken $\operatorname{sign}(D) = -1$, as is suitable for the present context.

Keeping terms containing both $\sqrt{-D}$ and R_U, we effectively assume that they are of the same order of magnitude. However, Ji et al. (2013) show that the resulting perturbation solution remains accurate up to $\sqrt{-D} \gtrsim 1$ (they consider the case $R_U = 0$). Then the requirement that $\sqrt{-D} = \mathcal{O}(R_U)$ is rather formal and not restrictive for practical purposes.

The eigensolutions of the unperturbed system $\widehat{W}\boldsymbol{b}_n = \lambda_n\boldsymbol{b}_n$ (with the above boundary conditions) are doubly degenerate and given by

$$\lambda_n = -\left(n + \tfrac{1}{2}\right)^2\pi^2, \quad n = 0, 1, 2, \ldots,$$

$$\boldsymbol{b}_n = \begin{pmatrix} \sqrt{2}\cos[(n + \frac{1}{2})\pi z] \\ 0 \end{pmatrix},$$

$$\boldsymbol{b}'_n = \begin{pmatrix} 0 \\ \sqrt{2}\cos[(n + \frac{1}{2})\pi z] \end{pmatrix},$$

where eigenfunctions have been normalized to $\int_0^1 \boldsymbol{b}_n^2 dz = \int_0^1 {\boldsymbol{b}'_n}^2 dz = 1$ (the eigenfunctions should not be confused with the small-scale magnetic field, denoted $\boldsymbol{b}$ in the main text).

The expansions

$$\gamma = \gamma_0 + \epsilon\gamma_1 + \epsilon^2\gamma_2 + \ldots,$$

$$\boldsymbol{\mathcal{B}} = C_0\boldsymbol{b}_0 + C'_0\boldsymbol{b}'_0 + \epsilon\sum_{n=1}^{\infty}(C_n\boldsymbol{b}_n + C'_n\boldsymbol{b}'_n) + \ldots$$

are substituted into equation (A.4), terms of like order in ϵ collected, the dot product of the resulting equations taken first with $\boldsymbol{b}_n$ and then with $\boldsymbol{b}'_n$, and the results integrated over $0 \leq z \leq 1$. [Note that the lowest order contribution to the eigenfunction can be assumed to be a linear combination of the fastest growing ($n = 0$) terms only.] To the lowest order this yields $\gamma_0 = \lambda_0$. A homogeneous system of algebraic equations for C_0 and C'_0 follows from terms of order ϵ, whose solvability condition yields

$$\gamma_1 = \frac{1}{2}\left\{(V_{00} + V_{0'0'}) + \left[(V_{00} - V_{0'0'})^2 + 4V_{00'}V_{0'0}\right]^{1/2}\right\} = -\frac{R_U}{2} + \frac{\sqrt{-\pi D}}{2},$$

and

$$C'_0 = \frac{(\gamma_1 - V_{00})}{V_{00'}}C_0 = -\frac{2}{\sqrt{\pi}}C_0,$$

where we have retained only the root corresponding to the growing solution. Here $V_{nm} \equiv \int_0^1 \boldsymbol{b}_n \cdot \widehat{V}\boldsymbol{b}_m dz$ are the perturbation matrix elements, whose direct calculation yields

$$V_{00'} = -\pi\sqrt{-D}/4, \quad V_{0'0} = -\sqrt{-D}, \quad V_{00} = V_{0'0'} = -\frac{R_U}{2}.$$

The eigenvalue can be evaluated to a higher order in ϵ than the eigenfunction since it depends on the matrix elements $V_{\tilde{0}n}$, $V_{\tilde{0}n'}$, $V_{n\tilde{0}}$, and $V_{n'\tilde{0}}$, where, e.g., $V_{\tilde{0}n} \equiv \int_0^1 \tilde{\boldsymbol{b}}_0 \cdot \widehat{V}\boldsymbol{b}_n dz$, and

$$\tilde{\boldsymbol{b}} \equiv C_0\boldsymbol{b}_0 + C'_0\boldsymbol{b}'_0 = C_0\begin{pmatrix} 1 \\ -2/\sqrt{\pi} \end{pmatrix}\sqrt{2}\cos\left(\frac{\pi z}{2}\right).$$

The above method then yields:

$$\gamma_2 = \sum_{n=1}^{\infty}\frac{V_{n\tilde{0}}V_{\tilde{0}n} + V_{n'\tilde{0}}V_{\tilde{0}n'}}{\lambda_0 - \lambda_n},$$

and

$$C_n = \frac{V_{n\tilde{0}}}{\lambda_0 - \lambda_n}, \quad C'_n = \frac{V_{n'\tilde{0}}}{\lambda_0 - \lambda_n},$$

where

$$V_{n\tilde{0}} = C_0 \times \begin{cases} \dfrac{3\sqrt{-\pi D}}{2} - \dfrac{3R_U}{4}, & n = 1; \\ \dfrac{2n+1}{n(n+1)} \dfrac{(-1)^n R_U}{2}, & n \geq 2. \end{cases}$$

$$V_{n'\tilde{0}} = C_0 \times \begin{cases} -\dfrac{2n+1}{n(n+1)} \dfrac{(-1)^n R_U}{\sqrt{\pi}}, & n \geq 1. \end{cases}$$

$$V_{\tilde{0}n} = C_0 \times \begin{cases} -\dfrac{2n+1}{n(n+1)} \dfrac{(-1)^n R_U}{2}, & n \geq 1. \end{cases}$$

$$V_{\tilde{0}n'} = C_0 \times \begin{cases} \dfrac{\pi\sqrt{-D}}{4} - \dfrac{3R_U}{2\sqrt{\pi}}, & n = 1; \\ \dfrac{2n+1}{n(n+1)} \dfrac{(-1)^n R_U}{\sqrt{\pi}}, & n \geq 2. \end{cases}$$

Using the fact that

$$\sum_{n=2}^{\infty} \frac{(2n+1)^2}{2n^3(n+1)^3} = -\frac{25}{16} + \frac{\pi^2}{6},$$

we find

$$\gamma_2 = \frac{3R_U}{4\sqrt{\pi}(\pi+4)} + \frac{R_U^2}{2\pi^2}\left(1 - \frac{\pi^2}{6}\right).$$

For the eigenfunction, we obtain

$$\begin{aligned} \sum_{n=1}^{\infty}(C_n \boldsymbol{b}_n + C_n' \boldsymbol{b}_n') =& \frac{C_0}{\pi^2}\Bigg\{ \frac{3}{4}\left[\sqrt{-\pi D}\boldsymbol{b}_1 - \frac{R_U}{2}\left(\boldsymbol{b}_1 - \frac{2\boldsymbol{b}_1'}{\sqrt{\pi}}\right)\right] \\ &+ \frac{R_U}{2}\sum_{n=2}^{\infty}\left[\frac{(-1)^n(2n+1)}{n^2(n+1)^2}\left(\boldsymbol{b}_n - \frac{2\boldsymbol{b}_n'}{\sqrt{\pi}}\right)\right]\Bigg\}. \end{aligned}$$

Thus, the final solution of second order perturbation theory, upon restoring $\epsilon = 1$, and also restoring the original definitions of $\mathcal{B}_r$ and $\mathcal{B}_\phi$ in equation (A.3), reduces to

$$\begin{aligned} \gamma &= -\frac{\pi^2}{4} + \frac{\sqrt{-\pi D}}{2} - \frac{R_U}{2} + \frac{3\sqrt{-\pi D}R_U}{4\pi(\pi+4)} + \frac{R_U^2}{2\pi^2}\left(1 - \frac{\pi^2}{6}\right), \\ \mathcal{B}_r =& C_0 R_\alpha \Bigg\{ \cos\left(\frac{\pi z}{2}\right) + \frac{3}{4\pi^2}\left(\sqrt{-\pi D} - \frac{R_U}{2}\right)\cos\left(\frac{3\pi z}{2}\right) \\ &+ \frac{R_U}{2\pi^2}\sum_{n=2}^{\infty}\frac{(-1)^n(2n+1)}{n^2(n+1)^2}\cos\left[\left(n+\tfrac{1}{2}\right)\pi z\right]\Bigg\}, \end{aligned} \tag{A.5}$$

$$\mathcal{B}_\phi = -\frac{2}{\pi} C_0 \sqrt{-\pi D} \left\{ \cos\left(\frac{\pi z}{2}\right) - \frac{3R_U}{8\pi^2} \cos\left(\frac{3\pi z}{2}\right) \right.$$
$$\left. + \frac{R_U}{2\pi^2} \sum_{n=2}^{\infty} \frac{(-1)^n (2n+1)}{n^2 (n+1)^2} \cos\left[\left(n + \tfrac{1}{2}\right) \pi z\right] \right\}, \tag{A.6}$$

where $C_0 = 1/\sqrt{1 + 4/\pi}$ for the solution normalized as $\int_0^1 B^2 dz = 1$. The eigenfunctions are plotted in Fig. A.1 and the magnetic pitch angle, in Fig. A.2. Solving for the critical ($\gamma = 0$) dynamo number we obtain

$$D_{\rm c} = -\frac{\pi^3}{4} \left\{ \frac{1 + 2R_U/\pi^2 - (2R_U^2/\pi^4)(1 - \pi^2/6)}{1 + 3R_U/[2\pi(\pi + 4)]} \right\}^2 .$$

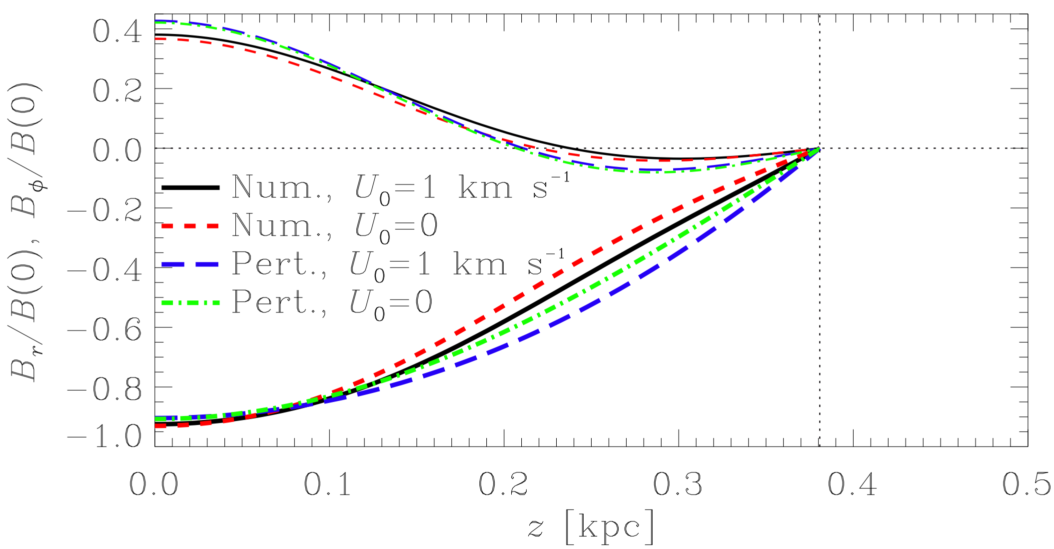

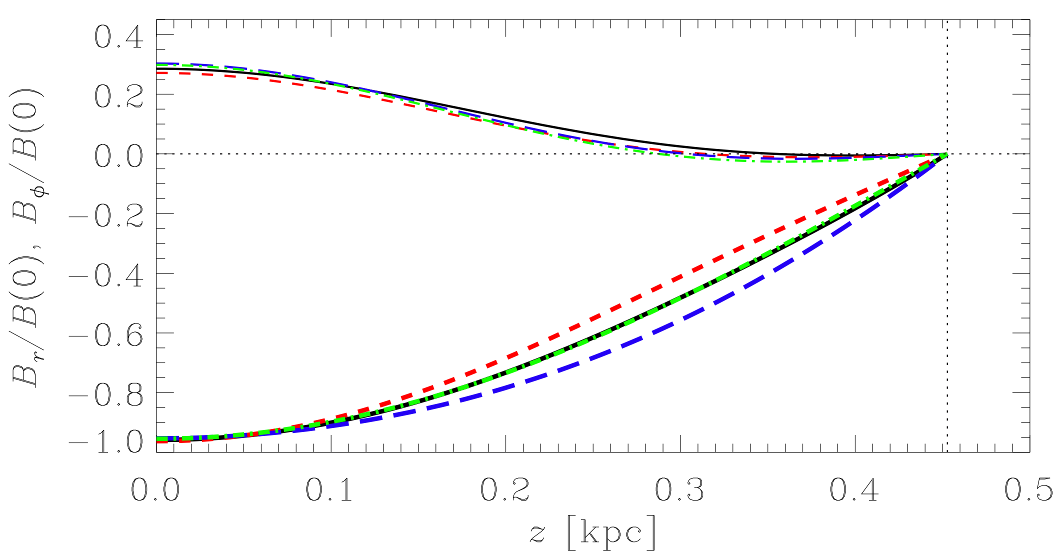

Figure A.1: Radial (thin) and azimuthal (thick) components of $\overline{\boldsymbol{B}}$ in the kinematic stage, normalized to the magnetic field strength at the midplane for parameters corresponding to $r = 4\,\mathrm{kpc}$ (top) and $r = 8\,\mathrm{kpc}$ (bottom). Solutions from perturbation theory [equations (A.5) and (A.6)] are compared with numerical solutions for $U_0 = 0$ and $U_0 = 1\,\mathrm{km\,s^{-1}}$. Solutions are symmetric about the midplane.

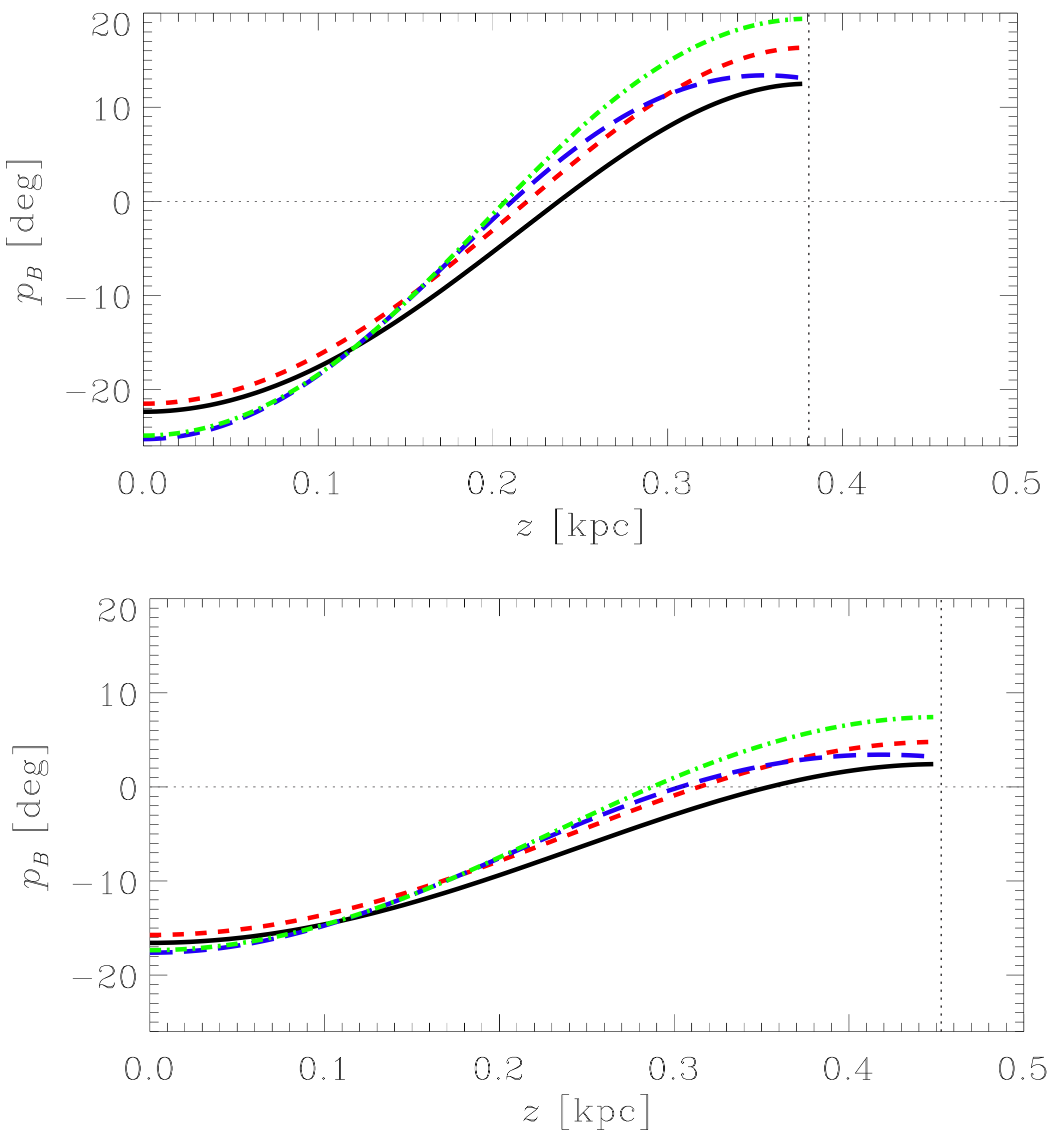

Figure A.2: Magnetic pitch angle $p_B \equiv \arctan(\overline{B}_r/\overline{B}_\phi)$ in the kinematic stage, as a function of the distance z from the midplane, for parameters corresponding to $r = 4\,\mathrm{kpc}$ (top) and $r = 8\,\mathrm{kpc}$ (bottom). p_B is not plotted for $z = h$, as it is undefined at the disc boundaries, where the boundary conditions enforce $\overline{B}_r = \overline{B}_\phi = 0$. (Legend is the same as for Fig. A.1.)

Appendix B

The no-z asymptotic solution

Equations (2.8)-(2.10) can be solved in an approximate way as a set of algebraic equations by setting time derivatives to zero (that is, by assuming the system reaches a steady state) and by using the no-z approximation to replace z-derivatives by simple divisions. This method allows for a determination of all relevant quantities, but these quantities now represent averages over the disc half-thickness h. The method is not new (Sur et al., 2007), but here we neglect Ohmic terms, include the diffusive flux, and do not assume that $\overline{B}_r^2/\overline{B}_\phi^2 \ll 1$. We do, however, adopt the $\alpha\Omega$ approximation for simplicity. We also include an expression for the growth rate γ in the kinematic regime, which is obtained by assuming $\overline{\boldsymbol{B}} \propto \mathrm{e}^{\gamma t}$.

Furthermore, we include as yet unspecified numerical factors in the no-z terms. There are in general four such factors that are not already specified in Phillips (2001): $C_{U,r}$, such that $\partial(\overline{U}_z\overline{B}_r)/\partial z \simeq C_{U,r}\overline{U}_z\overline{B}_r/h$, $C_{U,\phi}$, where, similarly, $\partial(\overline{U}_z\overline{B}_\phi)/\partial z \simeq C_{U,\phi}\overline{U}_z\overline{B}_\phi/h$, C_a, where $\partial(\overline{U}_z\alpha_\mathrm{m})/\partial z \simeq C_\mathrm{a}\overline{U}_z\alpha_\mathrm{m}/h$ for the advective flux term, and finally C_d, with $\partial^2\alpha_\mathrm{m}/\partial z^2 \simeq C_\mathrm{d}\alpha_\mathrm{m}/h^2$ for the diffusive flux term. For simplicity, we approximate $C_{U,r} = C_{U,\phi} = C_U$, which turns out to be fairly reasonable (see Fig. B.1 and the discussion in Section B.1).

Equations (A.1) and (A.2) can be written in the no-z approximation, in dimensionless form ($h = \eta_\mathrm{t} = 1$) as

$$\left(\gamma + \frac{\pi^2}{4}g\right)\overline{B}_r = -\frac{2}{\pi}R_\alpha\overline{B}_\phi,$$
$$\left(\gamma + \frac{\pi^2}{4}g\right)\overline{B}_\phi = R_\omega\overline{B}_r,$$

where $g \equiv 1 + 4C_UR_U/\pi^2$. From the solvability condition for the homogeneous equations

$(\gamma+\pi^2 g/4)^2 = -2D/\pi$, we set $\gamma = 0$ to obtain the critical dynamo number,

$$D_{\mathrm{c}} = -\frac{\pi^5}{32} g^2.$$

Solving for γ, we then obtain

$$\gamma = \frac{\pi^2}{4} t_{\mathrm{d}}^{-1} g \left(\sqrt{\frac{D}{D_{\mathrm{c}}}} - 1 \right),$$

where $t_{\mathrm{d}} = h^2/\eta_{\mathrm{t}}$ is the turbulent diffusion time-scale. Defining $p_B \equiv \arctan(\overline{B}_r/\overline{B}_\phi)$, and letting $R_\alpha = R_{\alpha,\mathrm{c}}$ since we are interested in the saturated solution, we obtain

$$\tan p_B = \sqrt{-\frac{2R_{\alpha,\mathrm{c}}}{\pi R_\omega}} = \frac{\pi^2}{4} \frac{g}{R_\omega}. \tag{B.1}$$

Finally, for the saturation field strength we use equation (2.10) with the left hand side equal to zero, the expression

$$(\boldsymbol{\nabla} \times \overline{\boldsymbol{B}}) \cdot \overline{\boldsymbol{B}} \simeq -\frac{3\sqrt{-\pi D_{\mathrm{c}}} \tan(p_B) B^2}{8h[1+\tan^2(p_B)]} \tag{B.2}$$

valid in the no-z approximation (Sur et al., 2007), along with the above expression (B.1) for $\tan p_B$ in terms of $R_{\alpha,\mathrm{c}}$. It is then straightforward to obtain

$$B^2 = B_{\mathrm{eq}}^2 \frac{\xi(p_B)}{C} \left(\frac{D}{D_{\mathrm{c}}} - 1 \right) (C_{\mathrm{a}} R_U - C_{\mathrm{d}} R_\kappa),$$

where $\xi(p_B) \equiv [1 - 3\cos^2(p_B)/(4\sqrt{2})]^{-1}$ and $C \equiv 2(h/l)^2$. We note that $C_{\mathrm{d}} < 0$ (Section B.1).

B.1 Refining the no-z approximation

The values of C_U, C_{a} and C_{d} are estimated in the following way. To estimate C_U, equations (2.8) and (2.9) are first solved numerically and the true value of the growth rate γ obtained. The no-z approximation is then applied *to only those terms involving* C_U, e.g. $\partial(\overline{U}_z\overline{B}_r)/\partial z$ is replaced with $C_U U_0 \overline{B}_r/h$ (but $\overline{B}_r$ is still z-dependent). The value of C_U is then varied iteratively until γ is equal to the true value. This is also done for $C_{U,r}$ and $C_{U,\phi}$ by using the method on each of the relevant terms, individually. To estimate C_{a} and C_{d}, the same approach is taken, with the relevant term involving C_{a} or C_{d} replaced with its no-z form,

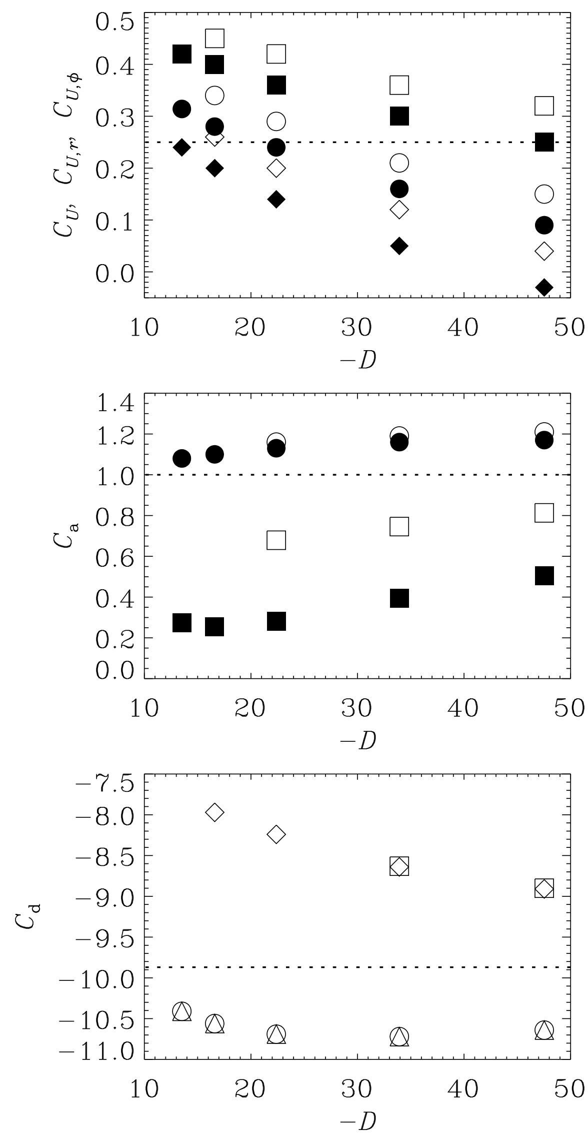

Figure B.1: **Top**: Parameter C_U for $U_0 = 1\,\mathrm{km\,s^{-1}}$ (filled circles) and $2\,\mathrm{km\,s^{-1}}$ (open circles), $C_{U,r}$ for $U_0 = 1\,\mathrm{km\,s^{-1}}$ (filled diamonds) and $2\,\mathrm{km\,s^{-1}}$ (open diamonds), $C_{U,\phi}$ for $U_0 = 1\,\mathrm{km\,s^{-1}}$ (filled squares) and $2\,\mathrm{km\,s^{-1}}$ (open squares). Middle: Parameter $C_{\rm a}$ for $U_0 = 1\,\mathrm{km\,s^{-1}}$ and $R_\kappa = 0$ (filled circles), $U_0 = 2\,\mathrm{km\,s^{-1}}$ and $R_\kappa = 0$ (open circles), $U_0 = 1\,\mathrm{km\,s^{-1}}$ and $R_\kappa = 0.3$ (filled squares), and $U_0 = 2\,\mathrm{km\,s^{-1}}$ and $R_\kappa = 0.3$ (open squares). **Bottom**: Parameter $C_{\rm d}$ for $R_\kappa = 0.3$ and $U_0 = 0$ (circles), $R_\kappa = 0.3$ and $U_0 = 1\,\mathrm{km\,s^{-1}}$ (diamonds), $R_\kappa = 0.3$ and $U_0 = 2\,\mathrm{km\,s^{-1}}$ (squares), and $R_\kappa = 0.6$ and $U_0 = 0$ (triangles). Data for five different dynamo numbers $D = -47.5, -33.9, -22.4, -16.6, -13.5$, corresponding to radii $r = 2, 4, 6, 8, 10\,\mathrm{kpc}$, respectively, is shown. Chosen values $C_U = 0.25$, $C_{\rm a} = 1$ and $C_{\rm d} = -\pi^2$ are shown by dashed lines on their respective graphs.

but now equations (2.8)-(2.10) are solved, and instead of matching the growth rate,

$$\langle B\rangle \equiv \frac{1}{2h}\int_{-h}^{h} B dz,$$

is matched to its true value. Alternatively, $\langle B^2\rangle^{1/2}$ could be chosen, but it was found that this choice leads to very similar results.

The results are summarized in Fig. B.1. Unfortunately, C_U, represented by circles in the top panel, has a fairly strong dependence on D, but luckily, a rather weak dependence on R_U. We adopt the value $C_U = 0.25$, which seems to be a reasonable choice given the data. The middle panel shows the values of C_a obtained for different D, R_U and R_κ. Values are close to unity for $R_\kappa = 0$, but drop quite drastically when $R_\kappa = 0.3$. We adopt $C_\mathrm{a} = 1$, keeping in mind that for cases with both advective and diffusive flux, this is an overestimate. Finally, the results for C_d are illustrated in the bottom panel of Fig. B.1. Its value does not stray very far from $-\pi^2$, which is the value that would be obtained if α_m were sinusoidal in z.

We therefore adopt the values $C_U = 1/4$, $C_\mathrm{a} = 1$, and $C_\mathrm{d} = -\pi^2$ in the present chapter and for chapter 6. It is worth mentioning that these choices may not be as suitable for a different $\overline{U}_z$ profile. With these choices, approximating a given term by its no-z form leads to errors in quantities such as γ, $\langle B/B_\mathrm{eq}\rangle$ or the pitch angle p_B of typically $< 10\%$ for parameters corresponding to $r = 4\,\mathrm{kpc}$ or $r = 8\,\mathrm{kpc}$ in our model. We fully realize that the values of these numerical factors, and the method used to determine them, are not exact or unique; the idea is to improve the no-z approximation in the same spirit as Phillips (2001), while admitting that the approximation itself is rather crude by nature. Note that the content of Chapter 3 predates this analysis: there we use $C_U = C_\mathrm{a} = 1$ and $C_\mathrm{d} = -\pi^2/4$, which anyway leads to qualitatively similar solutions.

Appendix C

The no-z approximation

C.1 Vertical diffusion

Under the no-z approximation, the second derivatives with respect to z can be approximated as $\partial^2\overline{B}_i/\partial z^2 \simeq -\pi^2\overline{B}_i/4h^2$ (where $i = r, \phi$), which gives the correct sign of the diffusion term. This approximation can be derived from the one-dimensional eigenfunctions obtained from the perturbation theory (Sur et al., 2007; Shukurov & Sokoloff, 2008).

C.2 The α effect

When applying the no-z approximation to the terms $\partial(\alpha\overline{B}_i)/\partial z$ in Eqs. (3.4) and (3.5), one must be careful about the sign. The sign must be chosen so that the α effect can contribute to a positive dynamo growth rate. This logic leads to the adoption of the approximations

$$-\frac{\partial}{\partial z}(\alpha\overline{B}_\phi) \simeq -\frac{|\alpha|\overline{B}_\phi}{h}, \quad \frac{\partial}{\partial z}(\alpha\overline{B}_r) \simeq -\frac{|\alpha|\overline{B}_r}{h}.$$

The second of these is only relevant when the α^2 effect is taken into consideration.

Furthermore, Phillips (2001) has shown that the no-z approximation can be made more accurate with the additional numerical factor $2/\pi$, at least for the $\alpha\Omega$ dynamo. As a matter of symmetry, we include the same numerical factor in front of both α terms, so that we may write

$$-\frac{\partial}{\partial z}(\alpha\overline{B}_\phi) \simeq -\frac{2|\alpha|\overline{B}_\phi}{\pi h}, \quad \frac{\partial}{\partial z}(\alpha\overline{B}_r) \simeq -\frac{2|\alpha|\overline{B}_r}{\pi h}. \tag{C.1}$$

It may be asked whether extending the no-z approximation to include the α term in the evolution equation for $\overline{B}_\phi$ (through Eq. 3.5), as we have done here for the first time, actually helps to improve the accuracy of the solution. To answer this, we compared the kinematic solutions obtained using simple two-dimensional (in $r-z$) $\alpha\Omega$ and $\alpha^2\Omega$ galactic dynamo model with those obtained from the corresponding one-dimensional (in r, with no-z) models. Interestingly, we found significantly better agreement between the 1D and 2D solutions when the α^2 effect was included in both models than when it was left out.

C.3 Vertical advection

The terms $-\overline{\boldsymbol{B}}\nabla\cdot\overline{\boldsymbol{U}}$ (divergence) and $-\overline{\boldsymbol{U}}\cdot\nabla\overline{\boldsymbol{B}}$ (advection) are approximated as

$$\frac{\partial \overline{B}_i}{\partial t} = ... - \frac{\partial \overline{U}_z}{\partial z}\overline{B}_i - \overline{U}_z\frac{\partial \overline{B}_i}{\partial z} \simeq ... - \frac{\overline{U}_z\overline{B}_i}{h}. \tag{C.2}$$

For the flux term $-\partial(\alpha_{\mathrm{m}}\overline{U}_z)/\partial z$ in (1.32), we have

$$\frac{\partial \alpha_{\mathrm{m}}}{\partial t} = ... - \frac{\alpha_{\mathrm{m}}\overline{U}_z}{h}. \tag{C.3}$$

C.4 Approximation for $\boldsymbol{\mathcal{E}}\cdot\overline{\boldsymbol{B}}$

For $\tau\to 0$, we have

$$\boldsymbol{\mathcal{E}}\cdot\overline{\boldsymbol{B}} = c_\tau\alpha(\overline{B}_r^2+\overline{B}_\phi^2) + c_\tau\eta_{\mathrm{t}}\left(\overline{B}_r\frac{\partial\overline{B}_\phi}{\partial z} - \overline{B}_\phi\frac{\partial\overline{B}_r}{\partial z}\right), \tag{C.4}$$

and the second bracketed term arising from the mean current helicity vanishes in the no-z approximation. Therefore, a more precise method must be used to estimate this term. With this in mind, Sur et al. (2007) substituted the one-dimensional perturbation solution of the dynamo equations,

$$\overline{B}_r = R_\alpha C_0\left(\cos\frac{\pi z}{2h} + \frac{3}{4\pi}\sqrt{\frac{-D}{\pi}}\cos\frac{3\pi z}{2h}\right), \tag{C.5}$$

$$\overline{B}_\phi = -2C_0\sqrt{\frac{-D}{\pi}}\cos\frac{\pi z}{2h}, \tag{C.6}$$

and its derivatives with respect to z into Eq. (C.4). The resulting expression for $\boldsymbol{\mathcal{E}}\cdot\overline{\boldsymbol{B}}$ was then averaged over $0\le z\le h$. In this way they obtained a non-zero estimate for $c_\tau\eta_{\mathrm{t}}(\overline{B}_r\partial\overline{B}_\phi/\partial z - \overline{B}_\phi\partial\overline{B}_r/\partial z)$, which stems from the term of order $\sqrt{-D}$ in Eq. (C.5).

In the general case of finite τ, the correction must come in the evolution equations

(3.7) and (3.8) for $\mathcal{E}_r$ and $\mathcal{E}_\phi$. Averaging Eqs. (C.5) and (C.6) and also their z-derivatives over $0 \le z \le h$, we find

$$\frac{\partial \overline{B}_r}{\partial z} \simeq -\frac{\pi}{2h}\left(1+\frac{3\sqrt{-D}}{4\pi^{3/2}}\right)\overline{B}_r, \tag{C.7}$$

$$\frac{\partial \overline{B}_\phi}{\partial z} = -\frac{\pi}{2h}\overline{B}_\phi. \tag{C.8}$$

These expressions are used in Eqs. (3.7) and (3.8) for calculating $\boldsymbol{\mathcal{E}} \cdot \overline{\boldsymbol{B}}$ in Eq. (1.32).

Substituting expressions (C.7) and (C.8) into Eq. (C.4), we find for the $\tau \to 0$ limit,

$$\boldsymbol{\mathcal{E}} \cdot \overline{\boldsymbol{B}} \simeq c_\tau \alpha(\overline{B}_r^2 + \overline{B}_\phi^2) + c_\tau \eta_\mathrm{t} \frac{3\sqrt{-D}}{8\pi^{1/2}h}\overline{B}_r\overline{B}_\phi. \tag{C.9}$$

The term involving η_t used here is smaller by a factor π than that of Sur et al. (2007) since we have taken the scalar product of the z-averages of $\boldsymbol{\mathcal{E}}$ and $\overline{\boldsymbol{B}}$, whereas those authors used the average of the scalar product. This difference does not appear to be important.

C.5 Testing the validity of the no-z approximation

We have performed 2D simulations in r-z with the same parameters as our r-ϕ-'no-z' simulation with an axisymmetric disc (as Models A and B but without disc flaring). For the r-z runs, we adopted the profiles $\alpha_\mathrm{k} = \overline{\alpha}\sin(\pi z/h)$, $\overline{U}_z = U_0 z/h$, as well as boundary conditions $\overline{B}_r = \overline{B}_\phi = 0$ at $z = \pm h$. Comparing the solution of the r-z model (averaged over the vertical extent of the disc) with that of the r-ϕ-'no-z' model, we find good qualitative agreement. We do, however, find that the saturation strength of the magnetic field is larger by a factor ~ 2 in the r-z model, which suggests that this quantity is underestimated somewhat in the solutions presented in this paper.

Appendix D

Details of the asymptotic solutions

In the no-z approximation, the vertical diffusion terms are approximated as

$$\frac{\partial^2 a_{\pm 2}}{\partial z^2} \simeq -\frac{\pi^2 a_{\pm 2}}{4h^2}, \quad \frac{\partial^2 b_{\pm 2}}{\partial z^2} \simeq -\frac{\pi^2 b_{\pm 2}}{4h^2},$$

where h is the disc half-thickness. Further, the terms containing α can be approximated as

$$\frac{\partial}{\partial z}(\alpha_0 b_0 + \alpha_2 b_{-2} + \alpha_{-2} b_2) \simeq \frac{2}{\pi h}(\alpha_0 b_0 + \alpha_2 b_{-2} + \alpha_{-2} b_2),$$
$$\frac{\partial}{\partial z}(\alpha_0 b_{\pm 2} + \alpha_{\pm 2} b_0) \simeq \frac{2}{\pi h}(\alpha_0 b_{\pm 2} + \alpha_{\pm 2} b_0).$$

For the radial diffusion terms, we start by representing $a_{\pm 2}$ and $b_{\pm 2}$ as

$$a_{\pm 2} = -\overline{a}(r)\mathrm{e}^{\mp i\theta_a(r)}, \quad b_{\pm 2} = \overline{b}(r)\mathrm{e}^{\mp i\theta_b(r)}, \tag{D.1}$$

where the minus sign in front of $\overline{a}$ is introduced for future convenience, and where we have removed the z-dependence of $\overline{a}$ and $\overline{b}$ due to the fact that we are now working in the no-z approximation. Note that $|a_2| = |a_{-2}|$ and $|b_2| = |b_{-2}|$, whereas the phases of a_2 and a_{-2} (or b_2 and b_{-2}) must be equal in magnitude and opposite in sign, since $\overline{B}_r$ and $\overline{B}_\phi$ are real. We then apply the WKBJ-type tight-winding approximation, assuming that the amplitude varies much less rapidly with radius than the phase, i.e.,

$$\left|\frac{d\overline{a}}{dr}\right| \ll \left|\overline{a}\frac{d\theta_a}{dr}\right|, \quad \left|\frac{d\overline{b}}{dr}\right| \ll \left|\overline{b}\frac{d\theta_b}{dr}\right|. \tag{D.2}$$

The radial diffusion terms are then approximated by

$$\frac{d}{dr}\left[\frac{1}{r}\frac{d}{dr}(ra_{\pm 2})\right] \simeq -\left(\theta_a'^2 \pm i\theta_a''\right) a_{\pm 2}, \tag{D.3}$$

$$\frac{d}{dr}\left[\frac{1}{r}\frac{d}{dr}(rb_{\pm 2})\right] \simeq -\left(\theta_b'^2 \pm i\theta_b''\right) b_{\pm 2}, \tag{D.4}$$

where prime stands for d/dr. It should be noted that in the region where the relative strength of non-axisymmetric components with respect to axisymmetric components is expected to be the largest (near the corotation radius), we expect $1/r \ll |d/dr|$ since the corotation radius is typically comparable to the size of the galaxy. Thus, we have dropped terms proportional to $1/r$. Since turbulent diffusion terms containing the ϕ-derivatives are proportional to $1/r^2$, they, too, can be neglected. We find these approximations to be suitable even for the essentially axisymmetric modes that are located much closer to the galactic centre, where the dynamo number is maximum, because even here the radial scale length of the field turns out to be small compared to r in the kinematic regime.

With the above approximations, Eqs. (4.15) and (4.16) yield, after some algebra,

$$b_{\pm 2} = b_0 \frac{\alpha_{\pm 2}}{\alpha_0}|D_0| X_{\pm 2}, \quad a_{\pm 2} = -Y_{\pm 2} b_{\pm 2}. \tag{D.5}$$

Here

$$X_{\pm 2}(r) = \frac{(A \mp iB)}{A^2 + B^2} = \frac{\mathrm{e}^{\mp i\beta}}{\sqrt{A^2 + B^2}} = X^*_{\mp 2}, \tag{D.6}$$

and

$$Y_{\pm 2}(r) = \widetilde{A} \mp i\widetilde{B} = \sqrt{\widetilde{A}^2 + \widetilde{B}^2}\,\mathrm{e}^{\mp i\widetilde{\beta}} = Y^*_{\mp 2}, \tag{D.7}$$

with the dynamo number defined as

$$D_0 = \frac{\alpha_0 G h^3}{\eta_{\mathrm{t}}^2} = \frac{\alpha_0 G t_{\mathrm{d}}^2}{h} < 0, \tag{D.8}$$

where $t_{\mathrm{d}} = h^2/\eta_{\mathrm{t}}$ is the vertical turbulent diffusion time scale and

$$\cos\beta = \frac{A}{\sqrt{A^2 + B^2}}, \quad \sin\beta = \frac{B}{\sqrt{A^2 + B^2}}, \tag{D.9}$$

with

$$
\begin{aligned}
A = D_0 + \frac{\pi}{2c_\tau}\Bigg\{ & t_\mathrm{d}^2(1+\Gamma\tau)(\Gamma^2 - 4\widetilde{\omega}^2) + 8\Omega_\mathrm{p}\Gamma\widetilde{\omega}\tau t_\mathrm{d}^2 + \Big[(1+\Gamma\tau)^2 + (2\Omega_\mathrm{p}\tau)^2\Big]^{-1} \\
& \times \Big[c_\tau^2(1+\Gamma\tau)(\tfrac{1}{4}\pi^2 + \theta_a'^2 h^2)(\tfrac{1}{4}\pi^2 + \theta_b'^2 h^2) \\
& \quad - 2c_\tau^2\Omega_\mathrm{p}\tau\left[\left(\tfrac{1}{4}\pi^2 + \theta_a'^2 h^2\right)\theta_b'' h^2 + \left(\tfrac{1}{4}\pi^2 + \theta_b'^2 h^2\right)\theta_a'' h^2\right] - c_\tau^2(1+\Gamma\tau)\theta_a''\theta_b'' h^4\Big] \\
& + c_\tau\Gamma t_\mathrm{d}\left(\tfrac{1}{2}\pi^2 + \theta_a'^2 h^2 + \theta_b'^2 h^2\right) - 2c_\tau\widetilde{\omega} t_\mathrm{d} h^2(\theta_a'' + \theta_b'')\Bigg\},
\end{aligned}
\tag{D.10}
$$

$$
\begin{aligned}
B = \frac{\pi}{2c_\tau}\Bigg\{ & -2\Omega_\mathrm{p}\tau t_\mathrm{d}^2(\Gamma^2 - 4\widetilde{\omega}^2) + 4(1+\Gamma\tau)\Gamma\widetilde{\omega} t_\mathrm{d}^2 + \Big[(1+\Gamma\tau)^2 + (2\Omega_\mathrm{p}\tau)^2\Big]^{-1} \\
& \times \Big[2c_\tau^2\Omega_\mathrm{p}\tau(\tfrac{1}{4}\pi^2 + \theta_a'^2 h^2)(\tfrac{1}{4}\pi^2 + \theta_b'^2 h^2) \\
& \quad + c_\tau^2(1+\Gamma\tau)\left[(\tfrac{1}{4}\pi^2 + \theta_a'^2 h^2)\theta_b'' h^2 + (\tfrac{1}{4}\pi^2 + \theta_b'^2 h^2)\theta_a'' h^2\right] - 2c_\tau^2\Omega_\mathrm{p}\tau\theta_a''\theta_b'' h^4\Big] \\
& + 2c_\tau\widetilde{\omega} t_\mathrm{d}\left(\tfrac{1}{2}\pi^2 + \theta_a'^2 h^2 + \theta_b'^2 h^2\right) + c_\tau\Gamma t_\mathrm{d} h^2(\theta_a'' + \theta_b'')\Bigg\}.
\end{aligned}
\tag{D.11}
$$

Further,

$$
\cos\widetilde{\beta} = \frac{\widetilde{A}}{\sqrt{\widetilde{A}^2 + \widetilde{B}^2}}, \quad \sin\widetilde{\beta} = \frac{\widetilde{B}}{\sqrt{\widetilde{A}^2 + \widetilde{B}^2}}, \tag{D.12}
$$

with

$$
\widetilde{A} = -\frac{\Gamma}{G} - c_\tau\frac{(1+\Gamma\tau)(\frac{1}{4}\pi^2 + \theta_b'^2 h^2) - 2\Omega_\mathrm{p}\tau\theta_b'' h^2}{[(1+\Gamma\tau)^2 + (2\Omega_\mathrm{p}\tau)^2]G t_\mathrm{d}}, \tag{D.13}
$$

$$
\widetilde{B} = \frac{2\widetilde{\omega}}{G} + c_\tau\frac{2\Omega_\mathrm{p}\tau(\frac{1}{4}\pi^2 + \theta_b'^2 h^2) + (1+\Gamma\tau)\theta_b'' h^2}{[(1+\Gamma\tau)^2 + (2\Omega_\mathrm{p}\tau)^2]G t_\mathrm{d}}. \tag{D.14}
$$

Substituting (4.11), (D.6) and (D.7) into Eq. (D.5), we arrive at

$$
a_{\pm 2} = -\frac{|D_0| b_0 \epsilon_\alpha}{2}\sqrt{\frac{\widetilde{A}^2 + \widetilde{B}^2}{A^2 + B^2}}\exp\Big[\mp i(\kappa r + \beta + \widetilde{\beta})\Big], \tag{D.15}
$$

$$
b_{\pm 2} = \frac{|D_0| b_0 \epsilon_\alpha}{2}\frac{1}{\sqrt{A^2 + B^2}}\exp\left[\mp i(\kappa r + \beta)\right]. \tag{D.16}
$$

Using Eqs. (D.1), we now make the identifications

$$
\theta_a = \kappa r + \beta + \widetilde{\beta}, \qquad \theta_b = \kappa r + \beta,
$$

and so

$$\theta_a' = \kappa + \beta' + \widetilde{\beta}', \quad \theta_b' = \kappa + \beta', \quad \theta_a'' = \beta'' + \widetilde{\beta}'', \quad \theta_b'' = \beta''. \tag{D.17}$$

Clearly, β and $\widetilde{\beta}$ depend on A, B, $\widetilde{A}$ and $\widetilde{B}$ (Eqs. D.9 and D.12), which, in turn, depend on the derivatives of β and $\widetilde{\beta}$ through θ_a', θ_b', θ_a'' and θ_b'' (Eqs. D.10, D.11, D.13 and D.14). This means that, unless β' and $\widetilde{\beta}'$ are completely neglected, it is not possible to obtain an analytical solution. We will see however that, if the terms involving β', $\widetilde{\beta}'$, β'' and $\widetilde{\beta}''$ are small compared with the turbulent diffusion terms that do not vary with r, then β and $\widetilde{\beta}$ can be determined semi-analytically, by successive iteration.

The need for the iterations can be understood as follows. Firstly, if β' and $\widetilde{\beta}'$ were zero, then the radial phase would be κr, which is the same as the radial phase of the α-spiral. Thus, the magnetic arms would be as tightly wound as the α-arms. In fact, the extra contributions to the radial phase $\beta + \widetilde{\beta}$ for $\overline{B}_r$ and β for $\overline{B}_\phi$, are finite, and turn out to have the same sign as κ. This implies that the magnetic arms (defined as the set of positions where $|\overline{\boldsymbol{B}}|$ is maximum), are more tightly wound than the material arms that produce them. This is because the enhancement of field due to the enhanced dynamo action within the α-arm is advected downstream with the differentially rotating gas. Ultimately a balance is set up between the competing effects of preferential magnetic field generation in the α-arms and advection downstream, resulting in stationary magnetic arms that are more tightly wound than the α-arms, and cross them near the corotation circle. Moreover, this balance, which determines the pitch angle of the magnetic arms (ridges), and thus the values of β and $\widetilde{\beta}$, involves many quantities, including the derivatives of β and $\widetilde{\beta}$ through the radial diffusion (as seen in the equations in this appendix). This self-dependence results from the fact that the radial diffusion is stronger when the magnetic arms (ridges) are more tightly wound, as can be seen from Eqs. (D.3) and (D.4). Thus, the radial diffusion feeds back onto itself, forcing us to iterate to obtain the functions β and $\widetilde{\beta}$.

Bibliography

Acharova I. A., Mishurov Y. N., Rasulova M. R., 2011, MNRAS, 415, L11

Baba J., Saitoh T. R., Wada K., 2013, ApJ, 763, 46

Bardou A., von Rekowski B., Dobler W., Brandenburg A., Shukurov A., 2001, A&A, 370, 635

Baryshnikova I., Shukurov A., Ruzmaikin A., Sokoloff D. D., 1987, A&A, 177, 27

Beck R., 2007, A&A, 470, 539

—, 2012, Space Sci. Rev., 166, 215

Beck R., Brandenburg A., Moss D., Shukurov A., Sokoloff D., 1996, ARA&A, 34, 155

Beck R., Fletcher A., Shukurov A., Snodin A., Sokoloff D. D., Ehle M., Moss D., Shoutenkov V., 2005, A&A, 444, 739

Beck R., Hoernes P., 1996, Nature, 379, 47

Beck R., Shukurov A., Sokoloff D., Wielebinski R., 2003, A&A, 411, 99

Beck R., Wielebinski R., 2013, Magnetic Fields in Galaxies, Oswalt T. D., Gilmore G., eds., p. 641

Berger M. A., Field G. B., 1984, Journal of Fluid Mechanics, 147, 133

Bernet M. L., Miniati F., Lilly S. J., 2013, ApJ, 772, L28

Bhat P., Blackman E. G., Subramanian K., 2014, MNRAS, 438, 2954

Binney J., Tremaine S., 2008, Galactic Dynamics, 2nd ed. Princeton University Press

Blackman E. G., 2014, Space Sci. Rev.

Blackman E. G., Brandenburg A., 2003, ApJ, 584, L99

Blackman E. G., Field G. B., 2000, ApJ, 534, 984

—, 2002, Physical Review Letters, 89, 265007

Blackman E. G., Subramanian K., 2013, MNRAS, 429, 1398

Boomsma R., Oosterloo T. A., Fraternali F., van der Hulst J. M., Sancisi R., 2008, A&A, 490, 555

Brandenburg A., 2001, ApJ, 550, 824

—, 2003, Computational aspects of astrophysical MHD and turbulence, Taylor & Francis, London and New York, p. 269

—, 2005, ApJ, 625, 539

Brandenburg A., Candelaresi S., Chatterjee P., 2009, MNRAS, 398, 1414

Brandenburg A., Käpylä P. J., Mohammed A., 2004, Physics of Fluids, 16, 1020

Brandenburg A., Subramanian K., 2005a, Phys. Rep., 417, 1

—, 2005b, A&A, 439, 835

—, 2007, Astronomische Nachrichten, 328, 507

Bykov A., Popov V., Shukurov A., Sokoloff D., 1997, MNRAS, 292, 1

Candelaresi S., Hubbard A., Brandenburg A., Mitra D., 2011, Physics of Plasmas, 18, 012903

Chyży K. T., 2008, A&A, 482, 755

Chyży K. T., Buta R. J., 2008, ApJ, 677, L17

Ciardullo R., Feldmeier J. J., Jacoby G. H., Kuzio de Naray R., Laychak M. B., Durrell P. R., 2002, ApJ, 577, 31

Comparetta J., Quillen A. C., 2012, ArXiv e-prints

Courant R., Hilbert D., 1989, Methods of mathematical physics. John Wiley & Sons, New York

Crosthwaite L. P., Turner J. L., Ho P. T. P., 2000, AJ, 119, 1720

Dobbs C. L., 2011, Memorie della Societa Astronomica Italiana Supplementi, 18, 109

Dobbs C. L., Theis C., Pringle J. E., Bate M. R., 2010, MNRAS, 403, 625

D'Onghia E., Vogelsberger M., Hernquist L., 2013, ApJ, 766, 34

Ebrahimi F., Bhattacharjee A., 2014, Physical Review Letters, 112, 125003

Ehle M., Beck R., Haynes R. F., Vogler A., Pietsch W., Elmouttie M., Ryder S., 1996, A&A, 306, 73

Eigenbrot A., Bershady M., 2013, ArXiv e-prints

Elmegreen B. G., Elmegreen D. M., Montenegro L., 1992, ApJS, 79, 37

Elmegreen B. G., Seiden P. E., Elmegreen D. M., 1989, ApJ, 343, 602

Elstner D., 2005, in The Magnetized Plasma in Galaxy Evolution, Chyzy K. T., Otmianowska-Mazur K., Soida M., Dettmar R.-J., eds., Jagiellonian University, Krakow, pp. 117–124

Elstner D., Gressel O., 2012, ArXiv e-prints

Eyink G. L., 2011, Phys. Rev. E, 83, 056405

—, 2012, Turbulence Theory, Course Notes, John Hopkins Univ., http://www.ams.jhu.edu/∼eyink/Turbulence/

Fathi K., Toonen S., Falcón-Barroso J., Beckman J. E., Hernandez O., Daigle O., Carignan C., de Zeeuw T., 2007, ApJ, 667, L137

Fletcher A., 2010, in Astronomical Society of the Pacific Conference Series, Vol. 438, Astronomical Society of the Pacific Conference Series, Kothes R., Landecker T. L., Willis A. G., eds., p. 197

Fletcher A., Beck R., Shukurov A., Berkhuijsen E. M., Horellou C., 2011, MNRAS, 412, 2396

Frick P., Beck R., Shukurov A., Sokoloff D., Ehle M., Kamphuis J., 2000, MNRAS, 318, 925

García-Burillo S., Combes F., Gerin M., 1993, A&A, 274, 148

Gent F. A., Shukurov A., Sarson G. R., Fletcher A., Mantere M. J., 2013, MNRAS, 430, L40

Gerhard O., 2011, Memorie della Societa Astronomica Italiana Supplementi, 18, 185

Germano M., 1992, JFM, 238, 325

Grand R. J. J., Kawata D., Cropper M., 2012, MNRAS, 421, 1529

Gressel O., 2010, PhD thesis, PhD Thesis, 2010

Gressel O., Bendre A., Elstner D., 2013, MNRAS, 429, 967

Griffiths D., 2005, Introduction to Quantum Mechanics. Pearson Education, Essex

Gruzinov A. V., Diamond P. H., 1994, Physical Review Letters, 72, 1651

Haverkorn M., 2014, ArXiv e-prints

Heald G. H., 2012, ApJ, 754, L35

Higdon J. C., Lingenfelter R. E., 2013, ApJ, 775, 110

Hirota A., Kuno N., Sato N., Nakanishi H., Tosaki T., Matsui H., Habe A., Sorai K., 2009, PASJ, 61, 441

Hubbard A., Brandenburg A., 2009, ApJ, 706, 712

—, 2010, Geophysical and Astrophysical Fluid Dynamics, 104, 577

—, 2011, ApJ, 727, 11

—, 2012, ApJ, 748, 51

Hubbard A., Rheinhardt M., Brandenburg A., 2011, A&A, 535, A48

Hughes D. W., Proctor M. R. E., 2010, Physical Review Letters, 104, 024503

Jałocha J., Bratek Ł., Kutschera M., Skindzier P., 2010, MNRAS, 406, 2805

Ji Y., Cole L., Bushby P., Shukurov A., 2013, ArXiv e-prints 1312.0408

Kalberla P. M. W., Dedes L., 2008, A&A, 487, 951

Kamphuis P., Rand R. J., Józsa G. I. G., Zschaechner L. K., Heald G. H., Patterson M. T., Gentile G., Walterbos R. A. M., Serra P., de Blok W. J. G., 2013, MNRAS, 434, 2069

Kawata D., Grand R. J. J., Cropper M., 2012, in European Physical Journal Web of Conferences, Vol. 19, Stellar dynamics around transient co-rotating spiral arms, p. 7006

Kennicutt Jr. R. C., Armus L., Bendo G. Calzetti D., Dale D. A., Draine B. T., Engelbracht C. W., Gordon K. D., et al., 2003, PASP, 115, 928

Khoperskov A. V., Eremin M. A., Khoperskov S. A., Butenko M. A., Morozov A. G., 2012, Astronomy Reports, 56, 16

Kleeorin N., Mond M., Rogachevskii I., 1996, A&A, 307, 293

Kleeorin N., Moss D., Rogachevskii I., Sokoloff D., 2000, A&A, 361, L5

—, 2002, A&A, 387, 453

Kleeorin N., Ruzmaikin A. A., 1982, Magnetohydrodynamics, 18, 116

Krasheninnikova I., Shukurov A., Ruzmaikin A., Sokoloff D., 1989, A&A, 213, 19

Krause F., Raedler K.-H., 1980, Mean-field magnetohydrodynamics and dynamo theory. Pergamon Press, Oxford

Krause M., Hummel E., Beck R., 1989, A&A, 217, 4

Kulsrud R. M., Zweibel E. G., 2008, Rep on Prog Phys, 71, 046901

Masset F., Tagger M., 1997, A&A, 322, 442

McComb W. D., 1990, The physics of fluid turbulence

Meidt S. E., Rand R. J., Merrifield M. R., 2009, ApJ, 702, 277

Mestel L., Subramanian K., 1991, MNRAS, 248, 677

Mitra D., Candelaresi S., Chatterjee P., Tavakol R., Brandenburg A., 2010, Astronomische Nachrichten, 331, 130

Moffatt H. K., 1969, Journal of Fluid Mechanics, 35, 117

—, 1978, Magnetic field generation in electrically conducting fluids. Cambridge University Press, Cambridge, England

Moss D., 1995, MNRAS, 275, 191

—, 1996, A&A, 308, 381

—, 1998, MNRAS, 297, 860

Moss D., Beck R., Sokoloff D., Stepanov R., Krause M., Arshakian T. G., 2013, ArXiv e-prints

Moss D., Shukurov A., Sokoloff D., 1998, Geophysical and Astrophysical Fluid Dynamics, 89, 285

—, 1999, A&A, 343, 120

—, 2000, A&A, 358, 1142

Moss D., Shukurov A., Sokoloff D., Beck R., Fletcher A., 2001, A&A, 380, 55

Moss D., Sokoloff D., Beck R., Krause M., 2010, A&A, 512, A61

Moss D., Stepanov R., Arshakian T. G., Beck R., Krause M., Sokoloff D., 2012, A&A, 537, A68

Otmianowska-Mazur K., Elstner D., Soida M., Urbanik M., 2002, A&A, 384, 48

Parker E. N., 1955, ApJ, 122, 293

Patrikeev I., Fletcher A., Stepanov R., Beck R., Berkhuijsen E. M., Frick P., Horellou C., 2006, A&A, 458, 441

Phillips A., 2001, Geophysical and Astrophysical Fluid Dynamics, 94, 135

Poezd A., Shukurov A., Sokoloff D., 1993, MNRAS, 264, 285

Pouquet A., Frisch U., Leorat J., 1976, Journal of Fluid Mechanics, 77, 321

Putman M. E., Peek J. E. G., Joung M. R., 2012, ARA&A, 50, 491

Quillen A. C., Dougherty J., Bagley M. B., Minchev I., Comparetta J., 2011, MNRAS, 417, 762

Rädler K.-H., Kleeorin N., Rogachevskii I., 2003, Geophysical and Astrophysical Fluid Dynamics, 97, 249

Rheinhardt M., Brandenburg A., 2012, Astronomische Nachrichten, 333, 71

Rheinhardt M., Devlen E., Rädler K.-H., Brandenburg A., 2014, MNRAS, 441, 116

Roberts P. H., Soward A. M., 1975, Astronomische Nachrichten, 296, 49

Rogachevskii I., Kleeorin N., 2000, Phys. Rev. E, 61, 5202

Rohde R., Beck R., Elstner D., 1999, A&A, 350, 423

Roškar R., Debattista V. P., Quinn T. R., Wadsley J., 2012, MNRAS, 426, 2089

Ruzmaikin A. A., Shukurov A. M., Sokoloff D. D., 1988, Magnetic Fields of Galaxies. Kluwer, Dordrecht

Ruzmaikin A. A., Turchaninov V. I., Zeldovich I. B., Sokoloff D. D., 1979, Ap&SS, 66, 369

Ryu D., Schleicher D. R. G., Treumann R. A., Tsagas C. G., Widrow L. M., 2012, Space Sci. Rev., 166, 1

Sellwood J. A., 2011, MNRAS, 410, 1637

Shapovalov D. S., Vishniac E. T., 2011, ApJ, 738, 66

Shetty R., Vogel S. N., Ostriker E. C., Teuben P. J., 2007, ApJ, 665, 1138

Shukurov A., 1998, MNRAS, 299, L21

Shukurov A., 2004, ArXiv e-prints

Shukurov A., 2005, in Lecture Notes in Physics, Berlin Springer Verlag, Vol. 664, Cosmic Magnetic Fields, Wielebinski R., Beck R., eds., p. 113

Shukurov A., Sarson G. R., Nordlund Å., Gudiksen B., Brandenburg A., 2004, Ap&SS, 289, 319

Shukurov A., Sokoloff D., 1998, Stud. Geoph. et Geod., 42, 391

Shukurov A., Sokoloff D., 2008, in Les Houches, Vol. 88, Dynamos, Cardin P., Cugliandolo L. F., eds., Elsevier, pp. 251–299

Shukurov A., Sokoloff D., Subramanian K., Brandenburg A., 2006, A&A, 448, L33

Smith A., 2012, PhD thesis, School of Mathematics and Statistics, Newcastle University, Newcastle Upon Tyne

Smith A., Fletcher A., Shukurov A., 2012, In preparation

Sokoloff D., Shukurov A., Krause M., 1992, A&A, 264, 396

Subramanian K., Brandenburg A., 2006, ApJ, 648, L71

Subramanian K., Mestel L., 1993, MNRAS, 265, 649

Subramanian K., Narasimha D., Chitre S. M., 1994, MNRAS, 271, L15

Sur S., Shukurov A., Subramanian K., 2007, MNRAS, 377, 874

Tabatabaei F. S., Krause M., Fletcher A., Beck R., 2008, A&A, 490, 1005

Thim F., Tammann G. A., Saha A., Dolphin A., Sandage A., Tolstoy E., Labhardt L., 2003, ApJ, 590, 256

Vainshtein S. I., Kitchatinov L. L., 1983, Geophysical and Astrophysical Fluid Dynamics, 24, 273

Van Eck C. L., Brown J. C., Stil J. M., Rae K., Mao S. A., Gaensler B. M., Shukurov A., Taylor A. R., Haverkorn M., Kronberg P. P., McClure-Griffiths N. M., 2011, ApJ, 728, 97

Vishniac E. T., 2012a, in American Astronomical Society Meeting Abstracts, Vol. 220, American Astronomical Society Meeting Abstracts #220, p. 308.05

—, 2012b, in SpS4-New Era for Interstellar and Intergalactic Magnetic Fields, IAU XXVIII General Assembly, Beijing

Vishniac E. T., Cho J., 2001, ApJ, 550, 752

Vishniac E. T., Shapovalov D., 2014, ApJ, 780, 144

Wada K., Baba J., Saitoh T. R., 2011, ApJ, 735, 1

Westfall K. B., Bershady M. A., Verheijen M. A. W., Andersen D. R., Martinsson T. P. K., Swaters R. A., Schechtman-Rook A., 2011, ApJ, 742, 18